Title

Mechanisms of Plasma Energization during Magnetotail Reconnection in Earth's Magnetosphere

Author

Beyene, Fekireselassie

Publication Date

2024

Peer reviewed|Thesis/dissertation

UNIVERSITY OF CALIFORNIA

Los Angeles

Mechanisms of Plasma Energization during Magnetotail Reconnection in Earth's Magnetosphere

A dissertation submitted in partial satisfaction
of the requirements for the degree
Doctor of Philosophy in Geophysics & Space Physics

by

Fekireselassie Beyene

2024

ABSTRACT OF THE DISSERTATION

Mechanisms of Plasma Energization
during Magnetotail Reconnection
in Earth's Magnetosphere

by

Fekireselassie Beyene
Doctor of Philosophy in Geophysics & Space Physics
University of California, Los Angeles, 2024
Professor Vassilis Angelopoulos, Co-Chair
Professor Hao Cao, Co-Chair

Magnetic reconnection, a process characterized by the mixing of distinct magnetic flux tubes within a magnetized plasma, results in the exchange of energy between the electromagnetic fields of these flux tubes and the confined plasma. This phenomenon is observed across various astrophysical entities, playing a pivotal role in the energization and global transport of plasma. On Earth, magnetic reconnection is integral to the dynamics of the magnetotail, facilitating the depressurization of the tail during earthward convection, markedly elevating the temperature of magnetotail plasma, and generating field-aligned particle beams that promote wave generation and growth. Observations across the magnetotail and under varying levels of geomagnetic activity have demonstrated magnetic reconnection's importance and prevalence. It significantly influences global magnetospheric plasma energy transport during both quiescent and active periods through episodic magnetic reconnection events that propel heated plasma ejecta in both earthward and tailward directions. Given its central role

in global plasma transport and energization within the magnetotail this Ph.D. thesis seeks to elucidate key aspects of magnetotail reconnection to enhance our understanding of the magnetotail's evolution.

Investigating the dynamics of magnetotail reconnection presents a multifaceted challenge. This Ph.D. thesis leverages ongoing inner-magnetosphere missions and advanced magnetic field models to dissect three critical aspects of this issue. 1) Assess whether global plasma convection during geomagnetic storms is influenced by intermittent or quasi-continuous magnetotail reconnection. While prior studies have primarily concentrated on relatively quiet conditions, revealing two distinct plasma transport modes in the magnetotail—substorms characterized by irregular reconnection at approximately 25-30 Earth radii (R_E) and steady magnetospheric convection featuring more consistent reconnection beyond 40 R_E—a detailed investigation during intense storm conditions is notably absent. This analysis aims to categorize magnetotail reconnection during storms as either intermittent or continuous, offering significant insights into energy transport mechanisms under such conditions. 2) Examine the frequency and impact of near-Earth magnetotail reconnection during storms, a phenomenon less understood compared to non-storm conditions traditionally located beyond 25 R_E. With the recent solar cycle prompting more frequent storms, emerging evidence supports the occurrence of very-near-Earth reconnection (VNERX). This study explores VNERX events and their contribution to storm dynamics. 3) Study the heating processes that take place during magnetotail reconnection. Simulations and observations show that most of the particle energy gained through reconnection is in the form of thermal energy. In the near-Earth tail, gradients in plasma pressure can transfer the kinetic energy from reconnection ejecta into plasma heat far away from the x-line. However, in the mid-tail, where reconnection occurs most frequently, these gradients are diminished. We study whether particle heating is still significant in magnetotail reconnection at these distances, and what factors control that heating. The heating process of mid-tail reconnection has important implications towards understanding the thermal profile of the plasma sheet, a major source of plasma for the inner

magnetosphere and the storm-associated ring current.

The dissertation of Fekireselassie Beyene is approved.

Roger Hale Varney

Marco CM Velli

Hao Cao, Committee Co-Chair

Vassilis Angelopoulos, Committee Co-Chair

University of California, Los Angeles

2024

To my mother and father

TABLE OF CONTENTS

LIST OF FIGURES

LIST OF TABLES

VITA

2016 B.S. (Physics), Augsburg University.

2016–2019 NSF GRFP Fellowship

2019 M.S. (Geophysics and Space Physics), UCLA.

2019–present Research Assistant, Earth, Planetary, and Space Sciences Department, UCLA.

PUBLICATIONS

Beyene, F., Angelopoulos, V.,Runov, A., Artemyev, A. (In review, 2024). Earthward-tailward asymmetry of plasma heating in reconnection outflow in Earth's magnetotail. JGR: Space Physics

Beyene, F., Angelopoulos, V. (2024). Storm-time very-near-earth magnetotail reconnection: A statistical perspective. Journal of Geophysical Research: Space Physics, 129, e2024JA032434. doi: 10.1029/2024JA032434

Beyene, F., Angelopoulos, V., Runov, A., Artemyev, A. (2022). Properties of storm-time magnetic flux transport. JGR: Space Physics, 127, doi: 10.1029/2022JA030357

Runov, A., Angelopoulos, V., Weygand, J.M., Artemyev, A.V., Beyene, F., et al. (2022). Thin current sheet formation and reconnection at X -10 R_E during the main phase of a magnetic storm. JGR: Space Physics, 127. doi: 10.1029/2022JA030669

Beyene, F., A. Artemyev, V. Angelopoulos, I. Vasko, Phys. Plasmas 25, 082901 (2018). doi: 10.1063/1.5032111

CHAPTER 1

Introduction

The magnetotail, which constitutes the nightside plasma environment, is characterized by dynamic magnetic and electric fields that operate across various temporal and spatial scales. Shown in Figure 1.1 this region is broadly divided into three distinct areas: the magnetotail lobes, the plasma sheet, and the inner magnetosphere. Each area is defined by unique attributes such as magnetic field strength and topology, and plasma pressure. Because of the complex structures of each region I describe them in more detail here.

The magnetotail lobes, located at high latitudes and bounded by the magnetopause, are crucial for understanding plasma dynamics in space. This region is composed of low density ($\sim 0.01 cm^{-3}$) and temperature (ion temperatures typically $< 1 - 2$ keV) [*Lu et al.*, 2017] plasma on open field lines [*Koleva and Sauvaud*, 2008]. The magnetic field strength follows a x^{-p} profile where $p \sim 1.2$ [*Nakai et al.*, 1991]. This region couples the ionospheric polar cap to the solar wind through open fieldlines that cross the magnetopause. Because of this coupling, the lobes can be composed of plasma from several sources. Solar wind sources of electrons directed earthward along lobe field lines contribute to polar rain electrons seen in the polar cap [*Shirai et al.*, 1998], and ionospheric origin ions escape along these field lines to create ion outflows [*Dandouras*, 2021]. These ion outflows can $\mathbf{E} \times \mathbf{B}$ drift and populate other regions of the magnetotail, thus the lobes act as a conduit for ionospheric sourced ions. Towards lower latitudes, the magnetic field magnitude decreases, and the plasma pressure, density, and temperature increase. The magnetic field lines also transition from being open, when one fieldline footpoint maps to the solar wind, to closed, when both footpoints map to

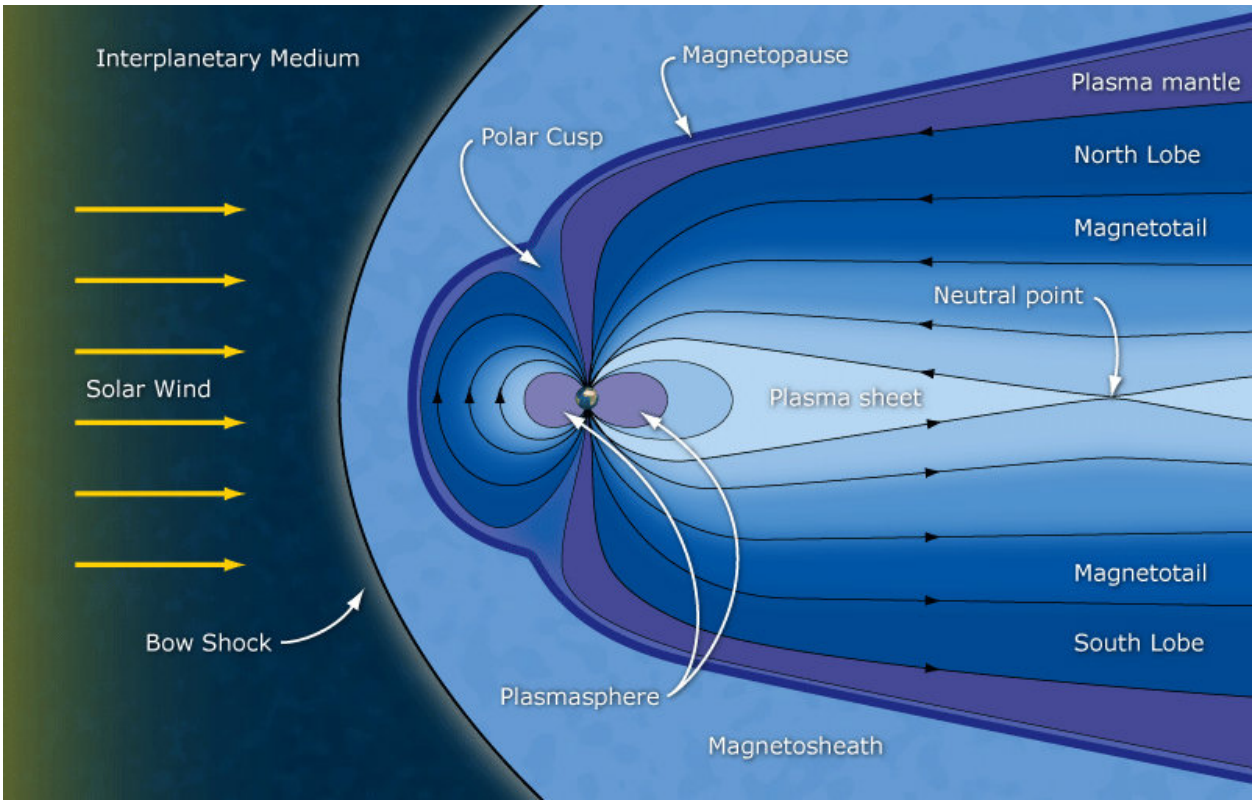

Figure 1.1: *2-D schematic of magnetosphere regions [Case, 2014]. The magnetotail lobes are located in the high latitude magnetotail, the plasma sheet is situated at the low latitude magnetotail, and the inner magnetosphere exists at near-Earth distances.*

the Earth. This closed fieldline region of the magnetotail is known as the plasma sheet.

The plasma sheet is the warm ($T \sim 1-10s$ keV) dynamic region of the magnetotail that straddles the magnetic equator. It extends anti-sunward from its near-Earth edge $\sim 8-10R_E$ and is bounded by the plasma sheet boundary layer [PSBL, *Eastman et al.*, 1984; *Frank*, 1976], which features intense field-aligned and bi-directional ion beams [*Eastman et al.*, 1984; *Grigorenko et al.*, 2009]. Embedded within the plasma sheet is the magnetotail current sheet [*Artemyev et al.*, 2021], a high-β regime that separates earthward- from tailward-directed magnetotail magnetic field lines. The characteristics of both the plasma sheet and the embedded current sheet depend on solar wind and magnetotail lobe conditions [*Birn et al.*,

2021]. The transport of momentum and energy within the plasma sheet primarily occurs through earthward flows at speeds close to the local Alfvén velocity ($V_A = \frac{B_{lobe}}{\sqrt{\mu_0 \rho_i}}$) known as "bursty bulk flows" [BBFs, *Angelopoulos et al.*, 1992]. BBFs typically coincide with localized enhancements in magnetic flux known as "dipolarizing flux bundles" [DFBs *Liu et al.*, 2014] that channel magnetic flux and energy towards the near-Earth magnetosphere region known as the inner magnetosphere.

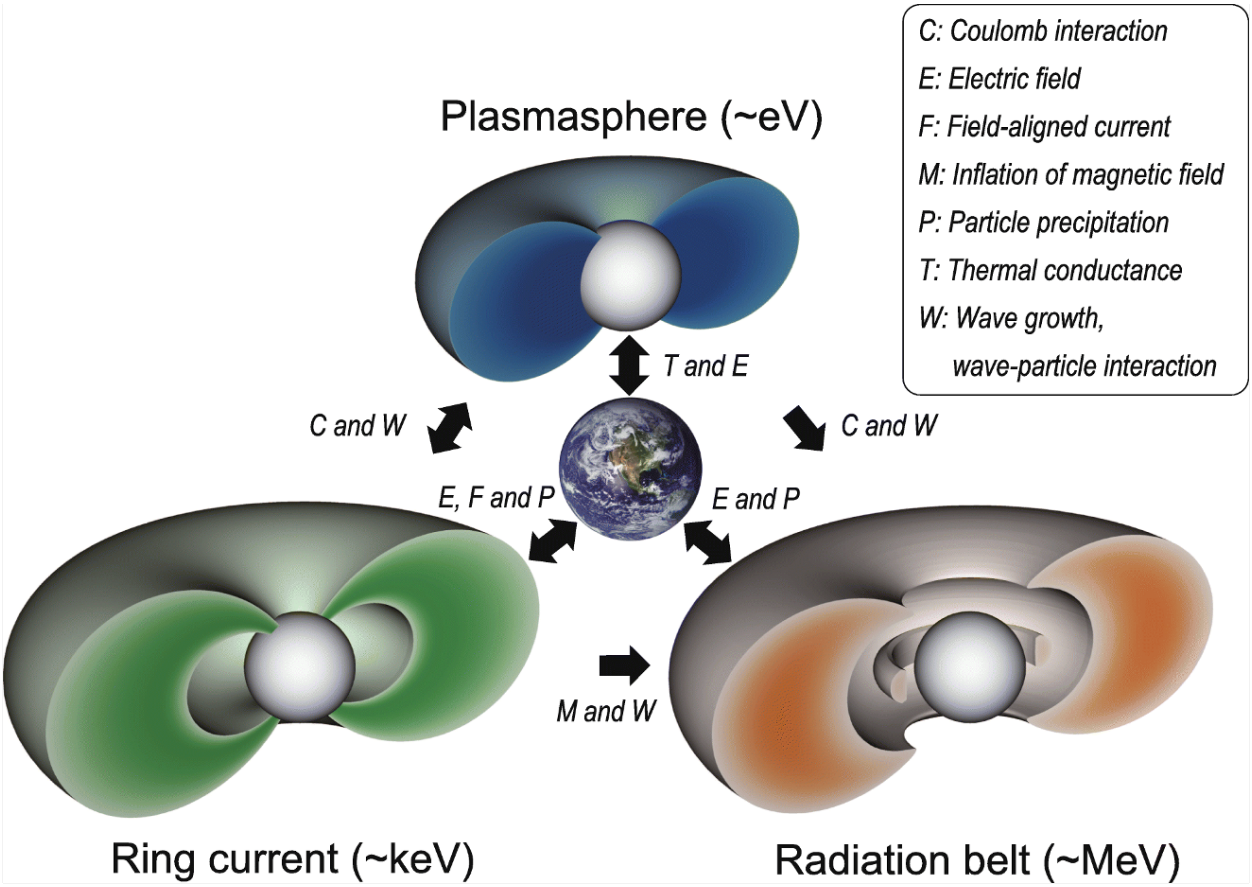

Figure 1.2: *Schematic of inner magnetosphere regions [Ebihara, 2019]. The black arrows between the subregions denote particle and wave mechanisms that couple each region.*

The inner magnetosphere [*Ebihara and Miyoshi*, 2011] houses strong dipolar magnetic fields and particles spanning a wide energy range ($\sim$ 1 eV $-10s$ MeV). Shown in Figure 1.2 this region is divided into several overlapping sub-regions: the inner and outer radiation

belts (typical energies > 100 keV), the cold and dense co-rotating plasmasphere ($\sim$ eV), and (near the magnetic equator) the ring current ($1 - 100$ keV). The magnetic field and plasma properties of these sub-regions vary with solar wind and outer magnetosphere conditions. The inner magnetosphere extends to L-shell [*McIlwain*, 1961] ~ 8 and couples to the ionosphere through field-aligned currents [*Vasyliunas*, 1970; *Wolf*, 1970] and field-aligned Poynting flux [*Keiling et al.*, 2003], allowing energy sourced from the solar wind and outer magnetosphere to heat the ionosphere and produce aurora.

To understand the evolution and stability of the magnetotail regions described above requires an understanding of the underlying energy transport that drive and couple these regions. Over the past 60 years research has been dedicated to describing the current systems and instabilities [*Birn et al.*, 2021] relevant to magnetospheric energy transports. Past literature has made clear that several instabilities are of major importance to the energy dynamics of the magnetotail. First, the ballooning/interchange (B/I) instability [*Pontius and Wolf*, 1990; *Bernstein et al.*, 1958; *Chen and Wolf*, 1999] arises from earthward gradients of flux tube entropy, driving the earthward motion of flux tubes depleted in entropy. Second, current sheet flapping [*Sergeev et al.*, 2004; *Sitnov et al.*, 2004, 2014] involves global north-south oscillations of the equatorial current sheet that propagate both earthward and azimuthally. Lastly, magnetic reconnection or tearing-type modes [*Sitnov et al.*, 2019; *Lu et al.*, 2018] occur, leading to changes in magnetic field topology and the transfer of magnetic field energy to particles. This transfer can happen through resistive particle collisions in the collisional regime or via electric fields such as Hall and reconnection fields in the collisionless regime. During magnetic reconnection plasma bulk kinetic energy, enthalpy, and heat flux can increase substantially several ion inertial lengths ($\lambda_i = c/\omega_{pi}$) away from the reconnection site. Of these processes, magnetic reconnection plays the unique role of explosively increasing the energy content of magnetotail plasma as well as initiating magnetotail convection [*McPherron*, 2015; *Drake et al.*, 2003; *Oka et al.*, 2010; *Lu et al.*, 2018]. Although considerable effort has been devoted to studying the physics of magnetotail reconnection

during periods of low to moderate activity, the dynamics and characteristics of magnetotail reconnection during highly active periods have been neglected. This is partially owed to the limited spacecraft observations at high time and energy resolution of the storm-time near-Earth and mid-tail regions. But the decades of high-resolution plasma and wave instruments onboard the Time History of Events and Macroscale Interactions during Substorms [THEMIS, *Angelopoulos et al.*, 2008] and Magnetospheric Multiscale [MMS, *Burch et al.*, 2016] missions have now made it feasible to address this gap. This Ph.D. is motivated to utilize these missions to investigate the role of magnetic reconnection in energy transport within a very active magnetotail. Because magnetic reconnection lies at the center of this Ph.D. I next provide a brief review of reconnection theory.

The theory of magnetic reconnection can be traced back to studies of heating related to solar flares [*Giovanelli*, 1939, 1947]. This theory was further developed when *Cowling* [1953] discovered that thin current sheets were susceptible to magnetic reconnection, and *Dungey* [1961] proposed that magnetic reconnection played a pivotal role in global magnetospheric convection. The initial model of reconnection depended on non-ideal magnetohydrodynamic (MHD) theory. Called the Sweet-Parker model [*Sweet*, 1958; *Parker*, 1957], it assumed a thin current sheet separates two regions of oppositely directed magnetic fields and maintains a finite and constant resistive diffusion region.The resistivity of the diffusion region is due to particle collisions, and thus this model explains collisional reconnection. This model is sometimes called the "slow" reconnection model because the magnetic field merging rate is much smaller than the inflow Alfvén speed [*Pontin and Priest*, 2022]. When this model was applied to the field of solar physics, it was found that in order to release energy on timescales relevant to solar flares required unreasonably large magnetic field gradients. Thus a new model was warranted, where the magnetic field merging rate was faster.

The next magnetic reconnection model developed was the Petschek model [*Petschek*, 1964]. This model, also describing collisional reconnection, differed from the earlier Sweet-Parker model by reducing the diffusion region to be a fraction of the total length of the

current sheet. This increased the merging rate to a maximum of 0.01 - 0.1 V_A. Since then, a family of collisional reconnection models have been developed [*Pontin and Priest*, 2022; *Priest and Forbes*, 2000]. It has been shown that reconnection can occur under driven conditions [*Pontin and Priest*, 2022] and spontaneously (where resistive instabilities initiate reconnection) [*Furth et al.*, 1963]. While these models were reasonable in certain plasma environments (e.g., the solar chromosphere), observations of Earth's magnetosphere revealed that the setting was largely collisionless. Observations of reconnection, both at Earth's magnetopause and magnetotail, showed characteristics that were not explainable by the previous collisional models. For example, the presence of an out-of-plane quadrupole magnetic field was frequently observed [*Øieroset et al.*, 2001] in Earths magnetosphere, but was absent in collisional reconnection models. With the development of collisionless reconnection theory, models were developed that were more physically applicable to these regions and better matched the observations.

The collisionless reconnection model differs from the collisional reconnection model in several ways. In collisionless reconnection the diffusion region is composed of an outer ion-diffusion region and an inner (embedded) electron-diffusion region that are both localized near the x-point [*Hesse and Cassak*, 2020]. This is due to the difference in the gyro-radii of ions and electrons, which causes ions to become demagnetized further from the x-line than electrons. Consequently, Hall electric fields pointing towards the neutral sheet form in the diffusion region [*Mandt et al.*, 1994]. The reconnection rate is dictated by standing whistler-mode waves at the external outflow region [*Mandt et al.*, 1994] consistent with the Hall currents generating an out-of-plane quadrupolar magnetic field [*Sonnerup*, 1979; *Øieroset et al.*, 2002; *Drake et al.*, 2008]. A significant difference between these collisional and collisionless models is the physics of dissipation in the diffusion region. In collisional reconnection, ideal Ohm's law breaks down due to the particle species collisions (or general plasma turbulence) that introduces a resistance (the $\eta\mathbf{J}$ term in the generalized Ohm's law). However, in collisionless reconnection, this effect is negligible, and dissipation is mediated

instead by the electron pressure tensor [*Hesse et al.*, 1999]. This difference in the breakdown of Ohm's law has consequences for the energy partitioning of the converted magnetic energy into particle energy. In collisional reconnection, the Sweet-Parker model suggests that the inflowing magnetic energy is equally partitioned between kinetic and thermal energy, while in the Petschek model, 2/5 of the inflowing magnetic energy is converted to heat and 3/5 to kinetic energy [*Pontin and Priest*, 2022]. In collisionless reconnection, the partitioning is less clear and has been an active area of research in the past decade. Observations concluded that more energy was partitioned to the ions than to the electrons [*Phan et al.*, 2013, 2014], but overall the majority of energy is converted to enthalpy flux (i.e., thermal energy) [*Lu et al.*, 2018; *Birn and Hesse*, 2010; *Aunai et al.*, 2011; *Lu et al.*, 2013]. These results demonstrate that magnetic reconnection plays a pivotal role in heating and energizing magnetotail plasma, however, there is a gap in our understanding of where and how often this occurs, especially during very-active times. One aspect where significant headway has been established, is the amount of heating to expect in magnetotail reconnection and the partitioning of magnetic energy between electron and ion thermal energy.

In collisionless reconnection, magnetic energy undergoes conversion into plasma energy, encompassing both kinetic energy and thermal energy. The distribution of energy among plasma species and between kinetic and thermal energies is currently an active area of research. Energy conversion due to magnetic reconnection is highly dependent on the background conditions, thus a comprehensive understanding of energy conversion to explain this observed variability is necessary. *Phan et al.* [2014] used observations of magnetopause reconnection exhausts from THEMIS to demonstrate that 20% of the inflowing magnetic energy is converted into ion thermal energy. The authors showed that ion heating in magnetic reconnection is linearly related to inflowing magnetic energy, $\Delta T_i = 0.13 m_i V_{A,inflow}^2$, where $V_{A_inflow} = \frac{B_i}{\sqrt{\rho_i \mu_0}}$ is the Alfvén velocity at the inflow regions of the reconnection site. Thus in the magnetotail, where lobe magnetic field strength is 10-30 nT and ion density is 0.05 cm^{-3}, about 1-10 keV increase in thermal energy is expected. *Phan et al.* [2013] con-

ducted a similar analysis of electron bulk heating and showed that electron thermal energy is linearly related to inflowing magnetic energy as $\Delta T_e = 0.017 m_i V_{A,inflow}^2$, thus approximately 1.7% of the inflowing magnetic energy is released as electron heating. However, it should be noted energy partitioning is dependent on upstream (inflow) parameters. Using 2.5D PIC simulations of antiparallel (no guide field) collisionless reconnection *Haggerty et al.* [2015] showed that while the total heating (ion + electron temperature increase) scales as $\Delta(T_i+T_e) = 0.15 m_i V_{A,inflow}^2$ (consistent with earlier work by [*Phan et al.*, 2013, 2014]),a large scale parallel electric field develops in the outflow region that is controlled by the upstream electron beta, $\beta_e = \frac{2T_{e,inflow}}{m_i V_{A,inflow}^2}$, throttling ion heating and boosting electron heating. It is clear then, that energy throughput during magnetotail reconnection depends on the magnetic field and plasma properties which are location dependent in the magnetotail. Not only is the location of magnetotail reconnection significant for energization, but the frequency of this process has severe implications for the dynamics of global energy transport. Establishing these factors is essential to contextualize the role of reconnection in this process.

Magnetotail reconnection plays a crucial role in magnetotail energy transport in two main ways: 1) by enabling global convection of magnetic flux and energy to persist without excessively high plasma pressures developing in the near-Earth region, disrupting the pressure balance with the pressure exerted by the magnetotail lobes [*Erickson and Wolf*, 1980], and 2) it heats and accelerates the ambient magnetotail plasma producing a source population that can energize the inner magnetosphere. While much research has focused on studying the role of magnetotail reconnection in these two aspects [*Otto*, 2004; *Birn et al.*, 2021], it has primarily concentrated on near-Earth plasmas during periods of low to moderate magnetospheric activity, [see *Birn et al.*, 2021; *Sitnov et al.*, 2019; *Petrukovich et al.*, 2016, for a review of results]. There is a gap in the literature on the role of magnetotail reconnection in energy transport during more active times. To address what the role of reconnection is in magnetotail energy transport this Ph.D. will investigate three aspects: the role of magnetotail reconnection in energy transport a) globally, b) in the near-Earth tail, and c) in

the mid-tail. Towards this goal I will address (a) by investigating: Is global energy transport in the active-time magnetotail controlled by intermittent or quasi-steady reconnection, or something more complicated? I will address (b) by investigating: How frequently does very-near-Earth reconnection occur during active times? And I will address (c) by investigating: Can magnetotail reconnection significantly heat and energize plasmas in the mid-tail?

To begin, I address the question: During active times, is global energy transport controlled by an intermittent, quasi-steady, or a unique reconnection mode? While tracking the global plasma energy content of the magnetotail is difficult, tracking the global open flux content of the tail is easy. A fraction of this open magnetic flux is converted into plasma energy, and thus by tracking the open magnetic flux in the magnetotail, I can track the global rate of energy throughput in the magnetotail. During low to moderately active times the magnetosphere responds to the solar wind in one of two ways: 1) there is a delayed response in magnetotail reconnection, thus the open magnetic flux tends to accumulate in the magnetotail. This is known as the loading-unloading mode of convection. In this mode, global energy transport is controlled by an intermittent global magnetotail reconnection rate. 2) The magnetotail exhibits a balanced response where the global magnetotail reconnection rate increases to close open flux at the same rate it is introduced at high latitudes, maintaining a constant total open flux in the tail. This is known as the steady magnetospheric convection (SMC) mode. In this mode, global energy transports is controlled by quasi-steady reconnection. I will estimate the global magnetotail magnetic flux content and demonstrate that during active times, the convection mode can include both quasi-steady and loading-unloading periods. I will present statistics to show that there is no preferred mode during these active times and that the majority of active time convection, and thus global energy transport, is most likely unsteady, but directly and strongly driven in response to the solar wind driver (Chapter 2).

To address my second question, I will study magnetotail reconnection that occurs very close to Earth. Previous studies have presented case studies of reconnection that occur

within R = 10 R_E [*Angelopoulos et al.*, 2020]. This study aims to understand how frequently reconnection occurs at these locations during active times. Reconnection occurring very close to Earth has access to a denser magnetic energy reservoir, thus plasma energization at these distances is much more powerful. Very-near-Earth reconnection is thus capable of energizing local plasma to ring current energies, making this process during active times potentially crucial for global convection and storm development. I will present a case study exemplifying the characteristics of very-near-Earth reconnection, followed by statistics on the location and frequency of such events. I will demonstrate that the MLT location of reconnection at these distances is consistent with the presumed dawn-dusk asymmetry of reconnection and that the current sheet is less than 2 R_E thick for these events (Chapter 3).

Most simulations of collisionless magnetic reconnection show that the total energy available for particle energization and heating is not equally distributed between kinetic and thermal energies [*Aunai et al.*, 2011]. When considering the reconnection jets away from the reconnection ion diffusion region there is a higher thermal energy density (internal energy) than kinetic energy density. Recent hybrid and MHD simulations have reproduced this result, showing that collisionless magnetic reconnection converts magnetic energy density predominantly into thermal energy density [*Lu et al.*, 2018; *Birn and Hesse*, 2010]. They conclude that the energy converted from magnetic to kinetic energy is due to the acceleration by the Lorentz force, and the kinetic energy is subsequently quickly converted to thermal energy by the work done by the pressure gradient force [*Birn and Hesse*, 2010]. However, whether magnetotail reconnection is still an effective thermalization process in the mid-tail, where the plasma pressure gradient is small is an open question. This gap motivates my third question: Can magnetotail reconnection significantly heat and energize plasmas in the mid-tail? To address this, I will study whether magnetotail reconnection can still be an effective energization process in the more distant tail (R > 30 R_E) where these gradients are presumably weaker. I will utilize conjunctions between the MMS and Acceleration, Reconnection, Turbulence and Electrodynamics of Moon's Interaction with the Sun (ARTEMIS) missions to

measure electron and ion temperatures simultaneously earthward and tailward of reconnection sites. By comparing these temperatures, I will demonstrate a strong earthward-tailward asymmetry, with the earthward populations being hotter than those tailward. I suggest that the mechanism may be related to the closed-field line topology that exist Earthward of the reconnection site that is absent tailward of it (Chapter 4). Reconnection sites propagate tailward as the flux pileup region grows tailward, pushing the thin current sheet tailward as well thus naturally these sites reach the mid and distant tail region. The source of hot plasma in the more distant tail has been an open question [e.g., *Mist et al.*, 2001] due to the lack of spacecraft observations there. This study suggests a natural sources of heated and energized plasma for the plasma sheet in this region. Following these chapters I will summarize my main findings and conclusions and discuss further work to be done to address the role of magnetotail reconnection in plasma energization during active times (Chapter 5).

CHAPTER 2

Properties of Storm-Time Magnetic Flux Transport

Abstract

Magnetospheric convection, the transport of magnetic flux, along with mass, and energy, plays a vital role in magnetosphere-ionosphere coupling and ring-current energization. It is particularly intense during magnetic storms, a mode of circulation driven by prolonged and strong solar wind driving. A large body of work has quantified the evolution of flux circulation during nonstorm times, in particular during substorms and steady magnetospheric convection events (SMCs). However, transport during storms has not been duly characterized. Using magnetotail flux observations we explore storm-time modes of convection and compare them to their nonstorm-time counterparts. We find that storm-time convection often encompasses loading- unloading periods (akin to substorms) and SMCs (akin to those during nonstorm times). However, loading- unloading events and SMCs are present during only 25% and 21% (respectively) of the (95) storms examined. We also investigate the solar wind conditions during these modes for storm versus nonstorm times. We find that these modes have characteristic profiles in AE, solar wind driving, and open flux content during storms that are similar to their nonstorm-time counterparts, but larger in magnitude. Therefore, these convection modes occur during storm and nonstorm periods alike, and in particular they are not required for a storm to progress. Thus, what makes storms special, their intense ring current, is likely not attributable to the (un)steadiness of flux circulation, but to the prolonged and intense background flux circulation within which these modes are embedded, and hence to the ultimate strength of the solar wind driver.

2.1 Introduction

When the solar wind magnetic field is antiparallel to that in the dayside magnetosphere, magnetic reconnection at the dayside and subsequent electrodynamic energy coupling between the solar wind and the magnetosphere at the high-latitude magnetopause are enhanced [*Dungey*, 1961]. Solar wind kinetic energy is subsequently transported through and converted within the magnetosphere via nightside reconnection at the magnetotail current sheet; it is ultimately dissipated in the ionosphere and ring current. This energy drives many of the dynamic processes in the near-Earth space environment. Different modes of circulation comprise this solar wind-magnetosphere interaction. Solar wind energy can be first stored (loaded) as magnetic energy in the magnetotail and then be quickly released and converted to kinetic energy (unloaded) by nightside reconnection. Conversely, solar wind energy can be channeled in a near-continuous fashion throughout the magnetosphere. The former mode is known as the magnetospheric substorm [*McPherron*, 1979; *Russell and McPherron*, 1973]. During it, the reconnected magnetic flux is accumulated in the magnetotail lobes for approximately an hour (magnetic flux loading), because night- side reconnection is too slow to remove the incoming flux. Then, very rapidly (on time scale of minutes to tens of minutes), the accumulated flux is reconnected in the magnetotail and is transported back toward the dayside (magnetic flux unloading). Thus, substorms are often referred to as a loading-unloading process [*Hones*, 1979; *McPherron*, 1979; *Russell and McPherron*, 1973]. The latter mode, enhanced quasi-steady convection, is also known as convection bays [*Pytte et al.*, 1978; *Sergeev et al.*, 2001], balanced reconnection intervals [BRIs, *Dejong et al.*, 2008; *DeJong et al.*, 2009], or steady magnetospheric convection events [SMCs, *Sergeev*, 1977; *Sergeev et al.*, 1996]. It represents a quasi-steady state of magnetospheric flux throughput, in response to low-to-moderate solar wind driving. As dayside reconnected magnetic flux is transported to the magnetotail, an equivalent amount of flux is reconnected in the magnetotail and transported earthward such that the net amount of magnetic flux in the tail stays approximately constant. However, when the solar wind driving is strong, a more complicated

magnetospheric response emerges.

During prolonged intervals of strong solar wind energy input, long duration magnetospheric responses appear, associated with intense AE and D_{ST} (disturbance storm-time) index signatures (on the order of +500 nT or higher and -100 nT or lower, respectively) and with bright aurorae throughout an expanded oval. These responses, known as geomagnetic storms [*Gonzalez et al.*, 1994], are accompanied by large energy deposition into the ring current [*Dessler and Parker*, 1959; *Sckopke*, 1966], an Earth-encircling current created by westward drifting ions and eastward drifting electrons, typically residing around 6–8RE. In fact, the D_{ST} changes are directly proportional to the total ring-current energy [*Dessler and Parker*, 1959; *Sckopke*, 1966], and storm intensity is measured by the magnitude of the (negative) excursion of D_{ST}, so understanding the origin of the ring current energization is tantamount to understanding the root cause of storm development. The ring current impacts all regions in near-Earth space, including the inner-magnetosphere-ionosphere system, which are coupled via field-aligned currents [*Iijima and Potemra*, 1976a,b] driven by magnetospheric pressure gradients and shear stresses. During storm times, inner-magnetosphere trapped populations are energized [*McIlwain*, 1966], and electromagnetic ion cyclotron (EMIC) and magnetosonic waves are generated, resulting in strong wave-particle interactions and particle pitch-angle and energy scattering [*Ebihara*, 2019, and references therein]. The question arises, however, how is the ring-current energized during such times and which (if any) mode of convection familiar to us from nonstorm times (the loading-unloading mode, the steady magnetospheric convection mode, or a combination of these two) may be responsible for that energization?

Two storm-time convection models were proposed during the early years of space research to address this question: the quasi-steady enhanced global convection model [*Axford*, 1969] and the superposition of substorms model [*Akasofu and Chapman*, 1961; *Chapman*, 1962]. These are akin to the modern-day steady magnetospheric convection mode and the loading-unloading mode, respectively, therefore they are still pertinent and deserve discussion here.

In the quasi-steady enhanced convection model of storms [*Clauer*, 2006; *Clauer and McPherron*, 1980; *Hori et al.*, 2005], large-scale, long duration cross-tail magnetospheric electric fields enabled by dayside-then-nightside reconnection cause plasma sheet particles to $\mathbf{E} \times \mathbf{B}$ drift into the inner magnetosphere. The earthward motion of finite energy (thermal) particles is accompanied by a diamagnetic drift that transports particles along magnetospheric electric fields, leading to further heating. As the inward pressure gradients get stronger near the Earth, ions (which carry most of the plasma sheet particle energy) start to experience very significant duskward diamagnetic transport [*Wolf*, 1970, 1983]. If the cross-tail electric field is weak, energetic plasma is thermalized and transported toward the dusk flank and is eventually lost to the solar wind [*Kivelson and Spence*, 1988] without the ability to affect the ring current substantially. If the cross-tail electric field is strong, however, as during storm times, it can bring plasma deep into the inner magnetosphere where it can energize the ring current. Although storm development has been attributed most often to quasi-steady enhanced convection [*Kamide et al.*, 1998, and references therein], satellite observations reveal that plasma injections (abrupt, large enhancements of energetic particle fluxes accompanied by intense earthward convection) also occur frequently during storms, implying that impulsive electric fields do play some role in ring-current energization. These observations give credence to the idea that the substorm mode, a mode where strong, impulsive electric fields [*Nishimura et al.*, 2008; *Wygant et al.*, 2000] are routinely seen, could potentially energize the ring current during storms.

In the superposition of substorms model, short-lived substorm electric fields inject particles into the ring current. If instances of nightside reconnection were to occur close to the inner magnetosphere in quick succession, their cumulative injections could be sufficient to energize the ring current, causing a large DST signature [see *Akasofu*, 1968]. During storms the strong and quite variable AE activity might be due to intense, recurrent substorms. However, those are hard to discern and separate in the AE index because that index is an average of magnetometer responses across many local times, and intense but localized

current systems, which are common during active times, may mask the signature of the large-scale substorm current system. Thus, AE signatures cannot be conclusively attributed to the defining characteristic of substorms, an imbalance in dayside-versus-night- side reconnection, as opposed to a direct response of magnetospheric convection to time-variations of the solar wind driver. Estimates of the magnetotail flux, and its loading and unloading (a key signature of substorms), is needed to address this question. Such flux loading/unloading information is not directly measurable and had to be inferred from measurements of the polar cap size determined by imaging or other means which is hard to come by. In the absence of such information, this model has been met with significant criticism [see e.g., *Kamide*, 1992]. It is therefore still unclear whether loading-unloading events exist during storms, and (if they do) whether they are germane to ring-current energization and hence storm-time development, or if they are merely coincidental. Clearly, the first step in addressing this question is to determine whether and how frequently loading-unloading events occur during storms, and if they preferentially occur during a particular storm phase.

Simulation studies of magnetospheric dynamics during geomagnetic storms have explored the role that various convection modes may play in energizing the ring current [e.g., *Ebihara and Ejiri*, 2000; *Fok et al.*, 1999]. These studies showed that intense but quasi-steady convection plays a major role in storm-time ring-current energization. However, they also revealed that loading-unloading intervals (akin to nonstorm-time substorms) indeed help further energize the ring current. Observational evidence of the roles of these mechanisms in ring-current energization, however, is not conclusive. Specifically, whether and how frequently either or both modes exist in the storm-time magnetotail are still open questions.

The primary method for determining magnetospheric modes of convection during the past three decades has been interpreting polar cap size observations using the Expanding-Contracting Polar Cap (ECPC) model [*Siscoe and Huang*, 1985]. By integrating the magnetic field over the polar cap, the total open flux content in the north (or south) lobe can be estimated. It is known that as the amount of polar cap open flux increases by flux input through

a localized magnetic local time sector at the dayside cusp, the polar cap size increases; as the amount of polar cap open flux decreases by flux output through one or several localized sectors at the nightside, the polar cap size decreases [*Siscoe and Huang*, 1985]. Because the entry and exit of polar cap flux occurs at localized sectors, most of the polar cap boundary moves with the plasma (the boundary is almost everywhere adiaroic). Therefore, given the nearly fixed intensity of the magnetic field in the ionosphere, the evolution of the polar cap area (in the approximation that the boundary is fully adiaroic and noting that ionospheric plasma is incompressible) provides a good a proxy for the evolution of the open flux in the magnetotail. Satellite imagery of the auroral oval, Super-Darn observations of ionospheric flows, and AMPERE estimates of the region-1 and region-2 (R1 and R2) type field-aligned current systems have all been used to estimate the location of the polar cap boundary and hence the polar cap size [*Hubert et al.*, 2006; *Milan et al.*, 2015, 2021]. However, studies using auroral imagery are often limited by gaps in observations that occur every orbit [e.g., *Milan*, 2009; *Milan et al.*, 2009] and studies using the R1 and R2 field-aligned currents are limited to periods when these currents are strong enough to resolve a boundary. Additionally, storm-time reconnection is strong and can extend across a sizeable portion of the night-side oval, leading to a significant deformation of the assumed circular polar cap boundary. This deformation can lead to an overestimate of the open flux of the magnetosphere [*Mooney et al.*, 2020].

Another way of determining magnetospheric open flux content, that does not rely on auroral images or multispacecraft global FAC observations, is to first estimate the cross-sectional area of the magnetotail (in the $Y_{GSM}-Z_{GSM}$ plane) and then multiply it by the magnetotail lobe field strength measured in situ (under the assumption that the lobe field is approximately constant). In this method, the cross-sectional area is determined from the magnetotail radius (R_{Tail}), found by integrating a fitted model of the flaring angle, α (the angle between the solar wind flow vector and the magnetopause surface), as a function of the downtail distance x, since $\tan(\alpha) = \mathrm{d}R_{Tail}/\mathrm{dx}$. (Note that the value of R_{Tail} at x = 0, the

terminator, has been tabulated as a function of solar wind parameters and can be considered known, and x is by choice far enough from Earth that the Earth's dipole field influence has been sufficiently reduced.) The cross-sectional area is then πR_{Tail}^2 and the magnetotail open flux (in each lobe) is $\Phi_{open} = \pi R_{Tail}^2 B_{lobe}$. *Shukhtina et al.* [2009] tested this method for a simulated magnetotail and a virtual satellite, using the *Petrinec and Russell* [1996] function to estimate the magnetotail flaring angle. The authors found good agreement between the open flux estimated from the virtual satellite's measurements and the actual open flux in the simulated magnetotail (correlation coefficient >0.90). Using the Petrinec and Russell flaring angle formula, *Angelopoulos et al.* [2013] calculated the flux loading and unloading during a substorm at lunar distances (-60 R_E, where R_E is Earth's radius) and found them in good agreement with estimates of dayside reconnection from concurrent solar wind measurements, as well as with expectation from past estimates of substorm-time polar cap size variations.

In this paper, we use the aforementioned tail flux estimation method to investigate the role of loading-unloading and quasi-steady convection in driving storm-time ring-current energization. We seek to determine if and when these modes (the loading-unloading mode and the quasi-steady enhanced convection mode) are present during storms, how often they occur, how critical they may be in storm development and what, if any is the associated ring-current energization. In Section 2.2, we describe our data sets and in Section 2.3 our methodology and event selection criteria. In Section 2.4, we first present a storm case study to demonstrate how modes of convection can be identified. We also demonstrate that both loading-unloading events (hereafter referred to as L-U events, or L-Us) and quasi-steady enhanced convection events (hereafter referred to as Steady Magnetospheric Convection events, or SMCs) exist within storms. We next investigate similarities and differences between storm-time and nonstorm-time L-Us and SMCs. Using superposed epoch analysis we examine the strength and temporal profiles of solar wind conditions and tail flux for L-U events and steady convection events under storm and nonstorm times to ascertain the similarities and differences of these modes. In Section 2.5, we summarize our findings and in Section 2.6, we

discuss their importance and implications.

2.2 Data Used

We used data collected by the Geotail mission [*Kokubun et al.*, 1994; *Mukai et al.*, 1994; *Nishida et al.*, 1992] from 1996 to 2001 and the ARTEMIS [*Angelopoulos*, 2011] mission from 2012 to 2018. We also use solar wind information from the OMNI data set (provided by King and Papitashvilli, NASA/GSFC). Geotail plasma ion density and temperature data are provided by the Low Energy Particle instrument (LEP) at a 12 s cadence; magnetic field data are provided by the Magnetic Field Instrument (MGF) at a 3 s cadence. Since 1996, Geotail has had an approximately 6 day orbit, and during the tail season (i.e., when the orbit apogee, $\sim 30\ R_E$, is within the tail) spends about 2 days in the midtail region (25-30 R_E). We also analyzed plasma data from the Electrostatic Analyzer [ESA; *McFadden et al.*, 2008] and magnetic field data from the fluxgate magnetometer [*Auster et al.*, 2008] on-board the ARTEMIS mission. The two ARTEMIS satellites, in lunar orbits, are within a few R_E from each other and from the moon, and therefore spend approximately 3 days per month in the magnetotail at a radial distance $\approx 60 R_E$ from Earth. We used 4-s resolution (spin-period) ESA plasma data from such satellite magnetotail passes to obtain electron and ion density and temperature. For the solar wind magnetic field, density, velocity, magnetic field, and dynamic pressure, we used 1-min resolution OMNI data. Both the ARTEMIS and Geotail plasma and magnetic field data were resampled to the 1-min resolution of the OMNI data. In this study, both the AE and SYM-H indices are used as a measure of ionospheric activity and storm strength, respectively. The AE index [*Mayaud*, 1980] tracks the deviations in the northward component of the horizontal magnetic field (H) around the auroral oval due to ionospheric currents and is used as a measure of geomagnetic activity. The SYM-H index [*Iyemori*, 1990] is a measure of the deviation of the same (horizontal-north) component magnetic field at middle and low latitudes due to changes in global magnetospheric current

systems, but responds predominantly to the ring current. We obtained both the AE and SYM-H indices from the World Data Center—C (Kyoto) at a 1-min time cadence. Following *Gonzalez et al.* [1994], a storm-time period must have a minimum SYM-H index ≤ -30 nT. In our data set, $\sim 9\%$ of all SYM-H values were less than or equal to -30 nT. We defined 95 storms in the aforementioned interval as periods that start when the SYM-H index drops below zero, end when the SYM-H index rises back to zero, and have a minimum of at least -30 nT, the rest of the times were our nonstorm times.

2.3 Methodology

2.3.1 Tail Flux Estimation

The tail flux $F_0 = 0.5\pi(R_{Tail})^2 B_{Lobe}$ (where R_{Tail} is the magnetotail radius and B_{Lobe} is the lobe magnetic field) is found using ARTEMIS or Geotail observations along with simultaneous solar wind measurements, as described in Section 2.1. The method to calculate F_0 is described in *Shukhtina et al.* [2016] as their F_0 algorithm, and in *Angelopoulos et al.* [2013]. As detailed in *Shukhtina et al.* [2016], this method relies on several assumptions that we will describe here. First, this method assumes a zero dipole-tilt angle when computing the flaring angle. The flaring of the magnetopause can change drastically in the near-Earth region ($<10R_E$) due to the dipole-tilt angle. However, in the midtail and distant-tail, the neutral sheet is aligned parallel with the solar wind magnetic field, even during times when the Earth's dipole is severely tilted, and thus this assumption is justified for much of our data. Second, when computing the tail flux, we assume all magnetic field lines threading the Y_{GSM}-Z_{GSM} cross-section are open. This neglects the plasma sheet area where the magnetic field lines are closed. Thus, our method gives an upper estimate of the magnetotail open magnetic flux. Third, this method maps the position of a spacecraft to a point on the magnetopause by assuming the isolines of the lobe magnetic field are straight lines that are normal to the magnetopause boundary. The isolines of lobe field are indeed normal to the

magnetopause at high latitudes, but at low latitudes, near the neutral sheet, the isolines are aligned normal to the neutral sheet. Thus, the isolines have a nonzero curvature, and the mapping of a spacecraft location onto the magnetopause is overestimated in this method. However, at lunar and midtail distances, the isolines may be less curved than at near-Earth distances, and so the straight-line approximation may be appropriate when using ARTEMIS and Geotail data.

2.3.2 Identification of Modes of Magnetospheric Flux Transport

To find nonstorm-time substorms and storm-time L-U events, we identified peaks in the tail flux time series. The peak-detection algorithm used is the scipy.signal.find_peaks function found in the python scipy library [*Virtanen et al.*, 2020]. We used identified peaks in the flux data that were at least 150 min apart from neighboring peaks. We only kept peaks exceeding 0.8 GWb, because this threshold best matched our visually identified list of peaks when tested on samples of flux data. When we changed this requirement by ±20% we found that the statistical results of this study did not change significantly. Due to noise in the flux estimates, this algorithm struggled to identify when flux began to increase and ceased to decrease, i.e., the beginning and end times of the peaks. Thus, the beginning and end of a substorm or L-U event could not be clearly assessed through the flux estimates alone. Empirically, substorm growth plus expansion lasts about 30–90 min and the recovery phase lasts >60 min. By defining the start and end of an event as 50 min prior to and 100 min after a peak, in tandem with our condition that no two peaks can occur within 150 min of each other, we selected a list of substorms and L-U events that did not overlap. Using this definition, we found 333 substorms in nonstorm interval and 49 L-U events in our list of storms.

SMC events [*Sergeev et al.*, 1996] are typically defined using the following criteria: (a) steady southward interplanetary magnetic field (IMF), (b) AE $\geq\sim$200 nT, and (c) the absence of substorms. Guided by these criteria we defined SMC events in our study as periods

when: (a) the tail flux is steady such that the absolute 10-min running-difference of the tail flux ($d\Phi_{Tail}(t) = \Phi_{Tail}(t + 10min) - \Phi_{Tail}(t)$) is <0.2 GWb, and (b) the AE was over 150 nT. We chose our running-difference window to be 10 min because most data gaps in the tail flux data were <10 min. The maximum difference threshold was picked by first visually identifying SMCs in a sample of flux data, and then tuning the parameter until the algorithmically selected SMCs matched the visually identified ones. A steadiness threshold of 0.2 GWb/10 min corresponds to a difference between dayside and nightside reconnection rates of ∼333 kV, which is unrealistically high. Unreasonably high fluctuations in our flux estimates were due to the uncertainties inherit to the assumptions described in Section 2.3.1. Keeping this in mind, our method does indeed pick-out the steadiest magnetic flux intervals within our data set. Barring the large fluctuations, we interpret these intervals as periods of quasi-steady convection. After using this procedure, we kept only the events that were longer than 150 min and found 122 nonstorm-time SMCs and 31 storm-time SMCs in our database.

2.4 Results

2.4.1 Storm-Time Case Study and Statistics of Storm-Time L-U and SMC Events

Here, we first present an intense storm case study that showcases storm-time modes of convection. The storm began at approximately 25 August 2018 08:00:00 UT as determined by the observed storm sudden commencement (Figure 2.1a), a typical signature of CME-driven storms [*Joselyn and Tsurutani*, 1990]. The SYM-H index crosses 0 nT at 25 August 2018 17:48 and reaches a minimum value (SYM-H = -206 nT) at 26 August 2018 07:14; we use these times as the starting time of the main phase and recovery phase, respectively, and label them as a vertical dotted blue and red line in Figure 2.1a. ARTEMIS was in the magnetotail between 25 August 2018 and 28 August 2018, an interval encompassing the

peak of the storm time and including its entire main phase. ARTEMIS P2 was used for our estimation of the tail flux for this event. (In other storm cases, a combination of P1 and P2 was used to prevent lunar shadows and lunar wake effects from complicating the analysis.) The solar wind B_z (Figure 2.1f) reached a minimum of -18 nT at 26 August 2018 05 UT, and the solar wind dynamic pressure (Figure 2.1g) was elevated concurrently (peak solar wind dynamic pressure = 9.3 nPa at 26 August 2018 08:17 UT). Figure 2.1h shows that the elevated solar wind dynamic pressure was in good part due to an elevated solar wind density (peak density = 34 cm^{-3} at 26 August 2018 08:17 UT). The solar wind dynamic pressure and density profiles are common features of interplanetary coronal mass ejections (ICME) type solar wind structures [*Richardson and Cane*, 2010]. We see that a rapid increase in solar wind dynamic pressure due most likely to a shock in front of the CME, then a period of large dynamic pressure, which is a signature of a compressed plasma sheath in between the shock and CME structure. In our case, the solar wind also exhibited a smooth rotation of the B_z and B_y field components while the total field remained relative constant (Figure 2.1f). This suggests a magnetic cloud was embedded within the ICME [*Klein and Burlaga*, 1982]. We use dotted black vertical lines that span panels 2.1F to 2.1I to denote the start and end observation times of the magnetic cloud. Figure 2.1b shows the cumulative flux input, Φ_{in}, from the solar wind into the magnetotail over the course of the storm. It is calculated as $\Phi_{in}(t) = r_{eff} \int_0^t R_{Tail} E_r dt$, where r_{eff} is the dayside reconnection efficiency [here taken to be 0.2, *Akasofu*, 1977; *Angelopoulos et al.*, 2013], R_{Tail} is the estimated tail radius from ARTEMIS data, and $E_r = |E_{sw}| \sin(\frac{\theta}{2})$ is the solar wind electric field parallel to the dayside magnetopause reconnection line, where θ is the solar wind clock angle defined as $\tan^{-1}(\frac{B_y}{B_z})$ and $|E_{sw}|$ is the magnitude of the solar wind electric field. About 25 GWb of flux entered the magnetotail over the entire storm period.

During this storm we identified six L-U events (denoted by the vertical solid lines in Figure 2.1c) and four SMCs (denoted by the four shaded red regions in Figure 2.1c) over the main and recovery phase of the storm. The events were identified by processing the

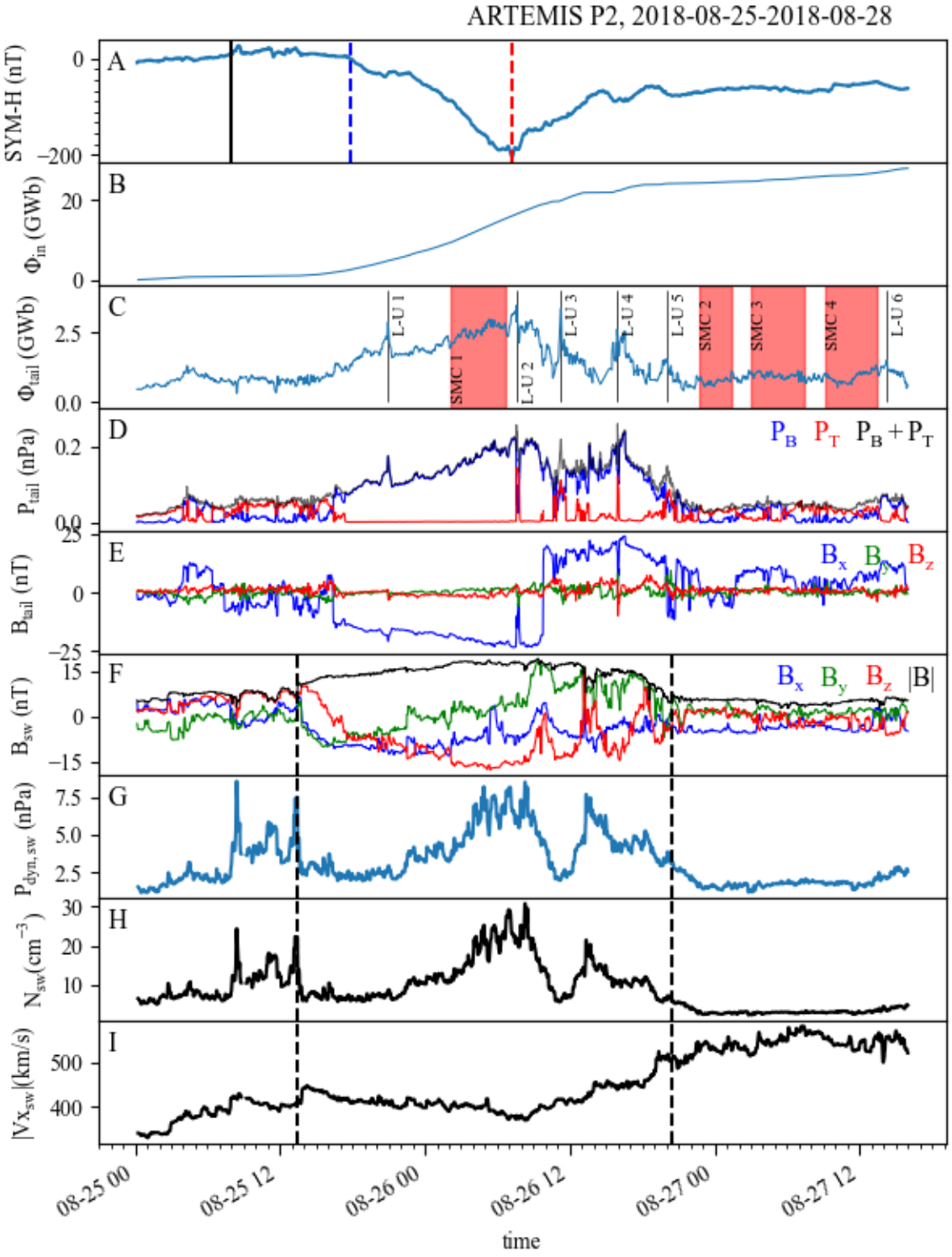
ARTEMIS P2, 2018-08-25-2018-08-28
A
SYM-H (nT)
0
−200
B
Φ_{in} (GWb)
20
0
C
Φ_{tail} (GWb)
2.5
0.0
L-U 1
SMC 1
L-U 2
L-U 3
L-U 4
L-U 5
SMC 2
SMC 3
SMC 4
L-U 6
D
P_{tail} (nPa)
0.2
0.0
P_B P_T $P_B + P_T$
E
B_{tail} (nT)
25
0
−25
B_x B_y B_z
F
B_{sw} (nT)
15
0
−15
B_x B_y B_z |B|
G
$P_{dyn,sw}$ (nPa)
7.5
5.0
2.5
H
N_{sw}(cm^{-3})
30
20
10
I
$|Vx_{sw}|$(km/s)
500
400
08-25 00
08-25 12
08-26 00
08-26 12
08-27 00
08-27 12
time

Figure 2.1: *Solar wind and magnetotail observations of the 25 August 2018 to 28 August 2018 storm period. (a) SYM-H index from the OMNI data set. The black vertical line denotes the sudden storm commencement (SSC), an abrupt increase in the SYM-H index seen in CME-driven storms. The SSC is used to mark the start of the storm. The blue dotted line denotes the beginning of the main phase, where the DST index crosses 0 nT. The red dotted line denotes the beginning of the recovery phase, where the D_{ST} begins to increase from a minimum value. (b) Cumulative open flux created by dayside reconnection. (c) Instantaneous estimate of global open flux content of the magnetotail. The solid vertical lines denote L-U events identified by our detection algorithm. The dashed vertical lines denote L-U events missed by the peak-detection algorithm but evident in the time series by eye. The red bars denote the storm-time SMCs found by our detection algorithm. (d) Pressure in the magnetotail at ARTEMIS location: red is thermal pressure, blue is magnetic pressure, and black is the sum of thermal and magnetic pressure. (e) Magnetic field in the magnetotail at ARTEMIS location, blue, green, and red correspond to x-component, y-component, and z-component, respectively. (f) Magnetic field in the solar wind from the OMNI data set, colors represent components as per panel (d). (g) Solar wind dynamic pressure from the OMNI data set. (h) The solar wind density. (i) The x-component of the solar wind velocity. The black dashed lines seen in panels (f)–(i) denote the ICME boundaries detected by eye, determined from the rotation in the magnetic field (b) of the solar wind.*

magnetotail flux data (Figure 2.1c) as described in Section 2.3.

To better understand what drives storm-time L-U events, we investigated the solar wind conditions during the L-U events during this storm. L-U 1 and 2 occurred during strong southward B_z (Figure 2.1f) and increasing solar wind dynamic pressure (Figure 2.1g) during the passage of a coronal mass ejection. Other than the strong southward B_z no special solar wind magnetic signature (such as an abrupt northward turning or an abrupt rotation) was seen in the solar wind magnetic field during these two events. Subsequently, during the storm recovery phase, from 26 August 10:40 UT to 26 August 21:00 UT, the tail flux showed periodic loading-unloading behavior. Three L-U events (L-U 3, 4, and 5) whose flux peaks were approximately 3–4 hr apart were identified during this time. During this time, there was a similarly periodic structure in the solar wind B_z (with period approximately 4 hr). The solar wind magnetic field magnitude (Figure 2.1f) showed no similar periodicity (it was rather steady) suggesting that these field oscillations were due to a large-scale Alfvén wave in the solar wind. This example shows that solar wind oscillations may be effective in producing produce L-U events in the magnetosphere during storms, similar to periodic substorms during nonstorm times [*Lee et al.*, 2006; *Tsurutani et al.*, 1995].

Like the L-U events, SMCs were also identified during both the main phase (such as SMC 1 in Figure 2.1) and during the recovery phase (such as SMC 2 in Figure 2.1). During SMC 1, the SYM-H (Figure 2.1a) decreased by 150 nT, showing that a large amount of energy was deposited into the ring current; this occurred under strong southward IMF (B_z varied between -10 and -17 nT, Figure 2.1f) and strong solar wind dynamic pressure (2.5-8.8 nPa, Figure 2.1g). SMC 2, 3, and 4 occurred from 26 August 2018 22:40 UT to 27 August 2018 13:30 UT during the recovery phase of the storm. During this time, the SYM-H was approximately -60 nT and the events occurred under weak solar wind conditions (solar wind B_z was near 0 nT, with an average value of -0.5 nT and the solar wind dynamic pressure was $\sim$1.7 nPa). While B_z was $\sim$0 nT during these SMCs, B_Y was $\sim$1.43 nT, thus SMC 2, 3, and 4 occurred while dayside reconnection was dominated by a solar wind B_y field. From

Figure 2.1b, it is seen that the amount of flux circulated during SMC 1 was significantly larger than during SMC 2, 3, and 4.

Next, we would like to characterize statistically how often L-U and SMC events occur during storms. Table 2.1 provides the number (and percentage) of storms in our data set that included L-U and SMC events; this is also reported separately for the storm main phase and the recovery phase. It is evident that L-U and SMC events can be found within storms, either in the main or the recovery phase, more than half of our storms did not have any L-Us and most (>78%) did not have any SMCs. We also found that more storms included L-U events than SMC events (25% versus 21%). These numbers are comparable to the nonstorm-time percentages (approximately 30% of nonstorm-time days had substorms, and 13% had SMCs). Previous studies [*Lockwood et al.*, 2009; *Milan et al.*, 2021] found similar occurrence rates of nonstorm-time substorms and SMCs (∼30% of their convection data set was categorized as either substorm growth, expansion or recovery, and ∼18% was categorized as SMC-like), giving confidence in the robustness of our results. Since these modes are not unique to storm or nonstorm times, their relative abundance is not controlled by dynamics unique to the storm or nonstorm time-magnetotail. Rather, the steadiness of the solar wind conditions that exists regardless of intensity determines when these modes occur. Also, more storms had recovery phase events than main phase events of either type. This is not unexpected given that storm recovery lasts longer than storm main phase.

In summary, in this section, we found that storms can exhibit both the SMC and L-U mode of convection, and that these modes can occur during either storm phase. Moreover, most storms do not rely on the presence of L-Us or SMCs to occur and evolve (these modes are not particularly clustered during a specific storm phase). Analysis of solar wind parameters during the case study presented showed that oscillations in the solar wind may, on occasion, drive periodic loading and unloading in the storm-time magnetotail but revealed no distinct features that can be responsible for the aperiodic L-U or SMC behavior. In other words, L-Us and SMCs can be embedded in the storm-time evolution but do not appear to be

necessary for storm development or storm evolution. With the statistical occurrence of these storm-time modes well established, we next want to understand if they have characteristics similar to or different from their nonstorm-time equivalents (the magnetospheric substorm and the SMC). This is done in the next two sections, Section 2.4.2 (addressing substorms versus L-Us) and Section 2.4.3 (addressing nonstorm and storm-time SMCs). We compared the flux transport, AE, and solar wind parameters to understand whether storm-time modes are stronger versions of their nonstorm-time counterparts or if they might represent fundamentally different modes.

Total number of storms	Number of storms with L-U or SMC mode (% rel. to total)	Number of storms with main phase L-U or SMC mode (% rel. to total)	Number of storms with recovery phase L-U or SMC mode (% rel. to total)	Hours of storm main or recovery phase observed	Number of nonstorm-time days	Number of nonstorm-time days with substorm or SMC mode (% rel. to total)
95	L-U: 24 (25%) SMC: 20 (21%)	L-U: 9 (9%) SMC: 12 (13%)	L-U: 17 (18%) SMC: 12 (13 %)	Main: 290 Recovery: 624	758	Substorms: 237 (30 %) SMC: 100 (13%)

Table 2.1: *Percentage of storms that had L-U events and SMC events*

2.4.2 Statistically Comparing Substorms and Storm-time L-U Events

In this section, we compare the evolution of the AE index, tail flux, and solar wind conditions during nonstorm-time substorms and storm-time L-U events. This is done by conducting a

superposed epoch analysis of both the tail flux and the AE index, by comparing histograms of the solar wind dayside reconnection potential (a measure of the rate of dayside reconnection) and solar wind reconnection electric field (a measure of the rate of energy deposition from the solar wind into the magnetosphere), and by conducting a superposed epoch analysis of the solar wind velocity and dynamic pressure during the two event categories. In these superposed epoch analyses, the reference epoch time (labeled T = 0) occurs at the peak of the tail flux. Because we defined each substorm and L-U event to start 50 min prior to the peak flux and end 100 min after, the superposed epoch curves span T = -50 min to +100 min. The superposed median curves of tail flux, AE, and solar wind velocity and dynamic pressure are constructed by taking the median of the set of curves. Additionally, we calculate the first (25%) and third (75%) quartiles of the AE, tail flux, and solar wind velocity and dynamic pressure for the L-U and nonstorm- time substorm event categories in a similar manner. We compare storm-time and quiet-time averaged profiles and assess how similar they are. Lastly, we compare the widths and averages of the histograms of the solar wind reconnection potential and electric field to establish how solar wind driving conditions might differ between the two modes.

2.4.2.1 Flux, AE, and D_{ST} Evolution

Figure 2.2a shows the median curves constructed from the superposed epoch analysis of the relative change in tail flux, $\Delta\Phi_{Tail}, (\Delta\Phi_{Tail}(t) = \Phi_{Tail}(t) - \Phi_{Tail}(t = -50))$ during the nonstorm-time substorm (blue curve) and storm-time L-U (red curve) modes. The figure shows that the storm-time L-U and nonstorm-time substorm events on average load approximately the same amount of flux, ∼0.7 GWb. Figure 2.2b shows the 25%, 50%, and 75% quartile curves for the absolute tail flux in the two modes. The median tail flux (the 50% quartile curve) during storm-time L-U events in on average 0.21 GWb (∼25%) larger than the nonstorm-time substorm events.

Table 2.2 shows the median absolute peak flux and relative flux (% relative to peak flux)

loaded and unloaded during substorms and storm-time L-U events (consistent with pictorial information presented in Figures 2.2a and 2.2b). The first column, median peak flux, is the peak of the two curves in Figure 2.2b. The second column is the median flux loaded, and the percentage relative to peak is found using $\frac{\Delta\Phi_{Tail}(t=0)}{\Phi_{Tail}(t=0)}$. The third column is constructed using the difference between the maximum of the median tail flux and the final value, and the percentage relative to peak flux is found using $\frac{\Delta\Phi_{Tail}(t=0)-\Delta\Phi_{Tail}(t=+100)}{\Phi_{Tail}(t=0)}$. Using the same value in the denominator also allows direct comparison between the two quantities.

From this table, we see that nonstorm-time substorms and storm-time L-U events load and unload approximately the same amount of flux. The only difference between these two modes is that the storm-time L-U events start at a higher baseline flux, thus the median peak flux for the storm-time events is 0.4 GWb larger, which is ∼25% higher than nonstorm-time substorms.

Figure 2.2c shows that the median ΔAE profiles ($\Delta AE(t) = AE(t) - AE(t = -50)$) for both event categories. The storm-time median has been further smoothed by applying an additional 20-min running average to compare the ΔAE profiles more easily for both categories. We find that both event categories exhibit three phases in succession: a gradual increase, indicative of a growth phase, a steep increase beginning at approximately T = 0 min, indicative of an expansion phase, and a decrease beginning at approximately T = 20 min. These are expected based on the three distinct phases of substorms [*McPherron*, 1979]. The main difference in the ΔAE profiles between the events is the variability. The storm-time ΔAE response is more variable than the nonstorm one. This variability is most likely due to the limited storm-time L-U events found (49 L-U events versus 333 nonstorm-time substorms). However, the ionosphere seems to respond to L-U events in the same three-phase progression as it does for nonstorm substorms.

Figure 2.2d shows that the AE during storm-time L-U events is much higher (by a factor of 2–4), on average, than during nonstorm substorms. As a result, storm-time L-U ionospheric energy dissipation (represented by the ΔAE excursion) is a small fraction of the

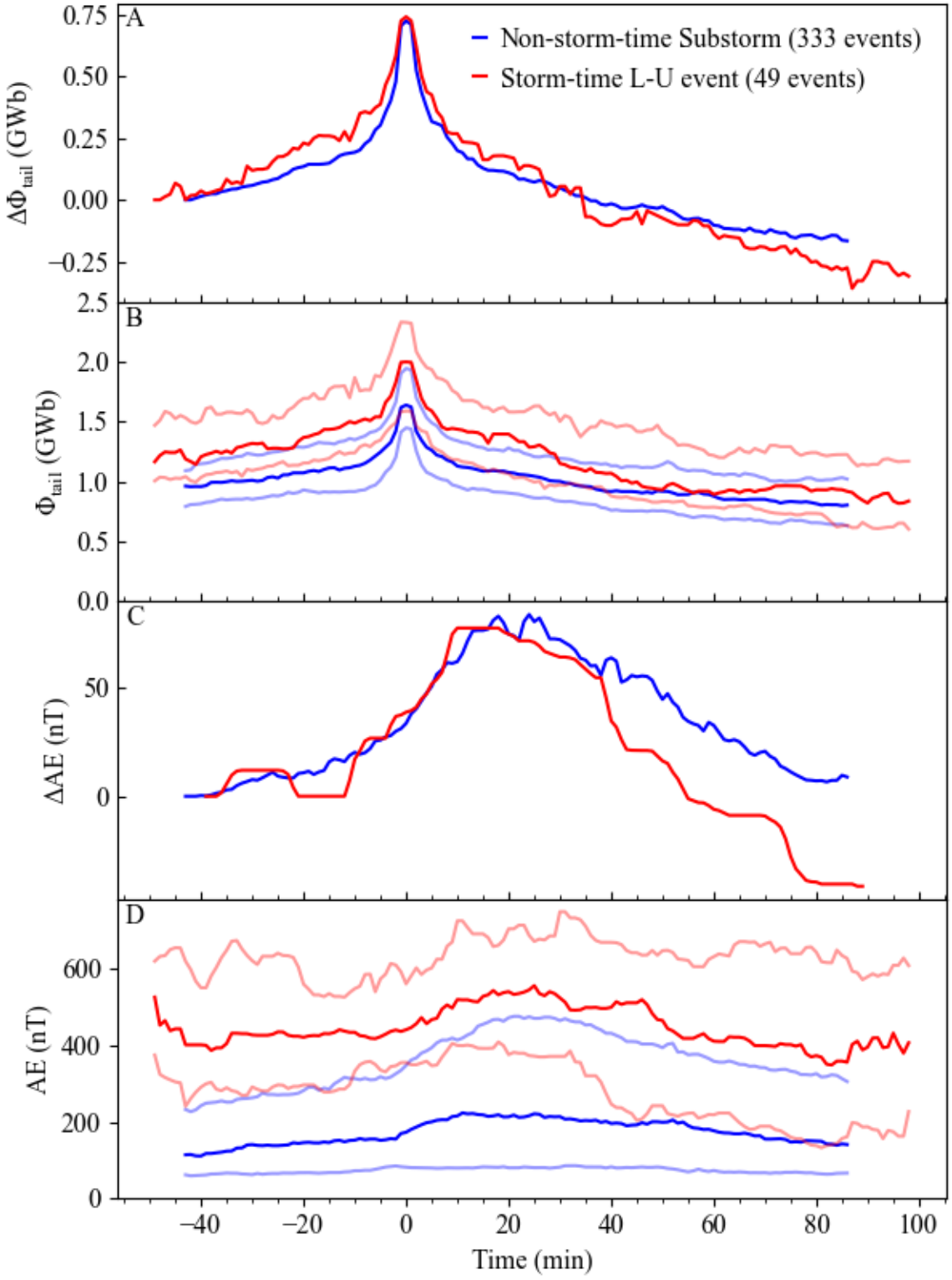
A
Non-storm-time Substorm (333 events)
Storm-time L-U event (49 events)
$\Delta\Phi_{tail}$ (GWb)
0.75
0.50
0.25
0.00
−0.25
B
Φ_{tail} (GWb)
2.5
2.0
1.5
1.0
0.5
0.0
C
ΔAE (nT)
50
0
D
AE (nT)
600
400
200
0
−40
−20
0
20
40
60
80
100
Time (min)

Figure 2.2: *Superposed epoch analysis results of magnetotail flux (in each hemisphere) and AE during nonstorm-time substorms (blue traces) and storm-time L-U events (red traces). Both the relative variations (denoted by* $\Delta\Phi_{Tail}, \Delta\Phi_{Tail}(t) = \Phi_{Tail}(t) - \Phi_{Tail}(t = -50)$*), and the absolute quantities were superposed and are shown in separate panels. Solid curves denote medians of the superposed quantities. Faded curves in the absolute quantity panels denote upper and lower quartiles of the superposed quantities. (a) Relative variation of the hemispheric magnetotail flux. (b) Absolute hemispheric magnetotail flux. (c) Relative variation in AE. For the storm-time profile, an additional 20-min running median was applied to further smooth the data. (d) Absolute value of AE.*

average dissipation as determined by the average AE (ΔAE/ $\langle$AE$\rangle$ $\sim$75 nT/450 nT–17%) compared to nonstorm times (for which ΔAE/$\langle$AE$\rangle$ $\sim$75 nT/150 nT–50%). Thus, substorms are a very significant mode of circulation during nonstorm times, but L-U events are merely a temporary enhancement of an otherwise elevated circulation during storms. While storm-time L-U events appear to be distinct modes of circulation very similar to substorms in flux evolution and transport, their significance for global energy dissipation is muted by their relative weakness compared to the storm-time AE.

Mode	Median peak tail flux (GWb)	Median flux loaded (GWb; % rel. to peak)	Median flux unloaded (GWb, % rel. to peak)
Nonstorm-time substorm	1.6	0.73(46%)	1.0 (63%)
Storm-time L-U	2.0	0.74(37%)	1.1 (55%)

Table 2.2: Median flux loaded and unloaded during substorms and storm-time L-U events

2.4.2.2 Solar Wind Conditions

To further explore the differences between substorms and storm-time L-U events, we study the solar wind conditions that drive them. We compare the dayside reconnection potential and the parallel (to the dayside reconnection x-line) electric field, E_r, to determine the different rates of dayside reconnection and energy transfer from the solar wind into the magnetosphere, respectively. During storm times, the solar wind ram pressure can compress the tail and promote nightside reconnection which can affect the modes of flux convection in the magnetosphere. Thus, we also compare the solar wind dynamic pressure and velocity between the two event categories to determine how these normal stresses change the modes of convection during storm and nonstorm times.

Figure 2.3a shows E_r in the solar wind along the reconnection line direction predicted by the antiparallel merging model of dayside reconnection [*Pulkkinen et al.*, 2010]. It was computed from solar wind **B** and **V** measurements obtained from the OMNI database during our selected L-U events, then projected along the nominal direction of the reconnection line assuming antiparallel merging. As in prior figures, blue and red traces correspond to the non-storm and storm-time data. Figure 2.3b shows the dayside reconnection potential calculated as $E_r \times R_{Tail} \times R_{eff}$, where R_{Tail} is the estimated dawn-dusk extent of the magnetotail, and R_{eff} is the reconnection efficiency (again taken to be 0.2). The median solar wind electric field during our storm-time L-U events is $E_r \sim 2.4$ mV/m, approximately 1.8 times higher than that during substorms ($E_r \sim 1.4$ mV/m). The dayside reconnection potential during storm-time events is approximately 1.6 times higher than that during the nonstorm-time events ($\sim$93 kV versus $\sim$60 kV). Thus storm-time L-U events are electrodynamically more strongly driven than substorms, as expected.

Next, we examine the solar wind dynamic pressure and velocity to identify if and how these quantities might affect the evolution of L-U and substorm modes. Figure 2.3c shows the x-component of the solar wind velocity. We note that the velocity is on average 19 km/s

(about 5%) faster during storm-time L-U events than during substorms. Figure 2.3d shows the solar wind dynamic pressure. The dynamic pressure of storm-time L-Us is also elevated compared to substorms.

We conclude that there exists enhanced electrodynamic coupling during storm-time L-Us compared to nonstorm substorms, as expected from the storm-time conditions prevailing during the former. The enhanced storm-time reconnection rate and reconnection potential are in part due to an increased solar wind velocity. The latter also manifests itself in a moderate enhancement in the solar wind dynamic pressure. These findings are consistent with the increased tail flux and energy dissipation in the ionosphere generic to storms (Figures 2.2b and 2.2d), but apparently do not lead to enhanced flux variations or dissipation (ΔAE) for storm-time L-Us compared to substorms (Figures 2.2a and 2.2c).

2.4.2.3 Summary of Storm-Time L-U and Nonstorm-Time Substorm Comparison

Storm-time L-U events load and unload about the same amount of flux and exhibit a comparable change in AE (ΔAE) as substorms. The absolute tail flux and AE are greater during storms, as expected, since these loading-unloading intervals occur during intervals of elevated solar wind-magnetosphere coupling when they occur during storms. Additionally, storm-time flux and AE profiles (not just their variations) are similar to the nonstorm-time ones, including the well-studied progression of loading, expansion, and recovery. We conclude that storm-time L-U events are likely similar processes to those during nonstorm-time substorms, except they occur during elevated electrodynamic coupling conditions concurrent with storms. It is not surprising, therefore, that we found storm-time L-U events to be correlated with more intense E_r, a faster solar wind velocity, and a stronger solar wind dynamic pressure compared to substorms. These conditions are all consistent with faster dayside reconnection and enhanced magnetospheric flux throughput expected during storms. The fact that the net flux variation and net AE changes between storm-time L-Us and substorms

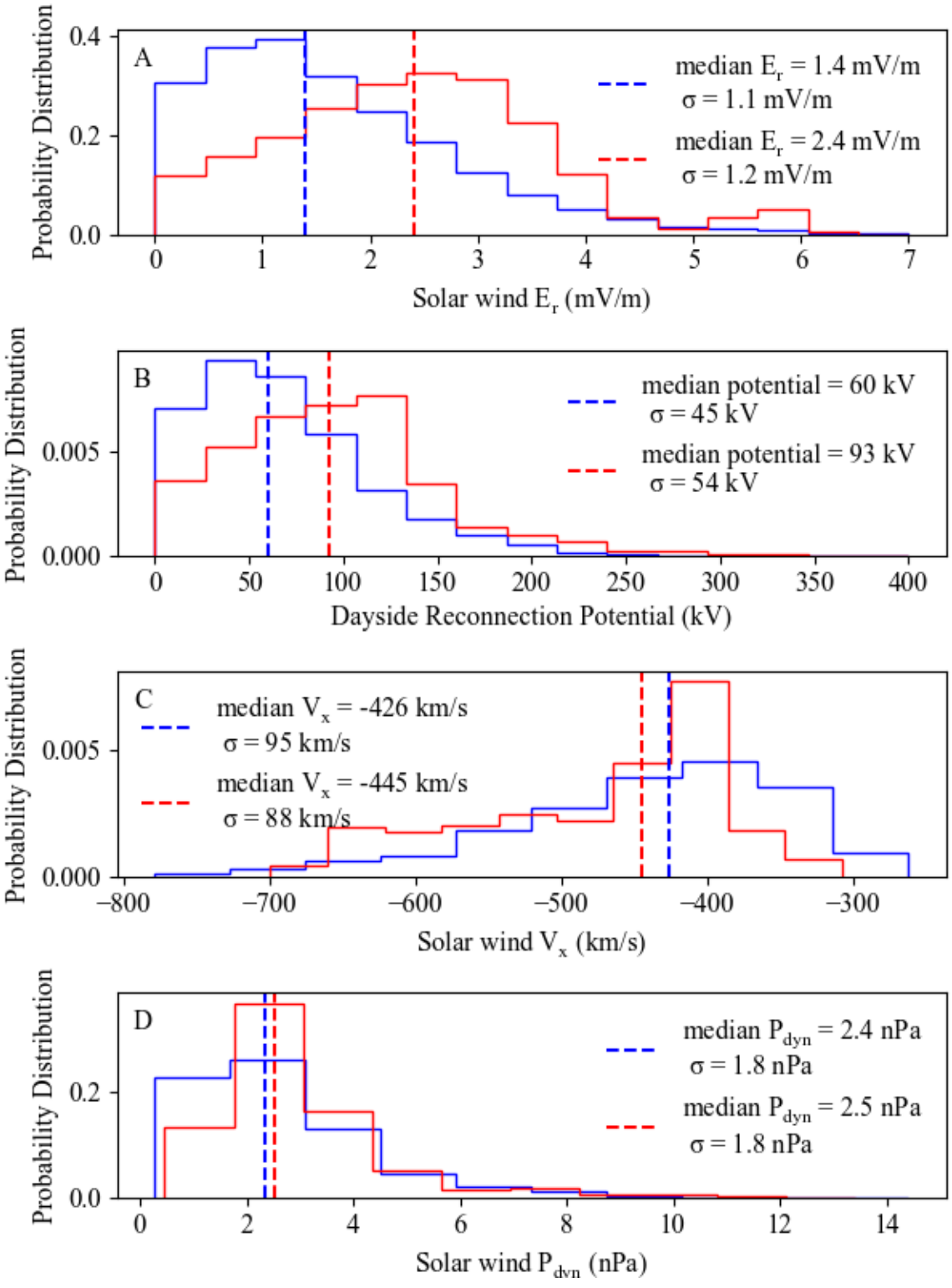
A
median E_r = 1.4 mV/m
σ = 1.1 mV/m
median E_r = 2.4 mV/m
σ = 1.2 mV/m
Probability Distribution
Solar wind E_r (mV/m)
B
median potential = 60 kV
σ = 45 kV
median potential = 93 kV
σ = 54 kV
Probability Distribution
Dayside Reconnection Potential (kV)
C
median V_x = -426 km/s
σ = 95 km/s
median V_x = -445 km/s
σ = 88 km/s
Probability Distribution
Solar wind V_x (km/s)
D
median P_{dyn} = 2.4 nPa
σ = 1.8 nPa
median P_{dyn} = 2.5 nPa
σ = 1.8 nPa
Probability Distribution
Solar wind P_{dyn} (nPa)

Figure 2.3: *(a) The probability distribution of solar wind E_r during nonstorm-time substorms (blue) and storm-time L-U events (red). The dashed vertical lines denote the median values of the distributions. (b), (c), and (d) are the probability distribution of the dayside reconnection potentials, x-component of the solar wind velocity, and solar wind dynamic pressure in a similar format to (a).*

are about same despite the stronger dayside coupling during storms suggests that storm-time L-Us, are quite similar to substorms—they represent merely a transient imbalance in dayside-to-nightside reconnection rate which happens to be elevated during storms.This imbalance appears to result in similar flux loading-unloading and ionospheric energy dissipation rate enhancement during storms as during nonstorm periods. Due to the similar intensity of loading-unloading but the significantly enhanced intensity of storm-time circulation, although substorms represent a significant increase of the overall convection during nonstorm periods they are only a small component of the flux and energy circulation enhancements during storm periods. Therefore, their importance may be in facilitating future storm studies by being fiducials of reconnection enhancements in the magnetotail, localized in time and space. Being easily identifiable increases in the storm-time reconnection rate they can facilitate storm-time reconnection studies with multiple spacecraft and ground-based assets.

2.4.3 Statistically Comparing Nonstorm-Time and Storm-Time SMCs

We now apply similar analysis methods as in Section 2.4.2 on the magnetotail flux content, AE index and solar wind drivers of SMC events in order to determine if there are any similarities or differences in these modes of convection between nonstorm and storm times. We find that the magnetotail holds more flux, the AE is more intense, the dayside reconnection rate, solar wind reconnection electric field, and solar wind dynamic pressure are on average the same, and the solar wind velocity is larger for storm-time SMCs than nonstorm-time SMCs.

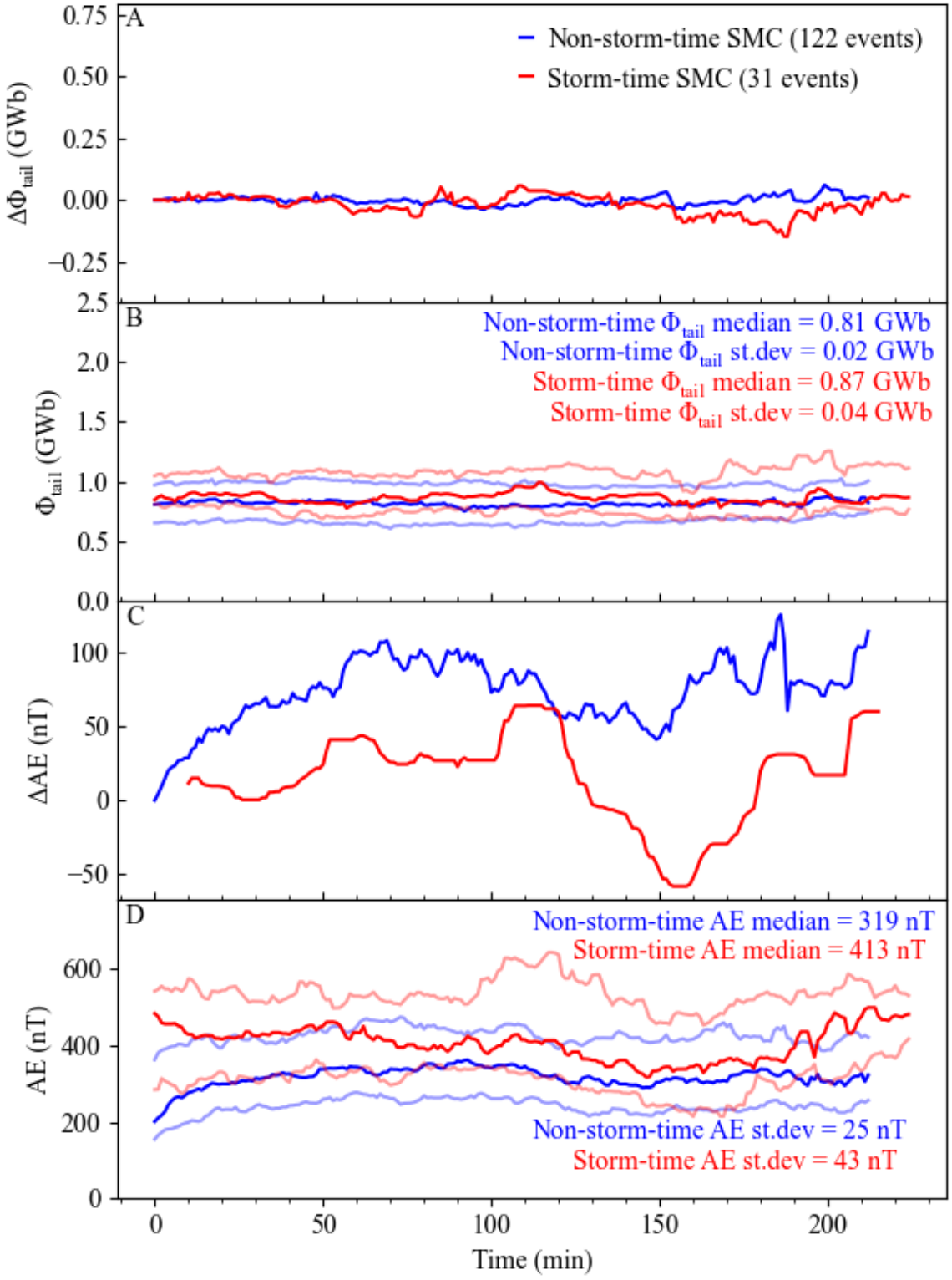
A
Non-storm-time SMC (122 events)
Storm-time SMC (31 events)
ΔΦtail (GWb)
0.75
0.50
0.25
0.00
–0.25
2.5
B
Non-storm-time Φtail median = 0.81 GWb
Non-storm-time Φtail st.dev = 0.02 GWb
Storm-time Φtail median = 0.87 GWb
Storm-time Φtail st.dev = 0.04 GWb
Φtail (GWb)
2.0
1.5
1.0
0.5
0.0
C
ΔAE (nT)
100
50
0
–50
D
Non-storm-time AE median = 319 nT
Storm-time AE median = 413 nT
AE (nT)
600
400
200
0
Non-storm-time AE st.dev = 25 nT
Storm-time AE st.dev = 43 nT
0
50
100
150
200
Time (min)

Figure 2.4: *Superposed epoch analysis of magnetotail flux (in each hemisphere) and AE during nonstorm-time SMCs and storm-time SMCs in a format similar to that of Figure 2. Both the relative variations (denoted by* $\Delta\Phi_{Tail}, \Delta\Phi_{Tail} = \Phi_{Tail}(t) - \Phi_{Tail}(t = 0)$*) and the absolute quantities were superposed and are shown in separate panels. Solid (blue or red) curves denote medians of the superposed quantities. Faded (blue or red) curves in the absolute quantity panels denote upper and lower quartiles of the superposed quantities. (a) Relative variation of the hemispheric magnetotail flux. (b) Absolute hemispheric magnetotail flux. (c) Relative variation in AE. For the storm-time profile, an additional 20-min running median was applied to further smooth the data. (d) Absolute value of AE.*

2.4.3.1 Flux, AE, and D_{ST} Profiles

To understand the absolute and relative variations of the electromagnetic energy content in the magnetotail and of its dissipation to the ionosphere during SMCs we employ superposed epoch analysis of the flux content in the magnetotail and of the AE index. Figure 2.4 shows a superposed epoch analysis of storm-time and nonstorm-time SMCs in the same format as in Figure 2.2 for L-U events (for this analysis $\Delta\Phi_{Tail}(t) = \Phi_{Tail}(t) - \Phi_{Tail}(t = 0)$). In this case, storm-time and nonstorm-time SMCs have similar Φ_{Tail} medians (Figure 2.4b). So, the magnetotail does not hold more flux during storm-time SMCs compared to nonstorm-time SMCs. Next, by studying the AE profiles we explore how energy is dissipated in the ionosphere during the storm-time and nonstorm-time SMCs. Figure 2.4c shows the ΔAE profiles ($\Delta AE = AE(t) - AE(t = 0)$), which show the energy dissipation in the ionosphere due to storm-time and nonstorm-time SMCs and Figure 2.4d shows the absolute value of AE during these times. To better compare the nonstorm-time and storm-time ΔAE profiles, we apply an additional 20-min running median on the storm-time ΔAE data to produce the smooth red curve in Figure 2.4c. To determine the relative change in energy dissipation in the ionosphere due to the SMC mode we compute the ratio $\frac{<\Delta AE>}{<AE>}$. During nonstorm-time SMCs $\frac{<\Delta AE>}{<AE>} = 0.24$ and during storm-time SMCs $\frac{<\Delta AE>}{<AE>} = 0.04$. Thus, during nonstorm-

time SMCs the energy dissipation in the ionosphere increases by approximately 25% and is steady ($\frac{\sigma \Delta AE}{<\Delta AE>} = 30\%$). During storm times, the energy dissipation in the ionosphere only increases by 4%; however, the dissipation is highly variable ($\frac{\sigma \Delta AE}{<\Delta AE>} = 200\%$). Moreover, from Figure 2.4d, we see that the median storm-time AE was much higher than the nonstorm-time case, so more energy is dissipated through the ionosphere during storm-time SMCs than nonstorm-time SMCs. So during nonstorm times the SMC mode can play a significant role in ionospheric energy dissipation, but during storm times the impact of the SMC to energy dissipation in the ionosphere is muted by the overarching storm dynamics.

2.4.3.2 Solar Wind Conditions

As in Section 2.4.2.2, here, we examine the solar wind conditions which drive the SMC modes to determine whether the storm-time modes are driven differently under stronger solar wind conditions. By quantifying the solar wind electric field and dayside reconnection potential during both modes, we can determine whether the flux throughput and energy transfer rates are greater during storm-time or nonstorm-time SMCs. Similarly, we can examine whether the solar wind velocity and dynamic pressure may contribute to the flux accumulation and the energy dissipation.

Figure 2.5 shows these results in the same format as in Figure 2.3. The solar wind conditions during storm-time and nonstorm-time SMCs are qualitatively similar. When comparing the median solar wind E_r (Figure 2.5a) and dayside reconnection potentials (Figure 2.5b) we find that they are approximately equal between the two types of SMCs within a fraction of a standard deviation ($< 0.1\sigma$). In fact, even the profiles of the respective probability distributions are similar. This shows that the storm-time and nonstorm-time solar wind conditions are very similar. Figures 2.5c and 2.5d show the x-component of the solar wind velocity and solar wind dynamic pressure histograms. We see that the solar wind velocity during storm-time SMCs is significantly larger (49 km/s, or 11%) than during nonstorm time ones, but apparently this is not sufficient to make a difference in the solar wind reconnection

electric field. We conclude that the southward IMF is sufficiently suppressed during storm-time SMC intervals to overcome the effect of the increased solar wind velocity (a common occurrence during storm times) in the reconnection electric field. The solar wind dynamic pressure (Figure 2.5d) for the storm-time and nonstorm-time SMCs is approximately the same, evidently due to the solar wind density decreasing at times of increased storm-time SMC solar wind velocity. Thus, storm-time SMCs are not driven more strongly (compared to nonstorm-time SMCs) by conditions of increased solar wind dynamic pressure that are often seen during storms.

Just like during nonstorm-times, storm-time SMCs were selected to represent on average a balanced reconnection rate. It is interesting, though, that the average absolute flux is also similar between these two data sets. This absolute flux, $\sim$0.8 GWb, is comparable to the end-value of loading-unloading events during storm-time L-U events and substorms (Figure 2.2b). At first this result is surprising. It would be expected for the tail flux during nonstorm-time SMCs to be similar to that at the end state of substorms, since nonstorm SMCs are known to be preceded by a substorm. In the aftermath of substorms the tail reconnection moves far enough from Earth, in the midtail region, which enables a special, quasi-static mode of convection to take hold during the SMCs [*Sergeev et al.*, 1996]. But such a low flux value is not expected during storms, which are more strongly driven and, by inference, are expected to accumulate more flux in the magnetotail. Upon second thought, however, it is possible that storm-time SMCs also commence when sufficient flux unloading has allowed the tail flux to reach a similarly low level as nonstorm SMCs, as it would be in the aftermath of storm-time L-U events. This may occur due to a reduction of the flux input rate, represented by a reduced dayside reconnection electric field, as we observed in Figure 2.5a. This reduced rate apparently attains values typical of nonstorm times, despite the increased solar wind velocity during storms (Figure 2.5c). Such conditions occur when the solar wind B_z is suppressed, as is the case in three out of the four storm-time SMCs identified in Figure 2.1, all during storm recovery phase. In fact, the first of these storm-

recovery SMCs occurred at the end of a storm-time L-U event. We surmise that such SMCs are not uncommon in our database.

We conclude that storm-time SMCs are very similar to nonstorm ones in the intensity of the external driver due to the interplanetary field orientation and lower-than-usual dynamic pressure intensity despite the elevated solar wind flow velocity during storms. Like their nonstorm counterparts, they may also commence on occasion in the aftermath of a nonstorm L-U, because under such conditions the tail flux has been depleted sufficiently and the tail reconnection site may be sufficiently distant in the downtail direction from Earth to enable quasi-steady convection.

It remains to explain why the observed energy dissipation during storm-time SMCs is larger than during nonstorm SMCs, as evidenced in the AE index (Figure 2.4d), even though the tail flux (Figure 2.4b), dayside reconnection electric field (Figure 2.5a), and reconnection potential (Figure 2.5b) are comparable. Enhanced solar wind dynamic pressure, which is often observed during storms, was not observed during storm-time SMCs (Figure 2.5d)—rather the dynamic pressure was found to be comparable to nonstorm times. The explanation may be elusive but the stronger ring current that is certainly present during storms suggests that the inner magnetosphere is also strongly driven during storm-time SMCs compared to nonstorm SMCs. It is not unreasonable to expect that either the near-Earth reconnection or quasi-static convection is more geoeffective under storm-time conditions for the same external driver. In other words, it is possible for the geoeffectiveness to be not simply due to the instantaneous solar wind conditions but also to the prior history of the solar wind that led to the development of a storm versus a nonstorm state. This hypothesis remains to be studied in the future.

2.4.3.3 Summary of Storm-Time and Nonstorm-Time SMC Comparison

We compared a set of 31 storm-time SMCs with 122 nonstorm-time SMCs using a superposed epoch analysis and found that the auroral electrojets are more intense during storm-time

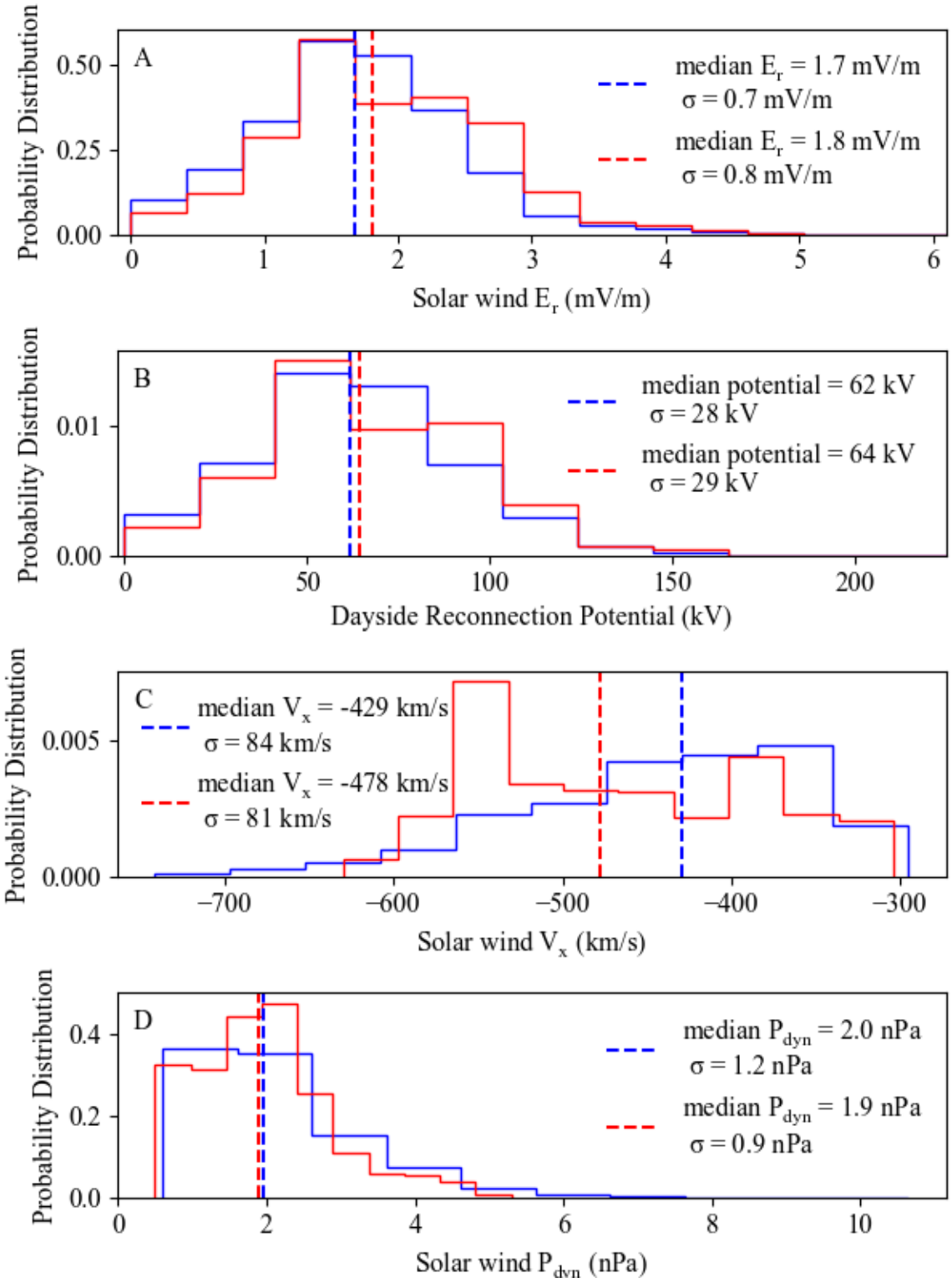
A
median E_r = 1.7 mV/m
σ = 0.7 mV/m
median E_r = 1.8 mV/m
σ = 0.8 mV/m
Probability Distribution
Solar wind E_r (mV/m)
B
median potential = 62 kV
σ = 28 kV
median potential = 64 kV
σ = 29 kV
Probability Distribution
Dayside Reconnection Potential (kV)
C
median V_x = -429 km/s
σ = 84 km/s
median V_x = -478 km/s
σ = 81 km/s
Probability Distribution
Solar wind V_x (km/s)
D
median P_{dyn} = 2.0 nPa
σ = 1.2 nPa
median P_{dyn} = 1.9 nPa
σ = 0.9 nPa
Probability Distribution
Solar wind P_{dyn} (nPa)

Figure 2.5: *(a) The probability distribution of solar wind E_r occurring during nonstorm-time SMCs (blue) and storm-time SMCs (red). The dashed vertical lines denote the median values of the distributions. (b), (c), and (d) are the probability distribution of the dayside reconnection potentials, x-component of the solar wind velocity, and solar wind dynamic pressure in a similar format to (a).*

SMCs than nonstorm-time SMCs. However, the magnetotail contains similar amounts of flux in these two categories of SMCs. Additionally, in our comparison of solar wind driving between these groups, we found that the dayside reconnection rate, global flux transfer rate, and solar wind dynamic pressure are also similar between them; however, the solar wind velocity was greater during storm times. We attributed the similar dayside reconnection rate despite the increased solar wind velocity to a reduced southward IMF. In every other aspect, then, we find storm-time SMCs to be similar to their nonstorm-time counterparts, including that, at least on occasion, there is evidence of them commencing in the aftermath of storm-time L-Us.

That storm-time SMCs dissipate more energy in the ionosphere (Figure 2.4d) despite the fact that the solar wind driving is similar to nonstorm-time SMCs is something that cannot be attributed to the instantaneous solar wind driving but likely due to the different magnetospheric configuration during storms and remains to be further studied in the future.

It appears that the existence of SMCs is not critical for the evolution of a storm. They can appear in either the main or the recovery phase and they occur whenever the solar wind driver is suppressed to a nonstorm SMC level for a sufficiently long time for the magnetosphere to enter a quasi-steady convection state. Apparently, this is only possible when the tail flux is sufficiently low that it is comparable to nonstorm SMC levels. Storm-time SMCs represent "the lulls within a storm" and although they are more geoeffective than their nonstorm counterparts they are very similar to them in every other respect. In particular we do not find any way that they are significant contributors to flux circulation or a critical mode

of storm development, but a happenstance when the instantaneous storm driver conditions reach sufficiently low level.

2.5 Summary

In this paper, we aimed to determine the existence, type, and significance of modes of convection during storms. Guided by the known nonstorm-time modes, we asked: (a) Do periods of flux loading and unloading and steady flux circulation exist during storms, and if so, how often? (b) How similar are these storm-time modes to the nonstorm-time substorm and SMC modes? To answer (a) we conducted case studies of the flux transport during storms (we presented one of them as a case-in-point) and addressed the question statistically for a large database of storms (95). To answer (b) we conducted a superposed epoch analysis of the average solar wind electric field, dayside reconnection potential and AE response for those modes. Our conclusions are the following:

1. As illustrated using a geomagnetic storm that occurred between 25 August 2018 and 28 August 2018, instances of L-U events and of steady magnetospheric convection can indeed arise during storms. These modes can occur during either the main or recovery phases of the storm (or both, as in the case presented). On other cases, however, these modes occur only in one storm phase, or do not occur at all (even when changing our definitions of L-U and SMC events), suggesting that neither of these modes is necessary for ring-current energization.

2. While both L-Us and SMCs can occur during storms, their occurrence rate is statistically not very high. Approximately a fourth (25%) of the storms had L-U events embedded within them, while less than a fourth (21%) had SMC events within them. Apparently, the rest of the time, storms have variable convection that cannot be classified as loading-unloading or quasi-steady.

3. L-U and SMC events can occur in any phase of a storm, and they are about 2.0 times as many in recovery phase compared to the main phase, consistent with the fact that storm recovery lasts approximately 2 times longer in our database. This suggests that these modes appear due to the steadiness and unsteadiness of the solar wind regardless of storm phase and are simply embedded in storms due to the overall intense driving by the solar wind that results in a storm.

4. The storm-time L-U events and nonstorm-time substorm events show a similar open flux evolution and three-phase AE evolution, with the main difference being that the quantities were elevated during storm times. Specifically:

   a) Storm-time L-U events load and unload about the same amount of flux as substorms.

   b)Storm-time L-U events are more strongly driven by the solar wind and have a faster dayside reconnection rate than nonstorm-time substorms.

These characteristics can be attributed to the intensity of the solar wind driver during the storms within which the L-Us are embedded, as compared to the weaker driving during to nonstorm periods within which the substorms are embedded.

1. Storm-time SMCs and nonstorm-time SMCs show very similar open flux evolution and have very similar solar wind characteristics, with the only difference being that the AE is more intense during storm times. Again, this is consistent with an interpretation that intervals of solar wind steadiness (resulting in SMCs) are embedded within storm-time conditions for the former, and nonstorm-time conditions for the latter.

2. The solar wind reconnection electric field E_r is 1.8 times higher and the dayside reconnection potential is 1.6 times higher during storm-time L-U events compared to nonstorm-time substorms. This is consistent with the stronger solar wind conditions during the storms within which L-Us are embedded, compared to substorms.

3. The solar wind E_r and dayside reconnection potential are the same between storm-time and nonstorm-time SMCs. This suggests that the SMCs develop during storms when the solar wind conditions are not only stable but also fall within a low-to-moderate range expected during nonstorm periods.

2.6 Discussion and Conclusions

The goal of this study was to determine if modes of convection like the ones we have known to exist during nonstorm times can also exist during storms. The study was motivated by the need to determine whether storm-time drivers of convection (ultimately responsible for powering a strong storm-time ring current, the distinguishing attribute of a storm) are associated with such modes of convection or not.

The role of substorm-like convection and quasi-steady convection has been a long-standing problem in magnetospheric physics [e.g., *Ebihara and Ejiri*, 2003; *Gonzalez et al.*, 1994; *Kamide et al.*, 1998]. Due to the complexity of storm-time convection, it has been unclear whether storms are due to enhanced SMC convection [e.g., *McPherron*, 1997; *Wolf et al.*, 1997] or substorm-like convection. In the study, we resolved this issue by tracking the magnetotail flux during storm-time periods.

We have found that storm-time loading-unloading intervals and SMC events are very similar if not identical to their nonstorm counterparts (substorms and nonstorm-time SMCs), and occur occasionally, but not always, during any storm phase. However, they are not required for storm-time evolution since approximately a quarter of storms have L-Us and fewer than a quarter of them have SMCs. Therefore, these modes are distinct modes of transport embedded within storms but are likely not responsible for storm-time evolution.

In the context of the storm-substorm relationship, this study resolves the debate of the necessity of substorm-like modes of convection during storms [e.g., *Gonzalez et al.*, 1994; *Kamide et al.*, 1998]. We have found that statistically, L-Us are unnecessary and do not

contribute to ring current growth. Additionally, we have determined unambiguously, that storms are not a sum of substorm-like events.

That these modes have similar characteristics during storm and nonstorm times suggests they represent unsteady or steady circulation in response to the solar wind time-history, arising under markedly different conditions of overall solar wind intensity and severity. If these modes occur within or adjacent to periods of stream-stream interactions, coronal mass ejections, or similar conditions conducive to storms then these modes find themselves embedded in storms; if not then they find themselves embedded in nonstorm periods. Since during nonstorm conditions these modes are easy to pick-out in indices, such as AE, they have therefore been recognized as special modes outside storms and have been the subject of significant study. However, during storms these modes are difficult to distinguish in indices and require methods like the one used here (polar cap flux estimates) to ferret from an intense background circulation. Therefore, they have previously not been widely recognized as special modes of convection within storms.

We have superposed the SYM-H response to these modes and found them to have an insignificant and uncorrelated effect on the ring current during storms (and, of course, during nonstorm times we well). Thus, even though more flux and energy are transported through the magnetosphere during storm-time L-Us, this energy does not result, in an aggregate sense, in significantly more energy imparted to the ring current. Again, this argues in favor of an interpretation that L-Us and SMCs are part of the overall enhanced convection, neither mode is responsible for sufficient enhancements to the storm-time convection rate affecting ring current or storm evolution. Rather, they are likely transient effects in an overall circulation that is dominated by the long-term solar wind conditions that drive the storm (and in particular the storm-time ring current). The ultimate geoeffectiveness of the circulation likely has to do with things that are unrelated to these specific modes.

One clue as to what controls such geoeffectiveness in the circulation comes from our observation that storm-time and nonstorm-time SMCs were remarkably similar in their re-

connection electric field and reconnection potential (which control the input of energy), but the solar wind velocity was higher and the AE was higher during storm-time SMCs. We interpreted the AE being higher as a consequence of this mode occurring during storms. However, the storm-time SMC on average is not more strongly driven than the nonstorm-time SMCs. So, why then is the AE response stronger? We suggest that the increase in solar wind velocity may cause the cross-tail currents to become stronger, bringing the peak of the tail currents earthward and enhancing the geoeffectiveness of nightside convection [*Sergeev et al.*, 1996].

The above clue is consistent with the observation in *Angelopoulos et al.* [2020] that the proximity of the thin current sheet to the Earth may be responsible for the geoeffectiveness of reconnection in powering storms. It is possible that the proximity of the intense, thin tail current sheet to Earth during storms helps both L-Us and SMCs be more geoeffective during storms, and may be the underlying reason why storms develop in the first place. This is a hypothesis that deserves investigation in future studies.

What then is the importance of L-Us and SMCs during storms, if they are only incidental and superfluous to the evolution of a storm? The answer may lie with their distinctiveness which lends themselves to detection and interpretation using circulation concepts developed from nonstorm times. If global convection indeed proceeds in an analogous (just stronger) manner during the storm-time equivalents of these modes, it may be possible to interpret observations of reconnection, flux transport, and evolution in a global context with few (coordinated) in situ measurements in the next few decades.

Data Availability Statement

ARTEMIS data are available through http://themis.ssl.berkeley.edu. Geotail data were accessed from https://www.darts.isas.jaxa.jp/stp/geotail/. The OMNI data, including solar wind parameters and geomagnetic indices, were obtained from the GSFC/SPDF OMNI-

Web interface at http://omniweb.gsfc.nasa.gov. ARTEMIS mission data, Geotail data, and OMNI data have been imported and analyzed using corresponding plug-ins to the SPEDAS analysis platform [http://spedas.org *Angelopoulos et al.*, 2019].

Acknowledgments

We acknowledge NASA contract NAS5- 02099 for use of data from the THEMIS mission. Specifically: C. W. Carlson and J. P. McFadden for use of ESA data and K. H. Glassmeier, U. Auster, and W. Baumjohann for the use of FGM data provided under the lead of the Technical University of Braunschweig and with financial support through the German Ministry for Economy and Technology and the German Center for Aviation and Space (DLR) under Contract 50 OC 0302. We thank SPDF for providing data access to GEOTAIL data. This material is based upon work supported by the National Science Foundation Graduate Research Fellowship under Grant (DGE-2034835). Any opinions, findings, and conclusions or recommendations expressed in this material are those of the author(s) and do not necessarily reflect the views of the National Science Foundation.

CHAPTER 3

Storm-time Very-Near-Earth Magnetotail Reconnection: A Statistical Perspective

Abstract

The ring current, an equatorial near-Earth current, fluctuates in response to solar wind plasma interactions with Earth's magnetosphere. Despite extensive research on storm-time ring current energization, direct evidence of the energy transport into the inner-magnetosphere that powers this current remains scarce. Recent observations revealing that very-near-Earth reconnection (VNERX, occurring at geocentric distance $< 14\ R_E$) can occur during storms suggest that such reconnection could play an important role in ring current development. Here we address how common VNERX is. We use inner-magnetosphere and plasma sheet observations from the Time History of Events and Macroscale Interactions during Substorms (THEMIS) satellites spanning 13 years. During this period, THEMIS observed 512 storms and 7 VNERX events. All VNERX events occurred during storm main-phase at or near the pre-midnight sector. (None were observed during storm recovery-phase.) The events occurred within 1 R_E of the modeled neutral sheet, suggesting that VNERX events are elusive because they lie near the neutral sheet. Since THEMIS spent 5253 hours within 1 R_E of the modeled neutral sheet during storm main-phase, the inferred observational VNERX occurrence rate is 1.3 per 1000 hours of storm main-phase. This rate is lower than published ion-diffusion-region occurrence rates seen in the near-Earth plasma sheet during non-storm times (likely substorms). These results suggest that while VNERX events might be sig-

nificant for the storm-time ring current's initial buildup (during storm main-phase), other transport mechanisms, like enhanced global convection, may be responsible for maintaining the strength of the ring current during storm recovery-phase.

3.1 Introduction

Geomagnetic storms are a global response [*Gonzalez et al.*, 1994] of the Earth's magnetosphere and currents to intense solar wind driving. Through magnetic reconnection at the dayside magnetopause, solar wind energy is deposited into the magnetosphere and a fraction of this energy reaches the nightside inner-magnetosphere in the form of heated ions that drift partially or fully around the Earth [*Baker et al.*, 2001; *Pulkkinen et al.*, 2002]. These ions power the equatorial electric current that flows toroidally around the Earth at 6-8 R_E, known as the ring current [*Daglis*, 2006].

During geomagnetic storms the ring current is energized significantly [*Frank*, 1967; *Smith and Hoffman*, 1973; *Kistler*, 2020], but its energization process remains unclear. It is thought that most transport of mass, energy, and magnetic flux earthward from the near-Earth magnetotail (15 – 30 R_E) occurs in the form of fast flows, known as bursty bulk flows, or BBFs [*Angelopoulos et al.*, 1992, 1994], propelled Earthward by the dipolarizing flux bundles (DFBs) embedded in the flows [*Liu et al.*, 2014]. However, it has been observed that most of these flows stop before reaching the inner magnetosphere or ring current, both during non-storm times [*Dubyagin et al.*, 2011; *Sergeev et al.*, 2012] and during storm-times [*Runov et al.*, 2021a]. Thus, ring-current energization due to energy transport into the inner-magnetosphere by BBFs, originating at a near-Earth reconnection site, is unlikely. Nevertheless, storm-time ring current energization is strong and continues for many hours to days while the storm lasts. Since transport from afar into the inner magnetosphere isn't sufficient to power the ring current at storm times either, another mechanism is required to explain the ring current energization.

Recent observations revealing the existence of very-near-Earth magnetotail reconnection (VNERX), at distances as close as 8-10 R_E, during storms [*Angelopoulos et al.*, 2020; *Runov et al.*, 2022] suggest that this process (instead of reconnection further down tail at 20-25R_E) may effectively energize particles to storm-time ring current energies. VNERX converts the large magnetic energy density stored in the very-near-Earth magnetotail lobes into plasma energy and heating, which may be sufficient to drive the ring current. The energetic particles transported by VNERX outflows can be readily supplied to the (nearby) ring current without being lost due to azimuthal curvature and gradient drift. Additionally, the very-near-Earth thin current sheet required for VNERX would allow ions with plasma sheet thermal energies (several keV) to be betatron- and Fermi-accelerated by the localized earthward convection electric fields in the presence of the strong earthward magnetic field gradient to ring-current energies. If such acceleration is initiated in a very-near-Earth thin current sheet (VNETCS), even cold (mantle) particles ushered into this region by reconnection inflows can be energized at the outflow to ring current energies. However, only a few case studies of VNERX have been reported, so the frequency of this process is unknown and, thus, its importance for ring current energization cannot yet be ascertained.

It is, therefore, important to establish how common VNERX is before assessing its potential impact on ring current energization. If VNERX is a rare process, this might suggest that other processes, like storm-time global convection, may dominate ring current energization during most storms [*Kamide*, 1992; *Fok et al.*, 2000].

Thirteen years of plasma moments, magnetic field and electric field data from the Time History of Events and Macroscale Interactions during Substorms (THEMIS) A, D, and E spacecrafts at the nightside equatorial magnetosphere allow us to quantify the occurrence rate of magnetotail VNERX during storms, and the typical strength of reconnection signatures such as reconnection electric fields and outflow speeds. We show that VNERX occurs during storm main phase, the current sheet is less than one R_E thick, and the observational occurrence rate is $\sim$1.3 VNERX events per 1000 hours of storm main phase. We found

no VNERX events occurring during the storm recovery phase, or during other (non-storm) times. Thus, for a good fraction of the storm main phase and for the entirety of its recovery phase, tail reconnection is not associated with that of VNERX and likely proceeds at larger distances from Earth. During those times, ring current energization would have to be enabled by other mechanisms like global enhanced convection (since fast reconnection outflows from large distances are rarely observed to protrude to the inner magnetosphere). THEMIS data, methods of data processing and event selections are presented in Section 3.2. Section 3.3 shows a case study and details a statistical study of VNERX, describing the average characteristics and occurrence frequency of the process. The results are further discussed in Section 3.4 and conclusions are presented in Section 3.5.

3.2 Dataset and Methods

3.2.1 Dataset

We use three-second period spin-fit magnetic field (FGS) and electric field (EFS) data from the THEMIS Fluxgate Magnetometer [FGM, *Auster et al.*, 2008] and Electric Field Instrument [EFI, *Bonnell et al.*, 2008], respectively. Ion and electron measurements come from the THEMIS Electrostatic Analyzer [ESA, *McFadden et al.*, 2008] and Solid State Telescope [SST, *Angelopoulos et al.*, 2008], ranging from 10 eV – 25 keV and 30 keV – 900 keV, respectively. ESA distributions are used to calculate ion and electron densities and ion bulk velocities. To determine changes in energetic particle fluxes and magnetic fields at geostationary orbit ($\sim$six R_E) during VNERX events we use the one-minute resolution Magnetospheric Electron Detector (MAGED), Magnetospheric Proton Detector (MAGPD) and five-minute resolution Magnetospheric Particle Sensor (MPSH) [*Kress et al.*, 2018], and magnetometers onboard the Geostationary Operational Environmental Satellite (GOES) 13, 15, 16, and 17 satellites. To study the solar wind magnetic field and dynamic pressure conditions during these events, we use one-minute resolution solar wind magnetic field and plasma

data from ACE, WIND, and IMP, time-shifted to the magnetopause nose, combined into the OMNI Dataset by, and available at, the Space Physics Data Facility. To put the VNERX events into the context of ring current energization and ionospheric dissipation we use the Symmetric H (SYM-H) and Auroral Electrojet (AE) indices from the World Data Center for Geomagnetism, Kyoto (WDC-Kyoto). The SYM-H index measures the change in the horizontal component of the ground magnetic field at low- and mid-latitudes. This index is used as a metric for storm strength and ring current energy [*Iyemori*, 1990]. Throughout this paper, the Geocentric Solar Magnetospheric (GSM) coordinates are used. In this coordinate system the x-axis is defined as the Sun-Earth line, positive defined as towards the Sun. The y-axis is defined as the cross-product of the GSM x-axis and the Earth's magnetic dipole axis, directed positive towards dusk. The z-axis is defined as the cross-product of the x and y-axes. Note that in this coordinate system, the Earth's dipole axis always lies within the x-z plane.

3.2.2 Event Detection Method

We examined THEMIS data covering Solar Cycle 24 and the beginning of Solar Cycle 25 (between 01/01/2010 and 01/01/2023). THEMIS A, D, and E (referred to herein as THA, THD, and THE, respectively) have highly eccentric, variable, low inclination (10deg) orbits, low perigee (1.1 – 1.7 R_E geocentric), and an apogee which varied over the years in the range 11.0-14.1 R_E. In a Sun-Earth fixed system, like GSM, the line of apsides naturally precesses due to Earth's motion around the Sun, such that the three apogees are in the tail for approximately three months per year.

In this paper we are concerned with identifying VNERX in general and during geomagnetic storm times, in particular. To that end, we searched all non-storm and storm times when THEMIS was in the magnetotail for VNERX events. We define a geomagnetic storm as a period starting when the SYM-H index last declines below 0 nT en-route to dropping below at least -30 nT, and thereafter first rises back to above 0 nT. These SYM-H zero-

crossing times define the beginning and the end of the storm. The peak of the storm is the time of minimum SYM-H. The main phase is the interval between the start and the peak of the storm; the remainder is the recovery phase. Over 13 years, THEMIS observed 512 storms while traversing the magnetotail. On average these lasted 3.4 days, with their main phase lasting 16.4 hours and the recovery lasting 64.7 hours. THEMIS, having a highly elliptical orbit, was not always in the plasma sheet for the entire duration of a storm. The magnetotail current sheet flaps in response to Earth's dipole diurnal variations (by $\pm 10^{\circ}$) and solar wind velocity variations (by $\pm$ 50 km/s or $\pm 5^{\circ}$); it also moves in the direction of its normal, due to the current sheet hinge point's inward and outward motion [*Fairfield*, 1980; *Fairfield et al.*, 1987; *Lopez*, 1990]. Thus, even when THEMIS is in the magnetotail, it is not always in a good position to observe tail reconnection. Using the 2015 Tsyganenko, Andreeva, and Gordeev neutral sheet model [hereafter referred to as TAG14, *Tsyganenko et al.*, 2015] to estimate the neutral sheet location, we find that the THEMIS satellites are located at a small distance (on average $< 2R_E$, see supplementary Figure 23 for the distribution of THEMIS distances from the TAG14 neutral sheet) above or below the model neutral sheet. We checked the accuracy of the TAG14 model by taking the difference between the modeled neutral sheet position and the THEMIS position during times when THEMIS observed a radial magnetic field $B_R < 0.5$ and thus should be close to the neutral sheet. Using a subset of our data from 2018-01-01 to 2023-01-01 we found that the median z-distance between the modeled neutral sheet position and the THEMIS neutral sheet crossing position was less than 0.2 R_E. Thus, we are confident that TAG14 can accurately estimate the neutral sheet position in the near-Earth tail. The natural variations of the sheet's location (on the order of $\pm 5^{\circ}$ or $\pm 1 R_E$ at 12 R_E), which are larger than the sheet's thickness (say, a few thousand km), place the spacecraft outside or within the nominal current sheet statistically with about the same probability, resulting in a total amount of time spent within the current sheet consistent with what a model current sheet would prescribe. Therefore, in our initial pass through the database in search for reconnection events, we do not control for the current

sheet thickness, but account for the total duration of time spent close to the current sheet using a neutral sheet model with the distance from the neutral sheet as a free parameter.

For the entire 13-year range considered, we searched for periods when either THA, THD, or THE were in the magnetotail tailward of the terminator ($X_{GSM} = 0R_E$) and at a radial distance greater than 4 R_E. We removed THEMIS magnetosheath periods by removing times when THEMIS observed ion densities, calculated from the observed ESA particle population, above four cm^{-3}. No restriction was initially placed on distance from the neutral sheet, as mentioned earlier.

To find VNERX we are guided by the expected characteristics of reconnection sites: (a) a strong positive EY signature throughout the ion diffusion region, spanning up to tens of ion inertial lengths ($1\lambda_i$ = 1000 km) in length [*Nagai*, 2021], and (b) fast earthward and tailward flows correlated with northward and southward magnetic fields [*Angelopoulos et al.*, 1992]. Reconnection sites are expected to move tailward (due to the pressure gradient force of the inner magnetosphere) at speeds of 100 km/s [*Russell and McPherron*, 1973], however earthward traveling reconnection has been suggested to occur as well [*Eastwood et al.*, 2005].

Guided by these reconnection characteristics we searched for both tailward-moving and earthward-moving VNERX. To find tailward-moving and earthward-moving VNERX we compiled a list of times when B_Z was observed to cross zero from negative to positive and a list of times when B_Z crossed zero from positive to negative respectively. For our tailward-moving VNERX list, we only kept the times where the maximum of the y-component of the EFI-measured electric field ($E_{Y,EFI}$) in the 2.5-minute interval prior to the B_Z zero-crossing time was greater than 5 mV/m and the average $E_{Y,EFI}$ in that same interval was greater than 0.5 mV/m. For our earthward-moving VNERX list, we only kept the times when the maximum $E_{Y,EFI}$ in the 2.5-minute interval after the B_Z zero-crossing time was greater than 5 mV/m and the average $E_{Y,EFI}$ during this period was greater than 0.5 mV/m. We further reduced our lists and only kept the events that observed a significant tailward ion bulk V_X ($V_X < -200$ km/s = -0.1 V_A, where V_A is the typical Alfven velocity near the neutral sheet at

that distance) in the 2.5 minute interval prior to (after) the B_Z zero-crossing for the tailward (earthward)-traveling VNERX list. Seven tailward-traveling, labeled Events 1-7, and zero earthward-traveling VNERX events were found.

Periods of significant neutral sheet tilt hindered our algorithm's ability to identify VNERX. This is because a neutral sheet tilt will rotate the current sheet normal such that the B_Z time-series profile of the passing reconnection site will no longer be symmetrically bipolar in GSM coordinates (it is distorted by the sheet planar component's finite projection into the Z direction). To avoid this issue, we ran a complementary search for VNERX using only ion bulk velocity V_X and E_Y. We searched for events by first identifying zero-crossings of V_X. We kept times when a tailward flow of $V_X < -250$ km/s was seen in the minute prior to the zero crossing and an earthward flow of $V_X > 250$ km/s was seen in the minute after the zero crossing. This procedure was used to find Event # 5, measured by THD, while Events 1-4, 6, and 7 were discovered using the procedure described in the previous paragraph. Because Event # 5 had a significant E_Y field, it was kept as a VNERX event.

To evaluate the importance of VNERX for ring current energization and during storm main phase (in particular), we determine the overall occurrence rate of storm-time VNERX and separately compute that rate specifically for storm main phase intervals. We compute the occurrence rate of VNERX activity (in events/1000 storm-time hrs and in events/1000 storm main-phase hrs) measured as a function of $X_{GSM} - Y_{GSM}$ position and distance from the (modeled) neutral sheet during storms. In other words, the number of VNERX events observed, normalized to the number of hours when THEMIS was near the neutral sheet and capable of witnessing reconnection outflows. In computing the temporal occurrence rate (from the number of measurement samples), we evaluated the denominator based on the duration that THEMIS was statistically close enough to the neutral sheet (based on the TAG14 model, as discussed earlier), such that observations of reconnection were deemed possible. This theoretical thickness of the reconnection process could be easily modified in this study (or in the future, by the reader) using orbit position data. Since we never saw

the aforementioned defining reconnection signatures simultaneously on any two THEMIS spacecraft (whose Z_{GSM} inter-spacecraft separations are typically $\sim$ 1 R_E), we conclude that storm-time tail reconnection observations are best identified within 1 R_E of the neutral sheet. This distance is a few to a few tens of ion inertial lengths and is consistent with expectation from the thickness of the ion diffusion region where the criteria would apply [*Nakamura et al.*, 2006; *Runov et al.*, 2008]. Accordingly, in our statistical evaluation of the occurrence rates, we treat the three satellite measurements as independent and evaluate the denominator (duration of storm-time near-neutral sheet location) to times within $\pm$1 R_E from the neutral sheet as determined by the TAG14 neutral sheet model. The TAG14 model is built from 79 yearly files of magnetic field observations from THEMIS, Polar, Cluster, and Geotail data between 1995-2013 and is particularly well-suited to describe the neutral sheet position in the dipole-tail transition region. Similarly, since the average Y separation between any two THEMIS satellites is roughly 2 R_E, we conclude that storm-time tail reconnection observations typically do not extend further than 2 R_E in Y. Thus, when constructing our 2D $X_{GSM} - Y_{GSM}$ encounter rate distributions chose to bin our encounter rates using 2 R_E by 2 R_E bins.

3.3 Results

Using the aforementioned criteria, we found that THEMIS observed seven VNERX events in the thirteen years considered in this study (regardless of whether a storm was on-going or not). Three of these events, which we identified as VNERX, have previously been identified as such in prior literature. The additional four, however, are newly introduced. We then determined that six of these events occurred during the 512 bona fide storms which took place in the months that THEMIS was in the magnetotail (identified based on their SYM-H dropping below -30 nT). The fifth event occurred during a depressed SYM-H interval with a SYM-H minimum of only -19 nT but otherwise had all the hallmarks of a storm-like SYM-H

profile and solar wind conditions. Thus, we treat that event as a storm event (albeit weaker than the others), rather than a non-storm. We proceed to incorporate it into our database due to its strong similarity with the others. All events took place during storm (or, for Event #5, storm-like) main phase. The resultant occurrence rate from the three spacecraft being in the magnetotail within ± 1 R_E of the neutral sheet for $\sim$ 25000 hrs (or $\sim$ 5300 hrs) during a storm (or a storm main phase) is one VNERX event per 3500 hours of a storm (or per 760 hrs of a storm main phase). Given our typical storm (storm main phase) duration of 82 (16.4) hrs, the observational occurrence rate of VNERX events is one VNERX event per 44 storms. We will discuss these statistics further, after a first look at the time-series of the data for one of them.

3.3.1 VNERX Case Study

Here we discuss, in detail, one of the four VNERX events in our database that have not been published previously (Event #4 in Table 3.1). We first look at the geomagnetic and solar wind conditions during the associated storm and then discuss the properties of the reconnection observed. The other six events are also presented in the same format in the Supplementary Material and are only briefly discussed herein.

3.3.1.1 AE and SYM-H Response, and Solar Wind Characteristics

Event #4 occurred during the main phase of the March 27, 2017 storm. This storm is in the event list published by *Qiu et al.* [2022] who labeled its solar wind source as a CIR. Figure 3.1 shows the AE and SYM-H indices and the solar wind magnetic field and dynamic pressure during the two days prior and after the event. The red vertical lines denote 30 minutes prior to and after the B_Z zero crossing time observed by THD. An increase in AE to over 1500 nT (Figure 3.1A), began on March 27 at $\sim$ 01:00 UT, was aligned with main phase onset evidenced by the decrease in the SYM-H index (Figure 3.1B). The storm main phase was

preceded by an increase in SYM-H from 0 nT to 15 nT on March 26 22:00 UT, a signature of storm sudden commencement (SSC) resulting from magnetospheric compression due to an increase in the solar wind dynamic pressure (Figure 3.1D). The storm main phase lasted $\sim$ 16 hours. Per Figure 3.1B, SYM-H decreased to -90 nT, thus this storm showed moderately strong ring current energization. The storm recovery phase began on March 27 at $\sim$ 16:00 UT and lasted through March 28. By March 29 the SYM-H was still -40 nT, thus the ring current was still significantly energized even 24 hours after the main phase had ended.

The solar wind magnetic field (Figure 3.1C, black curve is the magnitude) during the storm was intense. The solar wind magnetic field magnitude reached $\sim$20 nT on March 27, $\sim$ 09:00 UT, i.e. during storm main phase. The solar wind B_Z reached -12 nT during storm main phase; however, it was quite variable, frequently turning positive. Figure 3.1D shows that the solar wind dynamic pressure increased from 1 nPa pre-storm to 12 nPa during the SSC and (early) storm main phase. The dynamic pressure remained elevated above 6 nPa through storm main phase, and dropped abruptly to 4 nPa on March 27, $\sim$17:00 UT, approximately the same time that storm recovery phase began.

3.3.1.2 VNERX Equatorial Magnetotail Signatures

Between 09:30 - 10:30 UT THD was located at [-9.2, 7.5, -1.1] R_E in GSM coordinates. For this interval, Figure 3.2 shows AE, the THD magnetic field, ion bulk velocity, electric field, and ion energy flux spectrograms, and the GOES 15 magnetic field and ion and electron energy fluxes. Figure 3.2A shows that the AE index was quasi-steady at 200-300 nT until 10:00 UT when it abruptly increased, reaching 1500 nT by 10:30 UT.

Figure 3.2C shows the magnetic field components seen by THD in GSM coordinates. The B_X component (blue) shows that THD was below the neutral sheet for the entirety of this period. The large B_Y component (green) is partly due to the y position of the satellite, located well in the dusk sector. B_Z (red curve) shows a zero-crossing (negative-to-positive) at 10:00 UT. A bipolar progression in B_Z is evident surrounding that crossing and is suggestive

of an x-line retreating tailward, past THD.

Figure 3.2D shows the ion bulk velocity at THD. Coinciding with the minimum in B_Z at 09:58 UT, THD observed a strong, tailward $|V_X|$ flow, in excess of 250 km/s. From 09:58 to 10:03 UT, the V_X flow was $\leq$-250 km/s, and the V_Z increased to $\sim$ 100 km/s, suggesting strong inflow towards the neutral sheet (consistent with inflow towards a reconnection site), at the same time as the fast tailward flow. At that time $|V_Y|$ increased to 200 km/s, in the dawnward direction ($V_Y < 0$), suggesting that the fast flow event either originated earthward and duskward of THD, or initiated a vortical circulation pattern.

Figure 3.2E shows the E_Y observed by THD in DSL (Despun-Sun-L-vector, L signifying the spacecraft angular momentum, or spin axis vector) coordinates (red curve) from the EFI instrument, as well as E_Z in DSL coordinates, derived by assuming $\mathbf{E}\cdot\mathbf{B} = 0$ (blue curve). To reduce noise in the derived E_Z we only use this technique during times when the measured magnetic field makes a large angle ($> 10^\circ$) with respect to the spin-plane. Note that DSL represents a despun coordinate system native to the satellite, most natural for separating the spin-plane and spin-axis components of the electric field (spin-plane measurements are of much higher quality due to the longer, wire booms involved in conducting the electric field measurement). Since the satellite spin plane is controlled to be close to the ecliptic plane (to within $\pm 10^\circ$), the X component points roughly sunward and the Y-component roughly duskward. E_Y began to increase at 09:54 UT, during the period when the bipolar B_Z signature was observed. The maximum E_Y was 10 mV/m; an $E_Y > 5$ mV/m was observed for several minutes. From 09:54 – 09:56 UT E_Z increases from 0 mV/m to 8 mV/m. During this time THD was below the neutral plane ($B_X < 0$) thus this E_Z points towards the neutral plane. The strength and direction of E_Z suggests THD observed the Hall electric field of the reconnection site.

Figures 3.2F and 3.2G show the SST and ESA ion particle fluxes respectively. The ESA distribution lacks a peak of ion fluxes in the few hundred eV energy range during the high V_X flows, suggesting an absence of significant cold ionospheric outflow contribution to the

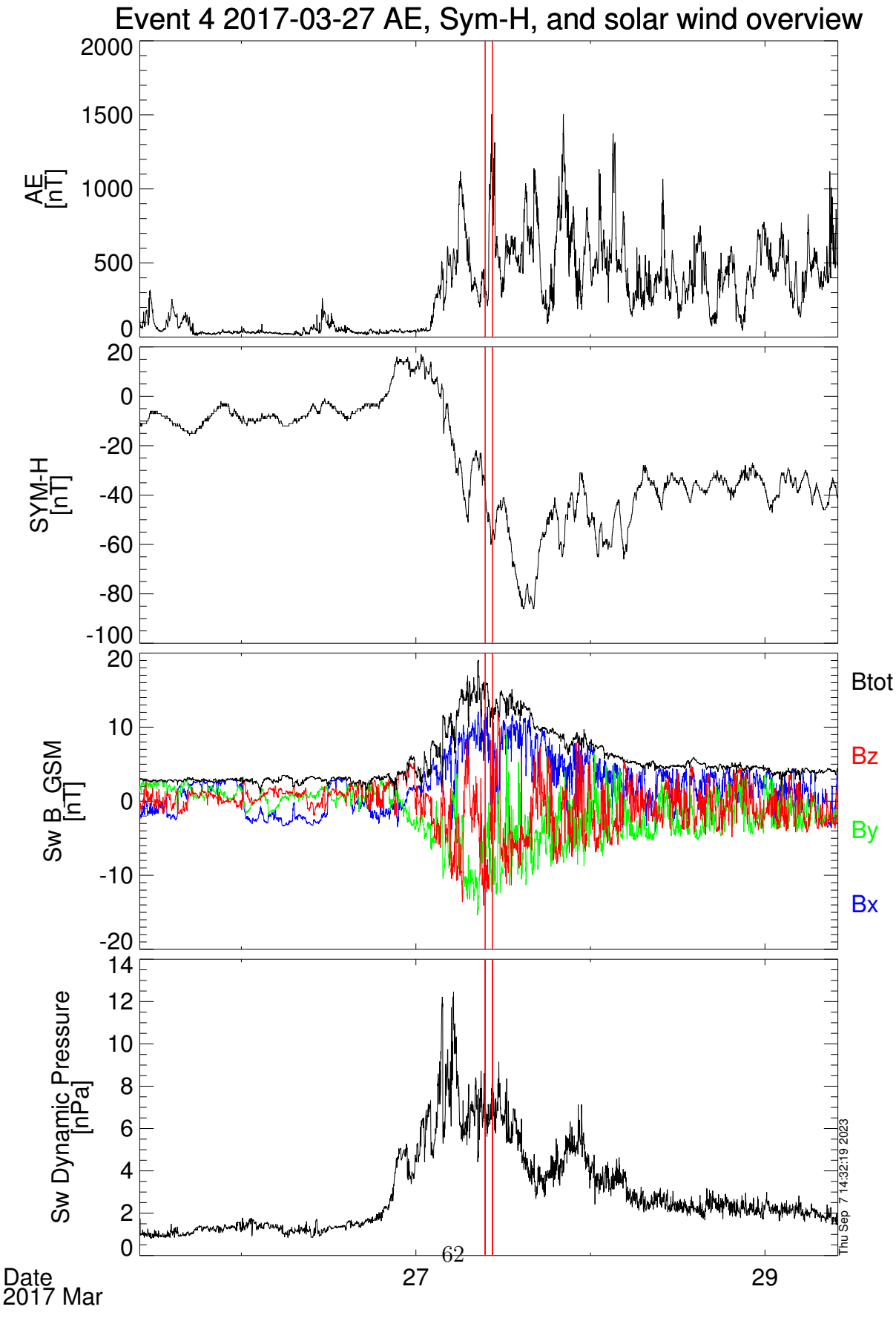
Event 4 2017-03-27 AE, Sym-H, and solar wind overview
AE [nT]
2000
1500
1000
500
0
SYM-H [nT]
20
0
-20
-40
-60
-80
-100
Sw B_GSM [nT]
20
10
0
-10
-20
Btot
Bz
By
Bx
Sw Dynamic Pressure [nPa]
14
12
10
8
6
4
2
0
Thu Sep 7 14:32:19 2023
Date
2017 Mar
27
29

Figure 3.1: *Solar wind and ground magnetometer observations of the 25 March 2017 to 29 March 2017 storm period. The red vertical lines denote the one-hour period surrounding the VNERX event studied. All data comes from the OMNI data set and have one-minute resolution. (a) AE index. (b) SYM-H index. (c) The solar wind magnetic field, blue, green, and red curves represent the x-, y-, and z-components respectively, and the black trace represents the magnitude. (d) Solar wind dynamic pressure*

tailward flow velocity. Thus, we conclude that the ion flow is due to the motion of the hot, plasma sheet plasma. The SST ion flux spectrogram shows an increase in high energy (> 100 keV) ions from 09:53-10:00 UT, suggesting ion acceleration.

Figure 3.2H shows the GOES 15-measured magnetic field in GSM coordinates. The magnetic field showed stretching, a gradual increase in the B_X (blue, positive at the time) component, until 09:54 UT. At that time, B_X decreased by $\sim$ 50 nT, while B_Z (red, also positive at the time) increased by $\sim$ 50 nT within a 2-minute interval. This is a signature of a dipolarizing field. Figures 3.2I and 3.2J show that proton and electron fluxes increased at all measured energies at GOES. These observations are consistent with GOES intercepting a dipolarizing flux tube.

This case study shows that very-near-Earth reconnection has the same hallmarks of reconnection as near-Earth reconnection previously reported farther downtail (at 20 – 25 R_E) distances: A bipolar B_Z and V_X indicative of a classic reconnection x-line. However, VNERX occurs much closer to Earth and the cross-tail electric fields seen at the reconnection site are stronger than typically seen in reconnection events at larger distances. This event exemplifies that VNERX occurs during storm main phase, and that an associated geo-synchronous dispersionless injection can occur within several minutes of such reconnection events.

The other events in our list have very similar signatures. They can be seen in Supplementary Materials Figures 1-18. They show that those events, including Event #5 which

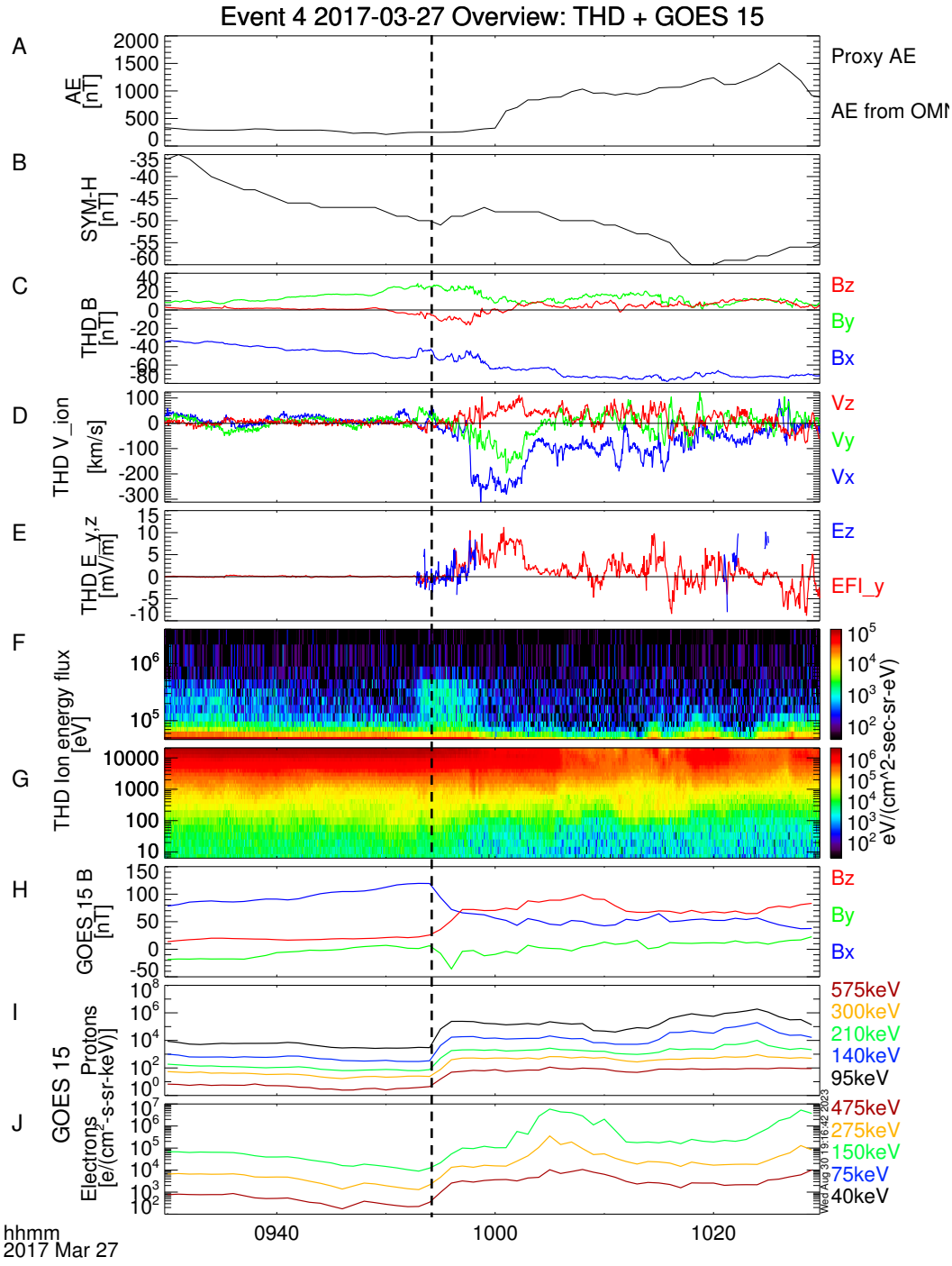
Event 4 2017-03-27 Overview: THD + GOES 15
A
AE [nT]
2000
1500
1000
500
0
Proxy AE
AE from OMN
B
SYM-H [nT]
-35
-40
-45
-50
-55
-60
C
THD B [nT]
40
20
0
-20
-40
-60
-80
Bz
By
Bx
D
THD V_ion [km/s]
100
0
-100
-200
-300
Vz
Vy
Vx
E
THD E_y,z [mV/m]
15
10
5
0
-5
-10
Ez
EFI_y
F
THD Ion energy flux [eV]
10^6
10^5
10^5
10^4
10^3
10^2
G
10000
1000
100
10
10^6
10^5
10^4
10^3
10^2
eV/(cm^2-sec-sr-eV)
H
GOES 15 B [nT]
150
100
50
0
-50
Bz
By
Bx
I
GOES 15 Protons [e/(cm^2-s-sr-keV)]
10^8
10^6
10^4
10^2
10^0
575keV
300keV
210keV
140keV
95keV
J
GOES 15 Electrons [e/(cm^2-s-sr-keV)]
10^7
10^6
10^5
10^4
10^3
10^2
475keV
275keV
150keV
75keV
40keV
Wed Aug 30 15:18:42 2023
hhmm
2017 Mar 27
0940
1000
1020

Figure 3.2: *THEMIS D (THD) and GOES magnetic field and plasma observations and ground magnetometer observations during VNERX Event #4. The black vertical dashed line denotes the time of dispersionless injection seen at geosynchronous orbit. (a) AE index from the OMNI dataset. (b) SYM-H index from the OMNI dataset. (c) Magnetic field seen at THD. The blue, green, and red curves represent the x, y, and z components of the magnetic field, respectively, in GSM coordinates. The black horizontal line marks 0 nT. (d) Ion bulk velocity at THD, derived from the ESA ion particle distribution. The colors follow the same format as in Panel (c). The black horizontal line is placed at 0 km/s. (e)* Y_{DSL} *and* Z_{DSL} *electric field seen by THD. The red curve is* E_Y *measured from the electric field instrument (EFI), and the blue curve is the normal to the s/c spin-plane electric field,* E_Z*. The black horizontal line marks 0 mV/m. (f) High energy ion energy spectra seen by the solid-state telescope on THD. (g) Low energy ion energy spectra seen by the electrostatic analyzer on THD. (h) Magnetic field seen at geosynchronous orbit by GOES 15. The colors follow the same format as in Panel (c). (i) The proton energy fluxes at GOES 15. The black, blue, green, yellow, and red curves represent proton fluxes at 95 keV, 140 keV, 210 keV, 300 keV, and 575 keV respectively. (j) Electron energy fluxes at GOES 15. The green, yellow, and red curves represent electron fluxes at 150 keV, 275 keV, and 475 keV respectively.*

occurred for a smaller absolute SYM-H have similar characteristics as Event #4 presented here. In particular, they all occurred during main phase, they have very strong reconnection and Hall electric fields and they result in ring current energization as evidenced by GOES injections.

3.3.2 Statistical Results

To quantify the importance of VNERX to storm-time ring current buildup we aim to show how often VNERX events are observed during storms and how strong the Hall and reconnection electric fields in VNERX sites are. Thus, in this section we present the statistical results that show the observational occurrence rate and average characteristics of storm-time VNERX. These results establish that one VNERX event per 44 storms is expected to be observed (per spacecraft in the near-Earth neutral sheet) during storm main phase and none during storm recovery suggesting that other modes of transport may play a significant role in building the storm-time ring current during main phase, and likely a crucial role during storm recovery phase.

3.3.2.1 VNERX Observational and Sampling Occurrence Rates

Figure 3.3 shows the X_{GSM}-Y_{GSM} distribution of total hours of storm-time and non-storm-time magnetotail residence in the region searched across all three THEMIS spacecraft (for clarity, if THA, THD, and THE were in the magnetotail in the same one-hour period, we count that as three hours of observation). Figure 3.3A, 3.3B, and 3.3C shows the X-Y residence distribution for storm main-phase, storm recovery-phase, and non-storm-time respectively. We assume that the x-line has a length in the y-direction of less than 2 R_E thus we use a bin size of 2 R_E by 2 R_E. We've also plotted this distribution assuming a larger x-line y-length of 4 R_E in Supplementary Figure 19. We see that in total THEMIS observed this magnetotail region in storm main-phase for 11543 hours, in storm recovery-phase for

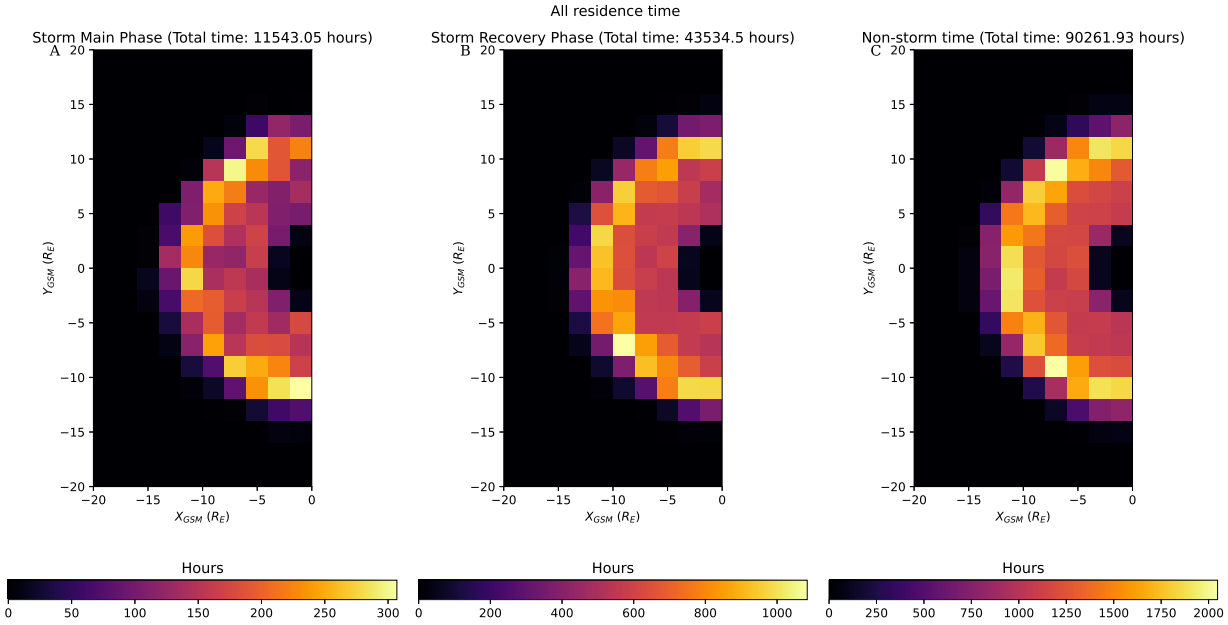

Figure 3.3: *X_{GSM}-Y_{GSM} distribution of THEMIS residence time within the magnetotail in hours. The bin resolution is 2 R_E by 2 R_E. Data from within $R < 4R_E$ has been removed. (A) Residence time distribution within the storm main-phase magnetotail. (B) Residence time distribution within the storm recovery-phase magnetotail. (C) Residence time distribution within the non-storm-time magnetotail.*

43535 hours, and in non-storm-time for 90262 hours. On average THEMIS spent 122 hours in each bin for storm main-phase, 435 hours in each bin for storm recovery-phase, and 894 hours in each bin for non-storm-times, however there is a slight maximum in bin coverage around $R_{GSM} = 14\ R_E$.

To quantify how often VNERX occurs in the magnetotail, we restricted our dataset to periods when THEMIS was well-positioned to see VNERX. Since VNERX was never seen simultaneously on more than one operating spacecraft, and the average Z_{GSM} separation of THEMIS spacecraft is $\leq 1\ R_E$, we expect that VNERX is confined to a region within one R_E of the neutral sheet. Thus, in our dataset we determine how much time each spacecraft spent within one R_E of the neutral sheet, where the neutral sheet position is derived from the TAG14 neutral sheet model. While there are discrepancies between the TAG14 modeled neutral sheet location and the observations of that location from THEMIS (arising from current sheet flapping and other effects), on average the modeled neutral sheet location should converge to the true location of the neutral sheet. This is because there is equal likelihood of the neutral sheet to be above and below the modeled location, so we assume the probability to miss VNERX is equal to the probability of observing VNERX from slightly farther away from the nominal neutral sheet.

Figure 3.4 shows the X_{GSM}-Y_{GSM} residence distribution like Figure 3.3 except restricted to only data when the THEMIS spacecraft were within one R_E in Z_{GSM} distance from the modeled TAG14 neutral sheet. Figure 3.4A, 3.4B, and 3.4C are the X_{GSM}-Y_{GSM} residence distributions for storm main-phase, storm recovery-phase, and non-storm-time with a 2 R_E by 2 R_E bin size (see Supplementary Figure 20 for the same distribution with bin size 4 R_E by 4 R_E). THEMIS observed the storm main-phase magnetotail within one R_E of the modeled neutral sheet for a total of 5253 hours, the storm recovery-phase magnetotail for a total of 19878 hours, and the non-storm-time magnetotail for a total of 41421 hours. On average THEMIS spent 59 hours in each bin for the storm main-phase distribution, 205 hours for the storm recovery-phase distribution, and 410 hours for the non-storm-time distribution.

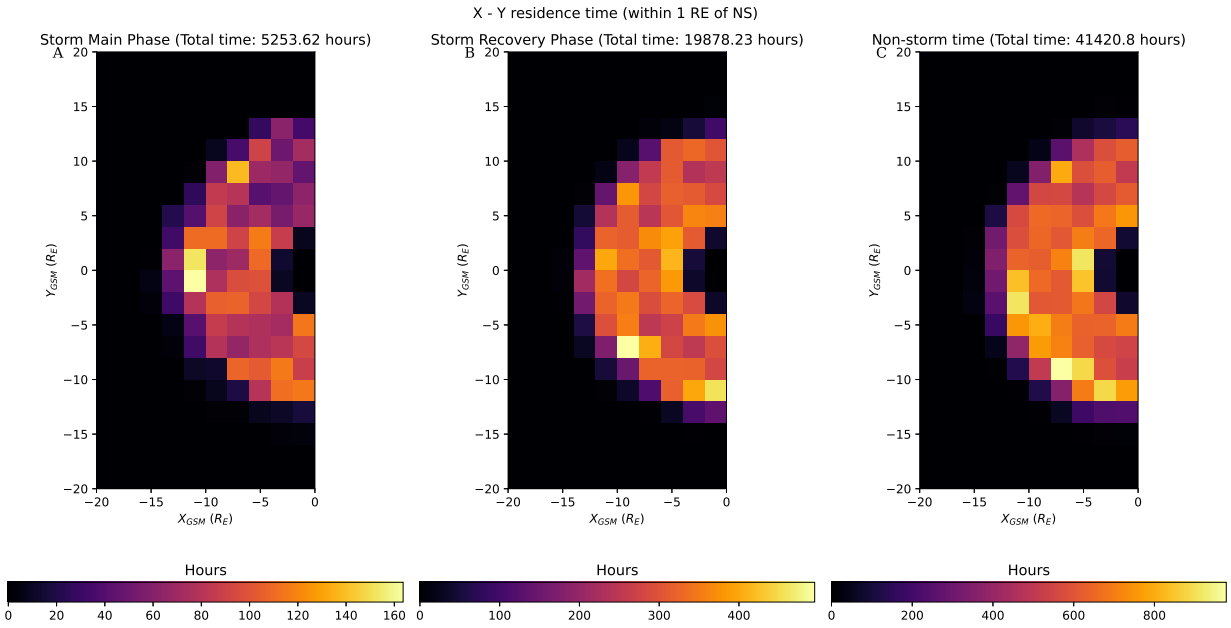

Figure 3.4: *X_{GSM}-Y_{GSM} distribution of THEMIS residence time within one R_E of the neutral sheet and within the magnetotail in hours. The bin resolution is 2 R_E by 2 R_E. Data from within $R < 4R_E$ has been removed. (A) Residence time distribution within the storm main-phase magnetotail. (B) Residence time distribution within the storm recovery-phase magnetotail. (C) Residence time distribution within the non-storm-time magnetotail.*

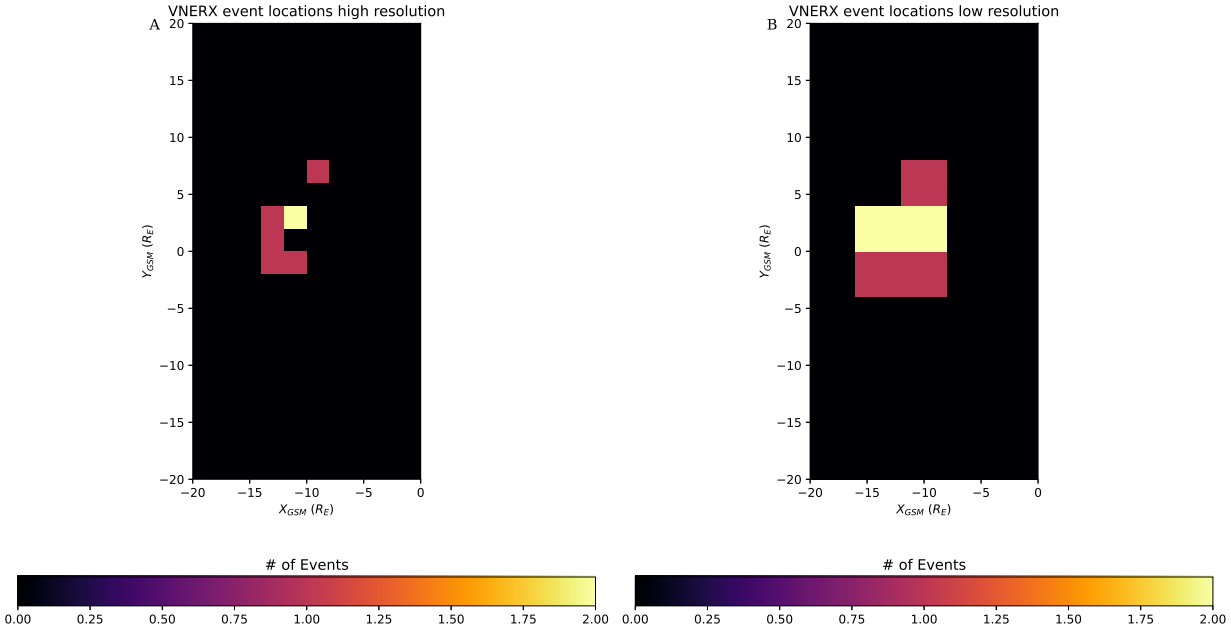

Figure 3.5: *X_{GSM}-Y_{GSM} distribution of THEMIS VNERX observation location. (A) Observation location distribution in 2 R_E by 2 R_E bin size resolution. (B) Observation location distribution in 4 R_E by 4 R_E bin size resolution.*

Figure 3.5 shows the X_{GSM}-Y_{GSM} of the THEMIS positions when they observed a VNERX event. Figure 3.5A and 3.5B show the distribution of event detection location in high resolution (bin size of 2 R_E by 2 R_E) and low resolution (bin size of 4 R_E by 4 R_E). The events were observed by THEMIS around midnight, with a slight bias towards the pre-midnight sector.

To estimate how close the THEMIS spacecrafts were to the neutral sheet during the VNERX observations we calculated the z-distance between the THEMIS satellite that observed the VNERX event and the TAG14 neutral sheet. Figure 3.6 shows the Z_{GSM} distance from the neutral sheet for the observing THEMIS satellite in a 30-minute period centered on the B_Z zero-crossing time. All events show that THEMIS was within 2 R_E of the TAG14 estimated current sheet location.

Next we estimate the VNERX occurrence rates using two different spacecraft dwell times, time spent within 1 R_E and time spent within 1000 km of the neutral sheet. The estimates of the VNERX observational occurrence rate given by the 1000 km and 1 R_E dwell times respectively give an upper and lower estimate of the true VNERX occurrence rate. We thus construct 2D encounter distributions, given in VNERX events / 1000 storm-hours, for both dwell times.

Since all the VNERX events detected were observed during storm main-phase, we chose to only consider magnetotail storm main-phase data when THEMIS was within one R_E of the storm-time neutral sheet when determining the VNERX encounter rate. Figure 3.7 shows the VNERX encounter rate (in events / 1000 hours of storm main-phase observation) in the X_{GSM}-Y_{GSM} plane. Figure 3.7A and 3.7B shows this encounter rate in high resolution and low resolution. In the high-resolution encounter rate distribution, the average rate per bin is 17.7 VNERX/1000 hours of storm main-phase observation, and for the low-resolution distribution the average is 8.8 VNERX/1000 hours of storm main-phase observation.

Figure 3.8 also displays the VNERX encounter distribution for periods when THEMIS is within 1000 km (few ion inertial lengths c/ω_{pi}) of the storm main-phase neutral sheet. Figure 3.8A and 3.8B show the encounter distributions in 2 R_E by 2 R_E and 4 R_E by 4 R_E bin sizes respectively. Since we expect the neutral sheet to be thin enough to reconnect, we are interested in this spatial scale, indicative of the ion diffusion region thickness, because signatures of VNERX, such as Hall fields, are expected to occur in this region. Supplementary Figure 21 and 22 shows the X-Y residence time distribution of THEMIS within 1000 km of the neutral sheet for storm main-phase, storm recovery-phase, and non-storm-time periods in high and low resolution respectively. We found that THEMIS spent a total of 935 hours within 1000 km of the storm main-phase neutral sheet. In the high-resolution and low-resolution plots, the average VNERX encounter rate is 128 VNERX/ 1000 hours and 62 VNERX/ 1000 hours respectively.

To quantify the importance of VNERX to storm time ring current energization it is also

important to understand the average and common characteristics of these events. In the next section we look at the common traits of VNERX.

3.3.2.2 VNERX Common Characteristics

In the seven VNERX events reported here, three had been previously reported in the literature (Table 3.1). Here we summarize the common traits among these events.

Using a one-dimensional Harris current sheet model [*Harris*, 1962] we can estimate the current sheet thickness during our VNERX events. Using differences in B_X measurements and positions from two THEMIS spacecraft and lobe magnetic field estimates derived from total pressure balance we inferred that the minimum current sheet thickness was less than 1.5 R_E in the 10 minutes prior to the B_Z-zero crossing times for all events. The minimum current sheet half-thickness in this 10-minute window is shown in the fourth column of Table 3.1. Supplementary Figure 24 shows the estimates of the Harris current sheet half-thicknesses for all events.

Using GOES 13,15,16, and 17 we found that all seven of the events showed ion injections at geosynchronous orbit. The ion injections were dispersionless, suggesting that the accelerated ions originated from an MLT near the observing satellite. All observed dispersionless ion injections showed a highly stretched tail at GOES that dipolarized at the time of the injection. The injections and dipolarization signatures that were observed occurred between 20 – 4 MLT.

We've learned that the current sheet prior to VNERX occurring can thin to less than two R_E. Reconnecting current sheets are usually observed to thin to one R_E prior to reconnection [*Sanny et al.*, 1994; *Zhou et al.*, 1997] which corroborate our findings. What we learned from GOES observations is that VNERX is correlated with dispersionless injections of high energy ion (100-500 keV) and electrons (40 – 500 keV) and that reconnection at this distance can occur in the pre-midnight to midnight sector. The observed increases in fluxes of 100s of

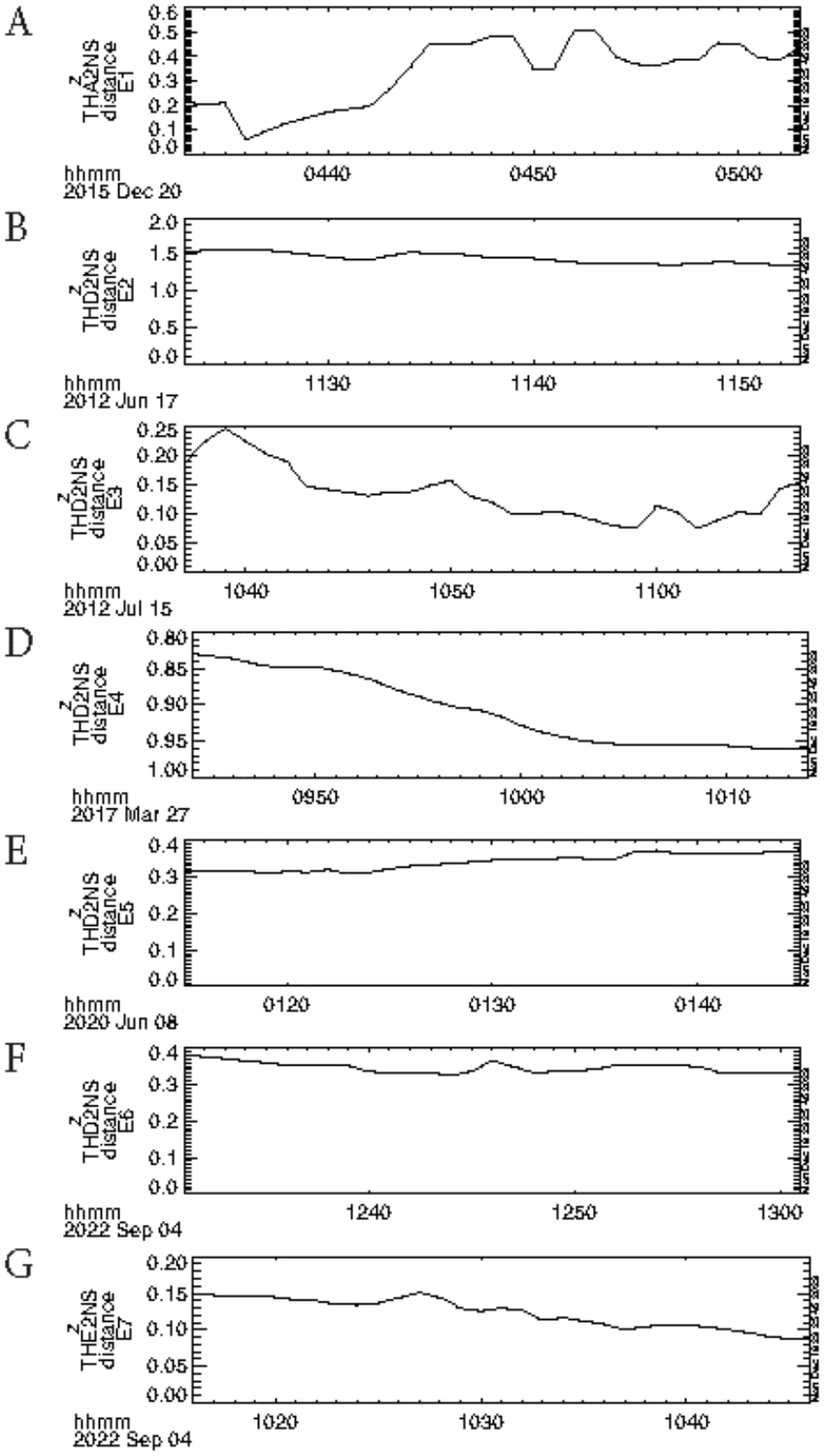
A
Z THA2NS distance E1
0.6
0.5
0.4
0.3
0.2
0.1
0.0
hhmm
2015 Dec 20
0440
0450
0500
B
Z THD2NS distance E2
2.0
1.5
1.0
0.5
0.0
hhmm
2012 Jun 17
1130
1140
1150
C
Z THD2NS distance E3
0.25
0.20
0.15
0.10
0.05
0.00
hhmm
2012 Jul 15
1040
1050
1100
D
Z THD2NS distance E4
0.80
0.85
0.90
0.95
1.00
hhmm
2017 Mar 27
0950
1000
1010
E
Z THD2NS distance E5
0.4
0.3
0.2
0.1
0.0
hhmm
2020 Jun 08
0120
0130
0140
F
Z THD2NS distance E6
0.4
0.3
0.2
0.1
0.0
hhmm
2022 Sep 04
1240
1250
1300
G
Z THE2NS distance E7
0.20
0.15
0.10
0.05
0.00
hhmm
2022 Sep 04
1020
1030
1040

Figure 3.6: *Z distance in R_E of THEMIS from TAG14 neutral sheet during VNERX observation. (A) THA z-distance from TAG14 neutral sheet during a 30-minute interval centered on the VNERX B_Z-zero crossing time of event 1. (B) THD distance during event 2 in the same format as (A). (C) THD distance during event 3 in the same format as (A). (D) THD distance during event 4 in the same format as (A). (E) THD distance during event 5 in the same format as (A). (F) THD distance during event 6 in the same format as (A). (G) THE distance during event 7 in the same format as (A).*

keV ions are significant: this is because such energy ions readily drift azimuthally and would typically miss the inner magnetosphere region if they originated further down-tail. The fact that they were observed at geosynchronous suggests that these ions were accelerated locally by the impulsive electric fields produced by reconnection outflows and the associated DFBs. At these distances these particles likely travel in fully trapped orbits and can efficiently build the ring current.

3.3.2.3 Statistical Summary of VNERX Signatures

In this section we establish that the events have all the hallmarks of a reconnection x-line. We show that the E_Y fields show the correct orientation as expected of the reconnection electric field, the inflows being directed towards the neutral plane, and the outflows away from the reconnection site.

Figure 3.9 shows the X-Y positions of THEMIS and GOES during the VNERX observations. The VNERX locations are distributed around 23:00 MLT. Given the uniform coverage of THEMIS at the nightside, this distribution demonstrates a preferential occurrence of VNERX in the pre-midnight sector, which resembles the preferential location of magnetic reconnection at non-storm times [*Nagai et al.*, 2013a; *Genestreti et al.*, 2014; *Rogers et al.*, 2019].

Figure 3.10 shows 2D histograms in B_X/B_{Lobe} – B_Z space, where B_{Lobe} was calculated

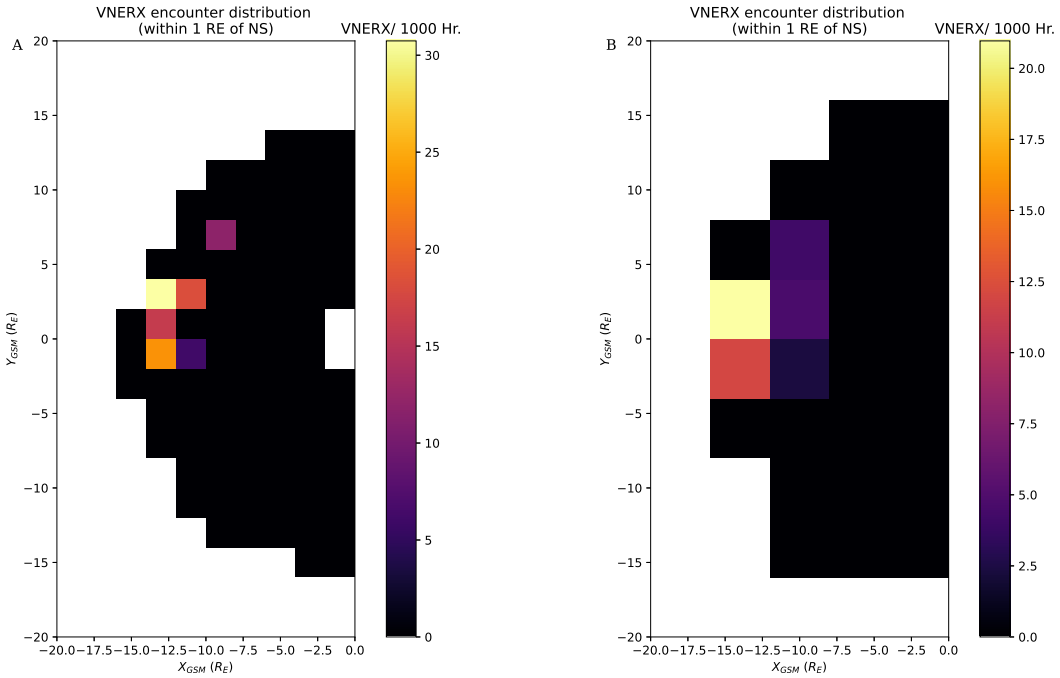

Figure 3.7: *VNERX encounter distributions in the X_{GSM}-Y_{GSM} plane in VNERX events / 1000 hours of storm main-phase magnetotail residence within one R_E of the modeled TAG14 neutral sheet. (A) VNERX encounter distribution with bin size resolution of 2 R_E by 2 R_E. (B) VNERX encounter distribution with bin size resolution of 4 R_E by 4 R_E.*

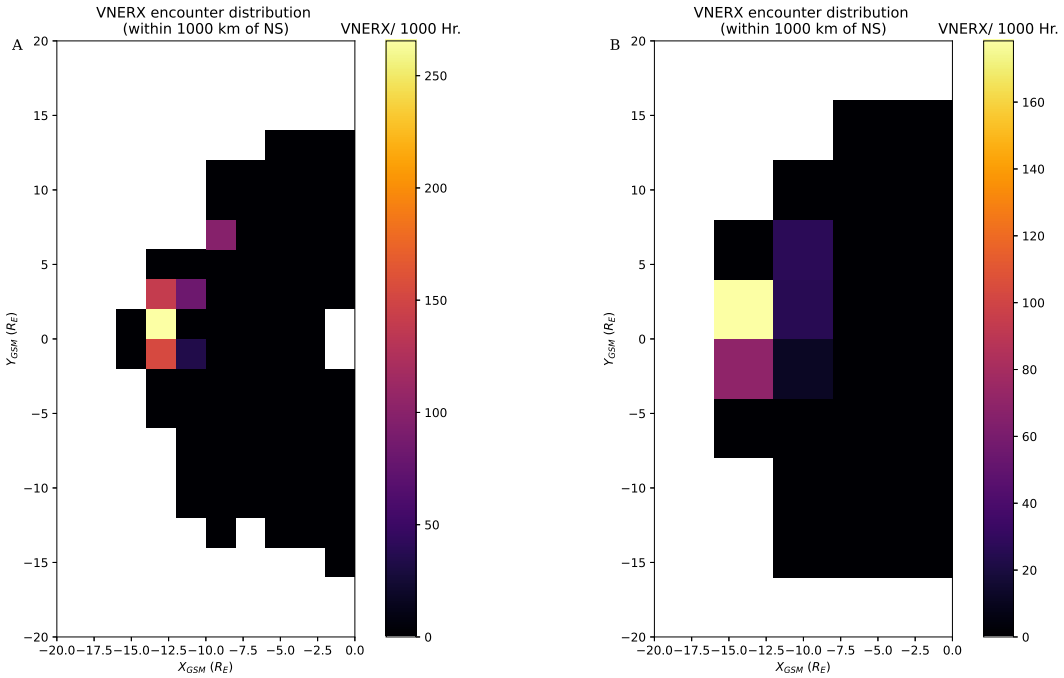

Figure 3.8: *VNERX encounter distributions in the X_{GSM}-Y_{GSM} plane in VNERX events / 1000 hours of storm main-phase magnetotail residence within 1000 km of the modeled TAG14 neutral sheet. (A) VNERX encounter distribution with bin size resolution of 2 R_E by 2 R_E. (B) VNERX encounter distribution with bin size resolution of 4 R_E by 4 R_E.*

VNERX Event	Comments	Figure location	Minimum current sheet half-thickness (R_E)
(1) 2015-12-20 04:20 – 05:20	Also in Angelopoulos et al., (2020)	Supp. Material	0.14
(2) 2012-06-17 11:10 – 12:10	Also in Runov et al. (2022)	Supp. Material	0.56
(3) 2012-07-15 10:22 – 11:22	DF in Table 1 of Runov et al. (2021)	Supp. Material	0.38
(4) 2017-03-27 09:30 – 10:30	First reported in this paper	Fig. 1 and 2	0.11
(5) 2020-06-08 01:00 – 02:00	First reported in this paper (Note: SYM-H min. was only -19nT)	Supp. Material	0.26
(6) 2022-09-04 12:16 – 13:16	First reported in this paper	Supp. Material	0.27
(7) 2022-09-04 10:05 – 11:05	First reported in this paper	Supp. Material	0.14

Table 3.1: *Timestamp of event (B_z zero crossing time), where it was first reported, where it can be found in the paper, minimum current sheet half thickness estimated using a Harris current sheet fit.*

using pressure balance ($P_{Thermal}(X_{THM}, Y_{THM}, Z_{THM}) + P_{Magnetic}(X_{THM}, Y_{THM}, Z_{THM}) = \frac{B^2_{Lobe}}{2\mu_0}$). B_X/B_{Lobe} – B_Z space allows us to put the observations into spatial context with the reconnection site: B_X/B_{Lobe} indicates the (signed) distance from the neutral sheet (positive

above and negative below) and B_Z denotes earthward ($B_Z > 0$) and tailward ($B_Z < 0$) sides of the reconnection site. The histograms are created using data from a fixed five-minute window centered on the B_Z crossing time from all events. Each bin color denotes the median value of all the data points that lie within it, thus each plot denotes the median distribution of the reconnection characteristics.

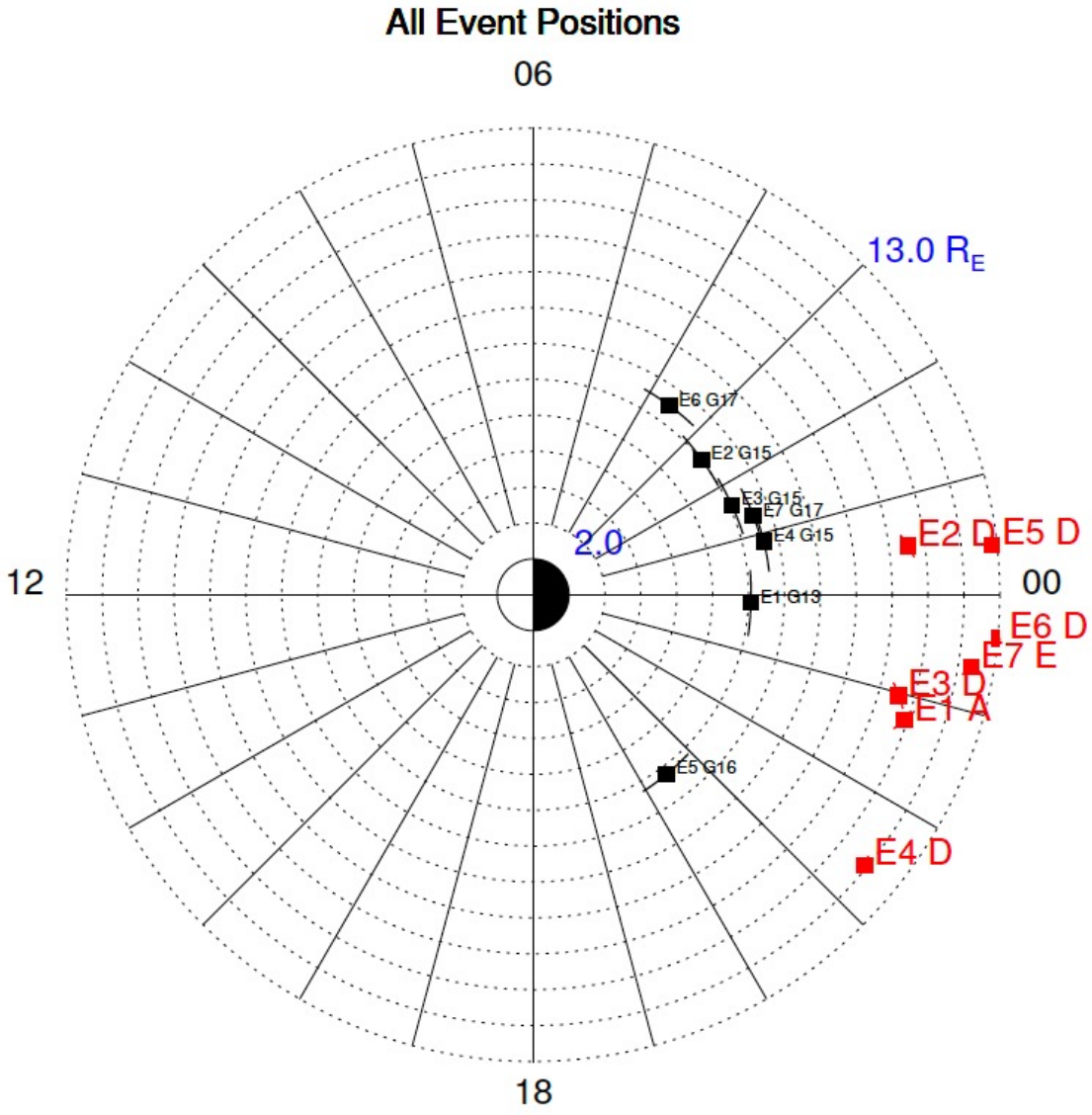

Figure 3.9: *Locations of the relevant THEMIS and GOES spacecraft for each VNERX event in red and black respectively plotted in the L, MLT coordinate system. The squares denote the spacecraft positions at the time of the VNERX event, and the thin lines threading the squares denote the satellite tracks during the one-hour time frame surrounding the event. E1 to E7 denotes the event number, the GOES satellites are labeled G13, G15, G16, G17, and the THEMIS satellites are labeled A,D, and E.*

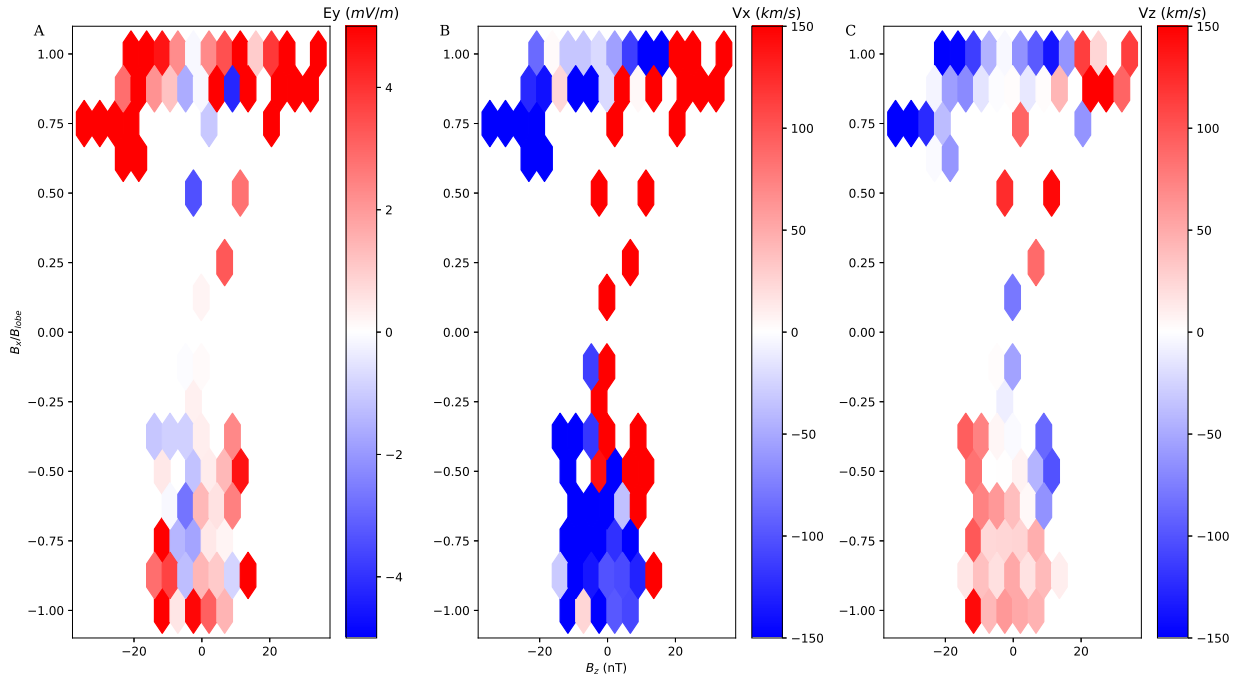

Figure 3.10: *Average characteristics of VNERX plotted in normalized B_X vs B_Z space. Applied to the reconnection x-line geometry B_Z positive/negative denotes earthward/tailward of the x-line respectively, while normalized BX positive/negative denotes above/below the neutral sheet, respectively (normalization is done using the lobe field magnitude, as determined from vertical pressure balance). (A) Y-component of the measured electric field from the EFI instrument. (B) X-component of the ion bulk velocity. (C) Z-component of the ion bulk velocity.*

Figure 3.10A shows the 2D histogram of E_Y. We see that E_Y is consistently positive throughout B_X/B_{lobe} – B_Z space, with magnitudes reaching $>$ 10 mV/m. Figure 3.10B shows ion bulk V_X. It shows that V_X is positive (earthward) for positive B_Z (earthward of the x-line) and negative (tailward) for negative B_Z (tailward of the x-line). The V_X flows are mostly greater than 100 km/s in magnitude. Figure 3.10C shows ion bulk V_Z. We see that on both sides of the neutral sheet the flows are directed towards the neutral sheet and can be larger than 150 km/s in magnitude. Care must be taken in interpreting these

results because the exact orientation of the neutral sheet in the X-Y and X-Z planes is not known, thus reconnection outflows may not strictly lie in the X_{GSM}-Y_{GSM} plane, and the reconnection electric field may not be exactly in the Y_{GSM} direction. The reconnection (E_Y) electric fields are greater than the average cross-tail convection electric field (0.1 mV/m) and greater than the typical reconnection electric fields further downtail ($\sim$ 1mV/m). These and the properties of V_X and V_Z flows are comparable to those previously in the VNERX region with multiple co-located satellites observing several of these signatures [*Angelopoulos et al.*, 2020]. They favor our interpretation that the events we identified are also VNERX events.

3.4 Discussion

Our statistical analysis of THEMIS observations of VNERX shows that these events occur in a very thin current sheet ($< 1.5\ R_E$ thick). During intense solar wind driving, the magnetotail thin current sheet moves earthward and allows for reconnection to commence at very-near-Earth locations. Once reconnection occurs there, reconnection outflows develop in the inner magnetosphere, near the ring current. There they can accelerate low energy particles from the lobe, the ionosphere and plasma sheet, and propel them over a close distance to the inner magnetosphere, allowing direct access of energetic particles into this region. It is plausible, then, that the persistence of a very-near-Earth thin current sheet (VNETCS) during storms may play a key role in storm-time ring current development.

We have shown that VNERX occurs at a rate of approximately once per 44 storms. Is this occurrence rate small? In other words, is VNERX rare? To quantify the rarity of VNERX, we compare our result to near-Earth reconnection occurrence rates during non-storm times. *Rogers et al.* [2019] compiled a list of 12 ion diffusion regions (IDRs), a proxy for the occurrence of reconnection, detected by MMS during the 2017 magnetotail campaign (Phase 2B) of the mission. Nine of those IDRs occurred during substorms. During this five-month campaign, MMS had its apogee in the magnetotail and observed the magnetotail

during a substorm for a total of 129 hours. This gives an observational occurrence rate of 1 IDR per 14 hours of substorm activity. Since substorms last on average three hours, MMS observed substorm IDRs at a rate of approximately 1 IDR per five substorms. Thus, our occurrence rate is 1/9 as frequent as the substorm IDR occurrence rate observed at MMS near apogee, i.e., at the nominal location of near-Earth reconnection, at a geocentric distance 20-30 R_E.

Why is VNERX so rarely observed? This may be partly due to the thinness of the VNETCS during storm times. As stated earlier, VNERX was only be observed within one R_E of the neutral sheet. Thus, it is very likely that THEMIS missed several events during our search. Also, the azimuthal extent of the VNERX region may have also contributed to the lack of observations. These events being limited in both Z and Y make VNERX observations elusive. We note that THEMIS only spent 1/2 of its total storm time observation duration within this distance (55078 hours vs 25131 hours).

However, there were no VNERX events we could identify during storm recovery phase, which typically lasts much longer than storm-time main phase. This means it is unlikely that VNERX can supply the ring-current energy during storm recovery phase. For storm recovery and, possibly, for a significant fraction of the time during storm-time main phase, other transport mechanisms should dominate the energization of the ring current.

Whether a VNERX will occur so close during a storm may be dictated by the solar wind dynamic pressure. Indeed, strong solar wind dynamic pressure was seen for all the events we identified. The solar wind dynamic pressure may compress the near-Earth magnetotail significantly, thus decreasing the current sheet thickness in that region to promote reconnection. Near the Earth the magnetopause is more flared than in the mid and distant tail, so the normal stress on the magnetopause due to this dynamic pressure is expected to be higher in the near-Earth magnetotail. Thus, a strong solar wind dynamic pressure may create and help maintain a VNETCS. The ongoing dayside reconnection may reduce flux pileup in the magnetotail, thus allowing the VNETCS to persist. Instead of flux tube pileup occurring

that would destroy the VNETCS, the earthward traveling flux tubes may travel quickly to the dayside, in order to replenish the dayside magnetosphere flux.

It should be noted that there is a competing effect between the ring current increasing the magnetotail magnetic field component normal to the neutral sheet and the solar wind dynamic pressure decreasing it. The increase in magnetic field strength due to an increasingly energetic ring current will act to thicken the current sheet in the very near-Earth (tailward of the ring current) region. Yet, at times when the ring current becomes energetic, i.e., storm times, the solar wind conditions are likely also very intense. Thus, if the solar wind dynamic pressure is large during storm times, this will still increase the normal stress on the magnetopause and act to thin the very near-Earth current sheet. One can study the relationship between these competing factors by understanding how the rate of flux tubes arriving at geo-synchronous orbit (seen by GOES, for example) depends on the solar wind dynamic pressure (or the time-integrated solar wind dynamic pressure over a finite period preceding the tail observations) during storms. If there is a positive correlation, then the solar wind dynamic pressure may overpower the ring current's influence on the magnetic field component normal to the current sheet and may thin the very-near-Earth current sheet. Observations of earthward-traveling dipolarizing flux tubes in the very-near-Earth region can also reveal how many of these flux tubes reach geo-synchornous orbit and determine whether the flux tubes seen at THEMIS more often reach GOES as solar wind dynamic pressure increases.

3.5 Summary

In this study we aimed to understand how significant VNERX is to storm-time ring current buildup. To that end, we asked: (a) How often is VNERX observed during storms? (b) What are the average signatures of VNERX? To answer (a) we used THEMIS and GOES plasma and magnetic field observations over Solar Cycle 24 and developed algorithms to find

signatures of a tailward retreating x-line observed at very-near-Earth distances (4 R_E < R <14 R_E). To answer (b) we conducted a 2d histogram analysis (in B_X/B_{lobe} - B_Z space) of the reconnection electric fields, and reconnection inflows and outflows seen in our events. This analysis displayed the average characteristics of the flows and electric fields of the VNERX events and placed them in the context of the x-line geometry. Our conclusions are the following:

1. We found VNERX is observed at a rate of once per 44 storms, which is nine times more rare than previously reported IDRs during substorm times in the near-Earth magnetotail (15 – 20 R_E).

2. The events all show classical reconnection signatures. The reconnection electric fields frequently peaked above 10 mV/m. These results are aligned with our interpretation that VNERX can contribute to the storm-time ring current energization by converting the energy available in the Earth magnetotail lobes into particle heating and energization from closer to Earth than classical tail reconnection occurring at larger tail distances. GOES dispersionless injections were seen for all the events, with simultaneous proton flux increases for energies from 10s to 100s of keV seen.

3. We have determined that storm-time VNERX are observed to occur closer than 2 R_E to our estimated location of the neutral sheet. This suggests that VNERX occur within a thin current sheet, typically thinner than 1 R_E. We suggest that this current sheet is thinned due to strong solar wind dynamic pressure compressing the tail.

More storm-time THEMIS observations and global MHD models may help elucidate how a thin current sheet persists during a storm, and how the formation of a thin current sheet depends on solar wind dynamic pressure. More observations of the magnetotail expected during the upcoming solar maximum can help better characterize the frequency of VNERX in terms of solar cycle.

Data and Software Availability Statement

THEMIS data are available through http://themis.ssl.berkeley.edu. The OMNI data, including solar wind parameters and geomagnetic indices, were obtained from the GSFC/SPDF OMNIWeb interface at http://omniweb.gsfc.nasa.gov. THEMIS mission data and OMNI data have been imported and analyzed using corresponding plug-ins to the SPEDAS analysis platform [http://spedas.org *Angelopoulos et al.*, 2019]. The Tsyganenko, Andreeva, and Gordeev 2015 neutral sheet model is available through https://geo.phys.spbu.ru/ tsyganenko/empirical-models/current_sheet/neutral_sheet/.

Acknowledgments

We acknowledge NASA contract NAS5-02099 for support and for use of data from the THEMIS mission. Specifically: The late C. W. Carlson and J. P. McFadden for use of ESA data, D. Larson and the late R. P. Lin for the use of the SST data, and K. H. Glassmeier, U. Auster, and W. Baumjohann for the use of FGM data provided under the lead of the Technical University of Braunschweig and with financial support through the German Ministry for Economy and Technology and the German Center for Aviation and Space (DLR) under Contract 50 OC 0302. We thank the SPEDAS software team and NASA's Coordinated Data Analysis Web (CDAWeb, https://cdaweb.gsfc.nasa.gov/) for their analysis tools and data access.

CHAPTER 4

Earthward-tailward asymmetry of plasma heating in reconnection outflow in Earth's magnetotail

Abstract

To explore the asymmetry in ion and electron heating at Earth's magnetotail at mid-tail distances (X_{GSM} < - 30 R_E), we analyze near-simultaneous observations of reconnection outflows from two opposite sides of reconnection sites at those distances using Magnetospheric Multiscale (MMS) and Acceleration, Reconnection, Turbulence and Electrodynamics of Moon's Interaction with the Sun (ARTEMIS) data. We report a pronounced temperature asymmetry between the earthward and tailward reconnection outflows. The asymmetry is more significant for electrons than for ions: Earthward moving ions are heated only three times more than tailward ones, but earthward moving electrons are heated 5-20 times more than tailward ones. The closed field-line topology on the earthward side of the reconnection region, as opposed to the open topology on the tailward side, is likely a critical contributor to this asymmetry. These findings cast light on the underlying mechanisms of particle heating and energization in magnetotail reconnection, highlighting the significant role of Earth's dipolar magnetic field. This study offers insights for refining magnetic reconnection models, emphasizing the importance of incorporating realistic magnetic field topologies to accurately simulate the heating and energization processes observed in space plasma environments.

4.1 Introduction

Magnetic reconnection enables the conversion of magnetic energy into plasma heating and the acceleration of charged particles [*Nagai*, 2021]. This process is widespread across magnetized astrophysical objects, playing a crucial role in the energy transport and plasma convection within these environments. Within Earth's magnetosphere, magnetic reconnection is pivotal to various plasma convection modes, including substorms [*McPherron*, 1979], steady magnetospheric convection events [*Gonzalez and Parker*, 2016; *Sergeev et al.*, 1996], and geomagnetic storms [*Gonzalez et al.*, 1999, 1994]. It facilitates the conversion of magnetic energy from the stretched and compressed magnetic field lines of the magnetotail lobes into plasma bulk kinetic energy and enthalpy, as evidenced in numerous studies [*Birn and Hesse*, 2005; *Birn and Hesse*, 2010; *Angelopoulos et al.*, 2013; *Eastwood et al.*, 2013]. During this process, inflowing plasma is accelerated to speeds reaching hundreds of km/s, as evidenced at reconnection jets [*Øieroset et al.*, 2000, 2001; *Runov et al.*, 2003], field-aligned currents are created [*Artemyev et al.*, 2018], and electromagnetic energy flows both earthward and tailward of the reconnection site [*Angelopoulos et al.*, 2013]. Magnetic reconnection is integral to the transport of magnetotail magnetic flux, allowing it to move earthward as dipolarizing flux bundles (DFBs) [*Liu et al.*, 2014] often accompanied by dipolarization fronts [*Runov et al.*, 2011] and tailward as rapid flux transfer events (RFTs) [*Schödel et al.*, 2001] often accompanied by antidipolarization fronts [*Li et al.*, 2014a]. It also plays a critical role in magnetotail dynamics by preventing the over-pressurization of the near-Earth magnetotail, thereby avoiding the so-called 'pressure catastrophe' [*Baumjohann*, 2002]. The pivotal role of magnetotail reconnection in both local and global processes underscores the significance of understanding the dynamics of energy conversion during magnetic reconnection and its subsequent effects, to gain insight into the underlying mechanisms governing these processes.

Recent simulations focusing on magnetotail reconnection have delved into how energy is distributed among kinetic, thermal, and electromagnetic forms. *Birn and Hesse* [2010]

employed 2.5-D MHD and PIC simulations to explore how energy is transformed in Harris-type current sheets. They showed that the predominant forms of outgoing energy flux were Poynting flux and enthalpy flux. Subsequent research into the energy dynamics of magnetic reconnection revealed that the thermal energy of electrons and ions increases significantly more than the bulk kinetic energy [*Lu et al.*, 2013, 2018]. This increase in thermal energy has been attributed to the action of the pressure-gradient force, which converts the bulk kinetic energy near the x-line into enthalpy flux. This is followed by quasi-adiabatic heating that transforms the enthalpy into thermal energy density [*Birn and Hesse*, 2010; *Lu et al.*, 2013].

The Earth's magnetotail is a dynamic arena for magnetic reconnection, characterized by diverse guide fields, initial conditions, and background pressure profiles. In the mid-tail region, which extends beyond 30 Earth radii [*Genestreti et al.*, 2014], the magnetic field topology typically exhibits a small positive B_z component within the neutral sheet, and a magnetic field strength that is relatively uniform along the tail's length [*Fairfield and Jones*, 1996]. Additionally, it is anticipated that the current sheet undergoes thinning prior to magnetic reconnection in the mid-tail, accompanied by a reduction in the B_z gradient to zero [e.g., *Baker et al.*, 1996; *Petrukovich et al.*, 2013; *Sitnov et al.*, 2019; *Runov et al.*, 2021b]. This setting is different from the initial conditions of recent simulations of near-Earth magnetotail reconnection [e.g., *Lu et al.*, 2018], because the mid-tail lacks the strong magnetic field and pressure gradients present in the near-Earth magnetotail. Thus, it serves as an excellent test bed to determine whether these gradients are a necessary or sufficient requirement for magnetotail reconnection driven plasma heating.

Recent investigations have leveraged concurrent, multi-point observations of reconnection outflows to elucidate the energy partitioning in magnetotail reconnection events. Several studies of reconnection outflows [*Angelopoulos et al.*, 2013; *Runov et al.*, 2018; *Birn et al.*, 2015] indicate pronounced particle energization earthward of the reconnection sites. Specifically, [*Runov et al.*, 2018] discerned a disparity in electron temperatures and electron fluxes

at energies exceeding 10 keV between earthward-directed DFBs in the near-Earth tail (X $> -14R_E$) and RFTs directed tailward at lunar distances. While electron temperatures and energies were markedly higher in earthward DFBs, ion ones remained relatively similar in both directions. They suggested that because tailward of the reconnection site electrons and ions move along open field lines into regions of diminishing magnetic field strength, they undergo limited energization and heating. Conversely, earthward of the reconnection site, the increasing pressure gradient facilitates substantial heating, and the closed field-line structure enables repeated interactions of the ambient plasma with the reconnection site and DFBs [see *Birn et al.*, 2014], leading to significant particle energization there.

Since past literature suggests pressure and magnetic field gradients play an important role in reconnection-driven plasma heating, we should expect negligible heating associated with magnetic reconnection in the absence of these gradients. However, due to the lack of coordinated satellite fleets to conduct a survey of plasma heating properties associated with reconnection at the mid-tail (X $< -30R_E$), where plasma and magnetic field gradients are small, it is unclear whether significant heating occurs there. In this paper we aim to address whether plasma heating driven by magnetotail reconnection can still occur at these distances.

We utilize data from the MMS and ARTEMIS missions, taking advantage of the opportune Sun-Earth alignment these missions provide in the magnetotail for 3 months per year when the MMS apogee is located in the magnetotail and ARTEMIS is also there for a few days per month. This unique dataset spans 2016-2024 and is the only dataset during this period that allows us to study mid-tail reconnection events simultaneously earthward and tailward of the reconnection site. We build upon the statistical work of [*Runov et al.*, 2018] by examining the temperature asymmetries of electrons and ions under controlled conditions of minimal, and well-characterized pressure and magnetic field B_z gradients from near simultaneous observations of reconnection outflows on both sides of the reconnection region. Such controlled conditions allow us to isolate and analyze the impact of the dipolar, closed-field

line boundary conditions on the thermalization process of particles. The paper is organized as follows: the dataset and event selection criteria are described in Section 4.2. A case study of plasma heating during midtail reconnection is described and the statistical results of ion and electron temperatures are presented in Section 4.3. Section 4.4 contains the discussion. A summary of our work is given in Section 4.5.

4.2 Method

4.2.1 Dataset

We use four second (spin-fit) magnetic field data from the THEMIS Fluxgate Magnetometer instrument [FGM, *Auster et al.*, 2008] and 0.125 second raw magnetic field data from the MMS Magnetometer instrument [*Russell et al.*, 2016] subsequently interpolated to match the THEMIS FGM cadence. The ion and electron measurements on THEMIS come from the Electrostatic Analyzer [ESA, *McFadden et al.*, 2008] ranging in energy from 10 eV/q to 25 keV/q and by construction match the THEMIS FGM spin fits. The ion and electron measurements for MMS come from the Fast Plasma Investigation instrument [FPI, *Pollock et al.*, 2016], which covers the energy range 10 eV/q to 30 keV/q. The ESA and FPI electron and ion distributions are integrated to derive the average density, temperature, and bulk velocity for ions and electrons. MMS moments are interpolated to match the THEMIS FGM time cadence.

4.2.2 Event Selection

To compare the properties of earthward and tailward reconnection ejecta we use MMS and ARTEMIS (its P1 and P2 probes, hereafter referred to as THB and THC, see *Angelopoulos* [2011]) as the earthward and tailward monitors, respectively. To ensure we capture ejecta from the same reconnection site, we use the following three criteria. 1) MMS and ARTEMIS

must have an inter-spatial separation in Y_{GSM} of less than 5 R_E: This ensures that MMS and ARTEMIS are co-aligned with the reconnection exhausts, whose azimuthal extent is approximately 5-10 R_E wide [*Li et al.*, 2014b; *Nakamura et al.*, 2004]. 2) MMS and ARTEMIS must both observe ion bulk flows with $|V_x| > 150$ km/s, MMS in the earthward direction and ARTEMIS in the tailward direction: Flows of this magnitude are large enough to be indicative of reconnection ejecta [*Nagai et al.*, 2013b, 2015]. 3) MMS and ARTEMIS must observe these flows within < 10 minutes of one another: This is a strong indication that we are indeed capturing ejecta from the same reconnection site.

4.3 Results

4.3.1 Summary of case study

On July 9th, 2017, between 21:10 and 21:22 UT, the MMS and ARTEMIS spacecraft were closely aligned, with their separation in the Y_{GSM} coordinate below 5 R_E. Figure 4.1 shows the X_{GSM}-Y_{GSM} positions of MMS, THB (ARTEMIS P1), and THC (ARTEMIS P2) during this period, marked by red and black circles, vertices of the blue triangle. During this interval, both spacecraft detected fast ion bulk flows surpassing speeds of 150 km/s. Figure 4.2 shows the plasma and magnetic field measurements captured by both spacecraft. Figure 4.2A shows the X_{GSM}-component of the ion bulk velocity at both MMS and ARTEMIS. MMS measured ion bulk flows, V_x, exceeding 150 km/s from 21:11:00 UT to 21:16:00 UT, a period delineated by solid vertical lines. Subsequently, from 21:16:40 UT to 21:20:00 UT—marked by dotted vertical lines—both THB and THC measured V_x below -150 km/s.

Figure 4.2B shows the X-component of the magnetic field at MMS and ARTEMIS. For most of the time, MMS observed a negative B_x, so it was positioned below the neutral sheet. Both THB and THC observed positive B_x, between 0 to 10 nT, for the entire period and were situated above the neutral sheet.

Figure 4.2C shows the Z-component of the magnetic field as recorded by MMS and

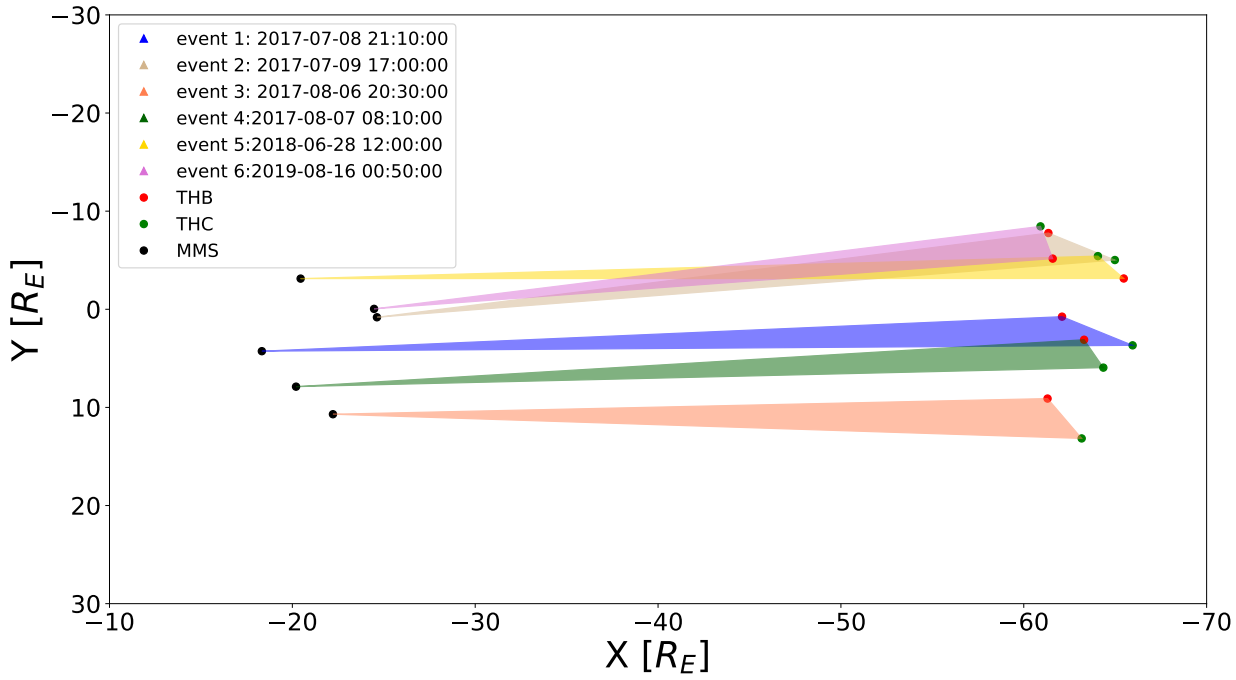

Figure 4.1: *X_{GSM},Y_{GSM} positions of MMS, THB, and THC for all six events in the study. The vertices of the colored-triangles show the positions of MMS, THB, and THC that correspond to a particular event.*

ARTEMIS. MMS detected a positive B_z while ARTEMIS detected a negative B_z throughout the interval. Specifically, during the period marked by solid vertical lines, MMS observed two local maxima in B_z at 21:14:30 UT and 21:15:30 UT, which correspond to peaks in the ion bulk V_x. This pattern is consistent with the anticipated behavior of earthward-traveling DFBs [*Liu et al.*, 2014]. We thus interpret these observations as MMS detecting two DFBs originating at a proximate reconnection site. Conversely, in the segment demarcated by dashed vertical lines, THB and THC recorded a negative B_z, reaching a minimum of -5 nT—a signature often associated with reconnection ejecta in the distant magnetotail [see *Runov et al.*, 2018].

Figures 4.2D, E, and F show energy spectrograms of ion energy flux for MMS, THB, and THC respectively, albeit with different energy-flux range (in the colorbar). Figure 2D shows

that at MMS the ion flux was mostly above 100 eV. Notably, during intervals coinciding with peaks in B_z and V_x around 21:14:30 UT and 21:15:30 UT MMS recorded an increase in energetic ion intensity and an increase in the energy of peak flux compared to adjacent times. Conversely, Figures 4.2E and F illustrate that while THB and THC initially observed an ion energy flux spectrum similar in shape to that of MMS (indicating the ion temperatures were comparable), a dramatic change occurred post-21:18:30 UT. A low-energy ion population ($<$ 100 eV) emerged, and the higher-energy ions gradually diminished. This shift, occurring simultaneously with a sustained, significant B_x, implies ARTEMIS observed outflowing cold ions from the ionosphere, streaming along the field and simultaneously convecting equatorward across the magnetotail towards and within the equatorial plasma sheet [*Poppe et al.*, 2016; *Runov et al.*, 2023]. Because these cold ions were observed simultaneously with hot ions (10-20keV peak in the same spectrograms), indicative of heated ambient plasma sheet ions, consistent with the tailward velocities observed in Panel A, this suggests that the cold ions likely entered the plasma sheet through magnetic reconnection somewhere earthward of the ARTEMIS satellites.

Figures 4.2G, H, and I display energy spectrograms of the electron energy flux observed at at MMS, THB, and THC. In Figure 4.2G, MMS captures an electron population primarily within the 20 eV to 2 keV range (accounting for a spacecraft potential of approximately +10 eV), with the flux of 2 keV to 10 keV electrons conspicuously increasing post-21:17 UT. The most significant fluxes were observed in the 500 eV to 1 keV range, consistent with the electron temperature. (Note that the large electron fluxes at <20eV at MMS and <80eV at ARTEMIS are due to spacecraft photoelectrons which extend to a higher energy due to the different spacecraft potentials in there different respective plasma environments.) Conversely, Figures 4.2H and I illustrate that THB and THC predominantly detected electron fluxes below 1 keV. Between 21:10 and 21:18 UT, both spacecraft recorded a consistent electron energy flux, peaking at 200 eV. After 21:18 UT, there was a noticeable decrease in energy flux for energies below 1 keV, coinciding with the emergence of the low-energy ion population

detailed in Figures 4.2E and F.

Through this case study, we have detailed the characteristics of ion and electron populations in the 10 eV to 30 keV range, alongside magnetic field and ion velocity measurements, both earthward and tailward of a reconnection site. Utilizing MMS and ARTEMIS for monitoring reconnection ejecta allows for a direct comparison of electron and ion properties on either side of the reconnection. Our study notably highlights the electron and ion temperatures on either side of reconnection sites. The following section will introduce a quantitative analysis of these temperatures and detail their asymmetries through a multi-event study involving six distinct reconnection events.

4.3.2 Statistics of Ion and Electron temperatures

In the 2016-2024 period we identified six instances where MMS, THB, and THC were positioned within 5 R_E of each other in the y-direction, capturing fast flows directed both earthward and tailward within a 10-minute window of each other. Table 4.1 lists these events and showcases the maximum (for MMS) and minimum (for THB and THC) X-component ion bulk velocities observed. Figure 4.1 depicts the spacecraft positions during these events, with the triangles forming between MMS, THB, and THC color-coded by event. Data from THB and THC were then combined into a single ARTEMIS dataset, facilitating a comparison with MMS data. The MMS and ARTEMIS datasets are refined to include only plasma and magnetic field data from MMS when V_x >150 km/s and plasma beta ($\frac{P_{thermal}}{P_{magnetic}}$) > 2., and from ARTEMIS when $V_x < -150$ km/s and plasma beta > 1, ensuring the focus is on the reconnection outflows within the plasma sheet. By incorporating the plasma beta condition we avoid including reconnection separatrix measurements, where only a fraction of the reconnected plasma sheet population (the most energetic field-aligned particles) are sampled.

This comparison was also supported by calculating the y-component of the convective electric field $E_y = -(\mathbf{V} \times \mathbf{B})_y$. Figure 4.3 shows scatterplots contrasting B_z with V_x across

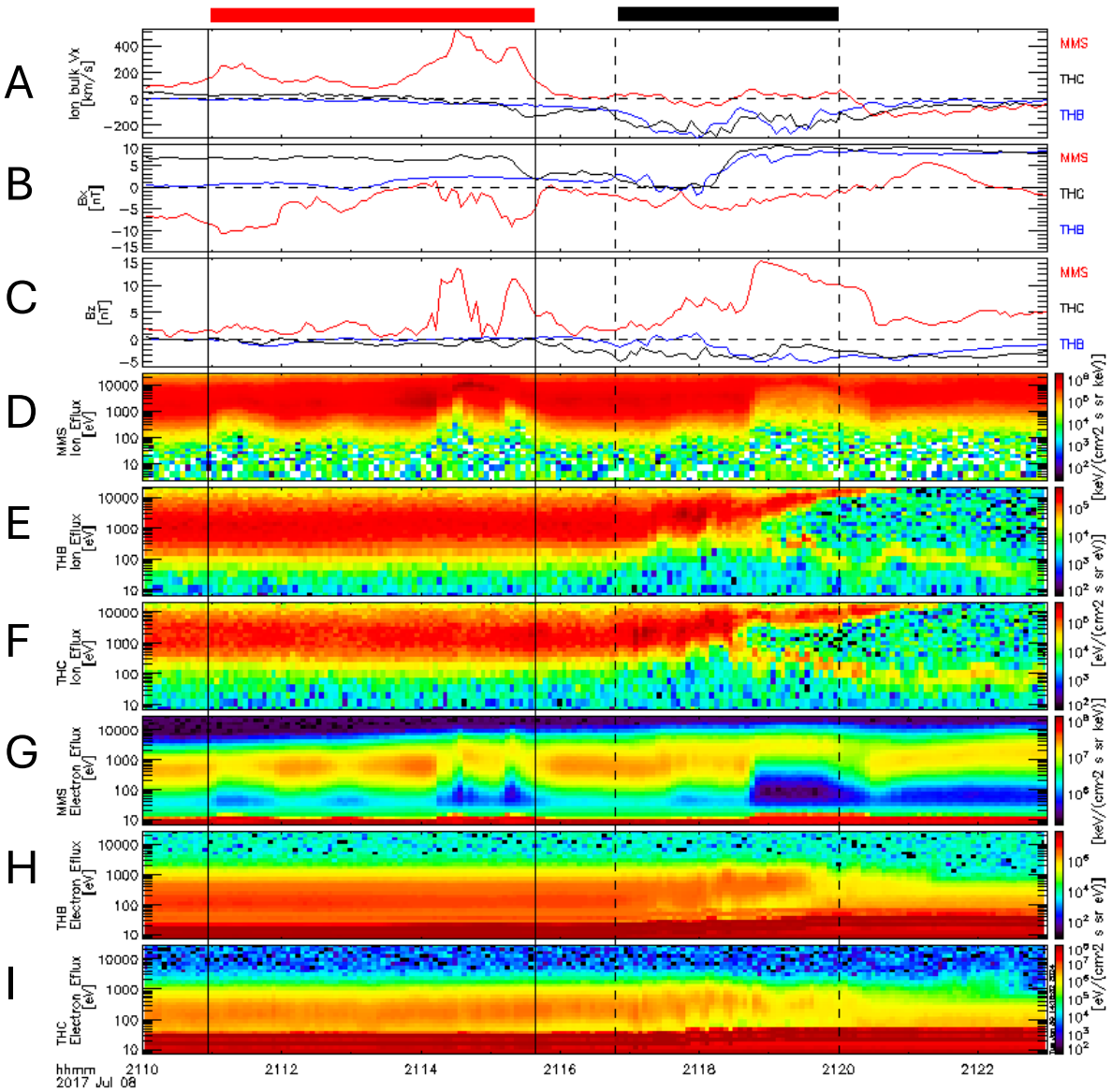
A
B
C
D
E
F
G
H
I
Ion bulk Vx [km/s]
Bx [nT]
Bz [nT]
MMS
THC
THB
MMS Ion_Eflux [eV]
THB Ion_Eflux [eV]
THC Ion_Eflux [eV]
MMS Electron_Eflux [eV]
THB Electron_Eflux [eV]
THC Electron_Eflux [eV]
[keV/(cm^2 s sr keV)]
[keV/(cm^2 s sr eV)]
hhmm
2017 Jul 08
2110
2112
2114
2116
2118
2120
2122

Figure 4.2: *Summary plot of magnetic field, ion bulk velocity, and plasma energy fluxes for Event 1. A) The x-component of the ion bulk velocity for MMS in red, THB in blue, and THC in black. The horizontal dashed line indicates* $V_x = 0$*. The vertical solid lines and the solid red dashed line above panel A demarcate the period when MMS observed a* $V_x > 150$ *km/s. The vertical dashed lines and the solid black dashed line above panel A demarcate the period when either THB or THC observed a* $V_x < -150$ *km/s. B)* B_x *observed by MMS in red, THB in blue, and THC in black. C)* B_z *observed by MMS in red, THB in blue, and THC in black. D) The ion energy-flux vs energy spectrogram recorded by FPI onboard MMS. E) The ion energy-flux vs energy spectrogram recorded by the ESA instrument onboard THB. F) The ion-energy-flux vs energy spectrogram recorded by the ESA instrument onboard THC. Note that the colorbars of the MMS, THB, and THC ion spectrograms cover different flux ranges. G) The electron energy-flux vs energy spectrogram recorded by the FPI onboard MMS. H) The electron energy-flux vs energy spectrogram recorded by the ESA instrument onboard THB. I) The electron energy-flux vs energy spectrogram recorded by the ESA instrument onboard THC.*

Event	max($V_{X,MMS}$) (km/s)	min($V_{X,ARTEMIS}$) (km/s)
1. 2017-07-08/21:10:00 - 21:23:00	524.4	-309.2
2. 2017-07-09/17:00:00 - 17:10:00	709.0	-732.3
3. 2017-08-06/20:30:00 - 20:50:00	373.0	-418.0
4. 2017-08-07/08:10:00 - 08:40:00	581.1	-661.0
5. 2018-06-28/11:59:00 - 12:20:00	532.0	-1068.0
6. 2019-08-16/00:50:00 - 01:10:00	625.0	-570.0

Table 4.1: *List of events used in this study, with time ranges considered for each event and maximum earthward and tailward velocities observed*

all identified events, where each scatter-point's color represents the E_y value. This visualization confirms the theoretical expectation of a positive correlation between V_x and B_z in magnetotail reconnection, attributed to the X-line geometry: positive V_x aligns with positive B_z periods and vice versa, with E_y maintaining positivity in both earthward and tailward flows [*Eastwood et al.*, 2010; *Baumjohann et al.*, 1990; *Ueno et al.*, 1999].

Figure 4.4 displays the average ion temperatures for MMS and ARTEMIS as a function of the ratio $\frac{B_X}{B_{LOBE}}$, which is used as a proxy of the distance from the neutral sheet. In this ratio, B_{LOBE} was derived under the assumption of vertical pressure balance [*Baumjohann et al.*, 2000; *Petrukovich et al.*, 1999].

Figures 4.4A-F depict ion temperatures observed by MMS (in red) and ARTEMIS (in blue) as scatter points, with step-plots in color illustrating the median temperatures for each, categorized according to the ratio $\frac{B_X}{B_{LOBE}}$. The median ion temperatures at ARTEMIS (blue step-plot) are uniformly lower than those at MMS (red step-plot), with ARTEMIS temperatures averaging between 0.7 keV and 2 keV, and MMS temperatures between 3 keV and 7 keV. The ratio of these temperatures is ~ 3. The temperatures do not change significantly with distance from the neutral sheet, in agreement with prior statistical analyses [see *Artemyev et al.*, 2017; *Runov et al.*, 2018].

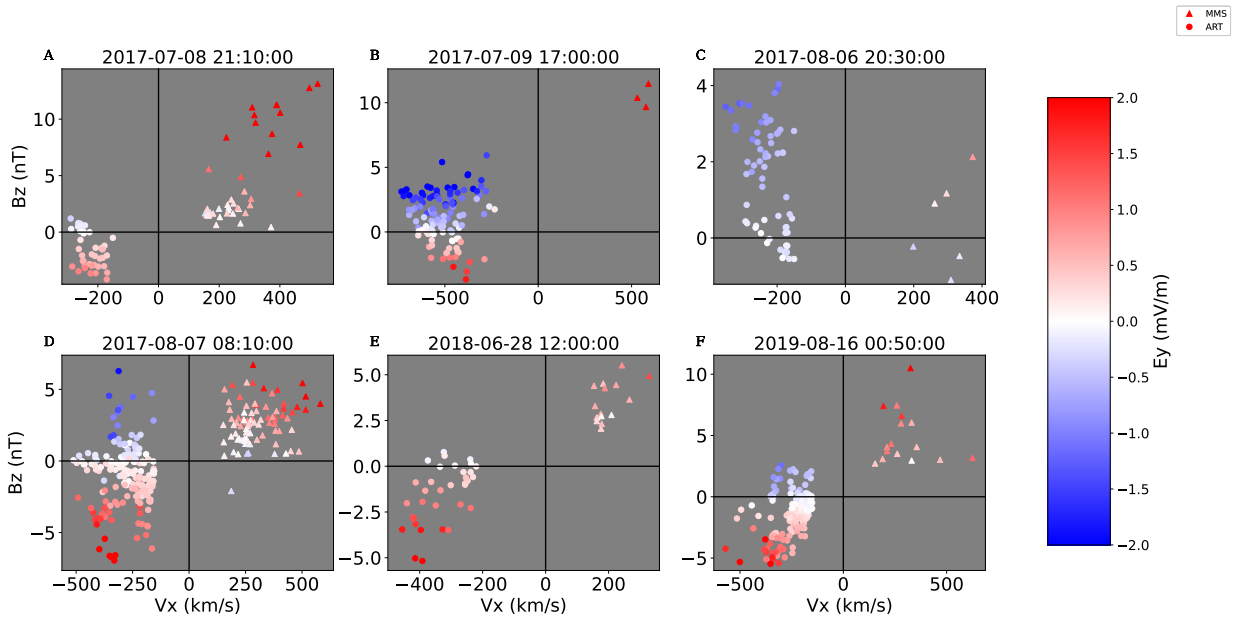

Figure 4.3: *The y-component of the convective electric field as a function of B_z and V_x for each event during periods of $|V_x| > 150$ km/s and plasma beta > 2 for MMS data and > 1 for ARTEMIS data. The colorbar saturates at ± 2 mV/m. The vertical and horizontal black bars in each subplot denote $V_x = 0$ and $B_z = 0$ respectively. Triangle points denote data from MMS and circle points denote data from ARTEMIS.*

Figure 4.5 extends the above analysis to electron temperatures. Figures 4.5A-F show MMS and ARTEMIS electron temperatures as scatter points and median step-plots, in the same format as Figure 4.4. Figure 4.5 indicates that the median electron temperatures recorded by MMS and ARTEMIS, with observed ranges of 0.4 keV to 10 keV and 0.1 keV to 1 keV respectively, are larger earthward than tailward with an asymmetry that is greater than those seen for ions. We note in passing that Figure 4.5D shows an peculiar scenario where electron temperatures from MMS and ARTEMIS are close to each other, around 1 keV, particularly for ratios of $\frac{B_X}{B_{LOBE}}$ less than 0.4. As detailed in Supplementary Figure S3, this occured because ARTEMIS detected two distinct fast tailward flows on 2017-08-07 (08:16 UT – 08:19 UT and 08:25 UT – 08:30 UT); it was likely the combined effect of

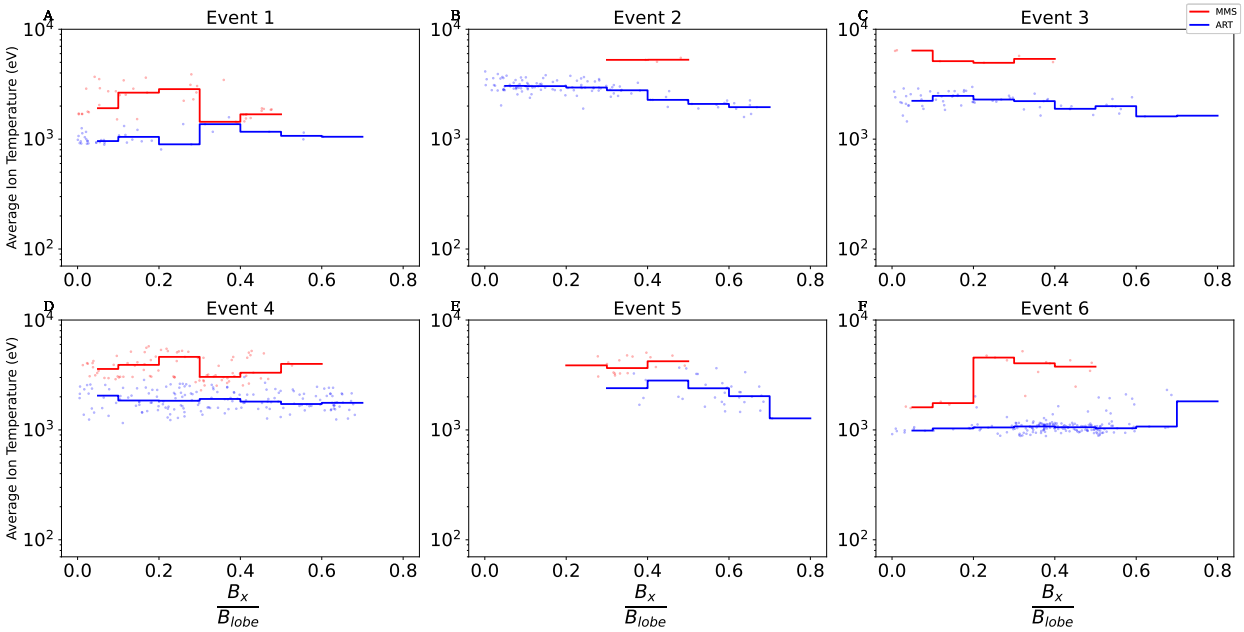

Figure 4.4: *The moments-derived average ion temperatures from MMS FPI and ARTEMIS ESA in red and blue scatterpoints respectively as a function of distance from the neutral sheet, estimated using* $\frac{B_x}{B_{LOBE}}$ *for each event. The red and blue overlaid step-plots give the bin median values of the MMS and ARTEMIS average ion temperatures respectively.*

these tailward flows which heated significantly the tailward plasma, resulting in electron temperatures in the tailward flows comparable to those in the earthward flows.

Our findings demonstrate a pronounced asymmetry in heating for both electrons and ions, with more significant heating observed earthward than tailward of the reconnection site. To quantify the disparity in heating between electrons and ions, we analyzed the earthward-to-tailward temperature ratios for both. Figure 4.6 compares these ratios, calculated by dividing the median MMS electron (ion) temperatures by those from ARTEMIS. Across Figures 4.6A – F, a consistent trend emerges: electrons exhibit a greater asymmetry in temperature compared to ions. Specifically, earthward electron temperatures are 5-20 times higher than their tailward counterparts, whereas earthward ion temperatures are only 2-4 times higher. Generally, all events show that the electron temperature ratio is much

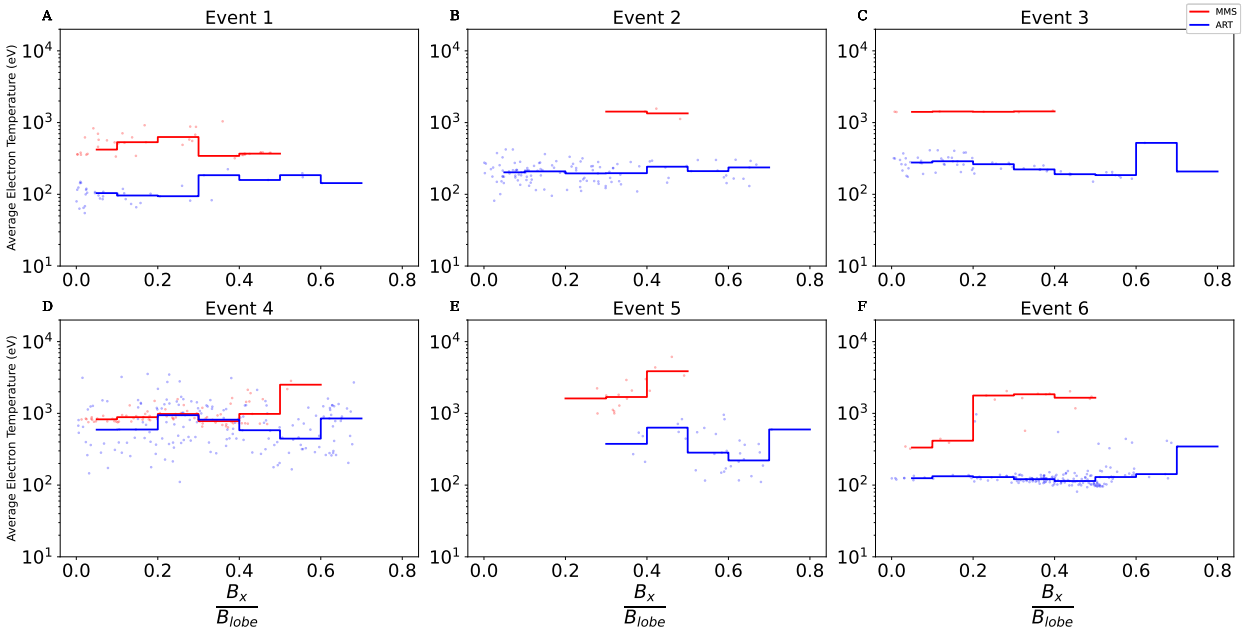

Figure 4.5: *The moments-derived average electron temperatures from MMS FPI and ARTEMIS ESA in red and blue scatterpoints respectively as a function of distance from the neutral sheet, estimated using* $\frac{B_x}{B_{LOBE}}$ *for each event. The red and blue overlaid step-plots give the bin median values of the MMS and ARTEMIS average electron temperatures respectively.*

larger than the ion temperature ratio, except for Event #4, which saw a comparable ion temperature ratio due to the prolonged tailward heating decreasing the asymmetry between earthward and tailward electron temperatures.

Figure 4.7 compares the earthward-to-tailward temperature ratios for electrons and ions across various events. It shows the median earthward-to-tailward ion temperature ratio (x-axis) plotted against the electron temperature ratio (y-axis), under the condition that MMS and ARTEMIS data points fall below a $\frac{B_X}{B_{LOBE}}$ ratio of 0.5. Error bars represent one-third of the standard deviation for these ratios, with horizontal bars for ions and vertical for electrons. The line y = x is shown for reference. This visualization underscores that, with the exception of event #4, electron temperature asymmetry consistently exceeds ion

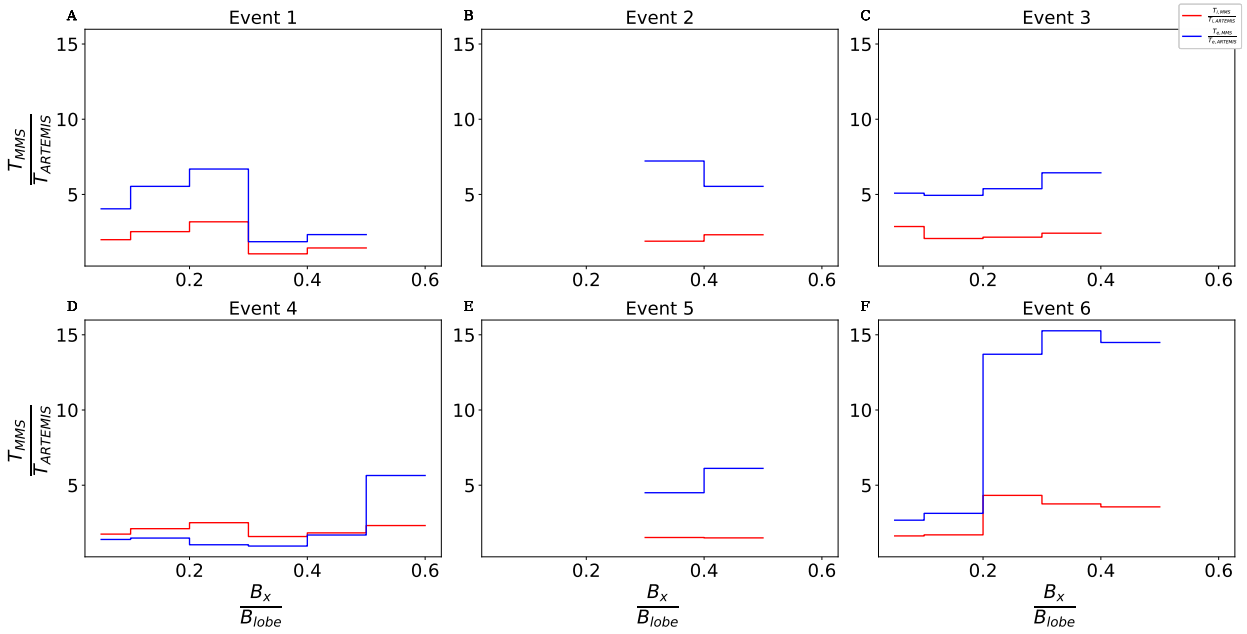

Figure 4.6: *Earthward-to-tailward average temperature ratios as a function of distance from the neutral sheet for ions in red and electrons in blue for each event.*

temperature asymmetry.

4.4 Discussion

In this study we have shown that an earthward-tailward asymmetry in ion and electron heating is present in magnetotail reconnection. We propose that this asymmetry is due the existence of a closed field-line topology on the earthward side of reconnection that is absent on the tailward side.

The magnetotail, particularly at these distances, provides an ideal setting to examine how this closed field-line topology influences heating and energization. Despite minimal gradients in magnetic field and pressure [*Fairfield and Jones*, 1996; *Wing and Newell*, 1998] indicating a negligible asymmetry in Lorentz and pressure gradient forces, we suggest that the differing conditions on the earthward and tailward regions still impact heating significantly.

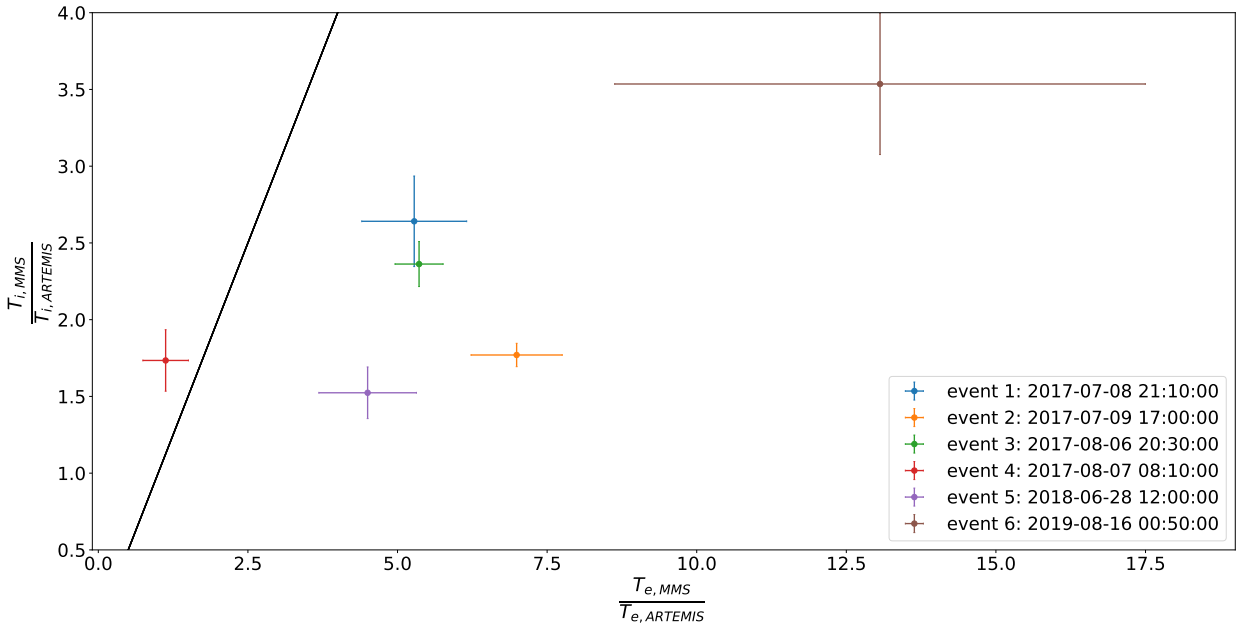

Figure 4.7: *Electron temperature ratio vs ion temperature ratio for each event. The vertical (horizontal) error bars for each event denote 1/3 the standard deviation of the ion (electron) temperature ratio. The black line is* $y = x$.

Specifically, the closed field lines earthward allow particles to have multiple interactions with the reconnection site, leading to substantial heating and energization, in contrast to the tailward scenario where particles, influenced by open field lines to the solar wind, undergo less energization due to limited interactions.

Our findings highlight that electrons have a more pronounced earthward-tailward temperature asymmetry than ions. This discrepancy could be attributed to electrons undergoing more frequent bounces between the magnetic field's north and south footpoints, compared to ions. Given electrons' faster bounce periods, they have more opportunities to interact with the reconnection site before being transported away by magnetic drifts. Conversely, ions having slower bounce rates, drift away more readily due to curvature-gradient and $\mathbf{E} \times \mathbf{B}$ drifts, leading to lesser heating and energization.

A central premise of our study is that the earthward pressure gradient in the mid-tail

region is minimal, thus the earthward or tailward movement of plasma along this gradient is unlikely to significantly influence temperature asymmetry. Should the primary factor for temperature asymmetry be repeated interactions with the magnetotail reconnection site, then the observed temperature asymmetries during reconnection should surpass those observed during inactive periods. Indeed, a statistical analysis by **?** reveals that the ion temperature ratio between lunar distances and the 20-30 R_E region is similar to our findings, suggesting the observed ion temperature asymmetries in this study stem from inherent background conditions in the magnetotail rather than specific interactions at the reconnection site.

The observed electron temperature asymmetry in this study, significant in the context of the mid-tail magnetotail, contrasts with near-Earth findings by [*Lu et al.*, 2018], who reported a more modest asymmetry in a closer magnetotail region (R $< 20R_E$). Their simulations showed electron temperature asymmetries (in normalized units) of 1.4 between earthward and tailward directions, indicating that near-Earth reconnection, characterized by stronger magnetic and pressure gradients, results in less pronounced temperature differences. Therefore, our findings suggest that the dipole's influence on plasma heating during reconnection is considerably more substantial in the mid-tail region.

4.5 Summary

Magnetotail reconnection significantly heats and energizes particles, introducing fast flows, dipolarizing flux bundles, and energetic plasma, thereby reducing magnetic pressure in the mid-tail and inner magnetosphere. Our study, leveraging MMS and ARTEMIS data, revealed a pronounced earthward-tailward asymmetry in electron and ion temperatures. Key findings include that earthward of the reconnection site ions are heated more compared to tailward of it with a ratio of 3:1, while for electrons that heating ratio is even larger, in the range of 5-20. The observed asymmetry in heating, particularly more substantial for electrons than ions, suggests a significant influence from the closed field-line topology earthward of

the x-line. Our results show that even in the absence of magnetic and plasma pressure gradients, significant heating associated with magnetotail reconnection can occur. This insight underscores the importance of incorporating Earth's dipole in magnetic reconnection simulations to accurately capture particle heating even for studies of mid-tail reconnection and highlights the need for further observations to assess temperature asymmetries in near-Earth reconnection events compared to the mid-tail.

Acknowledgments

We acknowledge support by NASA awards 80NSSC20K1788, 80NSSC22K0752, and 80NSSC18K1122. We acknowledge NASA contract NAS5-02099 for use of data from the THEMIS mission. We thank K. H. Glassmeier, U. Auster, and W. Baumjohann for the use of FGM data provided under the lead of the Technical University of Braunschweig and with financial support through the German Ministry for Economy and Technology and the German Aerospace Center (DLR) under contract 50 OC 0302.

Open Research

ARTEMIS data is available at http://themis.ssl.berkeley.edu. Data access and processing was done using SPEDAS V6.0 [*Angelopoulos et al.*, 2019] available at `https://spedas.org/`.

CHAPTER 5

Conclusions and Future Directions

In this dissertation, I addressed the question: What are the mechanisms of plasma energization during magnetotail reconnection in Earth's magnetosphere? To answer this question I focused on the energy transport properties of the active time magnetotail in three parts: a) global energy transport, b) energy transport in the near-Earth tail, and c) energy transport in the mid-tail.

My work provides three main new insights in understanding magnetotail energy dynamics. 1) During active times, a general enhancement of global plasma and energy convection is expected. This enhancement sometimes includes periods of convection similar to non-storm time convection states like the loading-unloading and SMC mode, however the majority of active times ($> 70\%$) do not. I demonstrated that these modes did not correlate with significant decreases in SYM-H - the plasma energy introduced by these modes did not substantially power the ring current. Instead, this study suggests that the geoeffectiveness of active times is controlled by other factors such as the inward propagation of the peak of the cross-tail current that enhances global convection. 2) Very-near-Earth reconnection occur frequenty during storm-time main phase. The reconnection regions reside <1 R_E from the neutral sheet, and the electric fields seen during these events is substantially stronger than quiet-time background levels. This study motivates future investigations prompting both modeling and in-situ observations of VNERX to better understand the storm dynamics which promote such close reconnection. 3) Magnetic reconnection in the mid-tail (30 - 45 R_E) has drastic plasma temperature asymmetries. These asymmetries are more pronounced

in the electron population than ions and result in 2-20 times hotter plasma earthward than tailward. The mid-tail region is a under-sampled area of the magnetotail, and thus this study takes the first steps in characterizing it. This study presented observations that show a novel heating mechanism in the magnetotail, discussed further below. This mechanism may play a large role in controlling the temperature profile of the magnetotail for all regions beyond the near-Earth tail.

The following sections will summarize the main conclusions of these studies, explore their implications, and discuss future research directions for further investigation of plasma energization in the magnetotail.

5.1 Main Conclusions

The open magnetic flux of the magnetotail serves as a reservoir for magnetic energy used in plasma heating and acceleration. To understand the global energy transport in an active magnetotail, I monitored the global open magnetic flux content. Using ARTEMIS magnetic field and plasma measurements, I estimated the temporal profile of total open magnetic flux in the magnetotail. I found that during storms, both loading-unloading (L-U) and quasi-steady state convection can occur, but these modes are not common ($\leq 25\%$ of storms encompassed these modes at least once during their evolution). I concluded that these modes are not necessary for storm development but rather coincide with steady or unsteady solar wind driving during storms. Comparing storm-time L-U modes with substorms, I found that they have a similar three-phased progression in their AE profile, indicating similar behavior. Storm-time L-U events have a total flux profile similar to substorms but with a higher baseline, suggesting an enhanced background flux content in the storm-time tail. Comparing storm-time and non-storm-time SMCs, I found that the magnetotail contains similar amounts of flux in both modes. While the solar wind driving was statistically stronger for storm-time L-Us compared to substorms, this was not the case for storm-time and non-

storm-time SMCs. Despite this, the AE signatures were stronger during storm-time SMCs, implying a change in the magnetospheric topology during these events. Thus, I concluded that the majority of global energy transport in the magnetotail during very active times is not controlled by intermittent or steady state reconnection but a more generalized reconnection mode, resulting in enhanced global energy throughput.

After examining global energy transport, I focused on energy transport in the near-Earth tail. This region is compelling for studying energy transport because the plasma here has access to a significantly larger amount of energy stored in the magnetic field. I analyzed THEMIS observations of magnetic and electric fields and plasma moments data in the very-near-Earth region (R $< 14\ R_E$) during both storm and non-storm times for signs of reconnection. I identified seven VNERX events during geomagnetic storm times, all clustered around pre-midnight. These events exhibited classical x-line reconnection characteristics, including Hall electric fields, diverging earthward and tailward flows, and positive reconnection electric fields throughout the reconnection site. None of the events occurred during the storm recovery phase. I calculated the VNERX occurrence rate using the total time spent at different distances from a modeled TAG14 neutral sheet, finding it to be approximately 1.3 per 10 hours of residence within 1000 km of the main phase neutral sheet. These findings indicate that VNERX events are common during storms and play an important role in energy transport during the storm main phase.

Finally, I examine energy transport in the mid-tail. Past hybrid simulations and in-situ observations of plasma heating driven by magnetotail reconnection conclude that the earthward-tailward pressure gradient plays a significant role in that heating. These studies suggest a significant portion of the kinetic energy flux produced close to the reconnection x-line is converted to thermal energy flux and enthalpy flux. A simple explanation for this energy conversion comes from considering the single fluid MHD energy continuity equation: $\frac{d}{dt}\left(\frac{\rho v^2}{2}\right) = -\nabla\cdot\left(\frac{\rho v^2 \mathbf{v}}{2}\right) + \mathbf{v}\cdot(\mathbf{J}\times\mathbf{B}) - \mathbf{v}\cdot\nabla P$. It is clear that the work done by the pressure gradient force on the plasma ($-\mathbf{v}\cdot\nabla P$) decreases plasma kinetic energy density. In this

simplified single fluid framework, the pressure gradient force acts to convert kinetic energy into thermal energy as shown by the single fluid MHD thermal energy continuity equation: $\frac{d}{dt}(u) = -\nabla \cdot (\mathbf{H} + \mathbf{Q}) + \mathbf{v} \cdot \nabla P$, where u is the plasma thermal energy and $\mathbf{H}, \mathbf{Q}$ are the enthalpy and heat flux respectively. In the near-Earth tail, where both the magnetic field and plasma pressure gradient are large, this analysis fits well. However, in the more distant tail where these gradients are weaker, it is unclear how or if plasma heating still exists. This study demonstrated that plasma heating indeed still occurs in a relatively weaker background of muted gradients. Using conjunctions between ARTEMIS and MMS, I observe simultaneous earthward and tailward reconnection jets. Comparing plasma temperatures within these jets, I find that the plasma is heated by up to an order of magnitude more on the earthward side. I propose that this heating asymmetry is due to closed field lines on the earthward side, allowing particles to bounce between their northern and southern mirroring points and interact with reconnection outflows multiple times. This interaction is absent on the tailward side, resulting in generally cooler plasma. Thus, even without significant gradients, magnetotail reconnection-driven heating can be significant.

5.2 Impact on Magnetotail Plasma Energization

The transport of energy in Earth's magnetotail is crucial to the development of the radiation belts and ring current, two regions which are coupled to the ionosphere and outer magnetosphere. The development of the ring current has been a long standing issue for the past 70 years [*Jordanova et al.*, 2020]. My work contributes to a better understanding of the origin of particle injections at geosynchronous orbit, which are frequently observed during ring current intensification.

Dispersionless particle injections at geosynchronous orbit are a common feature of the inner magnetosphere [*Gabrielse et al.*, 2014; *Sarris et al.*, 1976]. They feature an abrupt increase of particle fluxes at a broad range of energies and are seen for both ions and electrons.

However, the origin of these particle injections is unclear. Due to the differences in energy, the different populations should drift azimuthally at different speeds. Thus, it is expected that these injections should have some dispersion in energy. One way to achieve a simultaneous increase in particle fluxes at broad energy ranges is via very-near-Earth reconnection. Since VNERX occurs close to geosynchronous orbit, the locally energized plasma does not disperse significantly in azimuth by the time it reaches geosynchronous locations, resulting in a dispersionless signature when observed there. Our study shows that VNERX occurs very frequently during the storm main phase, suggesting that it may explain a notable fraction of the dispersionless signatures commonly observed.

While near-Earth reconnection has been extensively studied by several missions, the stability and dynamics of the distant tail have received less attention due to the lack of spacecraft observations. This Ph.D. research addresses this gap by describing the energy dynamics of the distant tail. The plasma in the distant magnetotail consists of cold and hot sub-populations [*Mist et al.*, 2001; *Richardson et al.*, 1987]. While the cold population is well understood and correlated with penetrating solar wind plasma and ionospheric outflow, the source of the hot plasma population in the distant tail remains unclear. My research helps to resolve this issue by suggesting that a fraction of the hot plasma is generated when particles on the earthward side of distant magnetic reconnection sites bounce along closed magnetic field lines, interacting multiple times with the reconnection site and outflow region.

5.3 Future Work

Our study on magnetotail plasma energy transport provides crucial details on plasma convection in Earth's magnetotail, yet further research is necessary. One area requiring investigation is the evolution of the magnetotail entropy profile during storms.

Under ideal MHD conditions, the flux tube entropy parameter, $S = PV^{5/3}$, where P is thermal pressure and V is the flux tube volume per unit flux, remains conserved during flux

tube transport [*Wolf*, 1983]. Flux tubes with an entropy parameter lower than that of the surrounding plasma will tend to move toward regions of lower entropy until reaching a region of equal entropy [*Pontius and Wolf*, 1990]. Given that the entropy of the magnetotail typically increases monotonically with distance, flux tubes with reduced entropy (compared to their surroundings) are expected to move earthward. Thus, depending on the magnetotail's entropy profile, flux tubes with depleted entropy may reach the inner magnetosphere and ring current regions.

It has been demonstrated through observations that during non-storm times, flux tubes with lower entropy do indeed move closer inward [*Dubyagin et al.*, 2011]. However, recent observations also indicate that during storm times, only a small fraction of dipolarizations observed at 10-12 R_E are associated with injections at geosynchronous distances [*Runov et al.*, 2021a]. The question arises: why do most fast flows fail to penetrate deeply into the inner magnetosphere? If the plasma bubble theory is correct, then fast flows do not penetrate because their entropy is too high to reach deep into the inner magnetosphere. To test whether storm-time fast flows have higher entropy compared to the background plasma, a model of the evolution of the storm-time magnetotail entropy profile is warranted.

Future studies should aim to answer the question, "What is the storm-time background entropy profile?" by employing a magnetic field model to estimate the entropy in the magnetotail. By modeling the storm-time entropy profile as a function of distance throughout a storm, researchers can track changes in the entropy profile as the storm evolves. Estimating the entropy of flux tubes observed at 10-12 R_E by THEMIS, and using the global model of flux tube entropy, researchers can estimate the fraction of the total storm-time tail flows that will penetrate to geosynchronous orbit. This study will address the question of what fraction of all storm-time fast flows are geoeffective (i.e., penetrate to geosynchronous orbit). The estimated entropy profile as a function of time can then be used to determine how the fraction of geoeffective flows changes as a function of storm phase.

What should be expected from this study? During the storm main phase, the magnetotail

field lines are highly stretched, implying that the entropy profile is shallow. This suggests that the entropy near Earth may be higher compared to non-storm times. Consequently, during storm times, a larger fraction of flux tubes should penetrate deep into the inner magnetosphere. However, during the recovery phase, the magnetotail returns to a non-storm time tail configuration, leading to a decrease in near-Earth flux tube entropy back to non-storm time levels. Therefore, during the recovery phase, we expect the fraction of storm-time tail flows to decrease relative to main-phase levels.

This Ph.D. lays the foundation in our understanding of storm-time magnetotail reconnection dynamics. In terms of geomagnetic storms, the space physics community needs to address two questions: how is the storm-time ring current energized, and how does the plasma sheet couple to the inner magnetosphere during highly disturbed times. The conclusions of this Ph.D. highlight the complexity of storm-time dynamics and the need to emphasize the role of reconnection especially in the near-Earth tail. These conclusions will influence the space physics community to focus on building future missions that explicitly address issues such as constraining the very near-Earth central plasma sheet thickness as a function of storm-time and local time, and a better estimate of the VNERX occurrence rate. My work justifies increased efforts in characterizing the storm-time magnetotail, which will complement the looming auroral and ENA imaging satellites that will provide a global perspective on magnetospheric dynamics.

APPENDIX A

Appendix: Supporting Information for "Storm-time Very-Near-Earth Magnetotail Reconnection: A Statistical Perspective"

Contents of this file

1. Figures S1-S24

Introduction

This supplementary file gives 24 figures that show time-series plots of magnetotail magnetic fields, SYM-H and AE indices, ion bulk velocities, ion energy spectrograms, and proton and electron fluxes at geosynchronous orbit. Several figures also include solar wind time-series data of solar wind dynamic pressure and magnetic field strength along with SYM-H and AE indices. Dial plots of positions of THEMIS and GOES are shown as well. Lastly, X-Y and X-Z residency distributions of THEMIS position and estimates of current sheet half-thicknesses are shown. The time-series stack plots for events 1-7 are created using the SPEDAS software. The distribution plots are made using python and the TAG14 neutral sheet model (https://geo.phys.spbu.ru/~tsyganenko/empirical-models/current_sheet/neutral_sheet/).

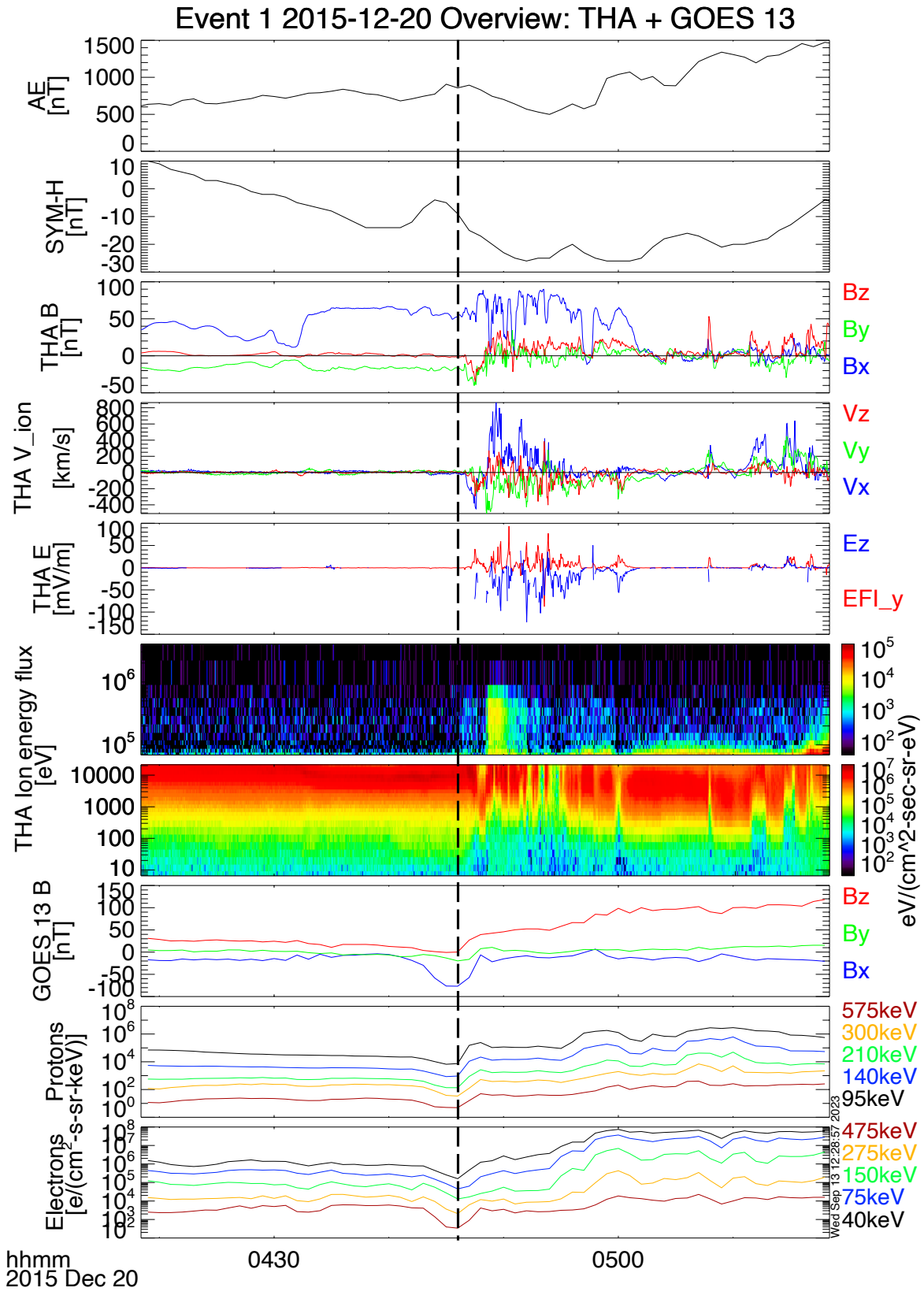
Event 1 2015-12-20 Overview: THA + GOES 13
AE [nT]
SYM-H [nT]
THA B [nT]
Bz
By
Bx
THA V_ion [km/s]
Vz
Vy
Vx
THA E [mV/m]
Ez
EFI_y
THA Ion energy flux [eV]
eV/(cm^2-sec-sr-eV)
GOES 13 B [nT]
Bz
By
Bx
Protons [e/(cm^2-s-sr-keV)]
575keV
300keV
210keV
140keV
95keV
Electrons [e/(cm^2-s-sr-keV)]
475keV
275keV
150keV
75keV
40keV
Wed Sep 13 12:28:57 2023
hhmm
2015 Dec 20
0430
0500

Figure A.1: Magnetotail characteristics during VNERX event. (A) Auroral electrojet index, (B) Sym-H index, (C) magnetotail magnetic field components measured at THA; thin horizontal black line denotes the zero nT, (D) bulk ion velocity components measured at THA, (E) EY measured by THA Electric Field instrument (red) and estimated EZ (blue), (F) omni-directional ion energy spectra from SST and (G) omni-directional ion energy spectra from ESA instruments, (H) GOES-13 measured magnetic field components, (I) GOES-13 measured proton and (J) electron fluxes. The vertical dashed black line denotes the time of dispersionless ion injection seen at GOES-13.

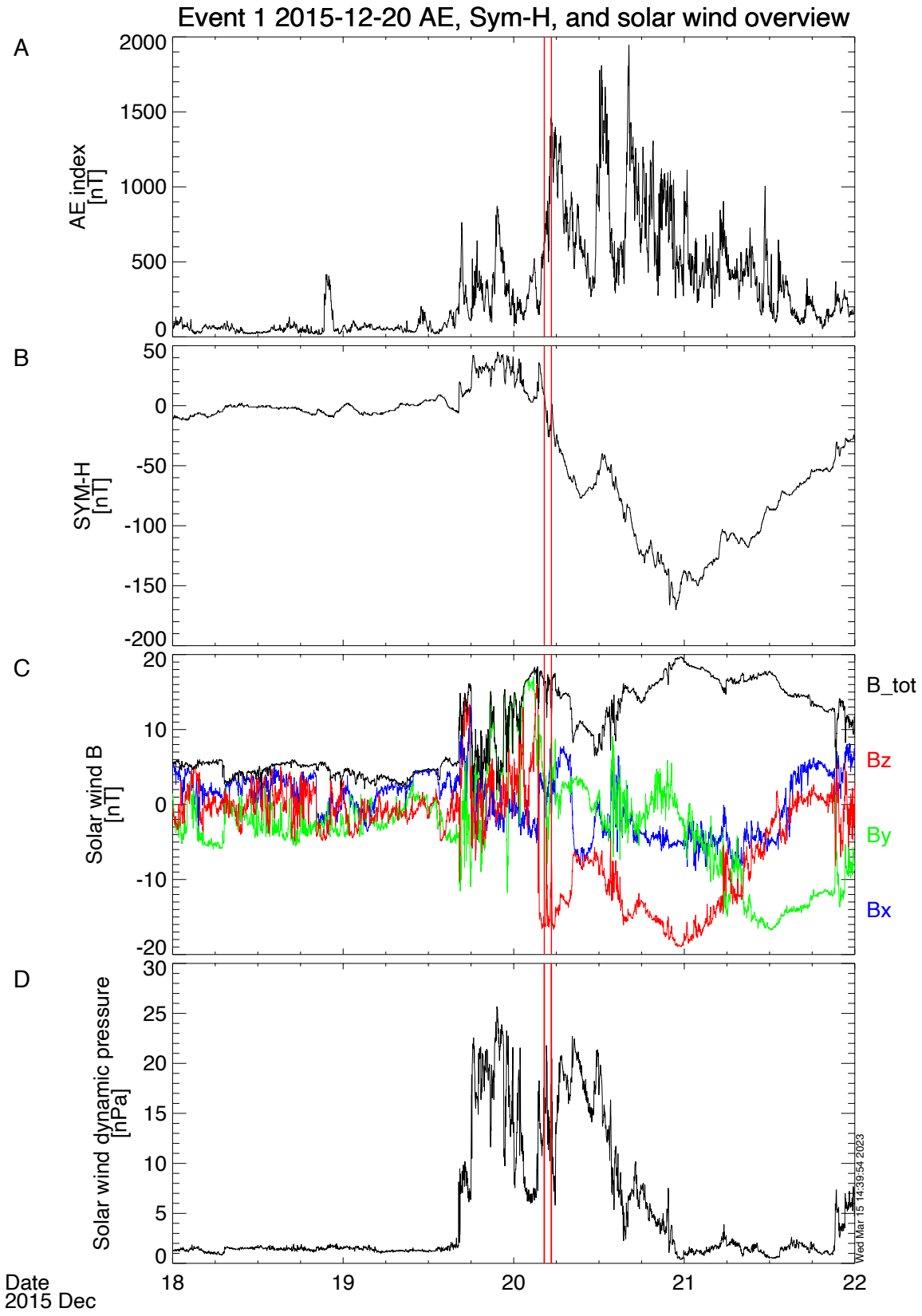
Event 1 2015-12-20 AE, Sym-H, and solar wind overview
A
AE index [nT]
2000
1500
1000
500
0
B
SYM-H [nT]
50
0
-50
-100
-150
-200
C
Solar wind B [nT]
20
10
0
-10
-20
B_tot
Bz
By
Bx
D
Solar wind dynamic pressure [nPa]
30
25
20
15
10
5
0
Wed Mar 15 14:39:54 2023
Date
2015 Dec
18
19
20
21
22

Figure A.2: Solar wind characteristics during the four days surrounding a VNERX event. (A) Auroral electrojet index, (B) Sym-H index, (C) solar wind magnetic field components and magnitude and (D) solar wind dynamic pressure from ACE, WIND, and IMP. The red vertical lines denote the 30 minutes prior to and after the observed B_Z bipolar signature of the VNERX event.

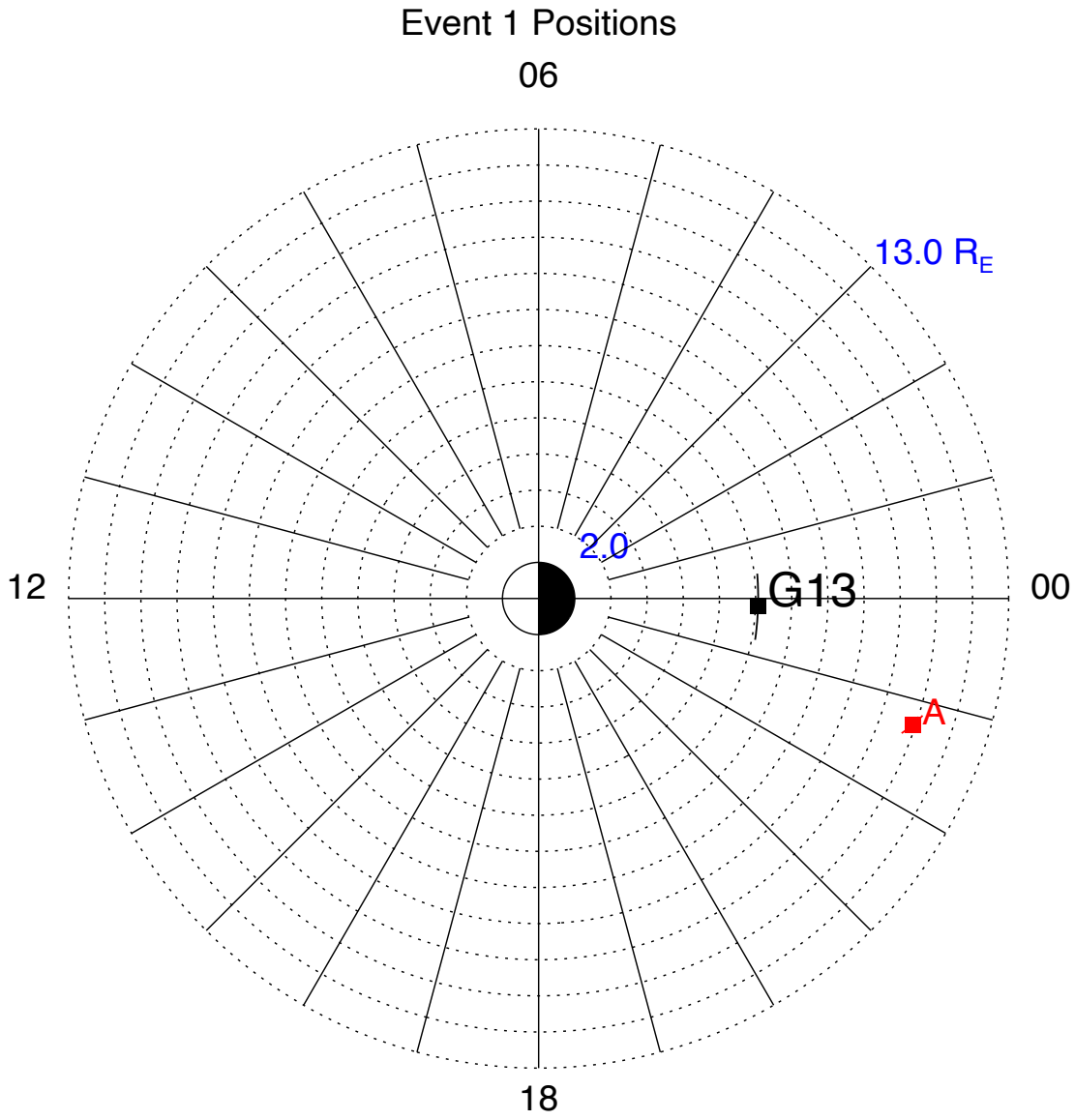

Figure A.3: Positions of spacecraft projected into the X-Y GSM plane that observed a VNERX site (red) and the corresponding position of a GOES satellite (black) during that event.

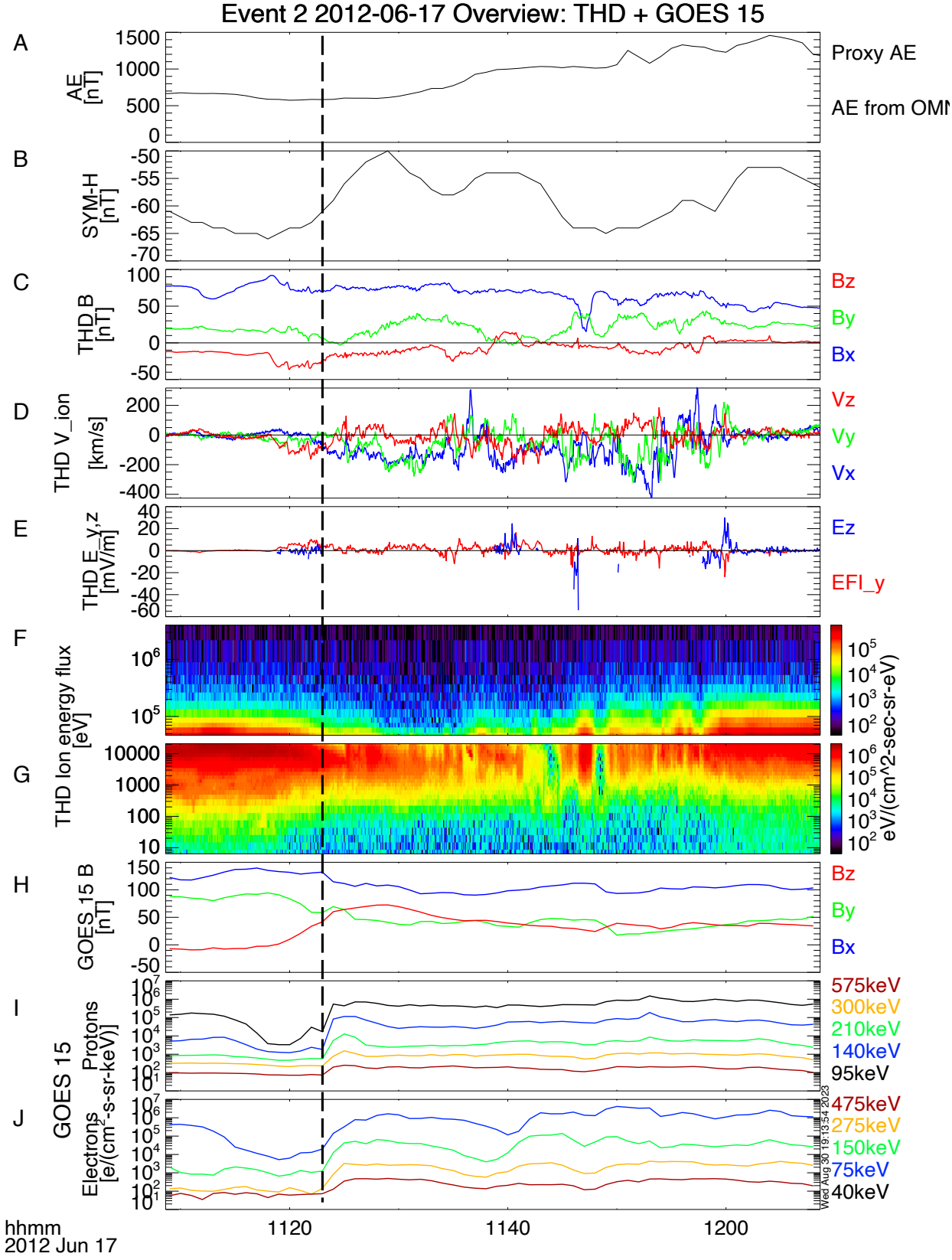
Event 2 2012-06-17 Overview: THD + GOES 15
A
AE [nT]
1500
1000
500
0
Proxy AE
AE from OMI
B
SYM-H [nT]
-50
-55
-60
-65
-70
C
THD B [nT]
100
50
0
-50
Bz
By
Bx
D
THD V_ion [km/s]
200
0
-200
-400
Vz
Vy
Vx
E
THD E_y,z [mV/m]
40
20
0
-20
-40
-60
Ez
EFI_y
F
THD Ion energy flux [eV]
10^6
10^5
10^5
10^4
10^3
10^2
G
10000
1000
100
10
10^6
10^5
10^4
10^3
10^2
eV/(cm^2-sec-sr-eV)
H
GOES 15 B [nT]
150
100
50
0
-50
Bz
By
Bx
I
GOES 15 Protons [e/(cm^2-s-sr-keV)]
575keV
300keV
210keV
140keV
95keV
J
Electrons
475keV
275keV
150keV
75keV
40keV
Wed Aug 30 19:13:54 2023
hhmm
2012 Jun 17
1120
1140
1200

Figure A.4: Magnetotail characteristics during VNERX event. (A) Auroral electrojet index, (B) Sym-H index, (C) magnetotail magnetic field components measured at THD; thin horizontal black line denotes the zero nT, (D) bulk ion velocity components measured at THD, (E) EY measured by THD Electric Field instrument (red) and estimated EZ (blue), (F) omni-directional ion energy spectra from SST and (G) omni-directional ion energy spectra from ESA instruments, (H) GOES-15 measured magnetic field components, (I) GOES-15 measured proton and (J) electron fluxes. The vertical dashed black line denotes the time of dispersionless ion injection seen at GOES-15.

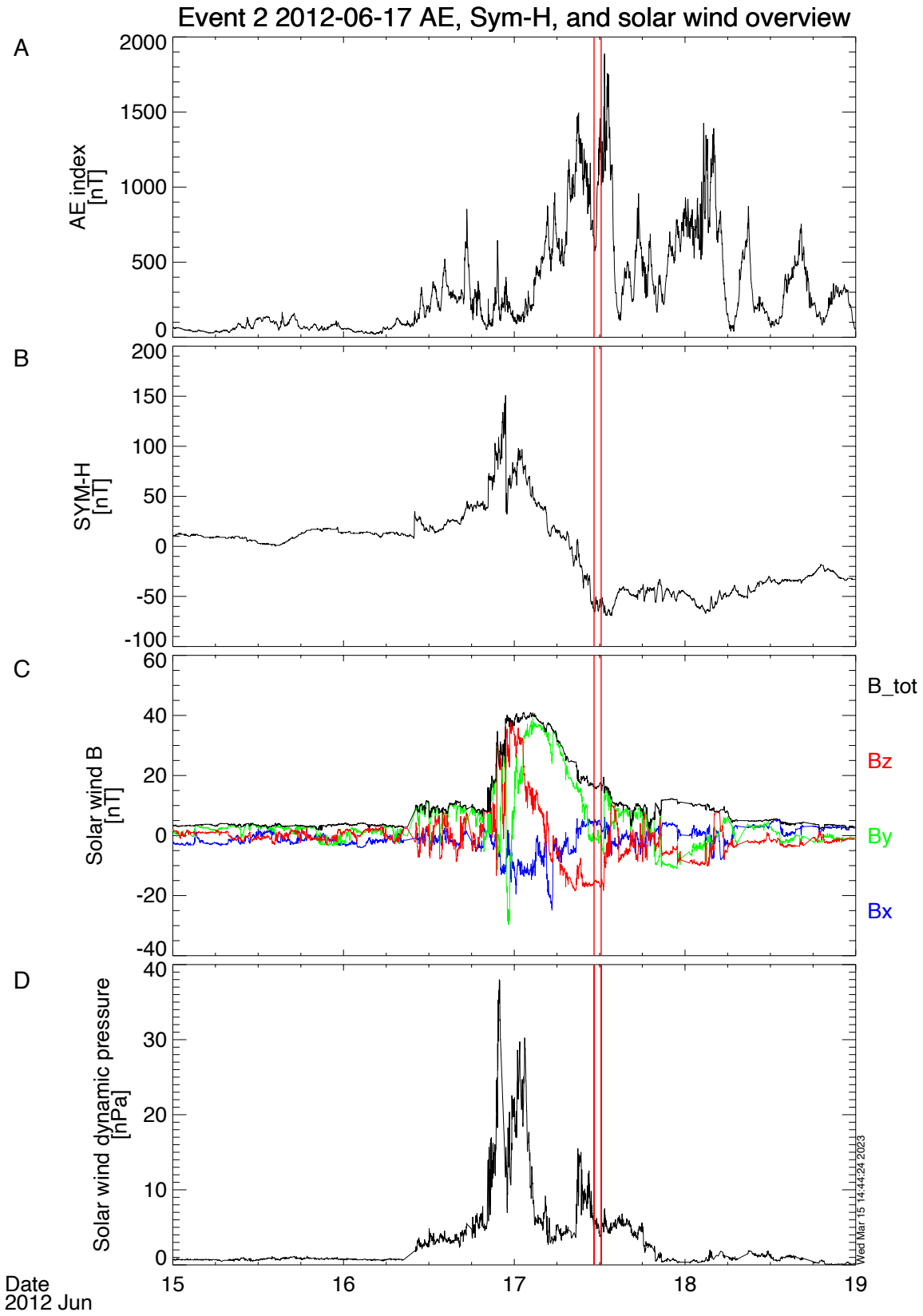
Event 2 2012-06-17 AE, Sym-H, and solar wind overview
A
AE index [nT]
2000
1500
1000
500
0
B
SYM-H [nT]
200
150
100
50
0
-50
-100
C
Solar wind B [nT]
60
40
20
0
-20
-40
B_tot
Bz
By
Bx
D
Solar wind dynamic pressure [nPa]
40
30
20
10
0
Wed Mar 15 14:44:24 2023
Date
2012 Jun
15
16
17
18
19

Figure A.5: Solar wind characteristics during the four days surrounding a VNERX event. (A) Auroral electrojet index, (B) Sym-H index, (C) solar wind magnetic field components and magnitude and (D) solar wind dynamic pressure from ACE, WIND, and IMP. The red vertical lines denote the 30 minutes prior to and after the observed BZ bipolar signature of the VNERX event.

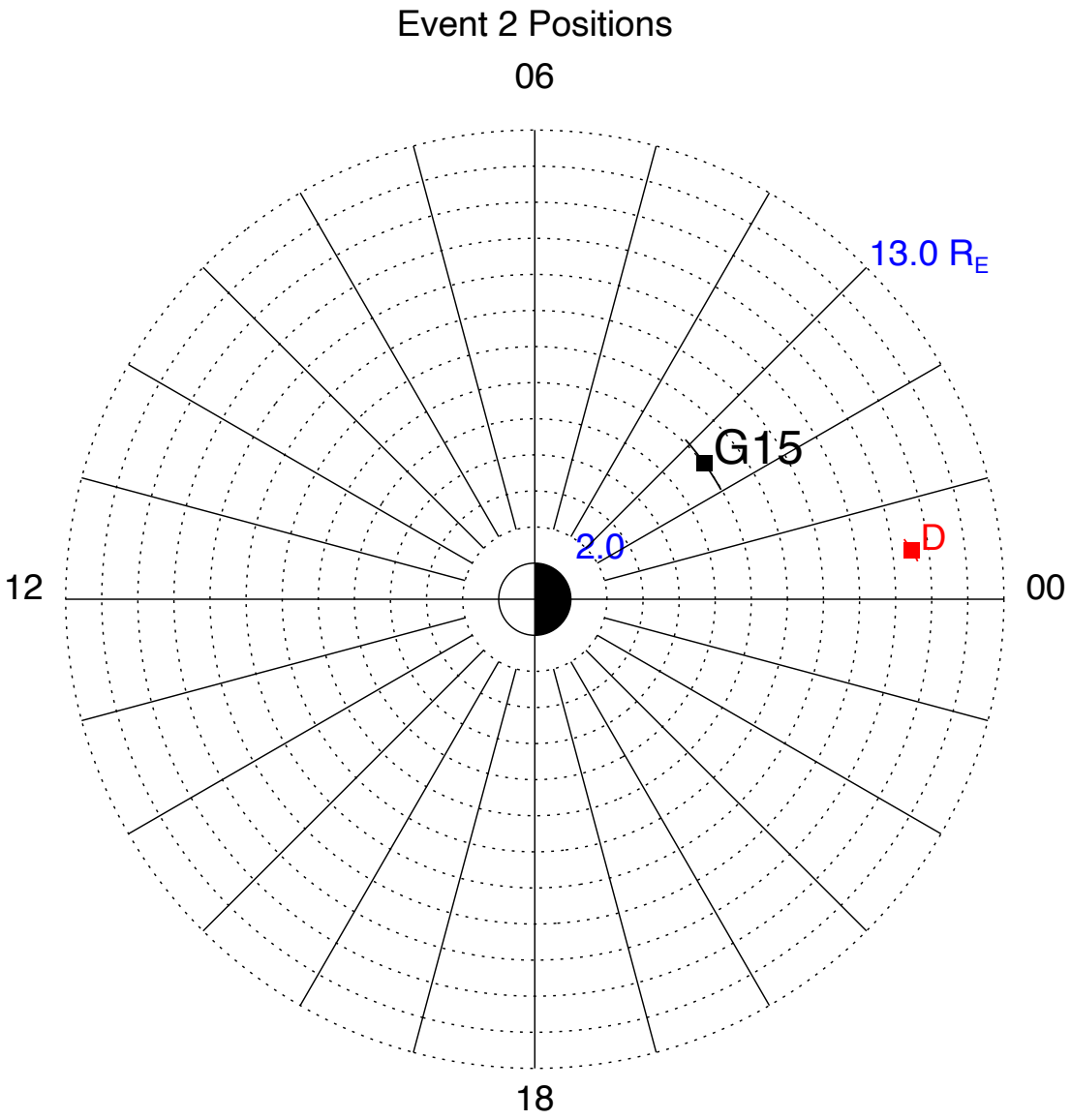

Figure A.6: Positions of spacecraft projected into the X-Y GSM plane that observed a VNERX site (red) and the corresponding position of a GOES satellite (black) during that event.

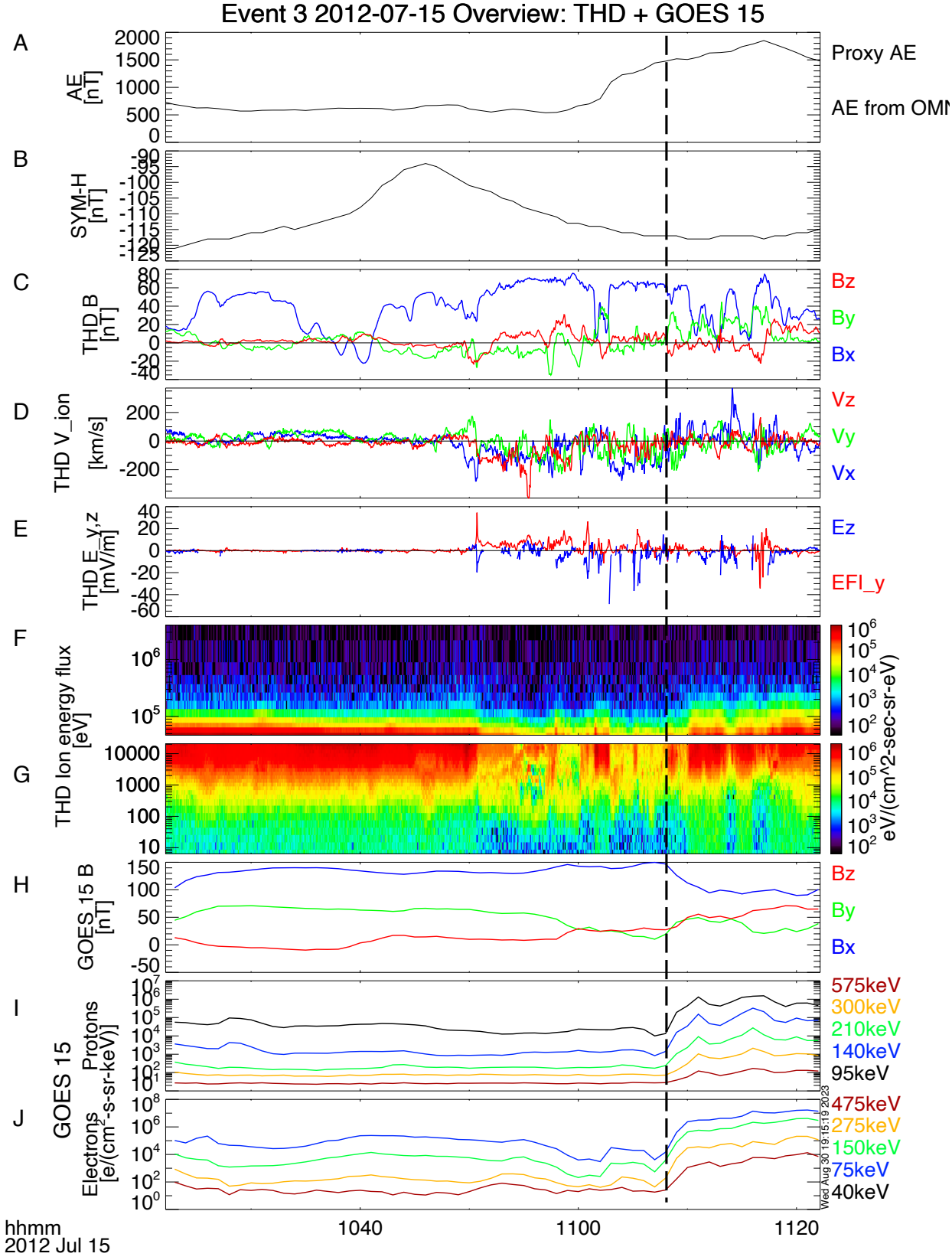
Event 3 2012-07-15 Overview: THD + GOES 15
A
AE [nT]
Proxy AE
AE from OMI
B
SYM-H [nT]
C
THD B [nT]
Bz
By
Bx
D
THD V_ion [km/s]
Vz
Vy
Vx
E
THD E_y,z [mV/m]
Ez
EFI_y
F
THD Ion energy flux [eV]
eV/(cm^2-sec-sr-eV)
G
H
GOES 15 B [nT]
Bz
By
Bx
I
GOES 15 Protons [e/(cm^2-s-sr-keV)]
575keV
300keV
210keV
140keV
95keV
J
GOES 15 Electrons [e/(cm^2-s-sr-keV)]
475keV
275keV
150keV
75keV
40keV
Wed Aug 30 19:15:19 2023
hhmm
2012 Jul 15
1040
1100
1120

Figure A.7: Magnetotail characteristics during VNERX event. (A) Auroral electrojet index, (B) Sym-H index, (C) magnetotail magnetic field components measured at THD; thin horizontal black line denotes the zero nT, (D) bulk ion velocity components measured at THD, (E) EY measured by THD Electric Field instrument (red) and estimated EZ (blue), (F) omni-directional ion energy spectra from SST and (G) omni-directional ion energy spectra from ESA instruments, (H) GOES-15 measured magnetic field components, (I) GOES-15 measured proton and (J) electron fluxes. The vertical dashed black line denotes the time of dispersionless ion injection seen at GOES-15.

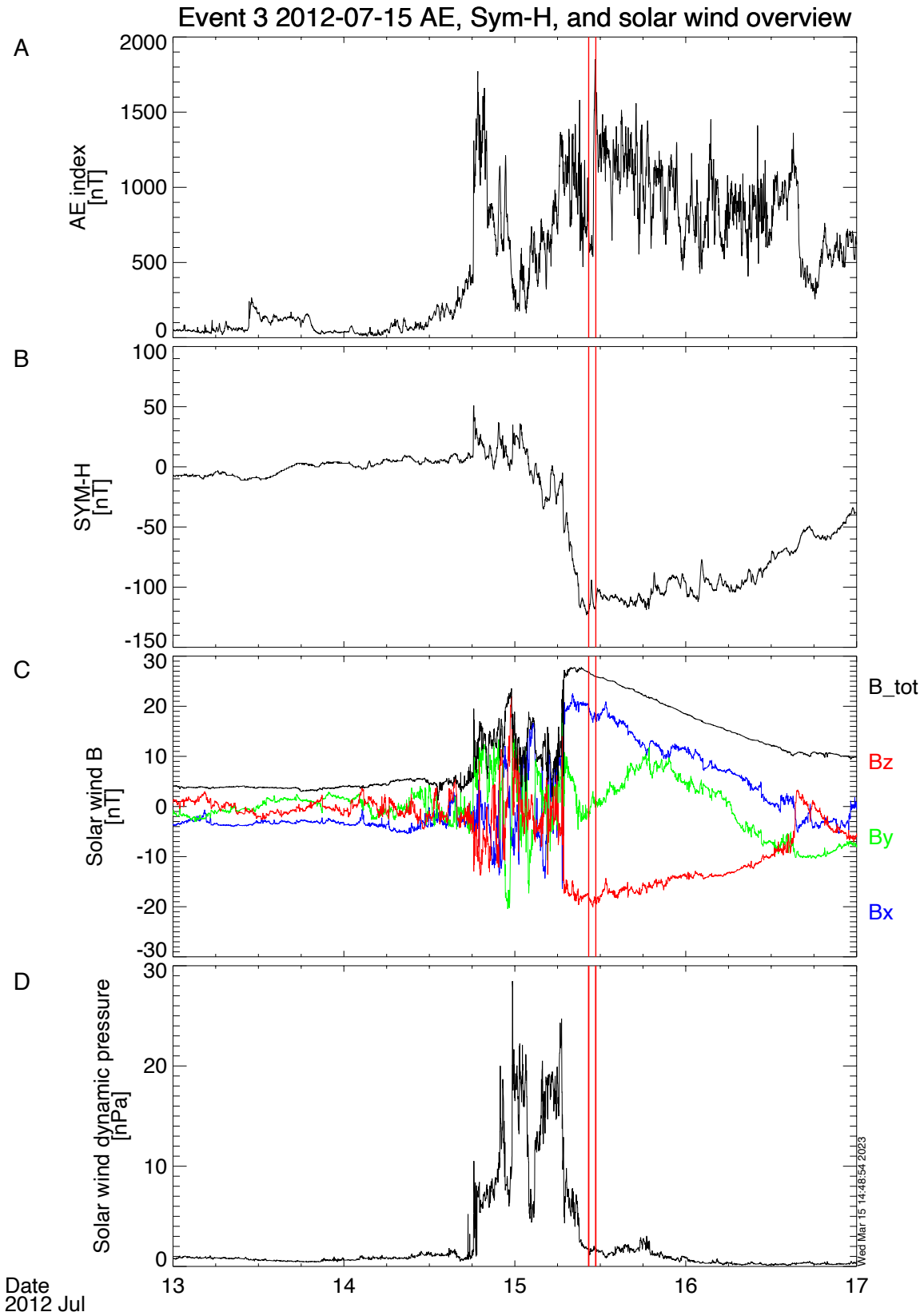
Event 3 2012-07-15 AE, Sym-H, and solar wind overview
A
AE index [nT]
2000
1500
1000
500
0
B
SYM-H [nT]
100
50
0
-50
-100
-150
C
Solar wind B [nT]
30
20
10
0
-10
-20
-30
B_tot
Bz
By
Bx
D
Solar wind dynamic pressure [nPa]
30
20
10
0
Wed Mar 15 14:48:54 2023
Date
2012 Jul
13
14
15
16
17

Figure A.8: Solar wind characteristics during the four days surrounding a VNERX event. (A) Auroral electrojet index, (B) Sym-H index, (C) solar wind magnetic field components and magnitude and (D) solar wind dynamic pressure from ACE, WIND, and IMP. The red vertical lines denote the 30 minutes prior to and after the observed BZ bipolar signature of the VNERX event.

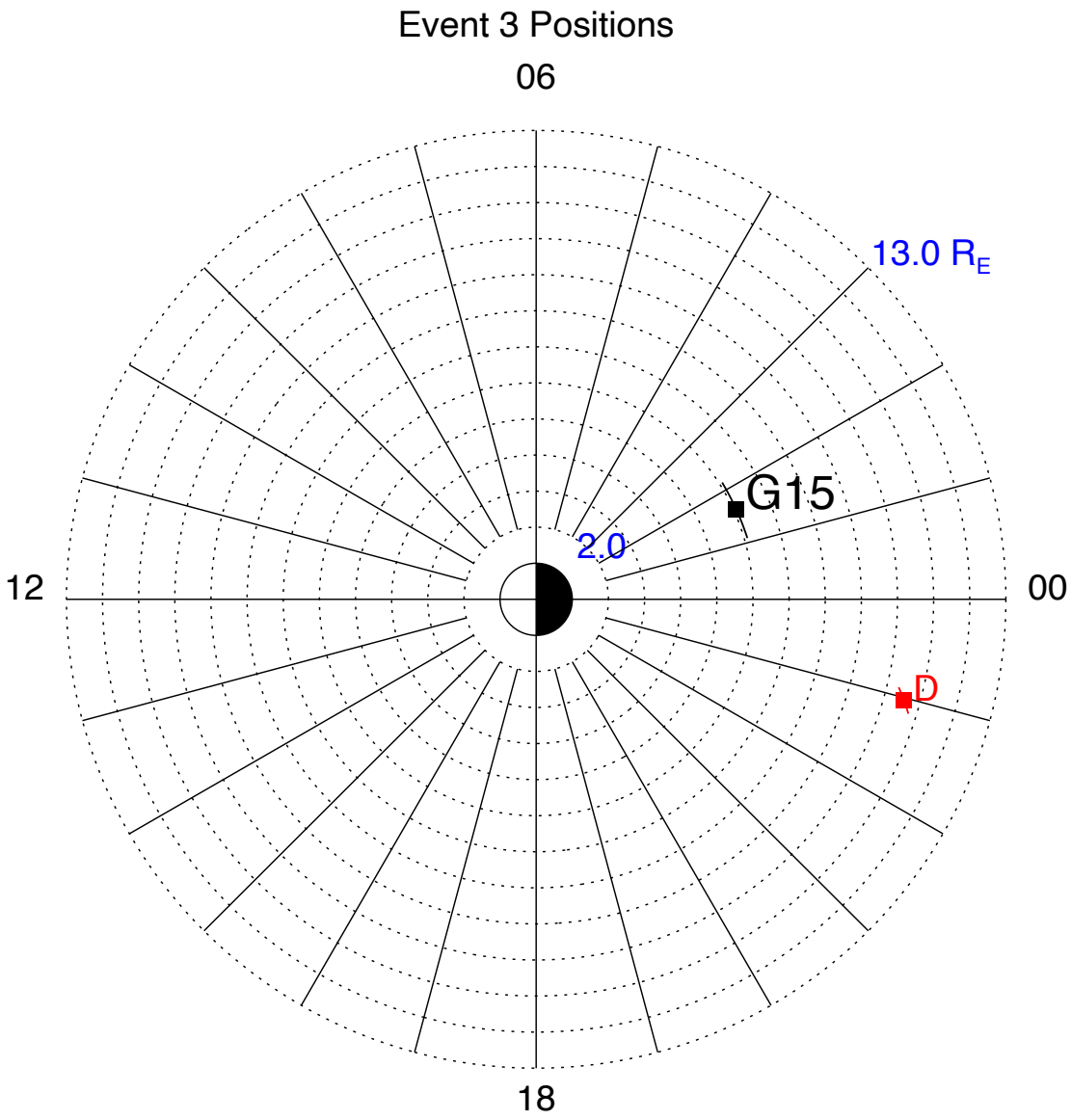

Figure A.9: Positions of spacecraft projected into the X-Y GSM plane that observed a VNERX site (red) and the corresponding position of a GOES satellite (black) during that event.

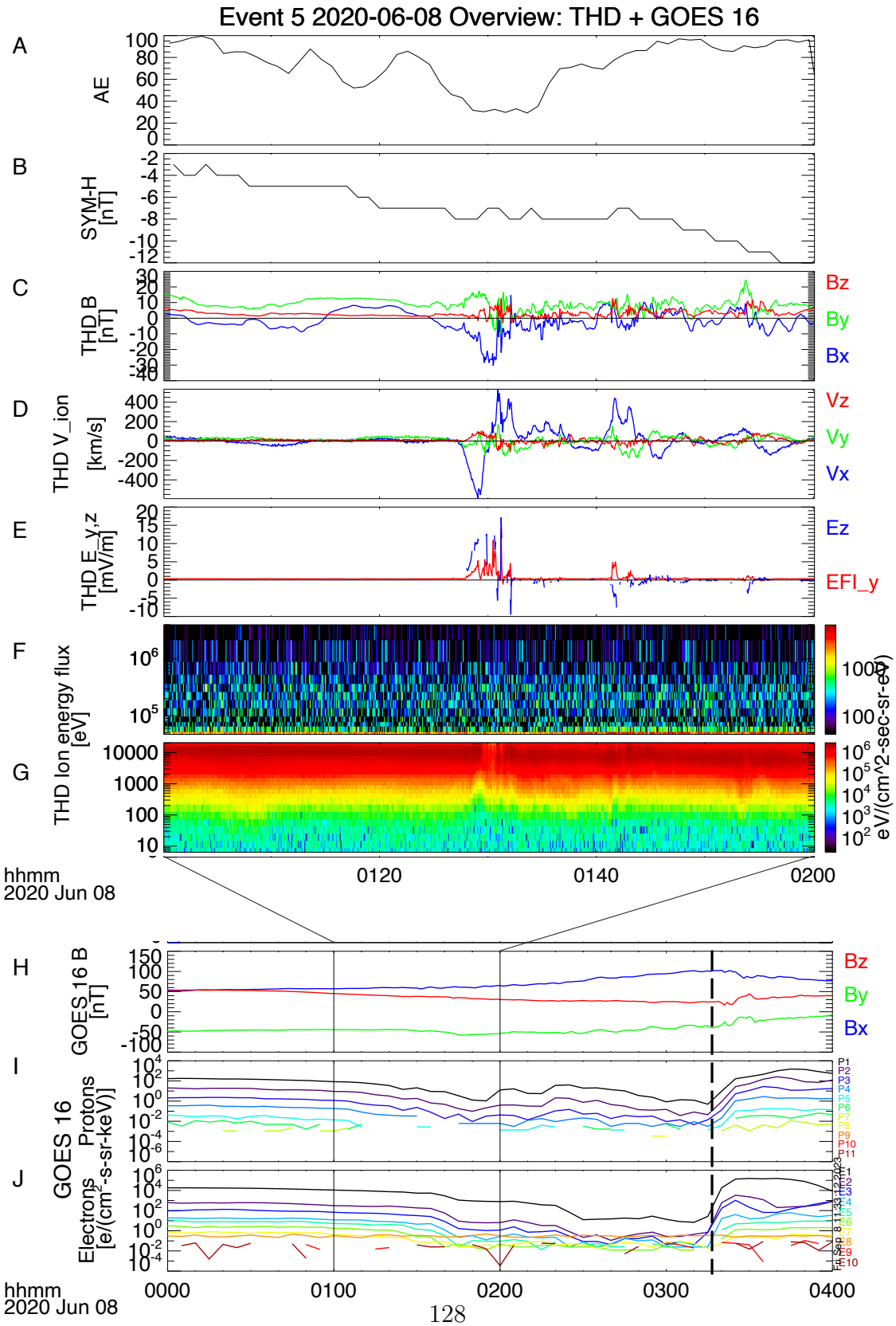
Event 5 2020-06-08 Overview: THD + GOES 16
A
AE
B
SYM-H [nT]
C
THD B [nT]
Bz
By
Bx
D
THD V_ion [km/s]
Vz
Vy
Vx
E
THD E_y,z [mV/m]
Ez
EFI_y
F
THD Ion energy flux [eV]
G
eV/(cm^2-sec-sr-eV)
hhmm
2020 Jun 08
0120
0140
0200
H
GOES 16 B [nT]
Bz
By
Bx
I
GOES 16 Protons [e/(cm^2-s-sr-keV)]
J
Electrons [e/(cm^2-s-sr-keV)]
hhmm
2020 Jun 08
0000
0100
0200
0300
0400

Figure A.10: Magnetotail characteristics during VNERX event. (A) Auroral electrojet index, (B) Sym-H index, (C) magnetotail magnetic field components measured at THD; thin horizontal black line denotes the zero nT, (D) bulk ion velocity components measured at THD, (E) EY measured by THD Electric Field instrument (red) and estimated EZ (blue), (F) omni-directional ion energy spectra from SST and (G) omni-directional ion energy spectra from ESA instruments, (H) GOES-16 measured magnetic field components, (I) GOES-16 measured proton and (J) electron fluxes. The vertical dashed black line denotes the time of dispersionless ion injection seen at GOES-16.

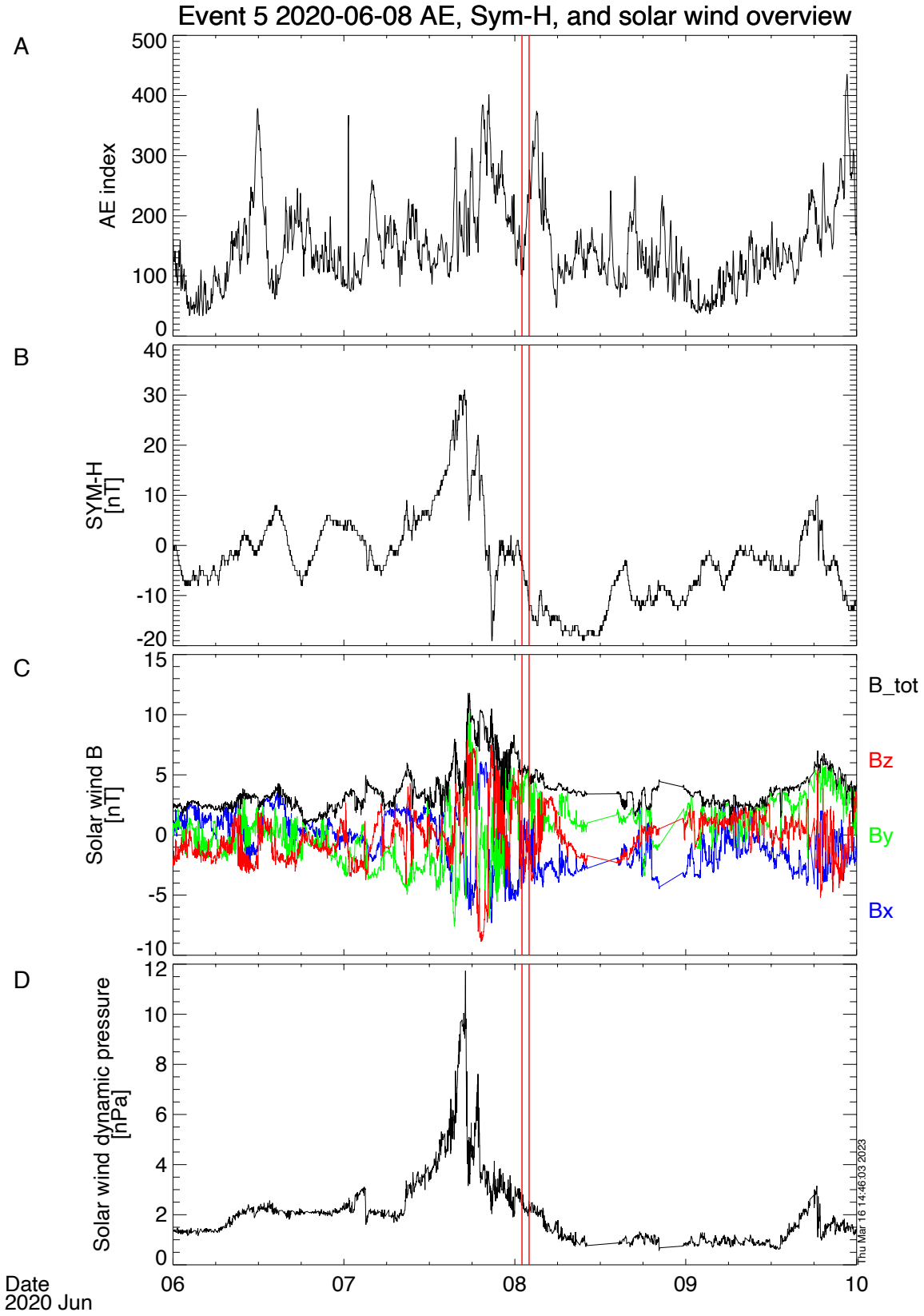
Event 5 2020-06-08 AE, Sym-H, and solar wind overview
A
AE index
500
400
300
200
100
0
B
SYM-H [nT]
40
30
20
10
0
-10
-20
C
Solar wind B [nT]
15
10
5
0
-5
-10
B_tot
Bz
By
Bx
D
Solar wind dynamic pressure [nPa]
12
10
8
6
4
2
0
Thu Mar 16 14:46:03 2023
Date
2020 Jun
06
07
08
09
10

Figure A.11: Solar wind characteristics during the four days surrounding a VNERX event. (A) Auroral electrojet index, (B) Sym-H index, (C) solar wind magnetic field components and magnitude and (D) solar wind dynamic pressure from ACE, WIND, and IMP. The red vertical lines denote the 30 minutes prior to and after the observed BZ bipolar signature of the VNERX event.

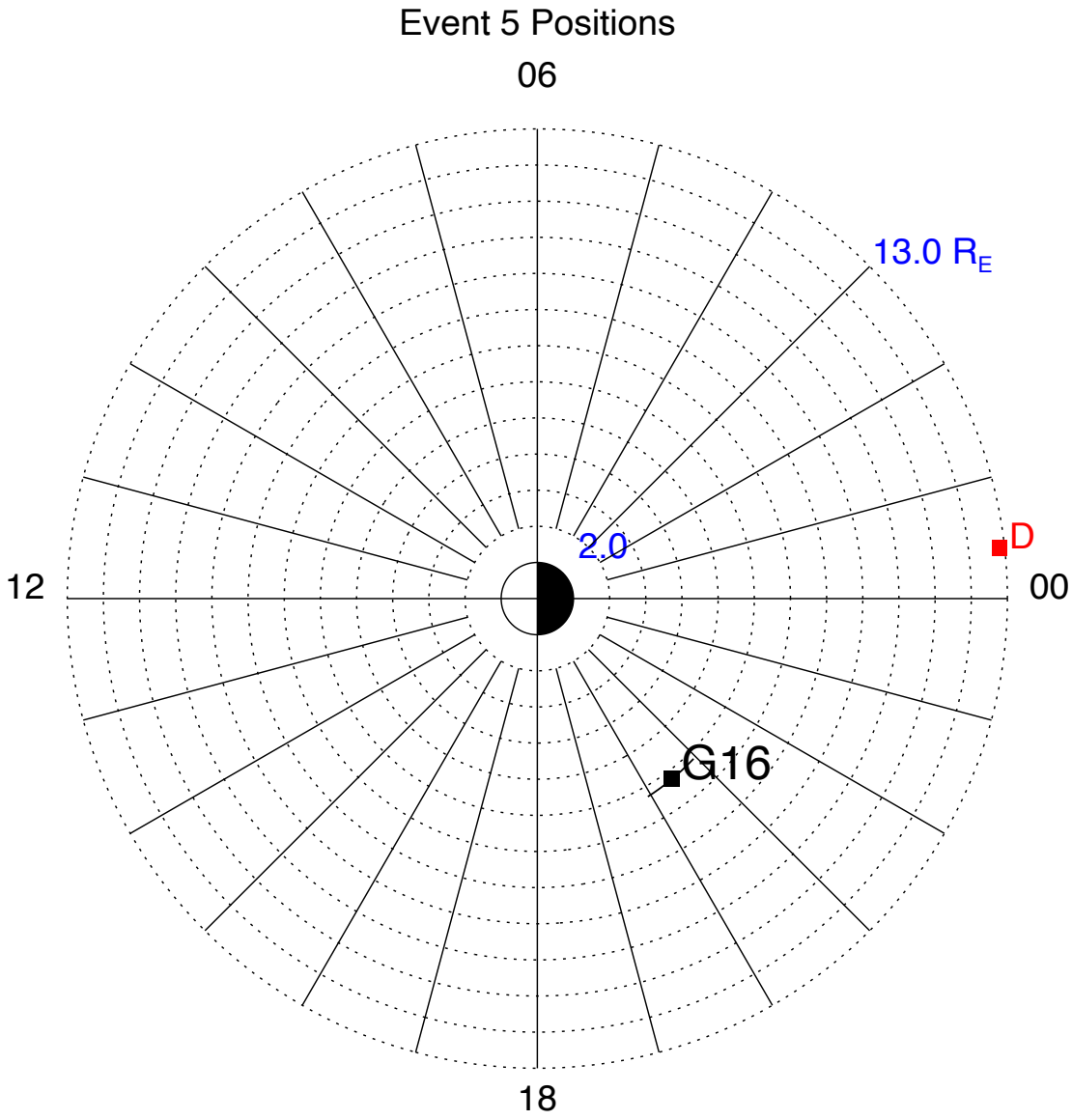

Figure A.12: Positions of spacecraft projected into the X-Y GSM plane that observed a VNERX site (red) and the corresponding position of a GOES satellite (black) during that event.

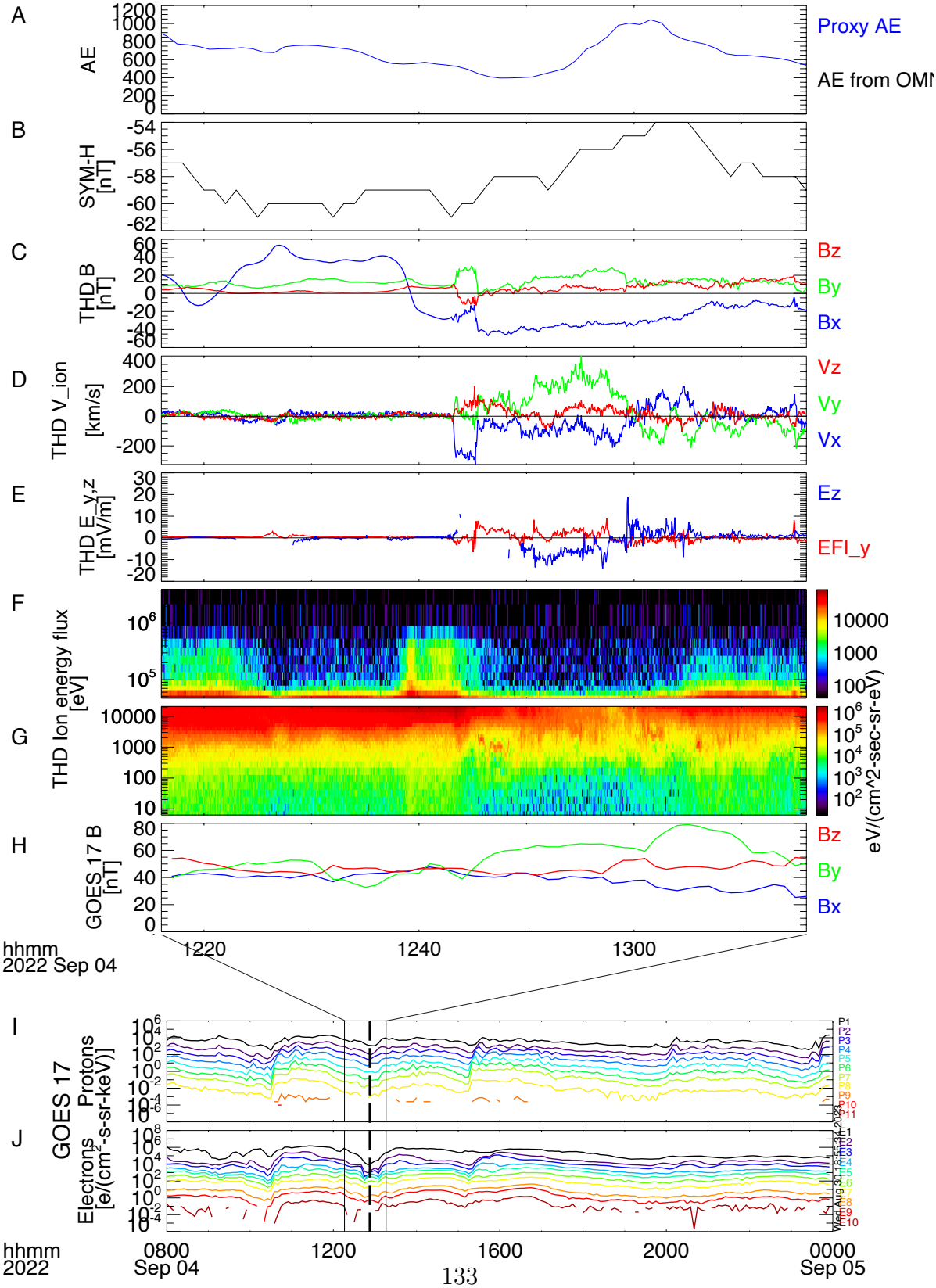
Event 6 2022-09-04 Overview: THD + GOES 17
A
AE
Proxy AE
AE from OMI
B
SYM-H [nT]
C
THD B [nT]
Bz
By
Bx
D
THD V_ion [km/s]
Vz
Vy
Vx
E
THD E_y,z [mV/m]
Ez
EFI_y
F
THD Ion energy flux [eV]
G
eV/(cm^2-sec-sr-eV)
H
GOES 17 B [nT]
Bz
By
Bx
hhmm
2022 Sep 04
1220
1240
1300
I
GOES 17 Protons [e/(cm^2-s-sr-keV)]
J
Electrons [e/(cm^2-s-sr-keV)]
hhmm
2022
0800
Sep 04
1200
1600
2000
0000
Sep 05

Figure A.13: Magnetotail characteristics during VNERX event. (A) Auroral electrojet index, (B) Sym-H index, (C) magnetotail magnetic field components measured at THD; thin horizontal black line denotes the zero nT, (D) bulk ion velocity components measured at THD, (E) EY measured by THD Electric Field instrument (red) and estimated EZ (blue), (F) omni-directional ion energy spectra from SST and (G) omni-directional ion energy spectra from ESA instruments, (H) GOES-17 measured magnetic field components, (I) GOES-17 measured proton and (J) electron fluxes. The vertical dashed black line denotes the time of dispersionless ion injection seen at GOES-17.

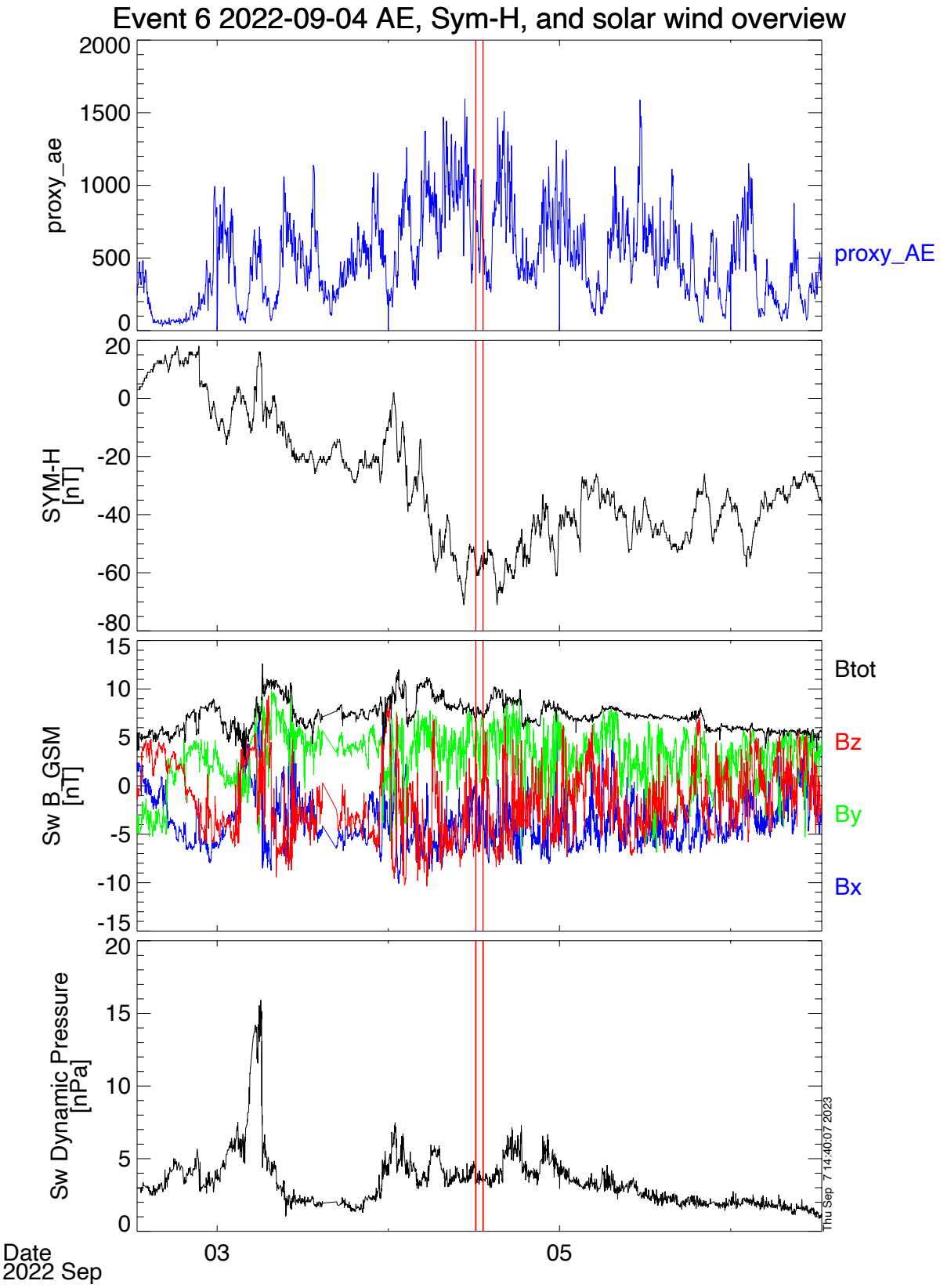
Event 6 2022-09-04 AE, Sym-H, and solar wind overview
proxy_ae
2000
1500
1000
500
0
proxy_AE
SYM-H [nT]
20
0
-20
-40
-60
-80
Sw B_GSM [nT]
15
10
5
0
-5
-10
-15
Btot
Bz
By
Bx
Sw Dynamic Pressure [nPa]
20
15
10
5
0
Thu Sep 7 14:40:07 2023
Date
2022 Sep
03
05

Figure A.14: Solar wind characteristics during the four days surrounding a VNERX event. (A) Auroral electrojet index, (B) Sym-H index, (C) solar wind magnetic field components and magnitude and (D) solar wind dynamic pressure from ACE, WIND, and IMP. The red vertical lines denote the 30 minutes prior to and after the observed BZ bipolar signature of the VNERX event.

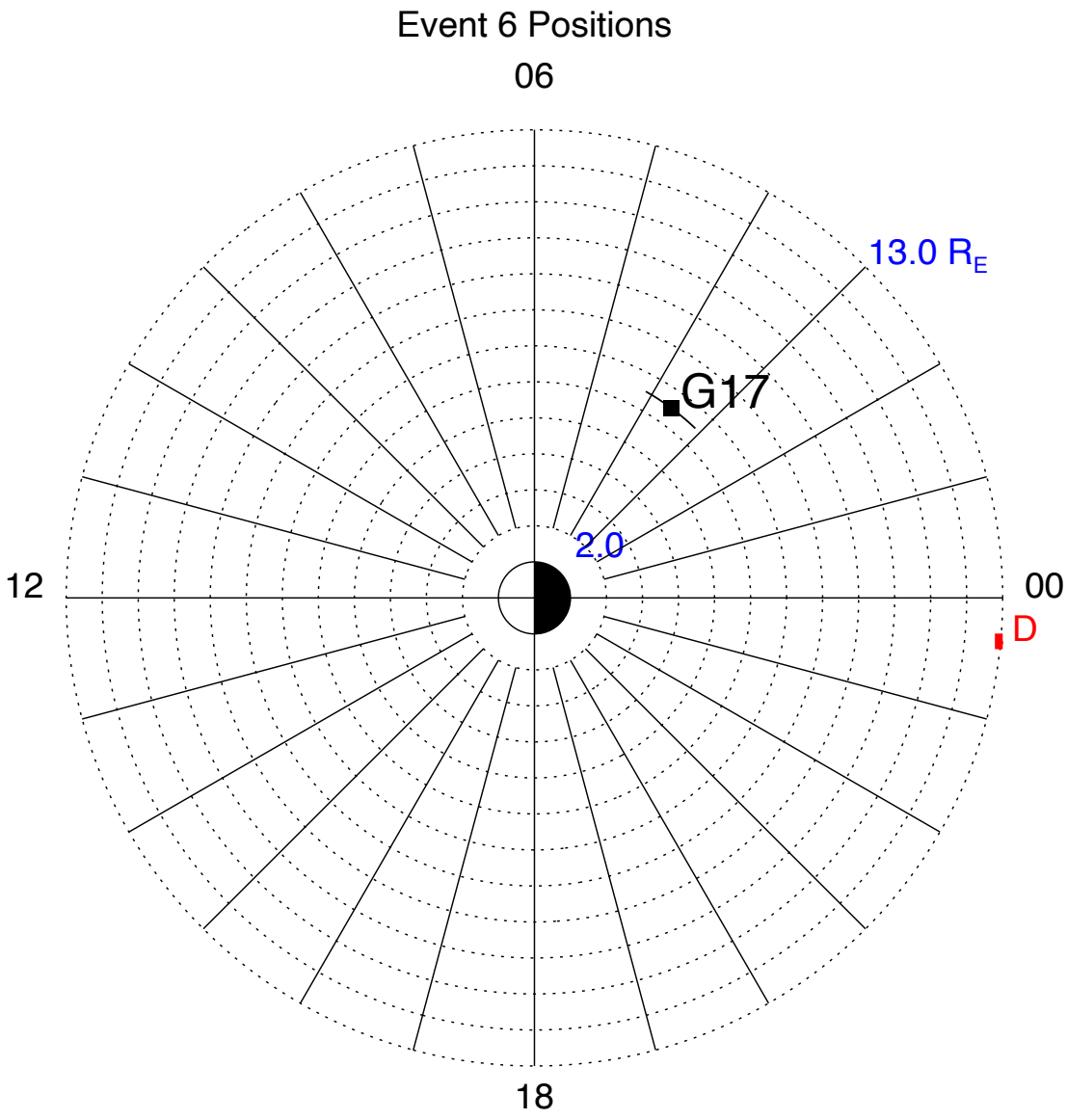

Figure A.15: Positions of spacecraft projected into the X-Y GSM plane that observed a VNERX site (red) and the corresponding position of a GOES satellite (black) during that event.

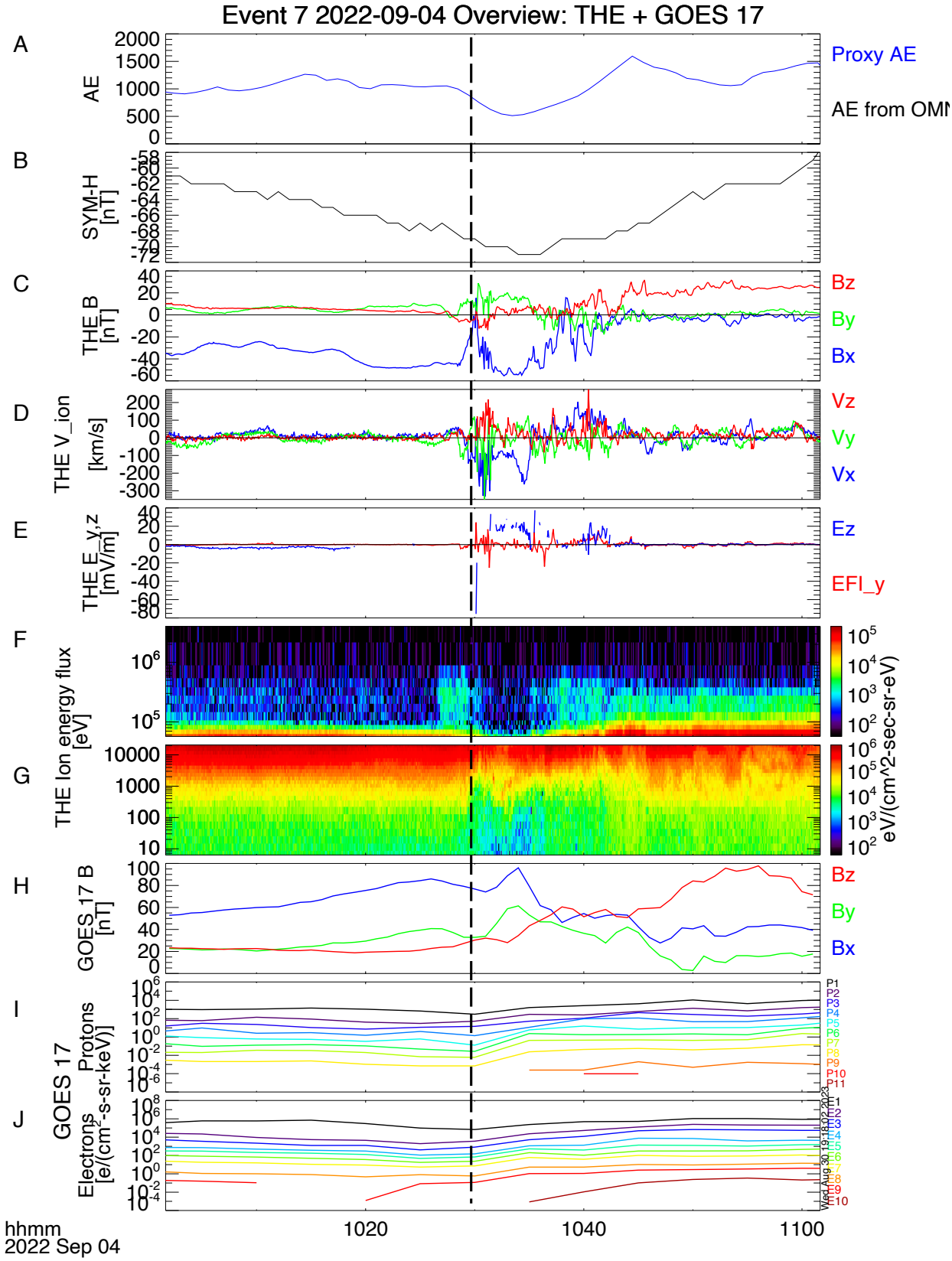
Event 7 2022-09-04 Overview: THE + GOES 17
A
AE
Proxy AE
AE from OMN
B
SYM-H [nT]
C
THE B [nT]
Bz
By
Bx
D
THE V_ion [km/s]
Vz
Vy
Vx
E
THE E_y,z [mV/m]
Ez
EFI_y
F
THE Ion energy flux [eV]
eV/(cm^2-sec-sr-eV)
G
H
GOES 17 B [nT]
Bz
By
Bx
I
GOES 17 Protons [e/(cm^2-s-sr-keV)]
J
Electrons
hhmm
2022 Sep 04
1020
1040
1100

Figure A.16: Magnetotail characteristics during VNERX event. (A) Auroral electrojet index, (B) Sym-H index, (C) magnetotail magnetic field components measured at THE; thin horizontal black line denotes the zero nT, (D) bulk ion velocity components measured at THE, (E) EY measured by THE Electric Field instrument (red) and estimated EZ (blue), (F) omni-directional ion energy spectra from SST and (G) omni-directional ion energy spectra from ESA instruments, (H) GOES-17 measured magnetic field components, (I) GOES-17 measured proton and (J) electron fluxes. The vertical dashed black line denotes the time of dispersionless ion injection seen at GOES-17.

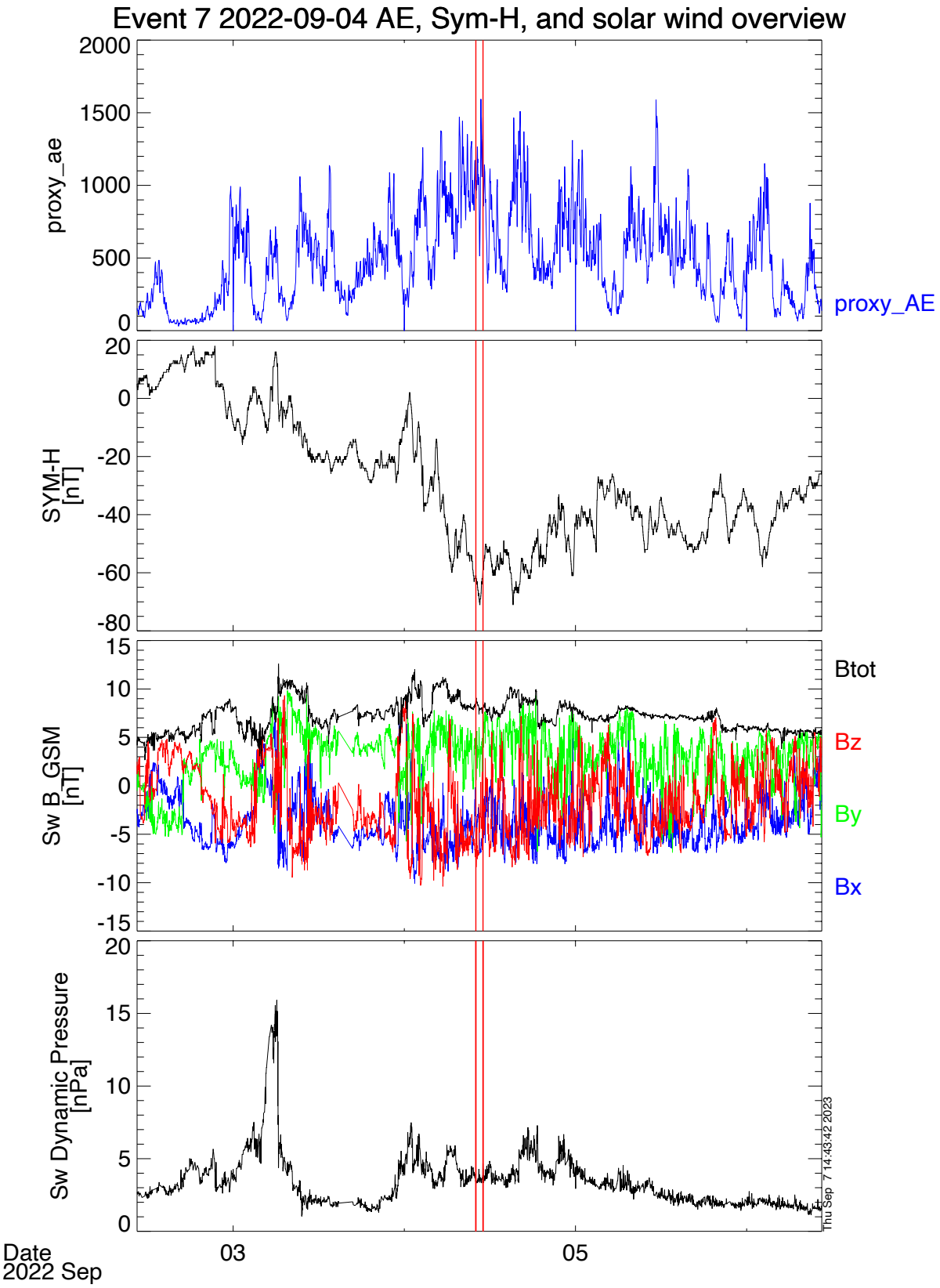
Event 7 2022-09-04 AE, Sym-H, and solar wind overview
proxy_ae
2000
1500
1000
500
0
proxy_AE
SYM-H [nT]
20
0
-20
-40
-60
-80
Sw B_GSM [nT]
15
10
5
0
-5
-10
-15
Btot
Bz
By
Bx
Sw Dynamic Pressure [nPa]
20
15
10
5
0
Thu Sep 7 14:43:42 2023
Date
2022 Sep
03
05

Figure A.17: Solar wind characteristics during the four days surrounding a VNERX event. (A) Auroral electrojet index, (B) Sym-H index, (C) solar wind magnetic field components and magnitude and (D) solar wind dynamic pressure from ACE, WIND, and IMP. The red vertical lines denote the 30 minutes prior to and after the observed BZ bipolar signature of the VNERX event.

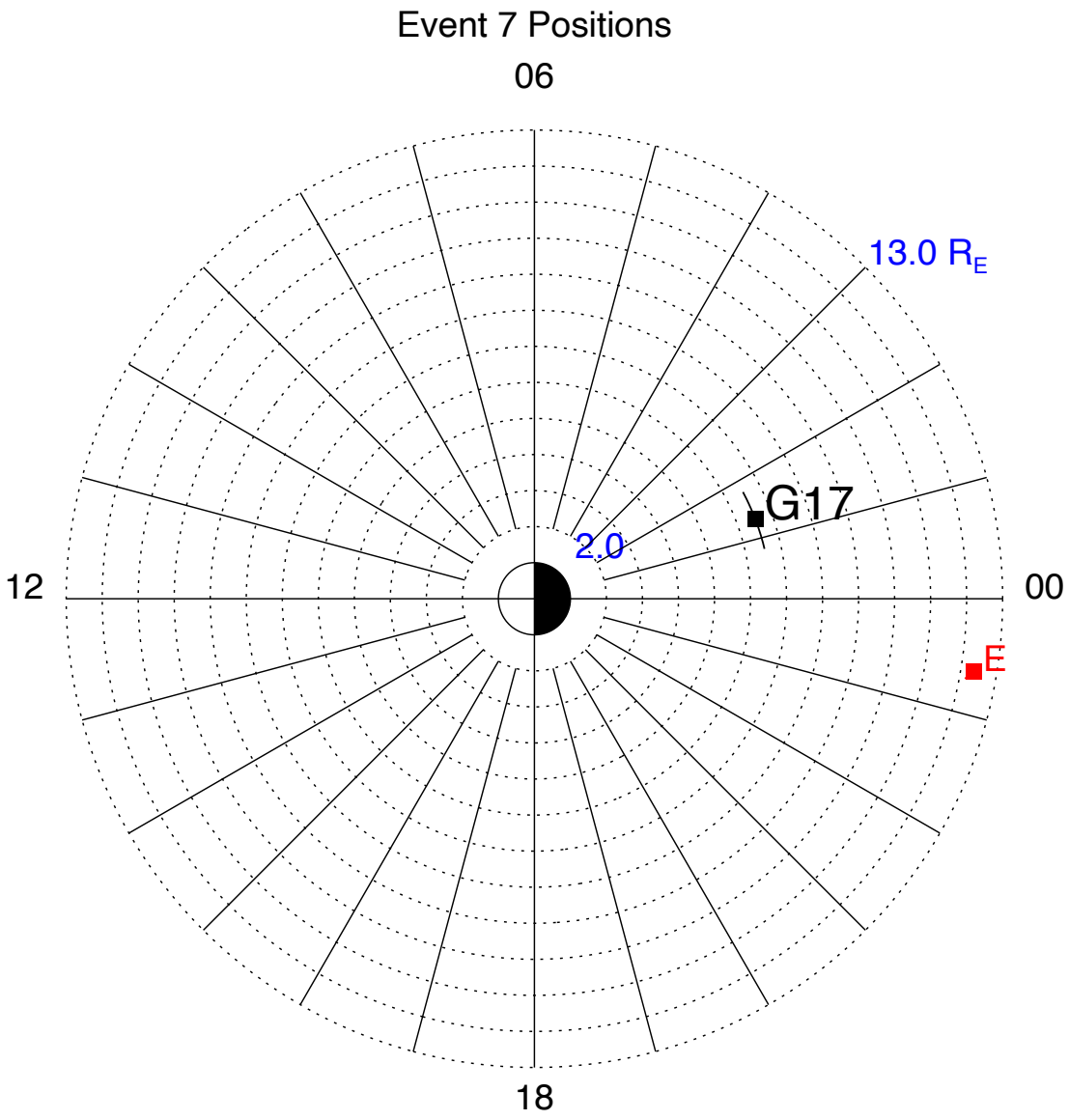

Figure A.18: Positions of spacecraft projected into the X-Y GSM plane that observed a VNERX site (red) and the corresponding position of a GOES satellite (black) during that event.

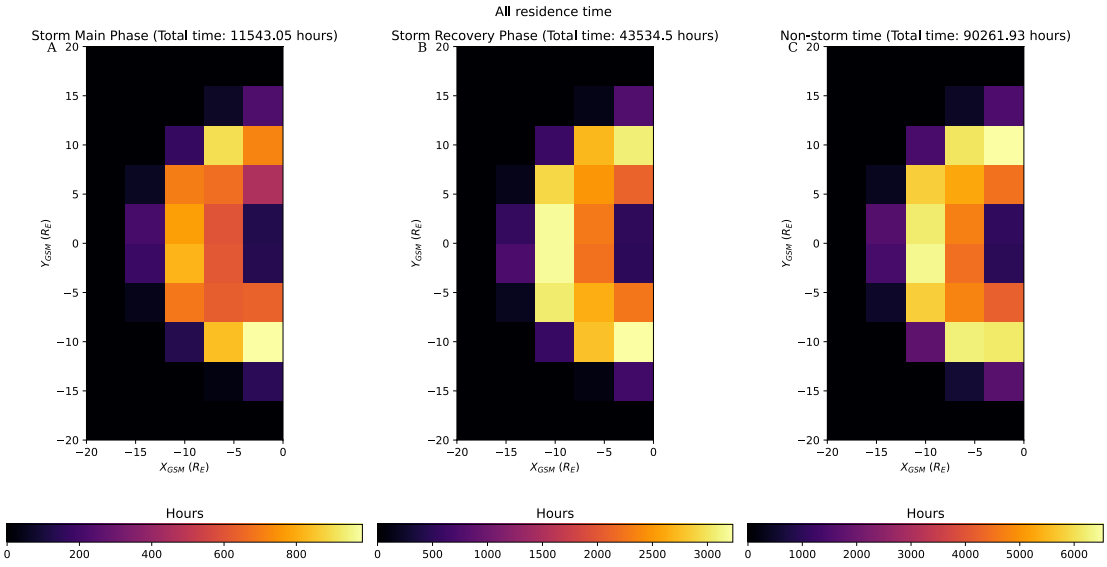

Figure A.19: X_{GSM}-Y_{GSM} distribution of total hours of storm-time and non-storm-time magnetotail residence across all three THEMIS spacecraft in 4 R_E by 4 R_E bin resolution. (A) X_{GSM}-Y_{GSM} storm main-phase magnetotail residence distribution. (B) X_{GSM}-Y_{GSM} storm recovery-phase magnetotail residence distribution. (C) X_{GSM}-Y_{GSM} non-storm-time magnetotail residence distribution.

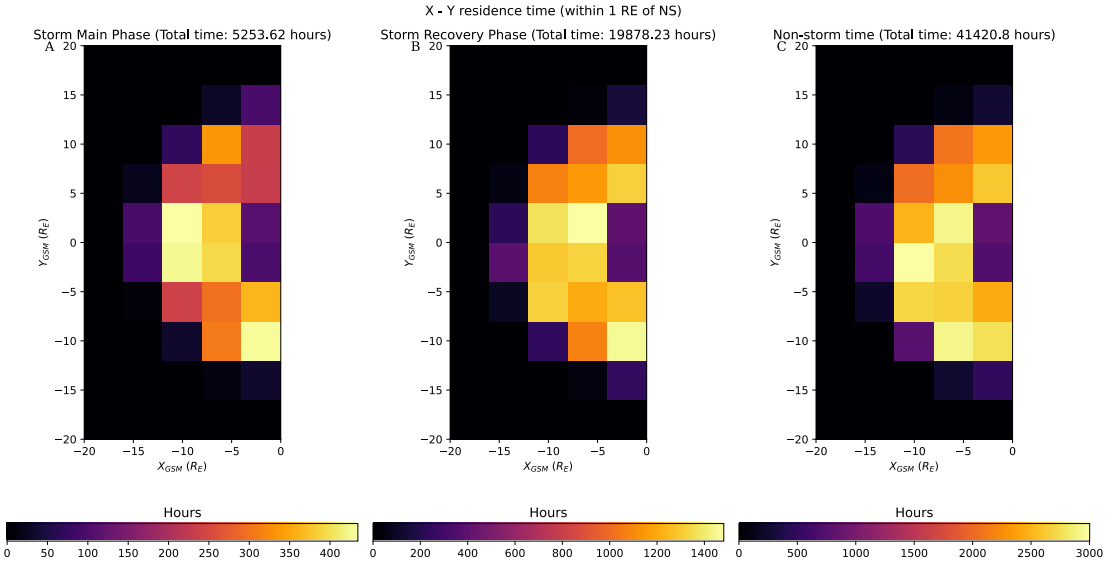

Figure A.20: X_{GSM}-Y_{GSM} distribution of total hours of storm-time and non-storm-time magnetotail residence within one R_E of the modeled TAG14 neutral sheet across all three THEMIS spacecraft in 4 R_E by 4 R_E bin resolution. (A) X_{GSM}-Y_{GSM} storm main-phase magnetotail residence distribution. (B) X_{GSM}-Y_{GSM} storm recovery-phase magnetotail residence distribution. (C) X_{GSM}-Y_{GSM} non-storm-time magnetotail residence distribution.

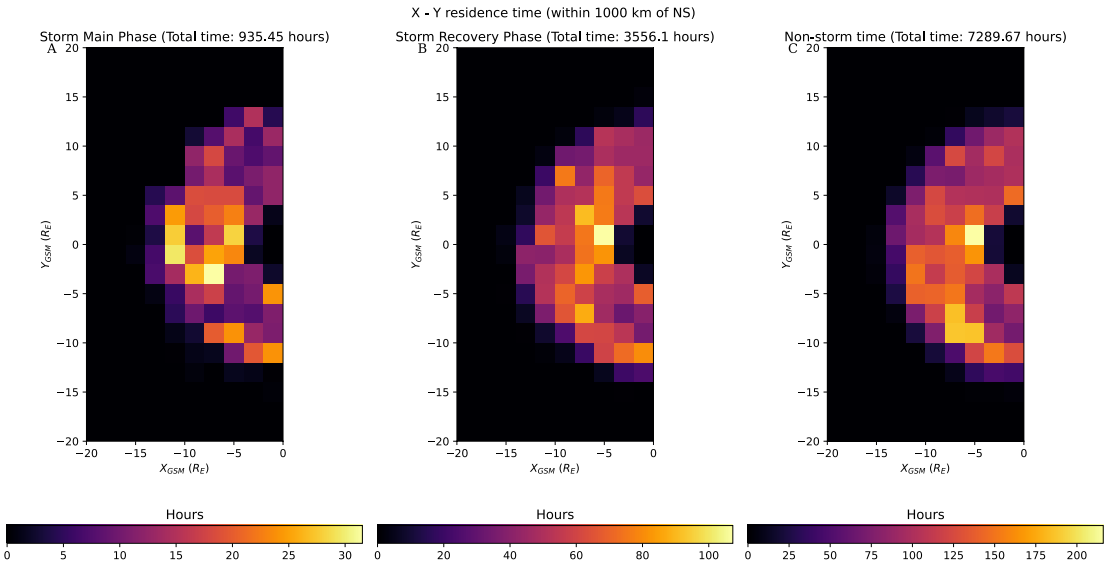

Figure A.21: X_{GSM}-Y_{GSM} distribution of total hours of storm-time and non-storm-time magnetotail residence within 1000 km of the modeled TAG14 neutral sheet across all three THEMIS spacecraft in 2 R_E by 2 R_E bin resolution. (A) X_{GSM}-Y_{GSM} storm main-phase magnetotail residence distribution. (B) X_{GSM}-Y_{GSM} storm recovery-phase magnetotail residence distribution. (C) X_{GSM}-Y_{GSM} non-storm-time magnetotail residence distribution.

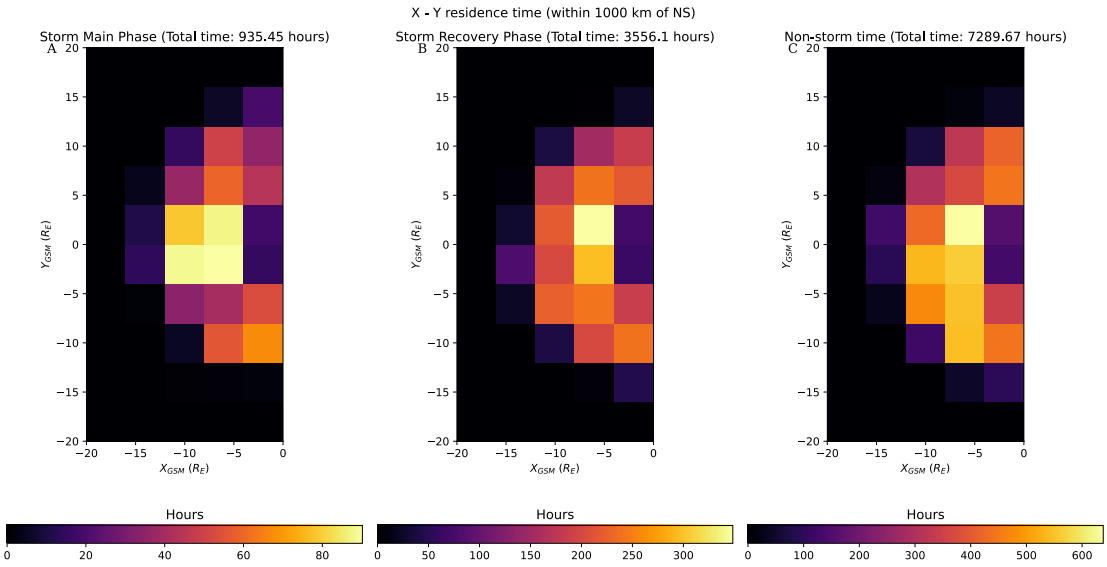

Figure A.22: X_{GSM}-Y_{GSM} distribution of total hours of storm-time and non-storm-time magnetotail residence within 1000 km of the modeled TAG14 neutral sheet across all three THEMIS spacecraft in 4 R_E by 4 R_E bin resolution. (A) X_{GSM}-Y_{GSM} storm main-phase magnetotail residence distribution. (B) X_{GSM}-Y_{GSM} storm recovery-phase magnetotail residence distribution. (C) X_{GSM}-Y_{GSM} non-storm-time magnetotail residence distribution.

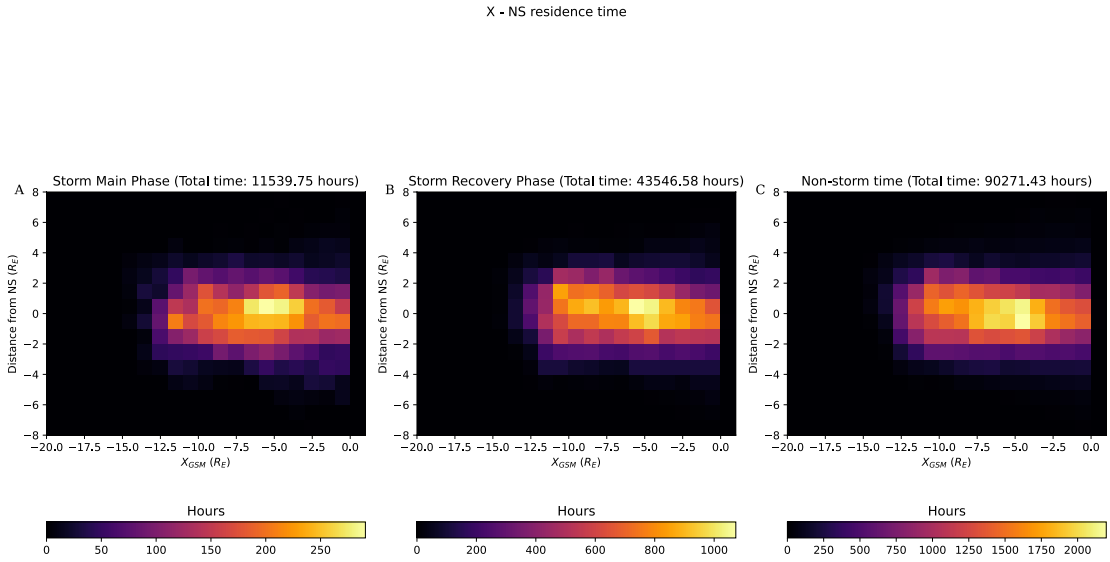

Figure A.23: X_{GSM}-Z-distance to the TAG14 neutral sheet distribution of total hours of storm–time and non-storm-time magnetotail residence across all three THEMIS spacecraft in 1 R_E by 1 R_E bin resolution. (A) storm main-phase magnetotail residence distribution. (B) storm recovery-phase magnetotail residence distribution. (C) non-storm-time magnetotail residence distribution.

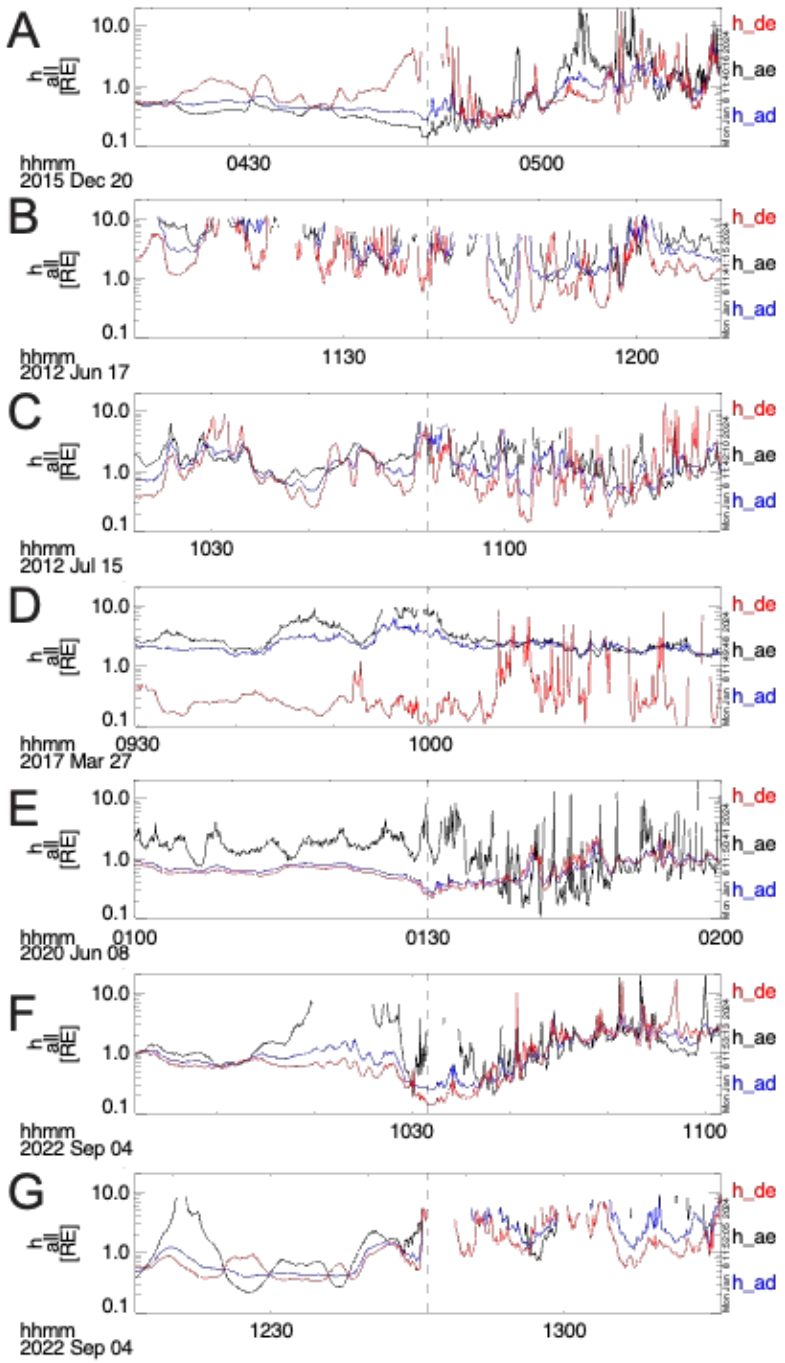

Figure A.24: Harris current sheet half-thickness estimates for the seven VNERX events. Red curves are estimates derived from THEMIS D and THEMIS E. Blue curves are estimates derived from THEMIS A and THEMIS D. Black curves are estimates derived from THEMIS A and THEMIS E. The black dashed vertical lines denote the time of Bz-zero crossing time.

APPENDIX B

Appendix: Supporting Information for "Earthward-tailward asymmetry of electron heating in reconnection outflow in the Earth magnetotail"

Contents of this file

1. Figures S1-S5

Introduction

This supporting information includes Figures S1-S5 showing overview of five events from the main text.

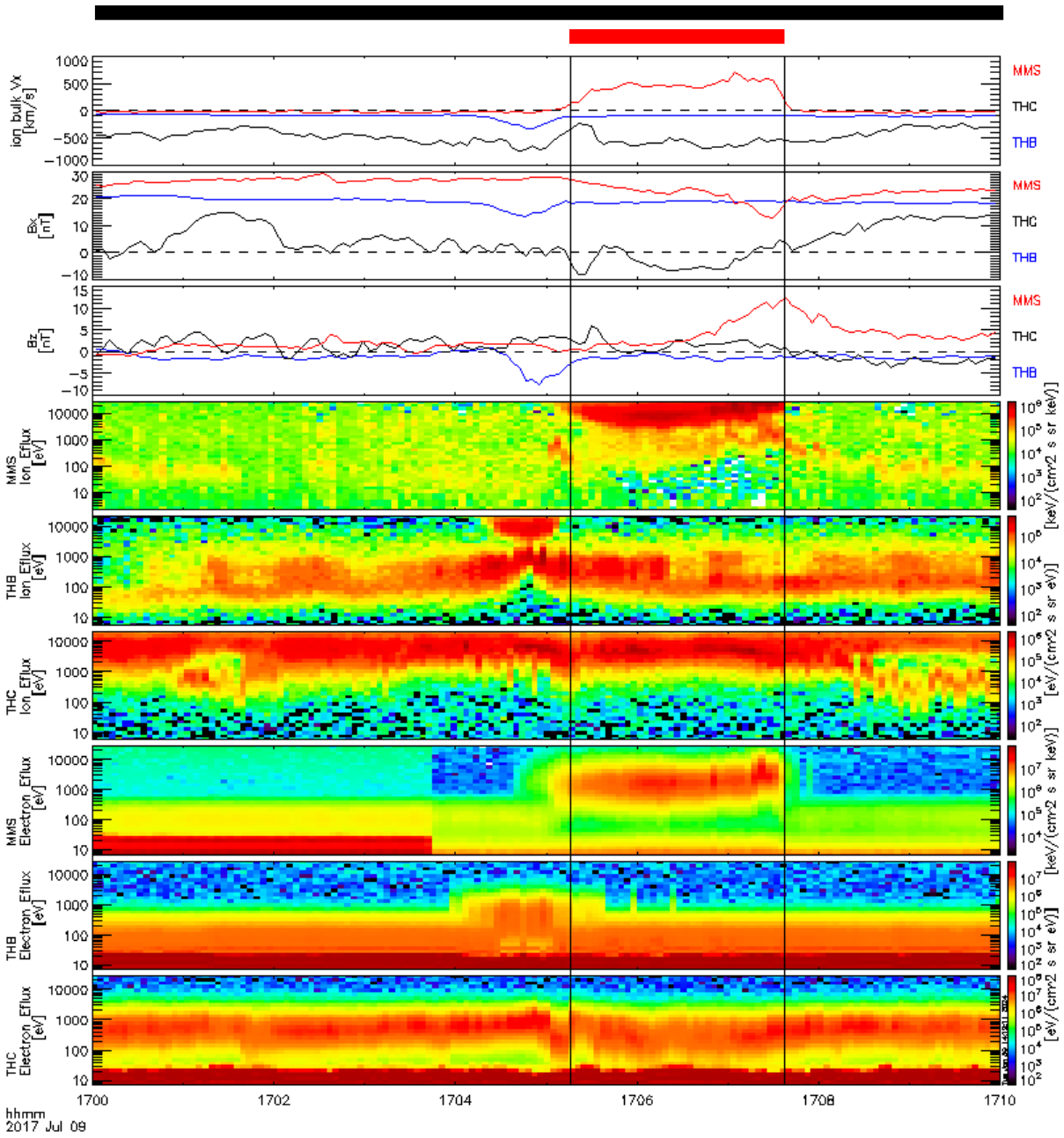
ion bulk Vx [km/s]
MMS
THC
THB
Bx [nT]
Bz [nT]
MMS Ion_Eflux [eV]
THB Ion_Eflux [eV]
THC Ion_Eflux [eV]
MMS Electron_Eflux [eV]
THB Electron_Eflux [eV]
THC Electron_Eflux [eV]
[keV/(cm^2 s sr keV)]
[eV/(cm^2 s sr eV)]
1700
1702
1704
1706
1708
1710
hhmm
2017 Jul 09

Figure B.1: Summary plot of magnetic field, ion bulk velocity, and plasma energy fluxes for Event 2. A) The x-component of the ion bulk velocity for MMS in red, THB in blue, and THC in black. The horizontal dashed line indicates $V_x = 0$. The vertical solid lines and the solid red dashed line above panel A demarcate the period when MMS observed a $V_x > 150$ km/s. The vertical dashed lines and the solid black dashed line above panel A demarcate the period when either THB or THC observed a $V_x < -150$ km/s. B) B_x observed by MMS in red, THB in blue, and THC in black. C) B_z observed by MMS in red, THB in blue, and THC in black. D) The ion energy-flux vs energy spectrogram recorded by FPI onboard MMS. E) The ion energy-flux vs energy spectrogram recorded by the ESA instrument onboard THB. F) The ion-energy-flux vs energy spectrogram recorded by the ESA instrument onboard THC. Note that the colorbars of the MMS, THB, and THC ion spectrograms cover different flux ranges. G) The electron energy-flux vs energy spectrogram recorded by the FPI onboard MMS. H) The electron energy-flux vs energy spectrogram recorded by the ESA instrument onboard THB. I) The electron energy-flux vs energy spectrogram recorded by the ESA instrument onboard THC.

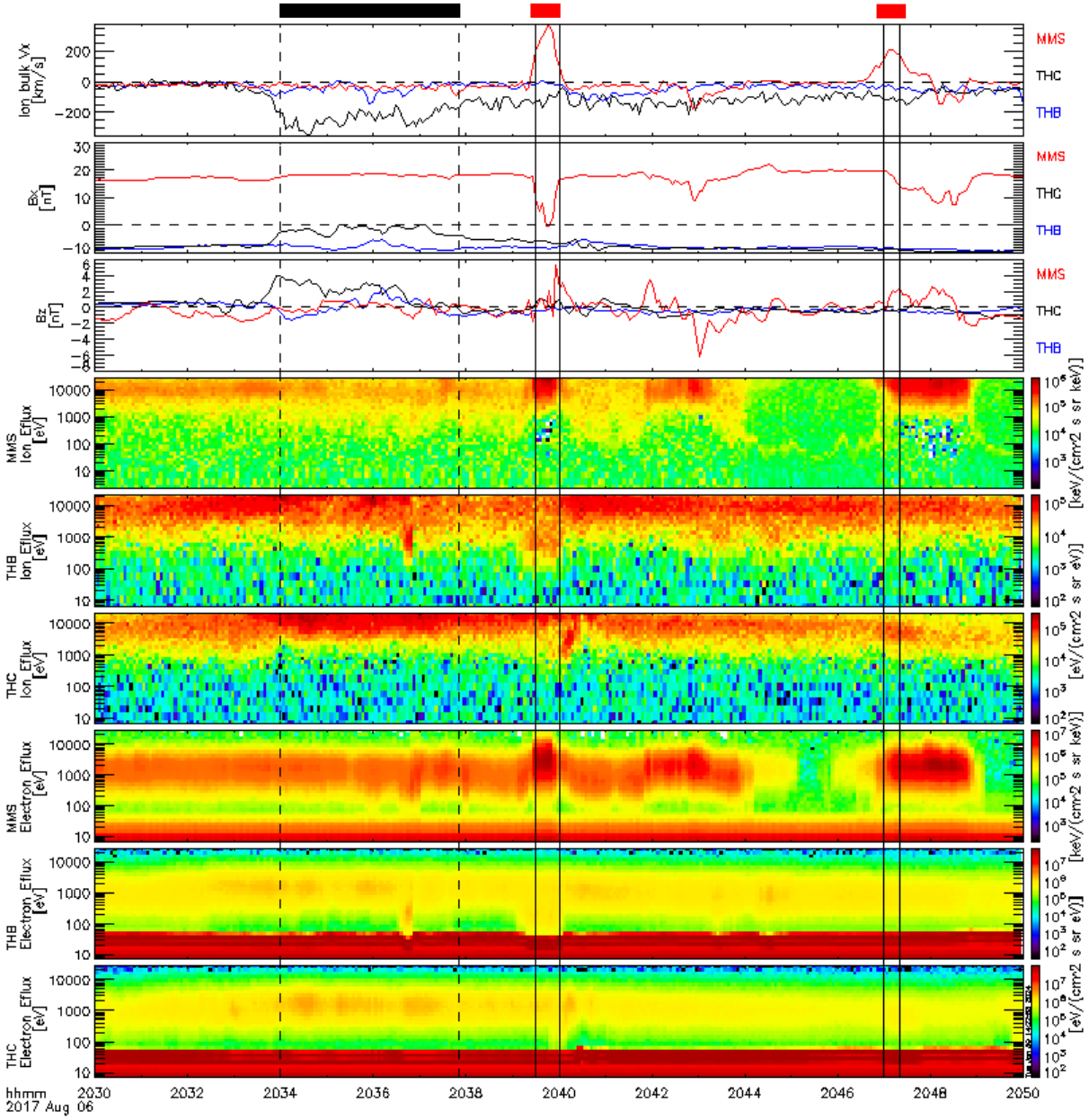
Ion bulk Vx [km/s]
MMS
THC
THB
Bx [nT]
Bz [nT]
MMS Ion_Eflux [eV]
THB Ion_Eflux [eV]
THC Ion_Eflux [eV]
MMS Electron_Eflux [eV]
THB Electron_Eflux [eV]
THC Electron_Eflux [eV]
[keV/(cm^2 s sr keV)]
[eV/(cm^2 s sr eV)]
hhmm
2017 Aug 06
2030
2032
2034
2036
2038
2040
2042
2044
2046
2048
2050

Figure B.2: Summary plot of magnetic field, ion bulk velocity, and plasma energy fluxes for Event 3. A) The x-component of the ion bulk velocity for MMS in red, THB in blue, and THC in black. The horizontal dashed line indicates $V_x = 0$. The vertical solid lines and the solid red dashed line above panel A demarcate the period when MMS observed a $V_x > 150$ km/s. The vertical dashed lines and the solid black dashed line above panel A demarcate the period when either THB or THC observed a $V_x < -150$ km/s. B) B_x observed by MMS in red, THB in blue, and THC in black. C) B_z observed by MMS in red, THB in blue, and THC in black. D) The ion energy-flux vs energy spectrogram recorded by FPI onboard MMS. E) The ion energy-flux vs energy spectrogram recorded by the ESA instrument onboard THB. F) The ion-energy-flux vs energy spectrogram recorded by the ESA instrument onboard THC. Note that the colorbars of the MMS, THB, and THC ion spectrograms cover different flux ranges. G) The electron energy-flux vs energy spectrogram recorded by the FPI onboard MMS. H) The electron energy-flux vs energy spectrogram recorded by the ESA instrument onboard THB. I) The electron energy-flux vs energy spectrogram recorded by the ESA instrument onboard THC.

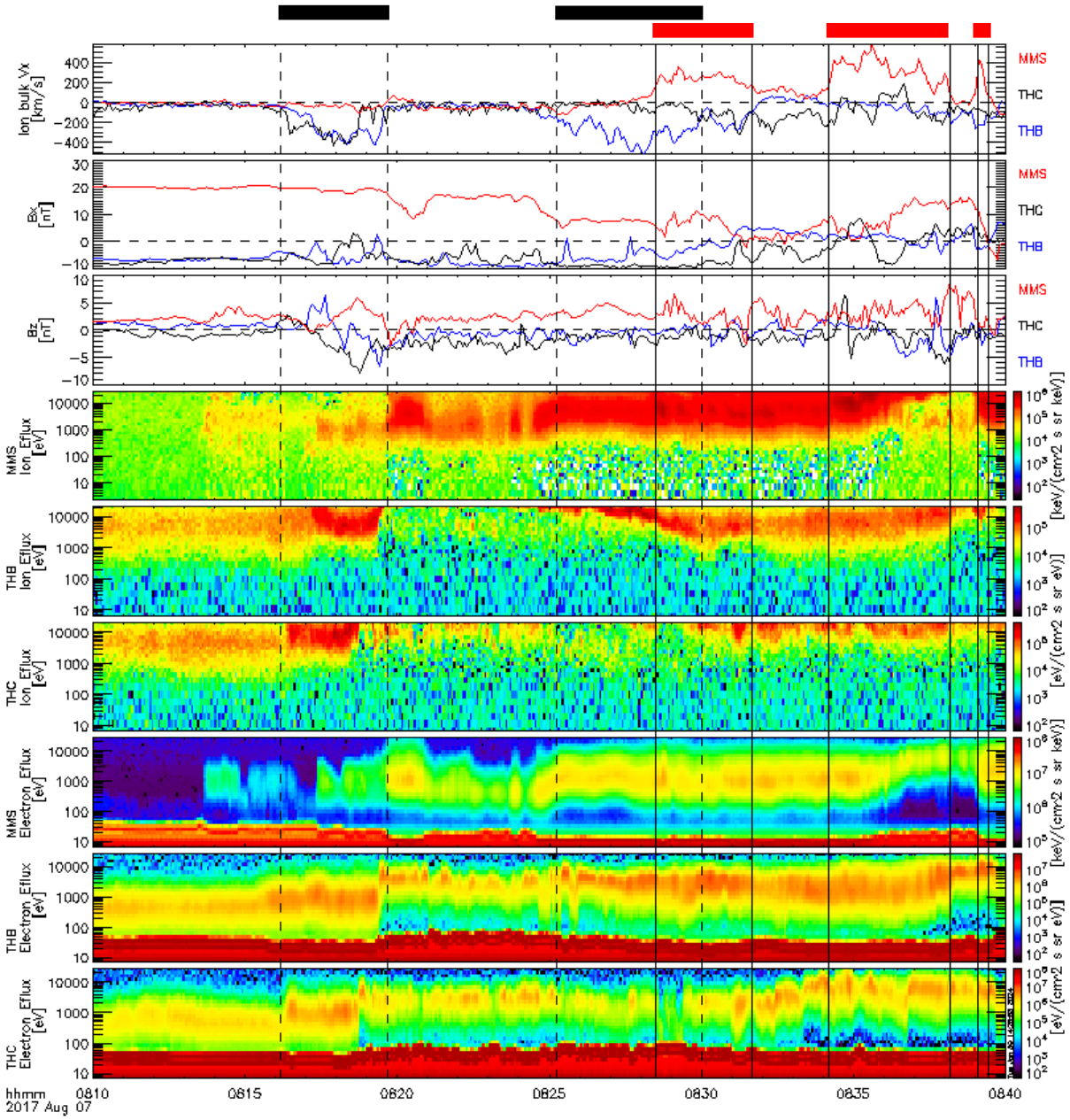
Ion bulk Vx [km/s]
400
200
0
−200
−400
MMS
THC
THB
Bx [nT]
30
20
10
0
−10
MMS
THC
THB
Bz [nT]
10
5
0
−5
−10
MMS
THC
THB
MMS Ion Eflux [eV]
THB Ion Eflux [eV]
THC Ion Eflux [eV]
MMS Electron Eflux [eV]
THB Electron Eflux [eV]
THC Electron Eflux [eV]
10000
1000
100
10
[keV/(cm^2 s sr keV)]
hhmm
0810
0815
0820
0825
0830
0835
0840
2017 Aug 07

Figure B.3: Summary plot of magnetic field, ion bulk velocity, and plasma energy fluxes for Event 4. A) The x-component of the ion bulk velocity for MMS in red, THB in blue, and THC in black. The horizontal dashed line indicates $V_x = 0$. The vertical solid lines and the solid red dashed line above panel A demarcate the period when MMS observed a $V_x > 150$ km/s. The vertical dashed lines and the solid black dashed line above panel A demarcate the period when either THB or THC observed a $V_x < -150$ km/s. B) B_x observed by MMS in red, THB in blue, and THC in black. C) B_z observed by MMS in red, THB in blue, and THC in black. D) The ion energy-flux vs energy spectrogram recorded by FPI onboard MMS. E) The ion energy-flux vs energy spectrogram recorded by the ESA instrument onboard THB. F) The ion-energy-flux vs energy spectrogram recorded by the ESA instrument onboard THC. Note that the colorbars of the MMS, THB, and THC ion spectrograms cover different flux ranges. G) The electron energy-flux vs energy spectrogram recorded by the FPI onboard MMS. H) The electron energy-flux vs energy spectrogram recorded by the ESA instrument onboard THB. I) The electron energy-flux vs energy spectrogram recorded by the ESA instrument onboard THC.

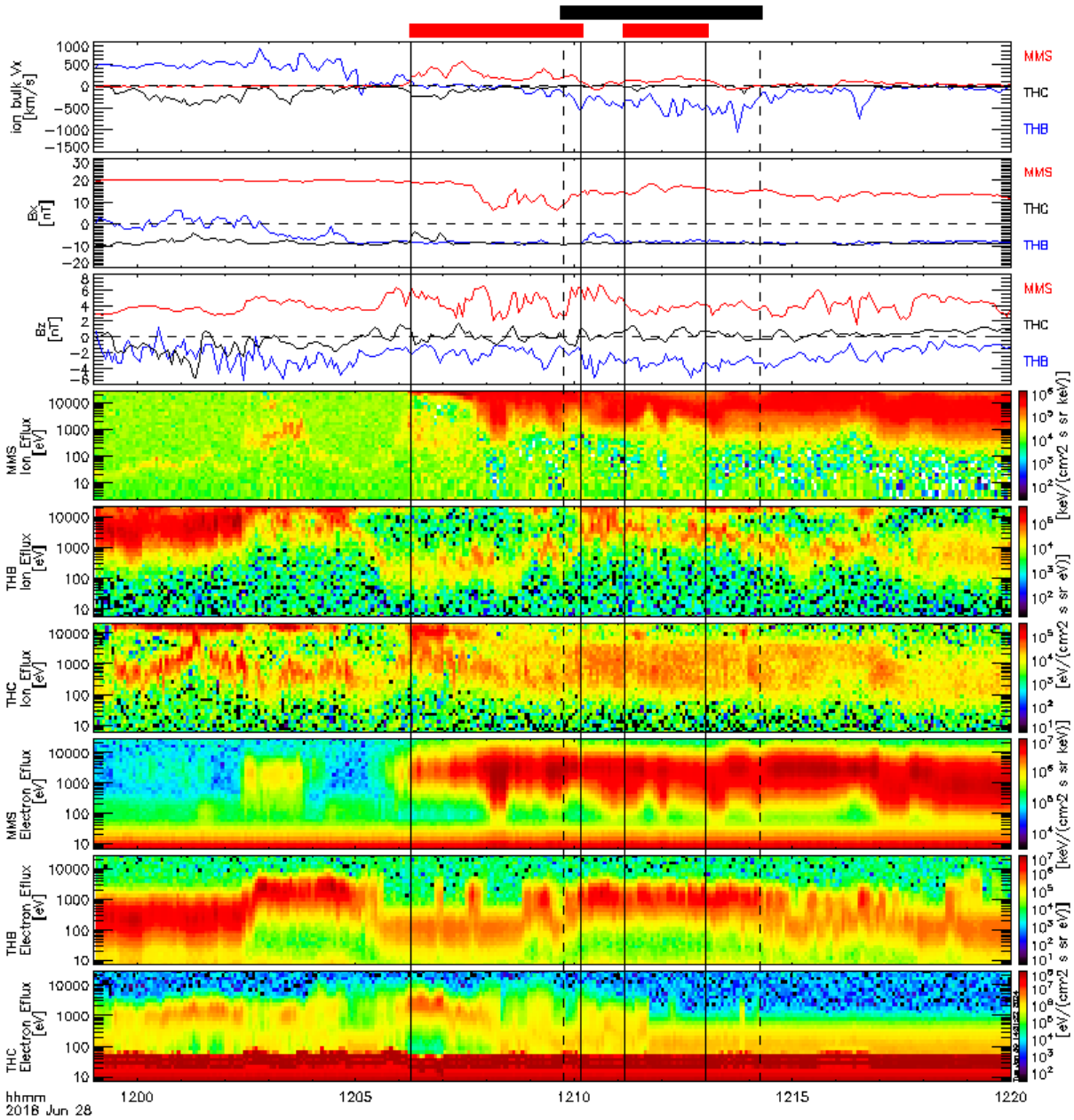
ion bulk Vx [km/s]
MMS
THC
THB
Bx [nT]
Bz [nT]
MMS Ion_Eflux [eV]
THB Ion_Eflux [eV]
THC Ion_Eflux [eV]
MMS Electron_Eflux [eV]
THB Electron_Eflux [eV]
THC Electron_Eflux [eV]
[keV/(cm2 s sr keV)]
[eV/(cm2 s sr eV)]
hhmm
2018 Jun 28
1200
1205
1210
1215
1220

Figure B.4: Summary plot of magnetic field, ion bulk velocity, and plasma energy fluxes for Event 5. A) The x-component of the ion bulk velocity for MMS in red, THB in blue, and THC in black. The horizontal dashed line indicates $V_x = 0$. The vertical solid lines and the solid red dashed line above panel A demarcate the period when MMS observed a $V_x > 150$ km/s. The vertical dashed lines and the solid black dashed line above panel A demarcate the period when either THB or THC observed a $V_x < -150$ km/s. B) B_x observed by MMS in red, THB in blue, and THC in black. C) B_z observed by MMS in red, THB in blue, and THC in black. D) The ion energy-flux vs energy spectrogram recorded by FPI onboard MMS. E) The ion energy-flux vs energy spectrogram recorded by the ESA instrument onboard THB. F) The ion-energy-flux vs energy spectrogram recorded by the ESA instrument onboard THC. Note that the colorbars of the MMS, THB, and THC ion spectrograms cover different flux ranges. G) The electron energy-flux vs energy spectrogram recorded by the FPI onboard MMS. H) The electron energy-flux vs energy spectrogram recorded by the ESA instrument onboard THB. I) The electron energy-flux vs energy spectrogram recorded by the ESA instrument onboard THC.

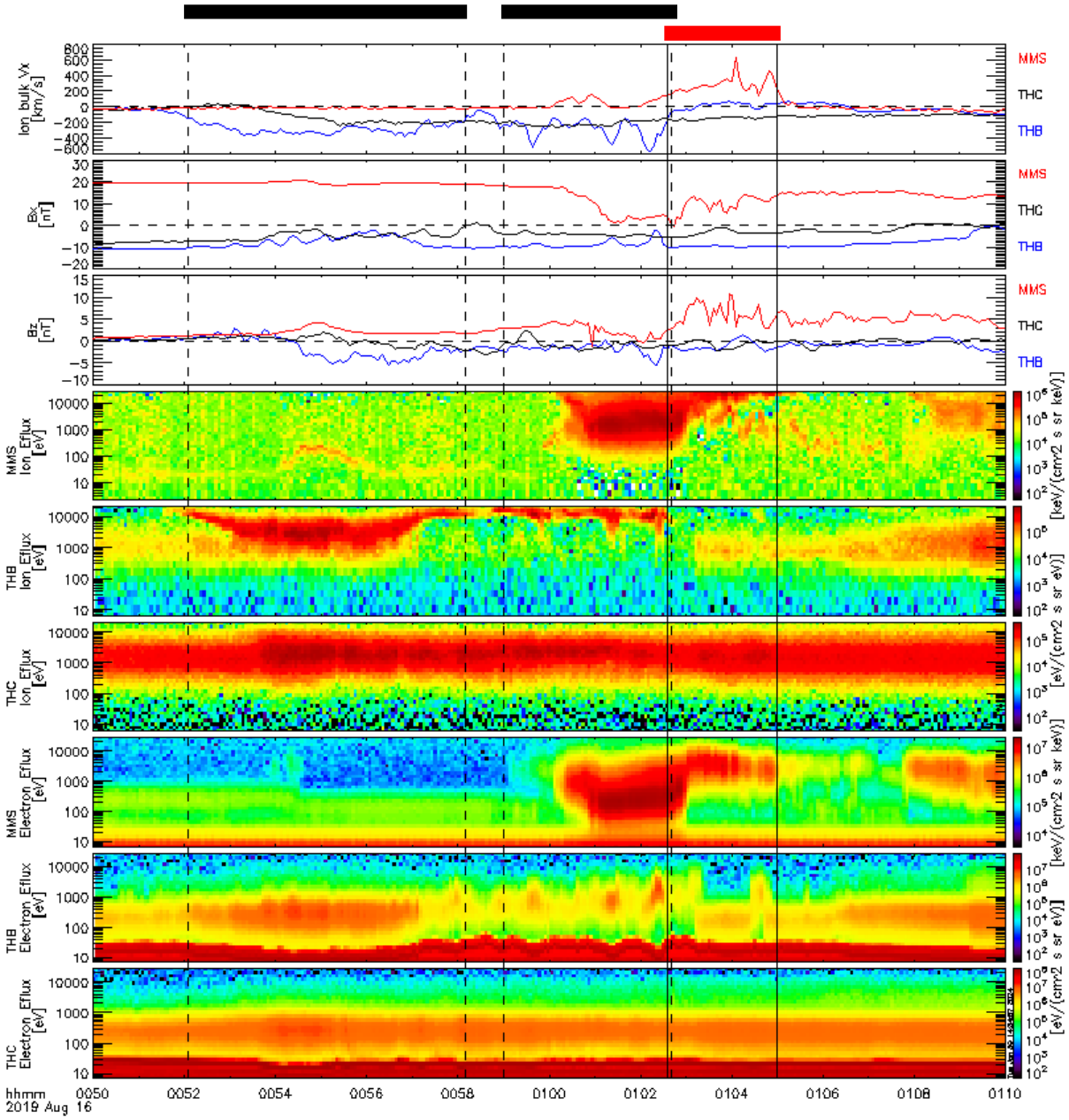
Ion_bulk_Vx [km/s]
MMS
THC
THB
Bx [nT]
MMS
THC
THB
Bz [nT]
MMS
THC
THB
MMS Ion_Eflux [eV]
THB Ion_Eflux [eV]
THC Ion_Eflux [eV]
MMS Electron_Eflux [eV]
THB Electron_Eflux [eV]
THC Electron_Eflux [eV]
[keV/(cm^2 s sr keV)]
hhmm
2019 Aug 16
0050
0052
0054
0056
0058
0100
0102
0104
0106
0108
0110

Figure B.5: Summary plot of magnetic field, ion bulk velocity, and plasma energy fluxes for Event 6. A) The x-component of the ion bulk velocity for MMS in red, THB in blue, and THC in black. The horizontal dashed line indicates $V_x = 0$. The vertical solid lines and the solid red dashed line above panel A demarcate the period when MMS observed a $V_x > 150$ km/s. The vertical dashed lines and the solid black dashed line above panel A demarcate the period when either THB or THC observed a $V_x < -150$ km/s. B) B_x observed by MMS in red, THB in blue, and THC in black. C) B_z observed by MMS in red, THB in blue, and THC in black. D) The ion energy-flux vs energy spectrogram recorded by FPI onboard MMS. E) The ion energy-flux vs energy spectrogram recorded by the ESA instrument onboard THB. F) The ion-energy-flux vs energy spectrogram recorded by the ESA instrument onboard THC. Note that the colorbars of the MMS, THB, and THC ion spectrograms cover different flux ranges. G) The electron energy-flux vs energy spectrogram recorded by the FPI onboard MMS. H) The electron energy-flux vs energy spectrogram recorded by the ESA instrument onboard THB. I) The electron energy-flux vs energy spectrogram recorded by the ESA instrument onboard THC.

Bibliography

Akasofu, S. I. (1968), *Polar and Magnetosphere Substorms*, vol. 11, doi:10.1007/978-94-010-3461-6.

Akasofu, S.-I. (1977), *Physics of magnetospheric substorms*, vol. 47, doi:10.1007/978-94-010-1164-8.

Akasofu, S.-I., and S. Chapman (1961), The Ring Current, Geomagnetic Disturbance, and the Van Allen Radiation Belts, , *66*(5), 1321–1350, doi:10.1029/JZ066i005p01321.

Angelopoulos, V. (2011), The ARTEMIS Mission, , *165*(1-4), 3–25, doi:10.1007/s11214-010-9687-2.

Angelopoulos, V., W. Baumjohann, C. F. Kennel, F. V. Coronti, M. G. Kivelson, R. Pellat, R. J. Walker, H. Luehr, and G. Paschmann (1992), Bursty Bulk Flows in the Inner Central Plasma Sheet, , *97*(A4), 4027–4039, doi:10.1029/91JA02701.

Angelopoulos, V., C. F. Kennel, F. V. Coroniti, R. Pellat, M. G. Kivelson, R. J. Walker, C. T. Russell, W. Baumjohann, W. C. Feldman, and J. T. Gosling (1994), Statistical characteristics of bursty bulk flow events, , *99*(A11), 21,257–21,280, doi:10.1029/94JA01263.

Angelopoulos, V., D. Sibeck, C. W. Carlson, J. P. McFadden, D. Larson, R. P. Lin, J. W. Bonnell, F. S. Mozer, R. Ergun, C. Cully, K. H. Glassmeier, U. Auster, A. Roux, O. Le Contel, S. Frey, T. Phan, S. Mende, H. Frey, E. Donovan, C. T. Russell, R. Strangeway, J. Liu, I. Mann, J. Rae, J. Raeder, X. Li, W. Liu, H. J. Singer, V. A. Sergeev, S. Apatenkov, G. Parks, M. Fillingim, and J. Sigwarth (2008), First Results from the THEMIS Mission, , *141*(1-4), 453–476, doi:10.1007/s11214-008-9378-4.

Angelopoulos, V., A. Runov, X. Z. Zhou, D. L. Turner, S. A. Kiehas, S. S. Li, and I. Shinohara (2013), Electromagnetic Energy Conversion at Reconnection Fronts, *Science*, *341*(6153), 1478–1482, doi:10.1126/science.1236992.

Angelopoulos, V., P. Cruce, A. Drozdov, E. W. Grimes, N. Hatzigeorgiu, D. A. King, D. Larson, J. W. Lewis, J. M. McTiernan, D. A. Roberts, C. L. Russell, T. Hori, Y. Kasahara, A. Kumamoto, A. Matsuoka, Y. Miyashita, Y. Miyoshi, I. Shinohara, M. Teramoto, J. B. Faden, A. J. Halford, M. McCarthy, R. M. Millan, J. G. Sample, D. M. Smith, L. A. Woodger, A. Masson, A. A. Narock, K. Asamura, T. F. Chang, C. Y. Chiang, Y. Kazama, K. Keika, S. Matsuda, T. Segawa, K. Seki, M. Shoji, S. W. Y. Tam, N. Umemura, B. J. Wang, S. Y. Wang, R. Redmon, J. V. Rodriguez, H. J. Singer, J. Vandegriff, S. Abe, M. Nose, A. Shinbori, Y. M. Tanaka, S. UeNo, L. Andersson, P. Dunn, C. Fowler, J. S. Halekas, T. Hara, Y. Harada, C. O. Lee, R. Lillis, D. L. Mitchell, M. R. Argall, K. Bromund, J. L. Burch, I. J. Cohen, M. Galloy, B. Giles, A. N. Jaynes, O. Le Contel, M. Oka, T. D. Phan, B. M. Walsh, J. Westlake, F. D. Wilder, S. D. Bale, R. Livi, M. Pulupa, P. Whittlesey, A. DeWolfe, B. Harter, E. Lucas, U. Auster, J. W. Bonnell, C. M. Cully, E. Donovan, R. E. Ergun, H. U. Frey, B. Jackel, A. Keiling, H. Korth, J. P. McFadden, Y. Nishimura, F. Plaschke, P. Robert, D. L. Turner, J. M. Weygand, R. M. Candey, R. C. Johnson, T. Kovalick, M. H. Liu, R. E. McGuire, A. Breneman, K. Kersten, and P. Schroeder (2019), The Space Physics Environment Data Analysis System (SPEDAS), , *215*(1), 9, doi:10.1007/s11214-018-0576-4.

Angelopoulos, V., A. Artemyev, T. D. Phan, and Y. Miyashita (2020), Near-Earth magnetotail reconnection powers space storms, *Nature Physics*, *16*(3), 317–321, doi:10.1038/s41567-019-0749-4.

Artemyev, A., S. Lu, M. El-Alaoui, Y. Lin, V. Angelopoulos, X.-J. Zhang, A. Runov, I. Vasko, L. Zelenyi, and C. Russell (2021), Configuration of the Earth's Magnetotail Current Sheet, , *48*(6), e92153, doi:10.1029/2020GL092153.

Artemyev, A. V., V. Angelopoulos, H. Hietala, A. Runov, and I. Shinohara (2017), Ion density and temperature profiles along (X_{GSM}) and across (Z_{GSM}) the magnetotail as observed by THEMIS, Geotail, and ARTEMIS, , *122*, 1590–1599, doi:10.1002/2016JA023710.

Artemyev, A. V., P. L. Pritchett, V. Angelopoulos, X.-J. Zhang, R. Nakamura, S. Lu, A. Runov, S. A. Fuselier, S. Wellenzohn, F. Plaschke, C. T. Russell, R. J. Strangeway, P.-A. Lindqvist, and R. E. Ergun (2018), Field-aligned currents originating from the magnetic reconnection region: Conjugate mms-artemis observations, , *45*(12), 5836–5844, doi:10.1029/2018GL078206.

Aunai, N., G. Belmont, and R. Smets (2011), Energy budgets in collisionless magnetic reconnection: Ion heating and bulk acceleration, *Physics of Plasmas*, *18*(12), 122901, doi:10.1063/1.3664320.

Auster, H. U., K. H. Glassmeier, W. Magnes, O. Aydogar, W. Baumjohann, D. Constantinescu, D. Fischer, K. H. Fornacon, E. Georgescu, P. Harvey, O. Hillenmaier, R. Kroth, M. Ludlam, Y. Narita, R. Nakamura, K. Okrafka, F. Plaschke, I. Richter, H. Schwarzl, B. Stoll, A. Valavanoglou, and M. Wiedemann (2008), The THEMIS Fluxgate Magnetometer, , *141*(1-4), 235–264, doi:10.1007/s11214-008-9365-9.

Axford, W. I. (1969), Magnetospheric convection., *Reviews of Geophysics and Space Physics*, *7*, 421–459, doi:10.1029/RG007i001p00421.

Baker, D. N., T. I. Pulkkinen, V. Angelopoulos, W. Baumjohann, and R. L. McPherron (1996), Neutral line model of substorms: Past results and present view, , *101*, 12,975–13,010, doi:10.1029/95JA03753.

Baker, D. N., N. E. Turner, and T. I. Pulkkinen (2001), Energy transport and dissipation in the magnetosphere during geomagnetic storms, *Journal of Atmospheric and Solar-Terrestrial Physics*, *63*(5), 421–429, doi:10.1016/S1364-6826(00)00169-3.

Baumjohann, W. (2002), Modes of convection in the magnetotail, *Physics of Plasmas*, *9*, 3665–3667, doi:10.1063/1.1499116.

Baumjohann, W., G. Paschmann, and H. Luehr (1990), Characteristics of high-speed ion flows in the plasma sheet, , *95*, 3801–3809, doi:10.1029/JA095iA04p03801.

Baumjohann, W., T. Nagai, A. Petrukovich, T. Mukai, T. Yamamoto, and S. Kokubun (2000), Substorm Signatures Between 10 and 30 Earth Radii, *Advances in Space Research*, *25*, 1663–1666, doi:10.1016/S0273-1177(99)00681-X.

Bernstein, I. B., E. A. Frieman, M. D. Kruskal, and R. M. Kulsrud (1958), An Energy Principle for Hydromagnetic Stability Problems, *Proceedings of the Royal Society of London Series A*, *244*(1236), 17–40, doi:10.1098/rspa.1958.0023.

Birn, J., and M. Hesse (2005), Energy release and conversion by reconnection in the magnetotail, *Annales Geophysicae*, *23*(10), 3365–3373, doi:10.5194/angeo-23-3365-2005.

Birn, J., and M. Hesse (2010), Energy release and transfer in guide field reconnection, *Physics of Plasmas*, *17*(1), 012109, doi:10.1063/1.3299388.

Birn, J., A. Runov, and M. Hesse (2014), Energetic electrons in dipolarization events: Spatial properties and anisotropy, *Journal of Geophysical Research (Space Physics)*, *119*(5), 3604–3616, doi:10.1002/2013JA019738.

Birn, J., A. Runov, and M. Hesse (2015), Energetic ions in dipolarization events, , *120*, 7698–7717, doi:10.1002/2015JA021372.

Birn, J., A. Runov, and Y. Khotyaintsev (2021), Magnetotail Processes, in *Magnetospheres in the Solar System*, vol. 2, edited by R. Maggiolo, N. André, H. Hasegawa, and D. T. Welling, p. 245, doi:10.1002/9781119815624.ch17.

Bonnell, J. W., F. S. Mozer, G. T. Delory, A. J. Hull, R. E. Ergun, C. M. Cully, V. Angelopoulos, and P. R. Harvey (2008), The Electric Field Instrument (EFI) for THEMIS, , *141*(1-4), 303–341, doi:10.1007/s11214-008-9469-2.

Burch, J. L., T. E. Moore, R. B. Torbert, and B. L. Giles (2016), Magnetospheric Multiscale Overview and Science Objectives, , *199*(1-4), 5–21, doi:10.1007/s11214-015-0164-9.

Case, N. (2014), Solar wind-magnetosphere interactions: A statistical analysis of spacecraft measurements, Ph.D. thesis, doi:10.13140/2.1.2588.8321.

Chapman, S. C. (1962), Earth storms: Retrospect and prospect.

Chen, C. X., and R. A. Wolf (1999), Theory of thin-filament motion in Earth's magnetotail and its application to bursty bulk flows, , *104*(A7), 14,613–14,626, doi:10.1029/1999JA900005.

Clauer, C. R. (2006), The geomagnetic storm-time response to different solar wind driving conditions, in *Proceedings of the ILWS Workshop*, edited by N. Gopalswamy and A. Bhattacharyya, p. 332.

Clauer, C. R., and R. L. McPherron (1980), The relative importance of the interplanetay electric field and magnetospheric substorms on partial ring current development, , *85*(A12), 6747–6759, doi:10.1029/JA085iA12p06747.

Cowling, T. (1953), Solar electrodynamics, in the sun, *Chicago*.

Daglis, I. A. (2006), Ring Current Dynamics, , *124*(1-4), 183–202, doi:10.1007/s11214-006-9104-z.

Dandouras, I. (2021), Ion Outflow and Escape in the Terrestrial Magnetosphere: Cluster Advances, *Journal of Geophysical Research (Space Physics)*, *126*(10), e29753, doi:10.1029/2021JA029753.

Dejong, A. D., A. J. Ridley, and C. R. Clauer (2008), Balanced reconnection intervals: four case studies, *Annales Geophysicae*, *26*(12), 3897–3912, doi:10.5194/angeo-26-3897-2008.

DeJong, A. D., A. J. Ridley, X. Cai, and C. R. Clauer (2009), A statistical study of BRIs (SMCs), isolated substorms, and individual sawtooth injections, *Journal of Geophysical Research (Space Physics)*, *114*(A8), A08215, doi:10.1029/2008JA013870.

Dessler, A. J., and E. N. Parker (1959), Hydromagnetic theory of geomagnetic storms, , *64*(12), 2239–2252, doi:10.1029/JZ064i012p02239.

Drake, J. F., M. Swisdak, C. Cattell, M. A. Shay, B. N. Rogers, and A. Zeiler (2003), Formation of Electron Holes and Particle Energization During Magnetic Reconnection, *Science*, *299*(5608), 873–877, doi:10.1126/science.1080333.

Drake, J. F., M. A. Shay, and M. Swisdak (2008), The Hall fields and fast magnetic reconnection, *Physics of Plasmas*, *15*(4), 042306, doi:10.1063/1.2901194.

Dubyagin, S., V. Sergeev, S. Apatenkov, V. Angelopoulos, A. Runov, R. Nakamura, W. Baumjohann, J. McFadden, and D. Larson (2011), Can flow bursts penetrate into the inner magnetosphere?, , *38*(8), L08102, doi:10.1029/2011GL047016.

Dungey, J. W. (1961), Interplanetary Magnetic Field and the Auroral Zones, , *6*(2), 47–48, doi:10.1103/PhysRevLett.6.47.

Eastman, T. E., L. A. Frank, W. K. Peterson, and W. Lennartsson (1984), The plasma sheet boundary layer, , *89*(A3), 1553–1572, doi:10.1029/JA089iA03p01553.

Eastwood, J. P., D. G. Sibeck, J. A. Slavin, M. L. Goldstein, B. Lavraud, M. Sitnov, S. Imber, A. Balogh, E. A. Lucek, and I. Dandouras (2005), Observations of multiple X-line structure in the Earth's magnetotail current sheet: A Cluster case study, , *32*(11), L11105, doi:10.1029/2005GL022509.

Eastwood, J. P., T. D. Phan, M. Øieroset, and M. A. Shay (2010), Average properties of the magnetic reconnection ion diffusion region in the Earth's magnetotail: The 2001-2005 Cluster observations and comparison with simulations, , *115*, A08215, doi:10.1029/2009JA014962.

Eastwood, J. P., T. D. Phan, J. F. Drake, M. A. Shay, A. L. Borg, B. Lavraud, and

M. G. G. T. Taylor (2013), Energy Partition in Magnetic Reconnection in Earth's Magnetotail, *Physical Review Letters*, *110*(22), 225001, doi:10.1103/PhysRevLett.110.225001.

Ebihara, Y. (2019), Simulation study of near-Earth space disturbances: 1. magnetic storms, *Progress in Earth and Planetary Science*, *6*(1), 16, doi:10.1186/s40645-019-0264-3.

Ebihara, Y., and M. Ejiri (2000), Simulation study on fundamental properties of the storm-time ring current, , *105*(A7), 15,843–15,860, doi:10.1029/1999JA900493.

Ebihara, Y., and M. Ejiri (2003), Numerical Simulation of the Ring Current: Review, , *105*(1), 377–452, doi:10.1023/A:1023905607888.

Ebihara, Y., and Y. S. Miyoshi (2011), Dynamic Inner Magnetosphere: A Tutorial and Recent Advances The Dynamic Magnetosphere, in *The Dynamic Magnetosphere*, vol. 3, edited by W. Liu and M. Fujimoto, p. 145, doi:10.1007/978-94-007-0501-2_9.

Erickson, G. M., and R. A. Wolf (1980), Is steady convection possible in the Earth's magnetotail?, , *7*(11), 897–900, doi:10.1029/GL007i011p00897.

Fairfield, D. H. (1980), A statistical determination of the shape and position of the geomagnetic neutral sheet, , *85*(A2), 775–780, doi:10.1029/JA085iA02p00775.

Fairfield, D. H., and J. Jones (1996), Variability of the tail lobe field strength, , *101*(A4), 7785–7792, doi:10.1029/95JA03713.

Fairfield, D. H., M. H. Acuna, L. J. Zanetti, and T. A. Potemra (1987), The magnetic field of the equatorial magnetotail: AMPTE/CCE observations at R¡8.8 R_E, , *92*(A7), 7432–7442, doi:10.1029/JA092iA07p07432.

Fok, M., T. Moore, S. Slinker, J. Fedder, and D. Delcourt (2000), Roles of convection and substorm electric fields on ring current growth, in *The First S-RAMP Conference Abstract Book*, p. 169.

Fok, M.-C., T. E. Moore, and D. C. Delcourt (1999), Modeling of inner plasma sheet and ring current during substorms, , *104*(A7), 14,557–14,570, doi:10.1029/1999JA900014.

Frank, L. A. (1967), On the extraterrestrial ring current during geomagnetic storms, , *72*(15), 3753–3767, doi:10.1029/JZ072i015p03753.

Frank, L. A. (1976), Hot plasmas in the earth's magnetosphere, in *Physics of Solar Planetary Environments*, vol. 2, edited by D. J. Williams, pp. 685–700.

Furth, H. P., J. Killeen, and M. N. Rosenbluth (1963), Finite-Resistivity Instabilities of a Sheet Pinch, *Physics of Fluids*, *6*(4), 459–484, doi:10.1063/1.1706761.

Gabrielse, C., V. Angelopoulos, A. Runov, and D. L. Turner (2014), Statistical characteristics of particle injections throughout the equatorial magnetotail, *Journal of Geophysical Research (Space Physics)*, *119*(4), 2512–2535, doi:10.1002/2013JA019638.

Genestreti, K. J., S. A. Fuselier, J. Goldstein, T. Nagai, and J. P. Eastwood (2014), The location and rate of occurrence of near-Earth magnetotail reconnection as observed by Cluster and Geotail, *Journal of Atmospheric and Solar-Terrestrial Physics*, *121*, 98–109, doi:10.1016/j.jastp.2014.10.005.

Giovanelli, R. G. (1939), The Relations Between Eruptions and Sunspots., , *89*, 555, doi:10.1086/144081.

Giovanelli, R. G. (1947), Magnetic and Electric Phenomena in the Sun's Atmosphere associated with Sunspots, , *107*, 338, doi:10.1093/mnras/107.4.338.

Gonzalez, W., and E. Parker (2016), *Magnetic Reconnection*, vol. 427, doi:10.1007/978-3-319-26432-5.

Gonzalez, W. D., J. A. Joselyn, Y. Kamide, H. W. Kroehl, G. Rostoker, B. T. Tsurutani, and V. M. Vasyliunas (1994), What is a geomagnetic storm?, , *99*(A4), 5771–5792, doi:10.1029/93JA02867.

Gonzalez, W. D., B. T. Tsurutani, and A. L. Clúa de Gonzalez (1999), Interplanetary origin of geomagnetic storms, , *88*, 529–562, doi:10.1023/A:1005160129098.

Grigorenko, E. E., M. Hoshino, M. Hirai, T. Mukai, and L. M. Zelenyi (2009), "Geography" of ion acceleration in the magnetotail: X-line versus current sheet effects, *Journal of Geophysical Research (Space Physics)*, *114*(A3), A03203, doi:10.1029/2008JA013811.

Haggerty, C. C., M. A. Shay, J. F. Drake, T. D. Phan, and C. T. McHugh (2015), The competition of electron and ion heating during magnetic reconnection, , *42*(22), 9657–9665, doi:10.1002/2015GL065961.

Harris, E. G. (1962), On a plasma sheath separating regions of oppositely directed magnetic field, *Il Nuovo Cimento*, *23*(1), 115–121, doi:10.1007/BF02733547.

Hesse, M., and P. A. Cassak (2020), Magnetic Reconnection in the Space Sciences: Past, Present, and Future, *Journal of Geophysical Research (Space Physics)*, *125*(2), e25935, doi:10.1029/2018JA025935.

Hesse, M., K. Schindler, J. Birn, and M. Kuznetsova (1999), The diffusion region in collisionless magnetic reconnection, *Physics of Plasmas*, *6*(5), 1781–1795, doi:10.1063/1.873436.

Hones, J., E. W. (1979), Transient Phenomena in the Magnetotail and Their Relation to Substorms (Article published in the special issues: Proceedings of the Symposium on Solar Terrestrial Physics held in Innsbruck, May- June 1978. (pp. 137-538)), , *23*(3), 393–410, doi:10.1007/BF00172247.

Hori, T., A. T. Y. Lui, S. Ohtani, P. C:Son Brandt, B. H. Mauk, R. W. McEntire, K. Maezawa, T. Mukai, Y. Kasaba, and H. Hayakawa (2005), Storm-time convection electric field in the near-Earth plasma sheet, *Journal of Geophysical Research (Space Physics)*, *110*(A4), A04213, doi:10.1029/2004JA010449.

Hubert, B., S. E. Milan, A. Grocott, C. Blockx, S. W. H. Cowley, and J. C. GéRard (2006), Dayside and nightside reconnection rates inferred from IMAGE FUV and Super Dual Auroral Radar Network data, *Journal of Geophysical Research (Space Physics)*, *111*(A3), A03217, doi:10.1029/2005JA011140.

Iijima, T., and T. A. Potemra (1976a), The amplitude distribution of field-aligned currents at northern high latitudes observed by Triad, , *81*(13), 2165, doi:10.1029/JA081i013p02165.

Iijima, T., and T. A. Potemra (1976b), Field-aligned currents in the dayside cusp observed by triad, , *81*(A34), 5971–5979, doi:10.1029/JA081i034p05971.

Iyemori, T. (1990), Storm-time magnetospheric currents inferred from mid-latitude geomagnetic field variations, *Journal of Geomagnetism and Geoelectricity*, *42*(11), 1249–1265, doi:10.5636/jgg.42.1249.

Jordanova, V. K., R. Ilie, and M. W. Chen (2020), Chapter 1 - introduction and historical background, in *Ring Current Investigations*, edited by V. K. Jordanova, R. Ilie, and M. W. Chen, pp. 1–13, Elsevier, doi:https://doi.org/10.1016/B978-0-12-815571-4.00001-9.

Joselyn, J. A., and B. T. Tsurutani (1990), Geomagnetic Sudden impulses and storm sudden commencements: A note on terminology, *EOS Transactions*, *71*(47), 1808–1809, doi:10.1029/90EO00350.

Kamide, Y. (1992), Is substorm occurrence a necessary condition for a magnetic storm, *Journal of geomagnetism and geoelectricity*, *44*, 109–117.

Kamide, Y., W. Baumjohann, I. A. Daglis, W. D. Gonzalez, M. Grande, J. A. Joselyn, R. L. McPherron, J. L. Phillips, E. G. D. Reeves, G. Rostoker, A. S. Sharma, H. J. Singer, B. T. Tsurutani, and V. M. Vasyliunas (1998), Current understanding of magnetic storms: Storm-substorm relationships, , *103*(A8), 17,705–17,728, doi:10.1029/98JA01426.

Keiling, A., J. R. Wygant, C. A. Cattell, F. S. Mozer, and C. T. Russell (2003), The Global Morphology of Wave Poynting Flux: Powering the Aurora, *Science*, *299*(5605), 383–386, doi:10.1126/science.1080073.

Kistler, L. M. (2020), Chapter 2 - observations and measurement techniques, in *Ring Current Investigations*, edited by V. K. Jordanova, R. Ilie, and M. W. Chen, pp. 15–51, Elsevier, doi:https://doi.org/10.1016/B978-0-12-815571-4.00002-0.

Kivelson, M. G., and H. E. Spence (1988), On the possibility of quasi-static convection in the quiet magnetotail, , *15*(13), 1541–1544, doi:10.1029/GL015i013p01541.

Klein, L. W., and L. F. Burlaga (1982), Interplanetary magnetic clouds at 1 AU, , *87*(A2), 613–624, doi:10.1029/JA087iA02p00613.

Kokubun, S., T. Yamamoto, M. H. Acuña, K. Hayashi, K. Shiokawa, and H. Kawano (1994), The GEOTAIL Magnetic Field Experiment., *Journal of Geomagnetism and Geoelectricity*, *46*(1), 7–21, doi:10.5636/jgg.46.7.

Koleva, R., and J. A. Sauvaud (2008), Plasmas in the near-Earth magnetotail lobes: Properties and sources, *Journal of Atmospheric and Solar-Terrestrial Physics*, *70*(17), 2118–2131, doi:10.1016/j.jastp.2008.03.025.

Kress, B., J. Rodriguez, and S. Codrescu (2018), GOES-R Series Level 2 Space Environment In Situ Suite (SEISS) Products, *NOAA National Centers for Environmental Information*.

Lee, D. Y., L. R. Lyons, K. C. Kim, J. H. Baek, K. H. Kim, H. J. Kim, J. Weygand, Y. J. Moon, K. S. Cho, Y. D. Park, and W. Han (2006), Repetitive substorms caused by Alfvénic waves of the interplanetary magnetic field during high-speed solar wind streams, *Journal of Geophysical Research (Space Physics)*, *111*(A12), A12214, doi:10.1029/2006JA011685.

Li, S. S., J. Liu, V. Angelopoulos, A. Runov, X. Z. Zhou, and S. A. Kiehas (2014a), Antidipo-

larization fronts observed by ARTEMIS, *Journal of Geophysical Research (Space Physics)*, *119*(9), 7181–7198, doi:10.1002/2014JA020062.

Li, S. S., V. Angelopoulos, A. Runov, and S. A. Kiehas (2014b), Azimuthal extent and properties of midtail plasmoids from two-point ARTEMIS observations at the Earth-Moon Lagrange points, *Journal of Geophysical Research (Space Physics)*, *119*(3), 1781–1796, doi:10.1002/2013JA019292.

Liu, J., V. Angelopoulos, X.-Z. Zhou, and A. Runov (2014), Magnetic flux transport by dipolarizing flux bundles, *Journal of Geophysical Research (Space Physics)*, *119*(2), 909–926, doi:10.1002/2013JA019395.

Lockwood, M., M. Hairston, I. Finch, and A. Rouillard (2009), Transpolar voltage and polar cap flux during the substorm cycle and steady convection events, *Journal of Geophysical Research (Space Physics)*, *114*(A1), A01210, doi:10.1029/2008JA013697.

Lopez, R. E. (1990), The position of the magnetotail neutral sheet in the near-Earth region, , *17*(10), 1617–1620, doi:10.1029/GL017i010p01617.

Lu, S., Q. Lu, C. Huang, and S. Wang (2013), The transfer between electron bulk kinetic energy and thermal energy in collisionless magnetic reconnection, *Physics of Plasmas*, *20*(6), 061203, doi:10.1063/1.4811119.

Lu, S., A. V. Artemyev, V. Angelopoulos, Y. Lin, and X. Y. Wang (2017), The ion temperature gradient: An intrinsic property of Earth's magnetotail, *Journal of Geophysical Research (Space Physics)*, *122*(8), 8295–8309, doi:10.1002/2017JA024209.

Lu, S., P. L. Pritchett, V. Angelopoulos, and A. V. Artemyev (2018), Magnetic reconnection in Earth's magnetotail: Energy conversion and its earthward-tailward asymmetry, *Physics of Plasmas*, *25*(1), 012905, doi:10.1063/1.5016435.

Mandt, M. E., R. E. Denton, and J. F. Drake (1994), Transition to whistler mediated magnetic reconnection, , *21*(1), 73–76, doi:10.1029/93GL03382.

Mayaud, P. N. (1980), *The AU, AL and AE Indices*, chap. 7, pp. 96–115, American Geophysical Union (AGU), doi:https://doi.org/10.1002/9781118663837.ch7.

McFadden, J. P., C. W. Carlson, D. Larson, M. Ludlam, R. Abiad, B. Elliott, P. Turin, M. Marckwordt, and V. Angelopoulos (2008), The THEMIS ESA Plasma Instrument and In-flight Calibration, , *141*(1-4), 277–302, doi:10.1007/s11214-008-9440-2.

McIlwain, C. E. (1961), Coordinates for Mapping the Distribution of Magnetically Trapped Particles, , *66*(11), 3681–3691, doi:10.1029/JZ066i011p03681.

McIlwain, C. E. (1966), Ring current effects on trapped particles, , *71*(15), 3623–3628, doi:10.1029/JZ071i015p03623.

McPherron, R. L. (1979), Magnetospheric substorms., *Reviews of Geophysics and Space Physics*, *17*, 657–681, doi:10.1029/RG017i004p00657.

McPherron, R. L. (1997), The role of substorms in the generation of magnetic storms, *Geophysical Monograph Series*, *98*, 131–147, doi:10.1029/GM098p0131.

McPherron, R. L. (2015), Earth's Magnetotail, in *Magnetotails in the Solar System*, vol. 207, pp. 61–84, doi:10.1002/9781118842324.ch4.

Milan, S. E. (2009), Both solar wind-magnetosphere coupling and ring current intensity control of the size of the auroral oval, , *36*(18), L18101, doi:10.1029/2009GL039997.

Milan, S. E., J. Hutchinson, P. D. Boakes, and B. Hubert (2009), Influences on the radius of the auroral oval, *Annales Geophysicae*, *27*(7), 2913–2924, doi:10.5194/angeo-27-2913-2009.

Milan, S. E., J. A. Carter, H. Korth, and B. J. Anderson (2015), Principal component analysis of Birkeland currents determined by the Active Magnetosphere and Planetary Electrodynamics Response Experiment, *Journal of Geophysical Research (Space Physics)*, *120*(12), 10,415–10,424, doi:10.1002/2015JA021680.

Milan, S. E., J. A. Carter, H. Sangha, G. E. Bower, and B. J. Anderson (2021), Magnetospheric Flux Throughput in the Dungey Cycle: Identification of Convection State During 2010, *Journal of Geophysical Research (Space Physics)*, *126*(2), e28437, doi:10.1029/2020JA028437.

Mist, R. T., C. J. Owen, and T. Mukai (2001), Survey of deep tail plasma sheet crossings: Plasma sheet distributions resulting from reconnection, , *28*(20), 3843–3846, doi:10.1029/2001GL013396.

Mooney, M. K., C. Forsyth, I. J. Rae, G. Chisham, J. C. Coxon, M. S. Marsh, D. R. Jackson, S. Bingham, and B. Hubert (2020), Examining Local Time Variations in the Gains and Losses of Open Magnetic Flux During Substorms, *Journal of Geophysical Research (Space Physics)*, *125*(4), e27369, doi:10.1029/2019JA027369.

Mukai, T., S. Machida, Y. Saito, M. Hirahara, T. Terasawa, N. Kaya, T. Obara, M. Ejiri, and A. Nishida (1994), The Low Energy Particle (LEP) Experlment onboard the GEOTAIL Satellite., *Journal of Geomagnetism and Geoelectricity*, *46*(8), 669–692, doi:10.5636/jgg.46.669.

Nagai, T. (2021), Magnetic Reconnection in the Near-Earth Magnetotail, in *Magnetospheres in the Solar System*, vol. 2, edited by R. Maggiolo, N. André, H. Hasegawa, and D. T. Welling, p. 49, doi:10.1002/9781119815624.ch4.

Nagai, T., I. Shinohara, S. Zenitani, R. Nakamura, T. K. M. Nakamura, M. Fujimoto, Y. Saito, and T. Mukai (2013a), Three-dimensional structure of magnetic reconnection

in the magnetotail from Geotail observations, *Journal of Geophysical Research (Space Physics)*, *118*(4), 1667–1678, doi:10.1002/jgra.50247.

Nagai, T., S. Zenitani, I. Shinohara, R. Nakamura, M. Fujimoto, Y. Saito, and T. Mukai (2013b), Ion and electron dynamics in the ion-electron decoupling region of magnetic reconnection with Geotail observations, , *118*, 7703–7713, doi:10.1002/2013JA019135.

Nagai, T., I. Shinohara, and S. Zenitani (2015), Ion acceleration processes in magnetic reconnection: Geotail observations in the magnetotail, *Journal of Geophysical Research (Space Physics)*, *120*(3), 1766–1783, doi:10.1002/2014JA020737.

Nakai, H., Y. Kamide, and C. T. Russell (1991), Influences of solar wind parameters and geomagnetic activity on the tail lobe magnetic field: A statistical study, , *96*(A4), 5511–5523, doi:10.1029/90JA02361.

Nakamura, R., W. Baumjohann, C. Mouikis, L. M. Kistler, A. Runov, M. Volwerk, Y. Asano, Z. Vörös, T. L. Zhang, B. Klecker, H. Rème, and A. Balogh (2004), Spatial scale of high-speed flows in the plasma sheet observed by Cluster, , *31*, L09804, doi:10.1029/2004GL019558.

Nakamura, R., W. Baumjohann, Y. Asano, A. Runov, A. Balogh, C. J. Owen, A. N. Fazakerley, M. Fujimoto, B. Klecker, and H. RèMe (2006), Dynamics of thin current sheets associated with magnetotail reconnection, *Journal of Geophysical Research (Space Physics)*, *111*(A11), A11206, doi:10.1029/2006JA011706.

Nishida, A., K. Uesugi, I. Nakatani, T. Mukai, D. H. Fairfield, and M. H. Acuna (1992), Geotail Mission to explore Earth's magnetotail, *EOS Transactions*, *73*(40), 425–429, doi:10.1029/91EO00314.

Nishimura, Y., J. Wygant, T. Ono, M. Iizima, A. Kumamoto, D. Brautigam, and F. Rich (2008), Large-amplitude wave electric field in the inner magnetosphere dur-

ing substorms, *Journal of Geophysical Research (Space Physics)*, *113*(A7), A07202, doi: 10.1029/2007JA012833.

Øieroset, M., T. D. Phan, R. P. Lin, and B. U. Ö. Sonnerup (2000), Walén and variance analyses of high-speed flows observed by Wind in the midtail plasma sheet: Evidence for reconnection, , *105*(A11), 25,247–25,264, doi:10.1029/2000JA900075.

Øieroset, M., T. D. Phan, M. Fujimoto, R. P. Lin, and R. P. Lepping (2001), In situ detection of collisionless reconnection in the Earth's magnetotail, , *412*, 414–417, doi: 10.1038/35086520.

Øieroset, M., R. P. Lin, T. D. Phan, D. E. Larson, and S. D. Bale (2002), Evidence for Electron Acceleration up to ~300 keV in the Magnetic Reconnection Diffusion Region of Earth's Magnetotail, , *89*(19), 195001, doi:10.1103/PhysRevLett.89.195001.

Oka, M., T. D. Phan, S. Krucker, M. Fujimoto, and I. Shinohara (2010), Electron Acceleration by Multi-Island Coalescence, , *714*(1), 915–926, doi:10.1088/0004-637X/714/1/915.

Otto, A. (2004), The Magnetosphere, in *Lecture Notes in Physics, Berlin Springer Verlag*, vol. 656, edited by K. Scherer, H. Fichter, and B. Herber, p. 133, doi:10.1007/978-3-540-31534-6_5.

Parker, E. N. (1957), Sweet's Mechanism for Merging Magnetic Fields in Conducting Fluids, , *62*(4), 509–520, doi:10.1029/JZ062i004p00509.

Petrinec, S. M., and C. T. Russell (1996), Near-Earth magnetotail shape and size as determined from the magnetopause flaring angle, , *101*(A1), 137–152, doi:10.1029/95JA02834.

Petrukovich, A., A. Artemyev, and R. Nakamura (2016), Magnetotail Reconnection, in *Magnetic Reconnection: Concepts and Applications*, *Astrophysics and Space Science Library*, vol. 427, edited by W. Gonzalez and E. Parker, p. 277, doi:10.1007/978-3-319-26432-5_7.

Petrukovich, A. A., T. Mukai, S. Kokubun, S. A. Romanov, Y. Saito, T. Yamamoto, and L. M. Zelenyi (1999), Substorm-associated pressure variations in the magnetotail plasma sheet and lobe, , *104*, 4501–4514, doi:10.1029/98JA02418.

Petrukovich, A. A., A. V. Artemyev, R. Nakamura, E. V. Panov, and W. Baumjohann (2013), Cluster observations of dBz/dx during growth phase magnetotail stretching intervals, , *118*, 5720–5730, doi:10.1002/jgra.50550.

Petschek, H. E. (1964), Magnetic Field Annihilation, in *NASA Special Publication*, vol. 50, p. 425.

Phan, T. D., M. A. Shay, J. T. Gosling, M. Fujimoto, J. F. Drake, G. Paschmann, M. Oieroset, J. P. Eastwood, and V. Angelopoulos (2013), Electron bulk heating in magnetic reconnection at Earth's magnetopause: Dependence on the inflow Alfvén speed and magnetic shear, , *40*(17), 4475–4480, doi:10.1002/grl.50917.

Phan, T. D., J. F. Drake, M. A. Shay, J. T. Gosling, G. Paschmann, J. P. Eastwood, M. Oieroset, M. Fujimoto, and V. Angelopoulos (2014), Ion bulk heating in magnetic reconnection exhausts at Earth's magnetopause: Dependence on the inflow Alfvén speed and magnetic shear angle, , *41*(20), 7002–7010, doi:10.1002/2014GL061547.

Pollock, C., T. Moore, A. Jacques, J. Burch, U. Gliese, Y. Saito, T. Omoto, L. Avanov, A. Barrie, V. Coffey, J. Dorelli, D. Gershman, B. Giles, T. Rosnack, C. Salo, S. Yokota, M. Adrian, C. Aoustin, C. Auletti, S. Aung, V. Bigio, N. Cao, M. Chandler, D. Chornay, K. Christian, G. Clark, G. Collinson, T. Corris, A. De Los Santos, R. Devlin, T. Diaz, T. Dickerson, C. Dickson, A. Diekmann, F. Diggs, C. Duncan, A. Figueroa-Vinas, C. Firman, M. Freeman, N. Galassi, K. Garcia, G. Goodhart, D. Guererro, J. Hageman, J. Hanley, E. Hemminger, M. Holland, M. Hutchins, T. James, W. Jones, S. Kreisler, J. Kujawski, V. Lavu, J. Lobell, E. LeCompte, A. Lukemire, E. MacDonald, A. Mariano, T. Mukai, K. Narayanan, Q. Nguyan, M. Onizuka, W. Paterson, S. Persyn, B. Piepgrass, F. Cheney,

A. Rager, T. Raghuram, A. Ramil, L. Reichenthal, H. Rodriguez, J. Rouzaud, A. Rucker, Y. Saito, M. Samara, J.-A. Sauvaud, D. Schuster, M. Shappirio, K. Shelton, D. Sher, D. Smith, K. Smith, S. Smith, D. Steinfeld, R. Szymkiewicz, K. Tanimoto, J. Taylor, C. Tucker, K. Tull, A. Uhl, J. Vloet, P. Walpole, S. Weidner, D. White, G. Winkert, P.-S. Yeh, and M. Zeuch (2016), Fast Plasma Investigation for Magnetospheric Multiscale, , *199*, 331–406, doi:10.1007/s11214-016-0245-4.

Pontin, D. I., and E. R. Priest (2022), Magnetic reconnection: MHD theory and modelling, *Living Reviews in Solar Physics*, *19*(1), 1, doi:10.1007/s41116-022-00032-9.

Pontius, J., D. H., and R. A. Wolf (1990), Transient flux tubes in the terrestrial magnetosphere, , *17*(1), 49–52, doi:10.1029/GL017i001p00049.

Poppe, A. R., M. O. Fillingim, J. S. Halekas, J. Raeder, and V. Angelopoulos (2016), ARTEMIS observations of terrestrial ionospheric molecular ion outflow at the Moon, , *43*(13), 6749–6758, doi:10.1002/2016GL069715.

Priest, E., and T. Forbes (2000), *Magnetic Reconnection: MHD Theory and Applications*, doi:10.1017/CBO9780511525087.

Pulkkinen, T. I., N. Y. Ganushkina, E. I. Kallio, G. Lu, D. N. Baker, N. E. Turner, T. A. Fritz, J. F. Fennell, and J. Roeder (2002), Energy dissipation during a geomagnetic storm: May 1998, *Advances in Space Research*, *30*(10), 2231–2240, doi:10.1016/S0273-1177(02)80232-0.

Pulkkinen, T. I., M. Palmroth, H. E. J. Koskinen, T. V. Laitinen, C. C. Goodrich, V. G. Merkin, and J. G. Lyon (2010), Magnetospheric modes and solar wind energy coupling efficiency, *Journal of Geophysical Research (Space Physics)*, *115*(A3), A03207, doi:10.1029/2009JA014737.

Pytte, T., R. L. McPherron, J. Hones, E. W., and J. West, H. I. (1978), Multiple-satellite

studies of magnetospheric substorms: Distinction between polar magnetic substorms and convection-driven negative bays, , *83*(A2), 663–679, doi:10.1029/JA083iA02p00663.

Qiu, S., Z. Zhang, H. Yousof, W. Soon, M. Jia, W. Tang, and X. Dou (2022), The interplanetary origins of geomagnetic storm with $Dst_{min} \leq$ - 50 nT during solar cycle 24 (2009-2019), *Advances in Space Research*, *70*(7), 2047–2057, doi:10.1016/j.asr.2022.06.025.

Richardson, I. G., and H. V. Cane (2010), Near-Earth Interplanetary Coronal Mass Ejections During Solar Cycle 23 (1996 - 2009): Catalog and Summary of Properties, , *264*(1), 189–237, doi:10.1007/s11207-010-9568-6.

Richardson, I. G., S. W. H. Cowley, J. Hones, E. W., and S. J. Bame (1987), Plasmoid-associated energetic ion bursts in the deep geomagnetic tail: Properties of plasmoids and the postplasmoid plasma sheet, , *92*(A9), 9997–10,013, doi:10.1029/JA092iA09p09997.

Rogers, A. J., C. J. Farrugia, and R. B. Torbert (2019), Numerical Algorithm for Detecting Ion Diffusion Regions in the Geomagnetic Tail With Applications to MMS Tail Season 1 May to 30 September 2017, *Journal of Geophysical Research (Space Physics)*, *124*(8), 6487–6503, doi:10.1029/2018JA026429.

Runov, A., R. Nakamura, W. Baumjohann, R. A. Treumann, T. L. Zhang, M. Volwerk, Z. Vörös, A. Balogh, K.-H. Glaßmeier, B. Klecker, H. Rème, and L. Kistler (2003), Current sheet structure near magnetic X-line observed by Cluster, , *30*, 1579, doi:10.1029/2002GL016730.

Runov, A., W. Baumjohann, R. Nakamura, V. A. Sergeev, O. Amm, H. Frey, I. Alexeev, A. N. Fazakerley, C. J. Owen, E. Lucek, M. André, A. Vaivads, I. Dandouras, and B. Klecker (2008), Observations of an active thin current sheet, *Journal of Geophysical Research (Space Physics)*, *113*(A7), A07S27, doi:10.1029/2007JA012685.

Runov, A., V. Angelopoulos, X. Z. Zhou, X. J. Zhang, S. Li, F. Plaschke, and J. Bonnell (2011), A THEMIS multicase study of dipolarization fronts in the magnetotail plasma

sheet, *Journal of Geophysical Research (Space Physics)*, *116*(A5), A05216, doi:10.1029/2010JA016316.

Runov, A., V. Angelopoulos, A. Artemyev, S. Lu, and X.-Z. Zhou (2018), Near-Earth Reconnection Ejecta at Lunar Distances, , *123*, 2736–2744, doi:10.1002/2017JA025079.

Runov, A., V. Angelopoulos, M. G. Henderson, C. Gabrielse, and A. Artemyev (2021a), Magnetotail Dipolarizations and Ion Flux Variations During the Main Phase of Magnetic Storms, *Journal of Geophysical Research (Space Physics)*, *126*(5), e28470, doi:10.1029/2020JA028470.

Runov, A., V. Angelopoulos, A. V. Artemyev, J. M. Weygand, S. Lu, Y. Lin, and X. J. Zhang (2021b), Global and local processes of thin current sheet formation during substorm growth phase, *Journal of Atmospheric and Solar-Terrestrial Physics*, *220*, 105671, doi:10.1016/j.jastp.2021.105671.

Runov, A., V. Angelopoulos, J. M. Weygand, A. V. Artemyev, F. Beyene, V. Sergeev, M. Kubyshkina, and M. G. Henderson (2022), Thin Current Sheet Formation and Reconnection at X $\sim$ -10 R_E During the Main Phase of a Magnetic Storm, *Journal of Geophysical Research (Space Physics)*, *127*(9), e30669, doi:10.1029/2022JA030669.

Runov, A., V. Angelopoulos, K. Khurana, J. Liu, M. Balikhin, and A. Artemyev (2023), Properties of Quiet Magnetotail Plasma Sheet at Lunar Distances, *Journal of Geophysical Research (Space Physics)*, doi:10.1029/2023JA031908.

Russell, C. T., and R. L. McPherron (1973), The Magnetotail and Substorms, , *15*(2-3), 205–266, doi:10.1007/BF00169321.

Russell, C. T., B. J. Anderson, W. Baumjohann, K. R. Bromund, D. Dearborn, D. Fischer, G. Le, H. K. Leinweber, D. Leneman, W. Magnes, J. D. Means, M. B. Moldwin, R. Nakamura, D. Pierce, F. Plaschke, K. M. Rowe, J. A. Slavin, R. J. Strangeway, R. Tor-

bert, C. Hagen, I. Jernej, A. Valavanoglou, and I. Richter (2016), The Magnetospheric Multiscale Magnetometers, , *199*, 189–256, doi:10.1007/s11214-014-0057-3.

Sanny, J., R. L. McPherron, C. T. Russell, D. N. Baker, T. I. Pulkkinen, and A. Nishida (1994), Growth-phase thinning of the near-Earth current sheet during the CDAW 6 substorm, , *99*(A4), 5805–5816, doi:10.1029/93JA03235.

Sarris, E. T., S. M. Krimigis, and T. P. Armstrong (1976), Observations of magnetospheric bursts of high-energy protons and electrons at $\sim$35 R_E with Imp 7, , *81*(13), 2341, doi:10.1029/JA081i013p02341.

Schödel, R., R. Nakamura, W. Baumjohann, and T. Mukai (2001), Rapid flux transport and plasma sheet reconfiguration, , *106*(A5), 8381–8390, doi:10.1029/2000JA900159.

Sckopke, N. (1966), A general relation between the energy of trapped particles and the disturbance field near the Earth, , *71*(13), 3125–3130, doi:10.1029/JZ071i013p03125.

Sergeev, V. (1977), On the state of the magnetosphere during prolonged period of southward oriented imf, *Phys. Solariterr. Potsdam*, *5*, 39.

Sergeev, V., A. Runov, W. Baumjohann, R. Nakamura, T. L. Zhang, A. Balogh, P. Louarnd, J. A. Sauvaud, and H. Reme (2004), Orientation and propagation of current sheet oscillations, , *31*(5), L05807, doi:10.1029/2003GL019346.

Sergeev, V. A., R. J. Pellinen, and T. I. Pulkkinen (1996), Steady Magnetospheric Convection: A Review of Recent Results, , *75*(3-4), 551–604, doi:10.1007/BF00833344.

Sergeev, V. A., M. V. Kubyshkina, K. Liou, P. T. Newell, G. Parks, R. Nakamura, and T. Mukai (2001), Substorm and convection bay compared: Auroral and magnetotail dynamics during convection bay, , *106*(A9), 18,843–18,856, doi:10.1029/2000JA900087.

Sergeev, V. A., I. A. Chernyaev, S. V. Dubyagin, Y. Miyashita, V. Angelopoulos, P. D. Boakes, R. Nakamura, and M. G. Henderson (2012), Energetic particle injections to geo-

stationary orbit: Relationship to flow bursts and magnetospheric state, *Journal of Geophysical Research (Space Physics)*, *117*(A10), A10207, doi:10.1029/2012JA017773.

Shirai, H., K. Maezawa, M. Fujimoto, T. Mukai, T. Yamamoto, Y. Saito, and S. Kokubun (1998), Entry process of low-energy electrons into the magnetosphere along open field lines: Polar rain electrons as field line tracers, , *103*(A3), 4379–4390, doi:10.1029/97JA02031.

Shukhtina, M. A., E. I. Gordeev, and V. A. Sergeev (2009), Time-varying magnetotail magnetic flux calculation: a test of the method, *Annales Geophysicae*, *27*(4), 1583–1591, doi:10.5194/angeo-27-1583-2009.

Shukhtina, M. A., E. I. Gordeev, V. A. Sergeev, N. A. Tsyganenko, L. B. N. Clausen, and S. E. Milan (2016), Magnetotail magnetic flux monitoring based on simultaneous solar wind and magnetotail observations, *Journal of Geophysical Research (Space Physics)*, *121*(9), 8821–8839, doi:10.1002/2016JA022911.

Siscoe, G. L., and T. S. Huang (1985), Polar cap inflation and deflation, , *90*(A1), 543–547, doi:10.1029/JA090iA01p00543.

Sitnov, M., J. Birn, B. Ferdousi, E. Gordeev, Y. Khotyaintsev, V. Merkin, T. Motoba, A. Otto, E. Panov, P. Pritchett, F. Pucci, J. Raeder, A. Runov, V. Sergeev, M. Velli, and X. Zhou (2019), Explosive Magnetotail Activity, , *215*(4), 31, doi:10.1007/s11214-019-0599-5.

Sitnov, M. I., M. Swisdak, J. F. Drake, P. N. Guzdar, and B. N. Rogers (2004), A model of the bifurcated current sheet: 2. Flapping motions, , *31*(9), L09805, doi:10.1029/2004GL019473.

Sitnov, M. I., V. G. Merkin, M. Swisdak, T. Motoba, N. Buzulukova, T. E. Moore, B. H. Mauk, and S. Ohtani (2014), Magnetic reconnection, buoyancy, and flapping motions in magnetotail explosions, *Journal of Geophysical Research (Space Physics)*, *119*(9), 7151–7168, doi:10.1002/2014JA020205.

Smith, P. H., and R. A. Hoffman (1973), Ring current particle distributions during the magnetic storms of December 16-18, 1971, , *78*(22), 4731, doi:10.1029/JA078i022p04731.

Sonnerup, B. U. Ö. (1979), Magnetic field reconnection, in *Solar System Plasma Physics*, vol. 3, pp. 45–108.

Sweet, P. A. (1958), The Neutral Point Theory of Solar Flares, in *Electromagnetic Phenomena in Cosmical Physics*, vol. 6, edited by B. Lehnert, p. 123.

Tsurutani, B. T., W. D. Gonzalez, A. L. C. Gonzalez, F. Tang, J. K. Arballo, and M. Okada (1995), Interplanetary origin of geomagnetic activity in the declining phase of the solar cycle, , *100*(A11), 21,717–21,734, doi:10.1029/95JA01476.

Tsyganenko, N. A., V. A. Andreeva, and E. I. Gordeev (2015), Internally and externally induced deformations of the magnetospheric equatorial current as inferred from spacecraft data, *Annales Geophysicae*, *33*(1), 1–11, doi:10.5194/angeo-33-1-2015.

Ueno, G., S. Machida, T. Mukai, Y. Saito, and A. Nishida (1999), Distribution of X-type magnetic neutral lines in the magnetotail with Geotail observations, , *26*(22), 3341–3344, doi:10.1029/1999GL010714.

Vasyliunas, V. M. (1970), Mathematical Models of Magnetospheric Convection and Its Coupling to the Ionosphere, in *Particles and Field in the Magnetosphere*, *Astrophysics and Space Science Library*, vol. 17, edited by B. M. McCormack and A. Renzini, p. 60, doi:10.1007/978-94-010-3284-1_6.

Virtanen, P., R. Gommers, T. E. Oliphant, M. Haberland, T. Reddy, D. Cournapeau, E. Burovski, P. Peterson, W. Weckesser, J. Bright, S. J. van der Walt, M. Brett, J. Wilson, K. J. Millman, N. Mayorov, A. R. J. Nelson, E. Jones, R. Kern, E. Larson, C. J. Carey, İ. Polat, Y. Feng, E. W. Moore, J. VanderPlas, D. Laxalde, J. Perktold, R. Cimrman, I. Henriksen, E. A. Quintero, C. R. Harris, A. M. Archibald, A. H. Ribeiro, F. Pe-

dregosa, P. van Mulbregt, and SciPy 1.0 Contributors (2020), SciPy 1.0: Fundamental Algorithms for Scientific Computing in Python, *Nature Methods*, *17*, 261–272, doi:10.1038/s41592-019-0686-2.

Wing, S., and P. T. Newell (1998), Central plasma sheet ion properties as inferred from ionospheric observations, , *103*(A4), 6785–6800, doi:10.1029/97JA02994.

Wolf, R. A. (1970), Effects of ionospheric conductivity on convective flow of plasma in the magnetosphere, , *75*(25), 4677, doi:10.1029/JA075i025p04677.

Wolf, R. A. (1983), The quasi-static (slow-flow) region of the magnetosphere, in *Solar-Terrestrial Physics: Principles and Theoretical Foundations*, *Astrophysics and Space Science Library*, vol. 104, edited by R. L. Carovillano and J. M. Forbes, pp. 303–368, doi:10.1007/978-94-009-7194-3_14.

Wolf, R. A., J. Freeman, J. W., B. A. Hausman, R. W. Spiro, R. V. Hilmer, and R. L. Lambour (1997), Modeling convection effects in magnetic storms, *Geophysical Monograph Series*, *98*, 161–172, doi:10.1029/GM098p0161.

Wygant, J. R., A. Keiling, C. A. Cattell, M. Johnson, R. L. Lysak, M. Temerin, F. S. Mozer, C. A. Kletzing, J. D. Scudder, W. Peterson, C. T. Russell, G. Parks, M. Brittnacher, G. Germany, and J. Spann (2000), Polar spacecraft based comparisons of intense electric fields and Poynting flux near and within the plasma sheet-tail lobe boundary to UVI images: An energy source for the aurora, , *105*(A8), 18,675–18,692, doi:10.1029/1999JA900500.

Zhou, X. Y., C. T. Russell, J. T. Gosling, and D. G. Mitchell (1997), Three spacecraft observations of the geomagnetic tail during moderately disturbed conditions: Structure and evolution of the current sheet, , *102*(A7), 14,415–14,424, doi:10.1029/97JA00038.